Wiskundige bepaling van reactienetwerken
uit niet-stationaire kinetische experimenten

Mathematical Determination of Reaction Networks
from Transient Kinetic Experiments

Raf Roelant

Promotoren: prof. dr. ir. G. B. Marin, dr. D. Constales
Proefschrift ingediend tot het behalen van de graad van
Doctor in de Ingenieurswetenschappen: Chemische Technologie

Vakgroep Chemische Proceskunde en Technische Chemie
Voorzitter: prof. dr. ir. G. B. Marin
Faculteit Ingenieurswetenschappen en Architectuur
Academiejaar 2010 - 2011

UNIVERSITEIT
GENT

ISBN 978-90-8578-402-9
NUR 952, 919
Wettelijk depot: D/2011/10.500/6

Promotoren:

Prof. dr. ir. Guy B. Marin	Universiteit Gent	
Dr. Denis Constales	Universiteit Gent	

Overige leden van de examencommissie:

Prof. dr. ir. Dirk Aeyels	Universiteit Gent	
Dr. Vladimir Galvita	Universiteit Gent	
Prof. dr. Alexander Gorban	University of Leicester	
Dr. ir. Yves Schuurman	IRCELYON	
Prof. dr. Roger Van Keer	Universiteit Gent	
Prof. dr. ir. Joris Thybaut	Universiteit Gent	Secretaris
Prof. dr. ir. Daniël De Zutter	Universiteit Gent	Voorzitter

Van oktober 2005 tot en met augustus 2010 was de doctorandus verbonden aan het Laboratorium voor Chemische Technologie van de Universiteit Gent. Tot en met augustus 2009 werkte hij er als aspirant voor het Fonds voor Wetenschappelijk Onderzoek - Vlaanderen. Daarna werkte hij er als assistent.

Laboratorium voor Chemische Technologie
Vakgroep Chemische Proceskunde en Technische Chemie
✉ Krijgslaan 281 (S5), B-9000 Gent, België
☎ +32 9 264 45 16 FAX +32 9 264 49 99
www.LCT.UGent.be

Dankwoord

Bij het verschijnen van dit proefschrift wil ik graag een aantal mensen bedanken. In de eerste plaats denk ik natuurlijk aan mijn promotoren. Guy, bedankt om me opgenomen te hebben in LCT. Vanwege je grote en gevarieerde takenpakket was het zeker zeker niet vanzelfsprekend om dit onderzoek mee te coördineren, maar je hebt je met verve van deze taak gekweten. Denis, met jouw snelle geest en grote wiskundige ervaring heb je inhoudelijk zeer belangrijke bijgedragen geleverd tot dit werk. Roger, hoewel geen promotor was jij van bij het begin betrokken bij alle vergaderingen. Je blijken van appreciatie hebben me keer op keer gemotiveerd. Hartelijk dank, Guy, Denis en Roger!

De TAP-opstelling van het LCT zal weldra worden vervangen door een nieuw exemplaar. Tijdens mijn jaren aan het LCT was ik er getuige van dat zes collega's de nukkige bejaarde dame in leven hielden. Met Isabelle Sack en René De Coster heb ik maar korte tijd samengewerkt, maar ik heb wel mee de vruchten geplukt van hun noeste arbeid. Isabelle en René, bedankt hiervoor. Veerle Balcaen is de collega waarmee ik het meest intensief heb samengewerkt. Veerle, je hebt me vaak de weg gewezen in de TAP-databank. Ik heb veel gehad aan onze niet altijd even wetenschappelijke babbels. Het zal me veel plezier doen als je binnen kort je bul in ontvangst mag nemen. Andy De Prez is als technisch medewerker niet heel lang werkzaam bent geweest aan het LCT. Niettemin heb ik met hem een goeie band gesmeed. Bedankt voor alles, Andy.
Unmesh Menon, when joining the lab as a PhD student, reminded me of myself as a disoriented novice. Unmesh, thanks to you I have learnt a lot of interesting facts about cricket and the culture, fauna and flora of Kerala and Tamil Nadu. I wish you good luck finishing your PhD and mapping out a route to a brilliant future. Vladimir Galvita joined the lab as a post-doctoral researcher when I was already wrapping up. Otherwise we would certainly have collaborated more intensively. Vladimir, your optimism as a researcher was inspiring! My collaboration with Kostas Alexopoulos and Hilde Poelman was less intense, but nonetheless pleasant and rewarding.

Jorge Aníbal Lobos Martín, María Fe Fernández Herrero and Sil-

via Fernández Rioseco prepared their master thesis under my guidance. Aníbal, Marifé and Silvia, I'm sure the thesis represented the least interesting part of your Erasmus experience in Ghent. Therefore I am extra grateful for your dedication! It was a very pleasant and interesting experience to meet you. I am particularly thankful to have met Marifé, who has made me love Spain and the Spaniards.

I would also like to thank all colleagues of the LCT not directly involved in this work. Allow me to mention some people in particular. Edward Baudrez, je hebt me cultuur bijgebracht door me te vormen tot Linux vrijbuiter. Ik herken veel van mezelf in jou. De die hard sportvrienden Rhona Van Borm, Georges Verenghen, Tom Ravelingien, Joris Thybaut, Joris Wieme en Philippe Heynderickx wil ik bedanken voor de vele olympische prestaties op de middag. Bij Jo staat het Christmas bier al fris! Rhona, we hebben vele kilometers in de benen, maar de finish is nu in zicht! Philippe, terugblikkend op onze camaraderie zeg ik u voorwaar... wat boertig is geweest, zal nog superboertig worden! Je hebt deze tekst zorgvuldig nagelezen, waarvoor veel dank! *I will always keep good memories of Lien Bentein, Dagmar D'hooge, Carolina Toloza, Evelyn Burrick, Paul Van Steenberge, members of the LCT's plastic group. There was always something interesting going on in the plastics corner. I will also miss the coffee breaks. Some of the frequent visitors not yet mentioned above were Etienne Van Damme, Marcel Vervust, Hans Heene and Geraldine Heynderickx. I am not going to mention all other colleagues by name, but I wish to thank them for the good times on the workfloor.* Graag wil ik ook de lieve mensen van ons secretariaat vermelden: mijn gouwgenoten Hilde Van Peteghem, Petra Vereecken en Kevin De Wolf, en daarnaast Kim Verbeeck.

Met het schrijven van dit doctoraal proefschrift eindigt een eerste fase van mijn leven: mijn jaren van opleiding. Die jaren zijn begonnen in mijn geboorteplaats Sint-Niklaas. Daar heb ik het voorrecht genoten mijn middelbare studies te mogen doorlopen aan de ijzersterke doch warme en pretentieloze humaniora van de Broederschool. In het bijzonder wil ik een wiskundeleraar bedanken: Philip Puylaert. Met zijn aanstekelijke manier van lesgeven heeft hij mijn wetenschappelijke interesse meer dan wie ook aangewakkerd. Aan mijn humanioratijd heb ik trouwens een schare trouwe vrienden te danken: Filip De Bock, Benny Colyn, Ineke van Gremberghe, Venessa Van Eeckhoven, Bert Van Bocxlaer, Pieter van Remortel, Bert Houcque, Kristof Van Royen, Michiel Van Bel, Dominiek Masschelein, Jeroen Vereecken, Wendy De Bruycker, Claudia Bollaert, Bavo Heeman, Ruben Jolie, Ans De Rouck, David Saeys, Kathleen Pippeleers, Yves Peirsman, Johan Leys, Wouter Goossens, Tess Grobben, Bert Verbist en Stephanie Van Weyenberg. Tijdens mijn jaren aan de universiteit zijn vrienden gekomen en gegaan, maar met enkelen

was het contact duurzaam. Ik denk in de eerste plaats aan de lichting scheikundig ingenieurs van 2005: Robin Matton, Kim De Brandt, Klaar Van Hecke, Bart De Smet, Matthias Braem, Kevin De Caluwé, Veronique Mariën, An Van Pottelberghe, Wim Wuytack, Ties Debruyne en wijlen Tine Van Camp. Ook mijn metallurgische connectie ligt me na aan het hard: Helger Delarbre, Erwin Van Eester en Annelies Wtterwulghe. Buiten de lessen en het werk maakte ik kennis met een sympathiek drietal uit Pamel: Klaas De Groote, Ellen Van Den Nest en Samuel Nieuwborg. Met al deze vrienden heb ik ontelbare oergezellige uurtjes doorgebracht. Zonder deze afleiding zou ik dit zware werk nooit hebben volgehouden. Heel veel dank!

Het laatste woord van dank wil ik richten aan mijn ouders Christine Verstraete en Fons Roelant en zus Katja Roelant. Doordat ik vaak met het werk bezig was en doordat jullie veel huishoudelijke klussen voor mij hebben opgeknapt, hebben we te weinig ontspannende tijd met elkaar doorgebracht. Het mag nu wat meer zijn! Oneindig veel dank voor alles!

Contents

Samenvatting

Heterogene katalysatoren zijn alom tegenwoordig in de chemische industrie. Zoals elke andere reactie is ook een heterogeen gekatalyseerde reactie het resultaat van een netwerk van elementaire stappen. De kennis van het reactienetwerk, of kenmerken ervan, is erg belangrijk. Ten eerste biedt ze een waardevol hulpmiddel in de steeds intensiever wordende zoektocht naar actievere en selectievere katalysatoren. Ten tweede kan ze gebruikt worden als basis bij het ontwerp en de optimalisatie van het bedrijf van productie-eenheden. De meest waardevolle gegevens voor de bepaling van reactienetwerken worden verschaft door niet-stationaire experimenten. Het doel van dit werk was de ontwikkeling van wiskundige middelen om dergelijke gegevens met dat doel te verwerken.

Tijdens niet-stationaire experimenten worden reactiekinetische fenomenen gemeten die het reactienetwerk weerspiegelen. De experimenten worden vaak zo ontworpen, dat de elementaire stappen pseudomonomoleculair kunnen worden beschouwd. In dit werk werd pseudomonomoleculaire kinetiek systeemtheoretisch benaderd als een lineair tijdsinvariant toestandsmodel. Dit model werd beschreven middels kinetische transferfuncties in het Laplace domein. Gewoonlijk gaat het over een compartimentenmodel, en zo niet kan het er vaak in worden omgezet. Dit maakt het mogelijk kinetische transferfuncties af te leiden uit een reactiegraaf, een gerichte graaf die het reactienetwerk voorstelt. Grafentheoretische regels werden hiertoe geformuleerd. Belangrijker is dat de symbolische vorm van de transfer functies blijkt af te hangen van connectiviteitskenmerken van de reactiegraaf: het aantal intermediairen en de lengte van het kortste reactiepad tussen tweetallen componenten.

In dit werk lag de klemtoon op een niet-stationair experiment genaamd *temporal analysis of products* (TAP). Dit experiment wordt uitgevoerd op een vastbedreactor beladen met katalysator. Aan de inlaat van de reactor worden pulsen van reagentia aangeleverd, terwijl aan de uitlaat doorlopend een vacuüm wordt onderhouden. Reactieproducten en niet omgezette reagentia verlaten de reactor hier, terwijl hun moldebieten in de vorm van tijdsreeksen worden geregistreerd door een massaspectrometer.

De kinetiek van de reactie(s) is typisch pseudomonomoleculair vanwege de kleine gepulste hoeveelheden (typisch 1 nmol), welke geen significante verandering veroorzaken van het katalysatoroppervlak. Er werd een reactiemodel gegeven en twee numerieke methoden werden voorgesteld om dit model te integreren. Er werd een gedetailleerde studie uitgevoerd naar de ruis aanwezig in de tijdreeksen verkregen door TAP, omdat deze ruis de hoeveelheid informatie beperkt die eruit kan worden afgeleid. Twee soorten ruis werden onderscheiden uit gegevens afkomstig van twee verschillende experimentele opstellingen: gekleurde Gaussische ruis en spectraal gelokaliseerde ruis. Terwijl de eerste soort verondersteld wordt essentieel te zijn, is de tweede te wijten aan interferentie door het lichtnet. Behalve de ruis is er een toevallige variabiliteit van de signaalsterkte te wijten aan een zwak reproduceerbare pulsgrootte en/of een veranderlijke gevoeligheid van de massaspectrometer.

De meest rigoureuze manier om niet-stationair kinetische gegevens kwantitatief te verwerken is door kleinste-kwadratenregressie. Nochtans veronderstelt dit strikt gesproken een ideale ruis, i.e., een Gaussische, homoskedastische en witte ruis. Deze voorwaarde is niet altijd vervuld. Voor TAP heeft voormelde analyse van de ruis bijvoorbeeld aan het licht gebracht dat dit algemeen gesproken niet zo is. Er werd gevonden dat een lineaire voorafgaande transformatie dit probleem verhelpt. De transformatie is gebaseerd op tweede-orde statistische kenmerken van de ruis, zoals geschat uit herhalingsexperimenten. De nieuwe regressiemethode werd daarom *second-order statistical regression* (SOSR) genoemd. De SOSR werd geïmplementeerd in een simulatie-regressieprogramma voor TAP, genaamd TAPFIT. Toepassing van dit programma op synthetische gegevens heeft aangetoond dat de SOSR resulteert in nauwkeurigere parameterschattingen en betrouwbaarheidsintervallen dan de onmiddellijke kleinste-kwadratenregressie. Het programma werd ook toegepast op experimentele gegevens verzameld voor enerzijds de studie van de adsorptie van zuurstof op een V_2O_5 katalysator en anderzijds de interactie van propaan met een CuO–CeO_2/γ–Al_2O_3 katalysator.

Zelfs als de kinetische gegevens geen ruis bevatten, kan het onmogelijk blijken alle kinetische parameters te schatten door regressie. Dit gebeurt vaak als alle gegevens verzameld werden bij dezelfde reactietemperatuur. Het voornoemde grafentheoretische kader werd toegepast om een nodige voorwaarde tot identificeerbaarheid te formuleren in termen van de connectiviteitskenmerken van de reactiegraaf. Het al dan niet vervuld zijn van deze voorwaarde is nagegaan voor enkele voorbeelden, o.a. de interactie van propaan met een CuO–CeO_2/γ–Al_2O_3 katalysator, zoals bestudeerd via TAP.

De klassieke methode om een reactienetwerk te bepalen behelst de veronderstelling van een aantal mogelijke netwerken, de implementatie

van elk ervan in een fysisch-chemisch reactiemodel en de regressie van de gegevens met elk van deze modellen. Een of meerdere reactienetwerken worden geselecteerd, overeenkomstig de modellen die de gegevens het best beschrijven. De lijst van mogelijke reactienetwerken is nooit volledig. Bovendien kunnen ze kinetische parameters bevatten die niet identificeerbaar blijken. Er werd een alternatieve, modelvrije werkwijze onderzocht die geen veronderstelling vereist van mogelijke reactienetwerken. Deze werkwijze steunt op de berekening van kinetische transferfuncties in een aantal frequenties. Een dergelijke berekening is mogelijk uitgaande van gegevens van dunne-zone-TAP, na toepassing van de Y-procedure. Hierboven werd vermeld dat de kinetische transferfuncties de connectiviteitskenmerken van de reactiegraaf weerspiegelen. Als de berekende waarden onder deze transferfuncties worden uitgezet in Bode diagrammen, kunnen deze kenmerken worden afgelezen. Er werden numerieke experimenten uitgevoerd om de uitvoerbaarheid van deze procedure te bevestigen.

Tenslotte werden een aantal richtlijnen gegeven om het hoofd te bieden aan de technische beperkingen van het TAP-apparaat: de zwakke reproduceerbaarheid van de pulsgrootte, de aanwezigheid van ruis en de onmogelijkheid voor één massaspectrometer om meer dan een massa op te volgen. In verband met de spectrometer werd aangeraden de collectietijd lang genoeg in te stellen, een bemonsteringsfrequentie van ongeveer 1 kHz in acht te nemen en spectraal gelokaliseerde ruis indien mogelijk te vermijden. In verband met de instelling van de pulskleppen werden verscheidene redenen gegeven om vele kleine pulsen te geven in plaats van één grote. Traditioneel worden ter voorbereiding van kleinste-kwadratenregressie de ruwe tijdsreeksen opgemeten in V getransformeerd tot tijdsreeksen die de moldebieten voorstellen, in mol/s. Aan de hand van synthetische gegevens werd echter aangetoond dat de onmiddellijke regressie van de ruwe tijdsreeksen meer accurate betrouwbaarheidsintervallen oplevert voor de schattingen. De reden hiervoor is dat met de transformatie van tijdsreeksen nadelige kruiscorrelaties worden geïntroduceerd. Schatting van logaritmen van kinetische parameters in plaats van die parameters zelf werd voorgesteld als manier om de robuustheid van de regressie te bevorderen. Indien mogelijk moeten fysische parameters, zoals pulsgroottes en diffusiecoëfficiënten, onafhankelijk geschat worden. Hierboven werd reeds vermeld dat de traditionele manier om reactienetwerken te bepalen erin bestaat gegevens te regresseren met verschillende mogelijke modellen. Het Bayesiaans informatiecriterium (BIC), dat eenvoudige kinetische modellen bevoordeelt, werd voorgesteld om de discriminatie door te voeren. De richtlijnen werden toegepast op de experimentele bepaling van de aard van de interactie van propaan en propeen op een V_2O_5 katalysator. Een reactienetwerk werd geselecteerd waarin propaan ofwel onmiddellijk ofwel via een oxidatieve dehydrogenering tot propeen wordt geoxideerd.

Summary

Heterogeneous catalysts are omnipresent in the chemical industry. Like any other reaction, a heterogeneous catalytic reaction occurs as a result of a network of elementary steps. Knowledge of the reaction network, or features of it, is highly relevant. Firstly, it provides an important tool in the ever-intensifying search for more active and selective catalysts. Secondly, such information can be used as a basis for the design and operational optimization of production units. In order to determine reaction networks, the most valuable data stem from transient experiments. The aim of the present work was to develop mathematical tools to process such data with that purpose.

During transient experiments, reaction-kinetic phenomena are measured, which reflect the reaction network. The experiments are often designed so, that the elementary steps can be considered pseudomonomolecular. In this work, pseudomonomolecular kinetics have been approached system-theoretically as a linear time-invariant state-space model. This model has been described in terms of kinetic transfer functions in the Laplace domain. Usually, the state-space model is, or can be made into, a compartmental one. This allows the determination of kinetic transfer functions from the reaction graph, a directed graph representing the reaction network. Graph-theoretical rules have been formulated. More importantly, the symbolic form of the transfer functions has been shown to depend only on connectivity features of the reaction graph: the number of intermediates and the length of the shortest reaction pathway between pairs of components.

In this work, the focus lay on a transient experiment referred to as temporal analysis of products (TAP). This experiment is performed on a fixed bed reactor loaded with catalyst. Pulses of reactants are admitted at the inlet the reactor, while the outlet is continuously evacuated by vacuum pumps. Reaction products and unconverted reactants leave the reactor there, their molar flow rates being recorded in the form of time series by a mass spectrometer. The kinetics of the reaction(s) are typically pseudomonomolecular because of the small size of the pulses (typically

1 nmol), which do not cause a significant change of the composition of the catalyst surface. A reactor model has been given and two numerical methods have been presented to integrate this model. A detailed study was devoted to the noise present in the time series obtained from TAP, as this noise limits the amount of information which can be extracted from them. Two types of noise have been distinguished in data from two different experimental setups: colored Gaussian noise and spectrally localized noise. While the first one is believed to be essential, the second one is due to mains frequency interference. Besides the noise, there is a random variability of the signal strength caused by a poorly reproducible pulse size and/or a variable mass spectrometer sensitivity.

The most rigorous way to process transient kinetic data quantitatively is through least-squares regression. However, strictly speaking, this requires the noise to be ideal, i.e., Gaussian, homoskedastic and white. This condition is not always fulfilled. For TAP, for example, the noise analysis revealed that it is generally not. A linear conditioning transform was found to overcome this issue. The conditioning transform is based on second-order statistical properties of the noise, as estimated from replicate-experimental data. The novel regression approach has therefore been termed second-order statistical regression (SOSR). The SOSR has been implemented in a simulation-regression program for TAP, called TAPFIT. Application of this program to synthetic data has demonstrated the SOSR to result in more accurate parameter estimates and confidence intervals than direct least-squares regression. The program has also been applied to experimental data concerning the adsorption of oxygen on a V_2O_5 based catalyst and the interaction of propane with a CuO–CeO_2/γ–Al_2O_3 catalyst.

Even if the kinetic data are not contaminated with noise, it may be impossible to estimate all of its kinetic parameters by regression. This occurs often if all data have been collected at the same reaction temperature. The graph-theoretical framework mentioned above has been applied to formulate a necessary condition for identifiability in terms of the connectivity features of the reaction graph. Whether this condition is fulfilled has been verified for some examples, including the interaction of propane with a CuO–CeO_2/γ–Al_2O_3 catalyst, as studied by TAP.

The classical way to determine a reaction network is by postulating a number of candidates, implementing each of them in a physico-chemical reaction model and regressing the data with each of these models. One or more reaction networks are selected, corresponding to the models providing the best description of the data. The list of candidate reaction networks is never exhaustive. Moreover, some of the reaction networks may have kinetic parameters which are unidentifiable. An alternative approach was explored, which is model-free, i.e., it does not require the

postulation of candidate reaction networks. The procedure relies on the calculation of kinetic transfer functions for equally spaced frequencies. Such a calculation is possible from thin-zone-TAP-data, after application of the Y-procedure. It was mentioned above that the kinetic transfer functions reflect the connectivity features of the reaction graph. Investigation of Bode plots representing the calculated values of these transfer functions allows the determination of these features. Numerical experiments have been performed to confirm the feasibility of the procedure.

Finally, a set of guidelines was presented in order for the TAP-user to deal with the technical limitations of the apparatus: the poor reproducibility of the pulse size, the presence of noise and the impossibility of one mass spectrometer to monitor more than one mass. Regarding the spectrometer, the advice was given to set the collection time long enough, to apply a sampling frequency of about 1 kHz and to prevent spectrally localized noise at its root if possible. Regarding the settings of the pulse valves, several reasons have been given for admitting many small pulses instead of one large one. Traditionally, in preparation of least-squares regression, the raw time series measured in V are transformed into time series representing molar flow rates in mol/s. It has been demonstrated by means of synthetic data that regressing the raw time series directly yields more accurate confidence intervals of the estimates, because transformation of the time series introduces cross-correlations. Estimating logarithms of kinetic parameters instead of the parameters themselves has been proposed to increase the robustness of the regression. If possible, physical parameters such as pulse sizes and diffusion coefficients should be estimated independently. It was mentioned above that the traditional approach to determine reaction networks is through regression with several competing models. The Bayesian information criterion (BIC), favoring parsimonious kinetic models, has been presented to carry out the discrimination. The guidelines have been applied to the experimental determination of the nature of the interaction of propane and propene with a V_2O_5 catalyst. A reaction network has been selected, where propane is oxidized either directly or via an oxidative dehydrogenation to propene.

List of Symbols

Roman symbols

A	Arrhenius pre-exponential factor	
A_j	component j, vertex in a digraph	
$A(t_j)$	amplitude of oscillating noise at time t_j	V
a_j	an arc in a directed graph	
B	set in which $\mathbf{b}$ takes its values	
BIC_j	score of model j according to the Bayesian information criterion (BIC)	–
$\mathbf{b}$	vector of values b_j	
b_j	possible value of the physico-chemical parameter β_j	
$C_Y(t_j, t_k)$	covariance of the samples at t_j and t_k of the stochastic process Y	
$\mathbf{c}$	vector of concentrations c_j	mol/kg
$\mathbf{c}^{(l)}$	vector $\mathbf{c}$ valid in zone l of a TAP-reactor	mol/kg
$\tilde{\mathbf{c}}^{(l)}$	vector resulting from selecting one element of $\mathbf{c}^{(l)}$ corresponding to each gas phase component	mol/kg
$\mathbf{c}_0$	vector of initial concentrations $c_{j,0}$	mol/kg
$\mathbf{c}_g^{(l)}$	vector of gas concentrations in zone l of a TAP-reactor	mol/m^3
$\mathbf{c}_{g,j}^{(l)}$	vector of gas concentrations in discretization interval j in zone l of a TAP-reactor	mol/m^3
$\mathbf{c}_{\text{in}}$	vector of gas concentrations at the inlet of a TAP-reactor	mol/m^3
$\mathbf{c}_{\text{out}}$	vector of gas concentrations at the outlet of a TAP-reactor	mol/m^3
$\mathbf{c}_s^{(l)}$	vector of surface concentrations in zone l of a TAP-reactor	mol/kg
$\mathbf{c}_{s,0}^{(l)}$	vector of the initial surface concentrations in zone l if a TAP-reactor	mol/kg

$\mathbf{c}_{s,j}^{(l)}$	vector of surface concentrations in discretization interval j in zone l of a TAP-reactor	mol/kg
c_j	concentration of A_j	
$c_{j,0}$	initial concentration of A_j	
$\boldsymbol{\mathscr{D}}_e^{(l)}$	diagonal vector holding in its diagonal the effective Knudsen diffusion coefficients of all gas components in zone l of a TAP-reactor	m^2/s
D	denominator polynomial of a kinetic transfer function $H_{j,k}$	
D_j	determinant of a vertex A_j in a digraph	
$\mathscr{D}_e^{(l)}$	effective Knudsen diffusion coefficient of a gas component in zone l of a TAP-reactor	m^2/s
$\mathscr{D}_{e,\mathrm{ref}}$	reference effective Knudsen diffusion coefficient	m^2/s
$\mathbf{E}_{e,v}$	error matrix, the jth column of which contains the estimated noise $\mathbf{y}_{e,v}^{(k)} - \overline{\mathbf{y}}_{e,v}$ in the $\mathbf{y}_{e,v}^{(k)}$	
$\mathbf{E}'_{e,v}$	transformed error matrix $\hat{\mathbf{U}}_{e,\,v}^{T} \cdot \mathbf{E}_{e,v}$	
E	activation energy	J/mol
$E[X]$	expected value of a random variable X	
$\mathbf{F}$	matrix transforming $\mathbf{u}$ into $\mathbf{f}$	–
$\mathbf{F}^{(l)}$	matrix $\mathbf{F}$ valid in zone l of a TAP-reactor	–
$\tilde{\mathbf{F}}^{(l)}$	reduced version of the matrix $\mathbf{F}^{(l)}$, containing only the columns corresponding to gas phase components	–
$\mathscr{F}$	(continuous) Fourier transform (of a function)	
$\mathcal{F}$	discrete Fourier transform (of a vector)	
$\mathscr{F}^{-1}$	inverse (continuous) Fourier transform (of a function)	
$\mathcal{F}^{-1}$	inverse discrete Fourier transform (of a vector)	
$\mathscr{F}_d$	discrete approximation of the Fourier transform (of a function)	
$\mathscr{F}_d^{-1}$	discrete approximation of the inverse Fourier transform (of a function), inverse of $\mathscr{F}_d$	
$\mathbf{f}$	vector of net sources f_j per unit mass of catalyst	mol/kg s
$\mathbf{f}$	vector function mapping $\mathbf{b}$ to a model-calculated analogue of $\mathbf{y}$, composite of the vector functions $\mathbf{f}_v$	
$\mathbf{f}'''$	vector function mapping $\mathbf{b}$ to a model-calculated analogue of $\mathbf{y}'''$, composite of the vector functions $\mathbf{f}_v'''$	
$\mathbf{f}^{(l)}$	vector of local gas component fluxes in zone l of a TAP-reactor	$mol/m^2\,s$

$\mathbf{f}_{\text{in}}$	vector of gas component inlet fluxes into a TAP-reactor	mol/m^2 s
$\mathbf{f}_{\text{out}}$	vector of gas component outlet fluxes from a TAP-reactor	mol/m^2 s
$\mathbf{f}'''_{\mathbf{T}}$	vector function mapping $\mathbf{b}$ to a model-calculated analogue of $\mathbf{y}'''_{\mathbf{T}}$, composite of the vector functions $\mathbf{f}'''_{v,\mathbf{T}}$	
$\mathbf{f}_v$	vector function mapping $\boldsymbol{\xi}_e$ and $\mathbf{b}$ to a model-calculated analogue of $\mathbf{y}_{e,v}$	
$\mathbf{f}''_v$	vector function $\boldsymbol{\Lambda}_{e,v}^{-1/2} \cdot \mathbf{U}_{e,v}^T \cdot \mathbf{f}_v$	
$\mathbf{f}'''_v$	vector function $\sqrt{n_{r,e}-1}\,\hat{\boldsymbol{\Lambda}}_{e,\,v}^{-1/2} \cdot \hat{\mathbf{U}}_{e,\,v}^T \cdot \mathbf{f}_v$	
$\mathbf{f}'''_{v,\mathbf{T}}$	vector function $\sqrt{n_{r,e}-1}\,\hat{\boldsymbol{\Lambda}}_{e,v,\mathbf{T}}^{-1/2} \cdot \hat{\mathbf{U}}_{e,v,\mathbf{T}}^T \cdot \mathbf{T} \cdot \mathbf{f}_v$	
f_j	net source of a vertex A_j in a reaction graph, representing a component, per unit mass of catalyst	mol/kg s
f_v	model-calculated value of η_v as a function of t, $\boldsymbol{\xi}_e$ and $\mathbf{b}$	
$\mathbf{J}$	Jacobian $\partial\boldsymbol{\Phi}/\partial\mathbf{b}$	
$\mathbf{H}$	kinetic transfer matrix	s
$\mathbf{H}^{(l)}$	kinetic transfer matrix valid in zone l if a TAP-reactor	s
$\tilde{\mathbf{H}}^{(l)}$	matrix resulting from selecting one row and column of $\mathbf{H}^{(l)}$ corresponding to each gas phase component	s
$H_{j,k}$	transfer function from $\mathscr{L}f_k + c_{k,0}$ to $\mathscr{L}c_j$, element of $\mathbf{H}$	s
$\mathbf{K}$	matrix of apparent rate coefficients, transforming the vector $\mathbf{c}$ of concentrations into the vector of corresponding rates of production	Hz
K	set of (apparent) rate coefficients	
k_j	(apparent) rate coefficient of s_j	Hz
L_j	likelihood of model j	
$\mathscr{L}$	Laplace transform	
$\mathscr{L}^{-1}$	inverse Laplace transform	
l	see $l_{j,k}$	–
$l_{j,k}$	length of the shortest reaction pathway from A_k to A_j, equal to zero if $j = k$	–
$\mathbf{M}_l(s)$	transfer matrix corresponding to zone l of a TAP-reactor	
$\mathcal{M}$	input-output mapping from $\mathbf{u}$ to $\mathbf{y}$	
M_0	zeroth moment of a TAP pulse response	Vs

M_j	molecular mass of A_j	kg/mol
M_{ref}	reference molecular mass	kg/mol
$m_f^{(l)}$	catalytic mass fraction of the material in zone l of a TAP-reactor	–
N	numerator polynomial of a kinetic transfer function $H_{j,k}$	
$\mathbf{n}$	vector of pulsed quantities n_j of gas components into a TAP-reactor	mol
n	see $n_{j,k}$	–
n	total number of data points: $n = n_e n_v n_t$	–
n'''	total number of replicate-experimental times series: $n''' = n_v \sum_{e=1}^{n_e} (n_{r,e} - 1)$	–
n_c	number of vertices in a reaction graph	–
n_e	number of transient experiments performed	–
n_g	number of monitored gases in a TAP-reactor	–
n_j	pulsed quantity of A_j in a TAP-experiment	mol
$n_{j,k}$	number of intermediates from A_k to A_j plus two if $j \neq k$ or plus one otherwise	–
n_l	number of discretization intervals in zone l of a TAP-reactor	–
$n_{r,e}$	number of replicates $\mathbf{y}_{e,v}^{(k)}$	–
n_t	number of samples in a time series or random sequence	–
n_v	number of physical variables simultaneously monitored during a transient experiment, especially number of masses monitored by mass spectrometry in TAP	–
n_z	number of zones in a TAP-reactor	–
p	number of unknown physico-chemical parameters b_j	–
$p_{j,k}^{(q)}$	qth least negative pole of $H_{j,k}$	Hz
$\tilde{p}_{j,k}^{(q)}$	corner frequency corresponding to the pole $p_{j,k}^{(q)}$	Hz
R	universal gas constant	J/K mol
$\overline{r}$	mean pore radius	m
$\mathbf{r}$	vector function mapping $\mathbf{c}$ to the vector of rates of production	mol/kg s
$\mathbf{r}_g^{(l)}$	vector of the rates of production of the gas components in zone l of a TAP-reactor	mol/m^3 s
$\mathbf{r}_{g,\phi}^{(l)}$	vector of the rates of production of the gas components in zone l of a TAP-reactor, per unit cross-sectional surface area	mol/m^2 s

$\mathbf{r}_s^{(l)}$	vector of the rates of production of the surface components in zone l of a TAP-reactor	mol/kg s
r_j	reaction rate of s_j	
r_s	particle radius	m
$\mathbf{S}$	calibration matrix containing as columns the mass spectra of the gas components at the monitored masses	V s/mol
S	reaction network: set of elementary steps s_j	
$\mathscr{S}$	vector space spanned by all sPCs	
$S_{\mathbf{b}}$	set of parameter vectors indistinguishable from $\mathbf{b}$	
$S(\mathbf{b})$	residual sum of squares for parameter vector $\mathbf{b}$	
s	Laplace variable	Hz
$s_{e,v,j}$	standard deviation of the orthogonal projection of the noise vector $\boldsymbol{\epsilon}_{e,v}$ onto the jth sample principal component $\hat{\mathbf{u}}_{e,v,j}$	
s_j	elementary step j	
s_{M_0}	standard deviation of M_0	
$\mathbf{T}$	square matrix representing a linear preconditioning transform of $\overline{\mathbf{y}}_{e,v}$	–
T	absolute temperature	K
T_{ref}	reference temperature	K
t	time	s
t_c	collection time of a time series or random sequence	s
Δt	sampling interval	s
$\mathbf{U}_{e,v}$	matrix holding in its columns the vectors $\mathbf{u}_{e,v,j}$	
$\hat{\mathbf{U}}_{e,\,v}$	matrix holding in its columns the vectors $\hat{\mathbf{u}}_{e,v,j}$	
$\hat{\mathbf{U}}_{e,v,\mathbf{T}}$	matrix holding in its columns the sample principal noise components of $\mathbf{T}\cdot\boldsymbol{\epsilon}_{e,v}$	
$\mathbf{u}$	vector of independent sources f_i in $\mathbf{f}$	mol/kg s
$\tilde{\mathbf{u}}^{(l)}$	vector of net molar flow rates of gas phase components into an infinitesimal slice of zone l of a TAP-reactor, per unit mass of catalyst	mol/kg s
$\mathbf{u}_{e,v,j}$	jth population principal component of the noise vector $\boldsymbol{\epsilon}_{e,v}$	
$\hat{\mathbf{u}}_{e,v,j}$	jth sample principal component of the noise vector $\boldsymbol{\epsilon}_{e,v}$	
u_0	baseline position of a TAP pulse response	V
$\mathbf{V}$	function mapping a random sequence to its (population) variance matrix	

$\hat{\mathbf{V}}(\boldsymbol{\epsilon}_{e,v})$	sample variance matrix of $\boldsymbol{\epsilon}_{e,v}$, estimate of $\mathbf{V}(\boldsymbol{\epsilon}_{e,v})$	
$\hat{\mathbf{V}}(\boldsymbol{\epsilon}'_{e,v})$	sample variance matrix of $\boldsymbol{\epsilon}'_{e,v}$	
$\hat{\mathbf{V}}(\boldsymbol{\epsilon}''_{e,v})$	sample variance matrix of $\boldsymbol{\epsilon}''_{e,v}$	
$\hat{\mathbf{V}}\left(\bar{\boldsymbol{\epsilon}}''_{e,v}\right)$	sample variance matrix of $\overline{\mathbf{y}}''_{e,v}$	
$\hat{\mathbf{V}}(\mathbf{T}\boldsymbol{\epsilon}_{e,v})$	sample variance matrix of $\mathbf{T}\boldsymbol{\epsilon}_{e,v}$	
V	set of all vertices of a directed graph	
x_j	a vertex in a directed graph	
Y	stochastic process	
$\mathbf{y}$	vector of direct or indirect experimental observations: random sequence	
$\overline{\mathbf{y}}'$	composite of the vectors $\overline{\mathbf{y}}'_{e,v}$	
$\mathbf{y}''$	transformed random sequence of $\mathbf{y}$, composite of the sequences $\mathbf{y}''_{e,v}$	
$\overline{\mathbf{y}}'''$	composite of the vectors $\overline{\mathbf{y}}'''_{e,v}$	
$\mathbf{y}_{e,v}$	random sequence of observed values of η_v under experimental conditions $\boldsymbol{\xi}_e$	
$\overline{\mathbf{y}}_{e,v}$	average of the replicates $\mathbf{y}^{(k)}_{e,v}$	
$\mathbf{y}'_{e,v}$	transformed random sequence $\mathbf{U}^T_{e,v} \cdot \mathbf{y}_{e,v}$ or $\hat{\mathbf{U}}^T_{e,\,v} \cdot \mathbf{y}_{e,v}$ of $\mathbf{y}_{e,v}$	
$\overline{\mathbf{y}}'_{e,v}$	transformed vector $\hat{\mathbf{U}}^T_{e,\,v} \cdot \overline{\mathbf{y}}_{e,v}$ of $\overline{\mathbf{y}}_{e,v}$	
$\mathbf{y}'^{(k)}_{e,v}$	transformed vector $\hat{\mathbf{U}}^T_{e,\,v} \cdot \mathbf{y}_{e,v}$ of $\mathbf{y}^{(k)}_{e,v}$	
$\mathbf{y}''_{e,v}$	transformed random sequence $\boldsymbol{\Lambda}^{-1/2}_{e,v} \cdot \mathbf{y}'_{e,v}$ or $\hat{\boldsymbol{\Lambda}}^{-1/2}_{e,\,v} \cdot \mathbf{y}'_{e,v}$ of $\mathbf{y}'_{e,v}$	
$\overline{\mathbf{y}}'''_{e,v}$	rescaled vector $\sqrt{n_{r,e}-1}\,\overline{\mathbf{y}}''_{e,v}$ of $\overline{\mathbf{y}}''_{e,v}$	
$\mathbf{y}^{(k)}_{e,v}$	kth replicate of $\mathbf{y}_{e,v}$	
$\overline{\mathbf{y}}'''_{e,v,\mathbf{T}}$	transformed vector $\sqrt{n_{r,e}-1}\,\hat{\boldsymbol{\Lambda}}^{-1/2}_{e,v,\mathbf{T}} \cdot \hat{\mathbf{U}}^T_{e,v,\mathbf{T}} \cdot \mathbf{T} \cdot \overline{\mathbf{y}}_{e,v}$ of $\overline{\mathbf{y}}_{e,v}$	
$\mathbf{y}_j$	jth time series (TAP pulse response)	V
$\overline{\mathbf{y}}'''_{\mathbf{T}}$	composite vector of the vectors $\overline{\mathbf{y}}'''_{e,v,\mathbf{T}}$	
y	direct or indirect experimental observation	
$y^{(k)}$	kth replicate of the observation y	
$y_{e,v}$	observed value of η_v as a function of t	
y_j	jth mass spectrometer signal in a TAP-experiment	
z	axial coordinate in the TAP-reactor	m
z_0	axial coordinate of the boundary of the first zone in a TAP-reactor towards its inlet)	m
$z^{(q)}_{j,k}$	qth least negative zero of $H_{j,k}$	Hz
$\tilde{z}^{(q)}_{j,k}$	corner frequency corresponding to the zero $z^{(q)}_{j,k}$	Hz

$z_{l\neq 0}$	axial coordinate of the boundary of zone l in a TAP-reactor towards its outlet)	m
$\Delta z^{(l)}$	width of zone l of a TAP-reactor	m
Δz_l	width of discretization intervals in zone l of a TAP-reactor	m

Greek symbols

α_q	qth order coefficient of the polynomial D	
$\boldsymbol{\beta}$	vector of physico-chemical parameters β_j	
$\hat{\boldsymbol{\beta}}$	vector of final parameter estimates $\hat{\beta}_j$	
β_j	actual, unknown value of the jth physico-chemical parameter	
$\hat{\beta}_j$	final estimate b_j of β_j	
β_q	qth order coefficient of the polynomial N	
Γ	Stochastic process representing spectrally localized noise	V
$\gamma_j^{(l)}$	parameter describing mass transfer of gas phase component A_j through zone l of a TAP-reactor	m/s
δ_{jk}	Kronecker delta: equal to one if $j = k$ and zero otherwise	–
$\boldsymbol{\epsilon}$	random sequence representing the noise in the vector $\mathbf{y}$ of observations, composite of the vectors $\boldsymbol{\epsilon}_{e,v}$	
$\boldsymbol{\epsilon}''$	random sequence representing the noise in the sequence $\mathbf{y}''$, composite of the vectors $\boldsymbol{\epsilon}''_{e,v}$	
$\overline{\boldsymbol{\epsilon}}'''$	random sequence representing the error of $\overline{\mathbf{y}}'''$, composite of the random sequences $\overline{\boldsymbol{\epsilon}}'''_{e,v}$	
$\boldsymbol{\epsilon}_{e,v}$	random sequence representing the noise in an experimental series $\mathbf{y}_{e,v}$	
$\boldsymbol{\epsilon}'_{e,v}$	random sequence representing the error of $\mathbf{y}'_{e,v}$	
$\boldsymbol{\epsilon}''_{e,v}$	random sequence representing the error of $\mathbf{y}''_{e,v}$	
$\overline{\boldsymbol{\epsilon}}''_{e,v}$	random sequence representing the error of $\overline{\mathbf{y}}''_{e,v}$	
$\overline{\boldsymbol{\epsilon}}'''_{e,v}$	random sequence representing the error of $\overline{\mathbf{y}}'''_{e,v}$	
$\epsilon_b^{(l)}$	porosity of the bed in zone l of a TAP-reactor	–
ζ	positive dimensionless constant much smaller than one	–
η_v	vth physico-chemical variable monitored during a transient experiment	
Θ	stochastic variable with uniform distribution over $[0, 2\pi]$	–
θ	correlation time	s

$\mathbf{\Lambda}_{e,v}$	diagonal matrix holding the eigenvalues $\sigma^2_{e,v,j}$ of $\mathbf{V}(\boldsymbol{\epsilon}_{e,v})$	
$\hat{\mathbf{\Lambda}}_{e,\,v}$	diagonal matrix holding the nonzero eigenvalues $s^2_{e,v,j}$ of $\hat{\mathbf{V}}(\boldsymbol{\epsilon}_{e,v})$	
$\hat{\mathbf{\Lambda}}_{e,v,\mathbf{T}}$	diagonal matrix holding the eigenvalues of $\hat{\mathbf{V}}(\mathbf{T}\cdot\boldsymbol{\epsilon}_{e,v})$	
Λ	stochastic variable with mean zero and standard deviation one	–
$\boldsymbol{\mu}_Y$	mean of a random sequence $\mathbf{y}$	
μ_Y	mean of the stochastic process Y	
ν	frequency	Hz
ν_k	frequency $k/(n_t\Delta t)$	Hz
$\nu_{\mathrm{p},j}$	stoichiometric coefficient of product A_j of an elementary step	–
$\nu_{\mathrm{r},j}$	stoichiometric coefficient of reactant A_j of an elementary step	–
$\boldsymbol{\xi}_e$	vector of experimental conditions for the eth transient experiment	
ρ	correlation coefficient between two successive samples of a random sequence	–
$\rho^{(l)}$	density of the material of zone l of a TAP-reactor	kg/m^3
$\rho_Y(t_j,\,t_k)$	correlation coefficient of the samples at t_j and t_k of the stochastic process Y	–
$\boldsymbol{\sigma}_Y$	standard deviation of a stochastic process	
$\sigma_{e,v,j}$	standard deviation of the orthogonal projection of the noise vector $\boldsymbol{\epsilon}_{e,v}$ onto the jth population principal component $\mathbf{u}_{e,v,j}$	
$\left(\sigma^2\right)_M$	time average variance of a random sequence	
$\sigma_Y(t_j)$	standard deviation of the sample at t_j of the stochastic process Y	
τ	tortuosity factor	–
$\tau_j^{(l)}$	parameter describing mass transfer of gas phase component A_j through zone l of a TAP-reactor	s
$\mathbf{\Phi}$	vector of invariants	
Φ	Ornstein-Uhlenbeck stochastic process	V
ϕ	cross sectional surface area of a TAP-reactor	m^2
Ψ	stochastic process representing random fluctuations of the M_0 of a TAP pulse response due to a poorly reproducible inlet pulse size	V
ψ	angle between $\mathbf{y}$ and the space $\mathscr{S}$	–

ω	pulsation	Hz
ω_k	pulsation $2\pi k/(n_t\Delta t)$	Hz
ω_N	Nyquist pulsation	Hz

Numerical symbols

$\mathbf{0}$	zero vector of appropriate dimension	–
$\mathbf{0}_n$	zero vector of dimension n	–
$\mathbf{I}$	unit matrix of appropriate dimensions	–
$\mathbf{I}_n$	unit matrix of dimensions $n \times n$	–

Acronyms

AC	Alternating Current
BIC	Bayesian Information Criterion
FFT	Fast Fourier Transform
LCT	Laboratory for Chemical Technology
NLSQ	Nonlinear Least-SQuares
pPC	population Principal Component
pPCA	population Principal Component Analysis
SNR	Signal-to-Noise Ratio
SSITKA	Steady-State Isotopic Transient Kinetic Analysis
SOSR	Second-Order Statistical Regression
sPC	sample Principal Component
sPCA	sample Principal Component Analysis
SVD	Singular Value Decomposition
TAP	Temporal Analysis of Products
TPD	Temperature Programmed Desorption
TZTR	Thin-Zone-TAP-Reactor
UGent	Ghent University
VOC	Volatile Organic Compound
WUStL	Washington University Saint Louis

Chapter 1

Introduction

1.1 Reaction networks, kinetics and catalysis

Almost all of the industrially relevant reactions take place as the net result of several, sometimes thousands of events at the molecular level. These events are called *elementary steps*. Apart from the reactants and products of the reaction, the elementary steps involve *intermediates*. A set of elementary steps is called a *reaction network*. As an example, consider a reaction network responsible for the conversion of ozone into dioxygen, $2\,O_3 \rightarrow 3\,O_2$ (Boudart, 1968).

$$O_3 \rightarrow O_2 + O \tag{1.1a}$$

$$O + O_3 \rightarrow 2\,O_2. \tag{1.1b}$$

In this case, there is one intermediate: atomic oxygen.

Consider a general elementary step

$$\sum_{j=1}^{n} \nu_{\mathrm{r},\,j} A_j \rightarrow \sum_{j=1}^{n} \nu_{\mathrm{p},\,j} A_j. \tag{1.2}$$

It is necessary to point out that elementary steps cannot be very complex. The number of reactant molecules, $\sum_{j=1}^{n} \nu_{\mathrm{r},\,j}$, the so-called *molecularity* of the step is usually one (*monomolecular* step) or two (*bimolecular* step), sometimes three (*trimolecular* step). The same is true for the number of product molecules, $\sum_{j=1}^{n} \nu_{\mathrm{p},\,j}$. An elementary step (1.2) is often reversible, which means that it coexists with its reverse step.

Within sufficiently narrow ranges of pressure and composition, the

rate of step (1.2) is given by the *kinetic law of mass action*[1]:

$$r = k \prod_{j=1}^{n} c_j^{\nu_{\mathrm{r},\,j}}, \tag{1.3}$$

where c_j is a concentration of A_j and k, the *rate coefficient*, is independent of pressure and composition. The rate coefficient does depend on the absolute temperature T, as described by the approximate *Arrhenius equation*:

$$k = A \exp\left(-\frac{E}{RT}\right), \tag{1.4}$$

in which A is the *pre-exponential factor*, E the *activation energy* and R the universal gas constant.

The intermediates of a reaction network do not appear in the overall reaction. This does not necessarily mean that they are absent before and after the reaction takes place. Sometimes the initial presence of an intermediate is essential for the reaction to start. This is the case in *catalysis*, where a catalyst enables a reaction without being consumed or produced. If the catalyst and the reaction mixture have the same state of aggregation, the term "*homogeneous catalysis*" applies. If not, the term "*heterogeneous catalysis*" is used. This thesis focuses on heterogeneous catalysis. For example, a reaction network responsible for the oxidation of hydrogen on the Ni(110) plane is

$$\mathrm{O_2} + 2* \rightarrow 2\,\mathrm{O}^* \tag{1.5a}$$
$$\mathrm{H_2} + 2* \leftrightarrows 2\,\mathrm{H}^* \tag{1.5b}$$
$$\mathrm{O}^* + \mathrm{H}^* \rightarrow {}^*\mathrm{OH} + * \tag{1.5c}$$
$${}^*\mathrm{OH} + \mathrm{H}^* \rightarrow 2* + \mathrm{H_2O} \tag{1.5d}$$

(Yablonskii et al., 1991). $*$ represents a free *active site* on the catalyst surface. O^*, H^* and ${}^*\mathrm{OH}$ represent atomic oxygen, atomic hydrogen and a hydroxyl group bonded with the active site. The intermediates $*$, O^*, H^* and ${}^*\mathrm{OH}$ are all present on the surface.

1.2 The relevance of knowing the reaction network

Most of the industrially relevant reactions are carried out with the aid of a heterogeneous catalyst. The importance of the knowledge of the reaction network almost goes without saying. It can indeed be argued

[1] For background information on the kinetic law of mass action, refer to (Pekař, 2005).

that any chemical comprehension of the activity of a catalyst must have its roots in notions about the reaction network. First of all, these notions provide a valuable tool in the ever intensifying search for more active and *selective* catalysts. The selectivity of a catalyst is the ratio of the quantity of desired products to the total quantity of products, including by-products. Secondly, knowledge about the reaction network is valuable in the design and operational optimization of chemical reactors or indeed whole production units. Indeed, elementary steps proceed at a rate given by the well-known law of mass action (1.3). Chemical reaction kinetics, knowledge of which is crucial for the design and operation of reactors, therefore reflect the reaction network.

The aim of this work is the development of procedures for the determination of reaction networks responsible for heterogeneously catalyzed reactions. The scope is limited to the field of transient kinetic experiments.

1.3 Transient kinetic experiments

As Section 1.1 pointed out, the reaction network is almost directly manifested in the reaction kinetics. Scientists therefore rely heavily on kinetic experiments to determine chemical reaction networks. In this regard, it was shown by several authors that more information can be extracted from *transient experiments* than from *stationary* ones, both for non-catalytic (Hulburt and Kim, 1966) and catalytic reaction systems (Tamaru, 1964; Boudart, 1968; Biloen, 1983; Zamostny and Belohlav, 2002). In transient experiments, a certain physical variable, such as temperature or a concentration, is changed in a controlled way, while the evolution of other variables is monitored as a response. Furusawa et al. (1976), Renken (1993), Mills and Lerou (1993), Efstathiou and Verykios (1997), Bennett (2000) and, recently, Berger et al. (2008) have reviewed the transient experimental techniques available.

The role of transient experiments becomes crucial if reactions are studied which take place in a transient regime in practice. The industrially most relevant example is fluid catalytic cracking, where the catalyst deactivates on a time scale comparable to that of the cracking itself. This has prompted the design of riser reactors. Next to this category of non-steady-state operation of catalysts, the existence of oscillations in the feed composition is an obvious reason for transient regimes, an important example being catalytic automotive emission converters, where exhaust gases are oscillatorily fed from a combustion engine.

The experimentalist controls the conditions at which experiments are performed. For kinetic experiments, these are typically the (inlet) temper-

ature, the inlet concentrations of the reactants and, for reactions involving gases, the (inlet) pressure. As a rule, during transient experiments, at least one of these physical variables is forced to undergo a well-defined variation in time. In *steady-state isotopic transient kinetic analysis*, for example, an isotopic concentration switch of a reactant is applied to a laboratory reactor, otherwise in stationary regime (Happel, 1978; Bennett, 1982; Biloen, 1983). In the *temperature programmed desorption* (TPD), the desorption of products from a catalyst surface is recorded in response to a reaction temperature ramp. Another transient technique is *Temporal Analysis of Products* (Gleaves et al., 1988; Yablonsky et al., 2003; Gleaves et al., 2010), where the inlet flow rate of the reactant into the reactor is a controlled Dirac pulse. The present work focuses on TAP. All experimental data used for illustration purposes are obtained from TAP-experiments.

1.4 Outline of the thesis

The Chapters 2 and 3 will introduce additional notions on reaction networks and kinetics, which will be applied in the subsequent chapters. Chapter 2 will present the analytical and graphical representations of catalytic kinetics, as they follow from the reaction networks. The attention will gradually be narrowed down to the important special case of pseudomonomolecular reaction networks, the kinetics of which can be described by a compartmental model. Chapter 3 will pursue the subject, developing a Laplace-domain description of such compartmental kinetics.

Pseudomonomolecular reaction networks are encountered in many experimental cases. This is especially true for TAP, the experimental technique on which this work focuses. Chapter 4 will familiarize the reader with the technique, focusing on the modeling aspects. Chapter 5, on the other hand, will report on a study of the noise present in the experimental data. This noise limits the level of detail achievable in an attempt to unravel reaction networks.

The traditional way to determine reaction network is through the postulation of several candidate reaction networks. A physico-chemical model is then derived for each of them. It is then attempted to discriminate between the candidate networks by submitting the data to least-squares regression with the different models. For each model, those kinetic parameters are identified which provide the best description of the experimental data. Discrimination between the candidate reaction networks is performed by comparing the quality of this optimal description. Inspired by the findings in Chapter 4, Chapter 6 will present a novel regression procedure for transient kinetic data. Its superiority to

normal least-squares regression lies in the use of second-order statistical information, extracted from replicate experiments. For isothermal data, irrespective of the manner in which the regression is carried out, there are essential limits to the identifiability of the kinetic parameters, i.c., the rate coefficients. Chapter 7, relying on the results presented in Chapter 3, presents a graph-theoretical test for revealing unidentifiability.

The traditional reaction network discrimination approach requires the postulation of several candidate reaction networks. The list of postulated networks is never exhaustive. Moreover, there may be unidentifiability problems. Similarly, it may prove impossible to discriminate between some candidate networks. Chapter 8 presents a novel procedure to reveal connectivity features of a pseudomonomolecular reaction network by TAP, without the need to postulate candidate networks. Such a model-free procedure is unique in chemical kinetics.

Chapter 9 will enumerate some concrete guidelines to the TAP-experimentalist. These guidelines will be based on the findings of this thesis and on the literature.

Finally, Chapter 10 will present the general conclusions of this work.

Chapter 2

Catalytic kinetics: Analytical and Graphical Representation

2.1 Introduction

Chapter 1 provided enough notions on chemical reaction networks and their kinetics to be able to understand the aim and an outline of the present work. With these notions in hand, this chapter will prepare the reader for Chapter 3, where a Laplace-domain description will be introduced for the important class of compartmental kinetics. The Sections 2.2 and 2.3 treat general kinetics, analytically and graphically. Section 2.4 introduces the special class of pseudomonomolecular reaction networks. As it will be pointed out in Section 2.5, pseudomonomolecular reaction networks have linear kinetics. In fact, most pseudomonomolecular reaction networks can have their kinetics described by a compartmental, i.e., a special type of linear, model. This will be pointed out in Section 2.6.

2.2 General kinetics

Consider an open system of uniform temperature, pressure and phasewise uniform composition, containing a heterogeneous catalyst. It is assumed that the system can be described in intensive macroscopic terms, even if it has an infinitesimal size. Consider a reaction network $S = \{s_j \mid j \in J\}$ of elementary steps taking place in the system, each having at least one component with non-quasiconstant concentration at the reactant side. Call c_j the concentration of the (gas or surface) component A_j: the quantity of A_j divided by the mass of the catalyst. Say $\mathbf{c} = [c_1, c_2, \ldots, c_n]^T$ is a column vector grouping the non-quasiconstant concentrations c_j involved in the reaction network S. According to the partial mass balances, its

time derivative has two contributions:

$$\frac{\mathrm{d}\mathbf{c}}{\mathrm{d}t}(t) = \mathbf{r}(\mathbf{c}(t)) + \mathbf{f}(t), \tag{2.1}$$

The first term to the right hand side, $\mathbf{r}(\mathbf{c})$, is due to the net production[1] by elementary steps of S. $\mathbf{r}$ is a kinetic vector function, based on the application of the law of mass action (1.3) applied to all elementary steps. The second term, the source vector $\mathbf{f} = [f_1, f_2, \ldots, f_n]^T$, is due to

- the net inward flow rate[2] of components at the system's boundary,
- the production and consumption of A_j by elementary steps not comprised in S, taking place inside the system.

Note that the concentrations c_j and the net molar sources f_j are expressed relative to the same extensive variable proportional to the system size. Such a variable can be the volume of the system or the mass of catalyst present, for example.

2.3 Reaction graphs

The reaction network S can be represented by a *directed graph* or digraph, for short (Feinberg, 1987). This digraph will be called the *reaction graph*. Call the expressions appearing at the reactant or product side of the elementary steps *complexes*. Each of the complexes is represented once as a vertex in the reaction graph. The complex appears as a label of the vertex. Each elementary step s_j is then represented as an arc directed from the vertex representing its reactant complex, its "*tail*", to the vertex representing its product complex, its "*head*".[3] Each arc is attributed a weight: the rate coefficient k_j of the corresponding elementary step s_j. Fig. 2.1 shows an example of a reaction graph.

Components which have a quasiconstant concentration can be omitted from the reaction graph. This will be illustrated for the reaction graph in Fig. 2.1, where A_7 is supposed to have a quasiconstant concentration.

1. In the complexes containing both components with quasiconstant and non-quasiconstant concentrations, the former are removed. If the reactant complex of an elementary step is thus changed, the

[1] Consumption if negative

[2] Net outward flow rate if negative

[3] Possibly, there are different elementary steps having the same reactant and product complex. Such steps would be represented by parallel arcs having the same tail and head. Strictly speaking, graphs with such parallel arcs are called "directed pseudographs" (Bang-Jensen and Gutin, 2008).

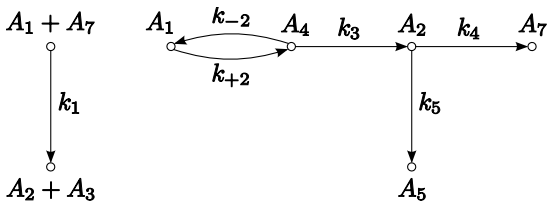

Figure 2.1: A reaction graph representing a reaction network.

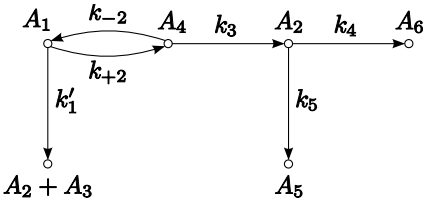

Figure 2.2: A simplified version of the reaction graph in Fig. 2.1, if A_7 has a quasiconstant concentration. A_6 represents a virtual component.

weight of its arc is changed from a rate coefficient to an apparent rate coefficient. Formerly different complexes can become identical, in which case their vertices have to be contracted. Here, vertex A_1+A_7 is relabeled A_1 and contracted with the vertex which already had this label. The rate coefficient k_1 is replaced by the apparent rate coefficient $k'_1 = k_1 c_7$.

2. It was assumed that all steps of S have at least one reactant with non-quasiconstant concentration. However, it is possible that some steps of S only have products with quasiconstant concentration. In this case, the label of the corresponding vertex is replaced by the name of a virtual component. Here the vertex A_7 is relabeled A_6, representing a virtual component.

The result of this transformation is shown in Fig. 2.2. Appendix A introduces some graph-theoretical notions which this thesis will rely on.

2.4 Pseudomonomolecular reaction networks

An elementary step (1.2) with molecularity greater than one is called *pseudomonomolecular* in A_j if it has a stoichiometric coefficient $\nu_{\mathrm{r},\,j} = 1$ for reactant A_j, while the other reactants have a quasiconstant concen-

tration. Then the rate expression (1.3) becomes quasilinear

$$r = \underbrace{\left(k \prod_{k \neq j} c_k^{\nu_{\mathrm{r},\,k}} \right)}_{k'} \cdot c_j, \tag{2.2}$$

defining the *apparent rate coefficient*, k', quasi-independent of pressure and the concentration c_j of A_j. Observe that pseudomonomolecularity is a property of the reaction conditions rather than of the elementary step. A set of pseudomonomolecular and monomolecular elementary steps can be called a pseudomonomolecular reaction network.

In catalytic reaction networks, there is at least one multimolecular step: the bonding of a reactant and a catalytic component, for example step (1.5a). However, in many experimental cases, all these multimolecular steps can be considered pseudomonomolecular. This is possible in three cases:

1. For a stationary experiment, all concentrations are constant. Theory for linear reaction networks has been developed and applied extensively to find the overall steady-state reaction rate as a function of the concentration of the overall reactants (King and Altman, 1956; Evstigneev and Yablonskii, 1979; Yablonskii et al., 1991).

2. The concentration of all species except those bonded with the catalyst is quasiconstant. Goldstein (1983, 2009) developed a linear theory for transient homogeneous-catalytic, enzymatic kinetics based on this assumption.

3. The concentration of the free active site is quasiconstant. This is possible if it is present in much larger quantities than the overall reactants. This is typical for SSITKA and TAP, see Section 1.3.

2.5 Linear kinetics

If, in the reaction network represented by the reaction graph in Fig. 2.1, A_7 has a quasiconstant concentration, $S = \{s_1, s_{+2}, s_{-2}, s_3, s_4, s_5\}$ represents a pseudomonomolecular reaction network. Pseudomonomolecular reaction networks are common in many experimental situations, see Section 2.4. Those reactants and products of the steps in S which have a non-quasiconstant concentration, have this concentration described by a linear model. Indeed, vector function $\mathbf{r}$ in Eq. (2.1) becomes linear:

$$\mathbf{r}(\mathbf{c}(t)) = \mathbf{K} \cdot \mathbf{c}(t), \tag{2.3}$$

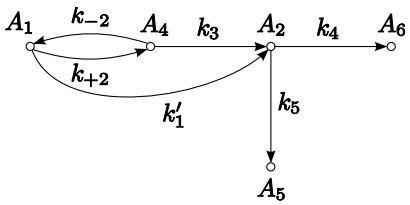

Figure 2.3: A simplified version of the reaction graph in Fig. 2.1, if A_3 has a quasiconstant concentration.

where $\mathbf{K}$ is a constant matrix. It follows directly from the simplified reaction graph. Based on the graph in Fig. 2.2, Eq. (2.1) becomes

$$\frac{\mathrm{d}}{\mathrm{d}t}\begin{bmatrix} c_1 \\ c_2 \\ c_3 \\ c_4 \\ c_5 \\ c_6 \end{bmatrix} = \begin{bmatrix} -k_1' - k_{+2} & 0 & 0 & k_{-2} & 0 & 0 \\ k_1' & -k_4 - k_5 & 0 & k_3 & 0 & 0 \\ k_1' & 0 & 0 & 0 & 0 & 0 \\ k_{+2} & 0 & 0 & -k_3 - k_{-2} & 0 & 0 \\ 0 & k_5 & 0 & 0 & 0 & 0 \\ 0 & k_4 & 0 & 0 & 0 & 0 \end{bmatrix} \begin{bmatrix} c_1 \\ c_2 \\ c_3 \\ c_4 \\ c_5 \\ c_6 \end{bmatrix} + \begin{bmatrix} f_1 \\ f_2 \\ f_3 \\ f_4 \\ f_5 \\ f_6 \end{bmatrix} \tag{2.4}$$

The linear expression (2.3) allows the application of powerful analytical tools based on integral transformations. Here, the Laplace transform will be applied.

2.6 Compartmental kinetics

Suppose that in the reaction graph in Fig. 2.1, A_3 has a quasiconstant concentration. Then a simplified reaction graph is shown in Fig. 2.3 and Eq. (2.1) becomes

$$\frac{\mathrm{d}}{\mathrm{d}t}\begin{bmatrix} c_1 \\ c_2 \\ c_4 \\ c_5 \\ c_6 \end{bmatrix} = \begin{bmatrix} -k_1' - k_{+2} & 0 & k_{-2} & 0 & 0 \\ k_1' & -k_4 - k_5 & k_3 & 0 & 0 \\ k_{+2} & 0 & -k_{-2} - k_3 & 0 & 0 \\ 0 & k_5 & 0 & 0 & 0 \\ 0 & k_4 & 0 & 0 & 0 \end{bmatrix} \begin{bmatrix} c_1 \\ c_2 \\ c_4 \\ c_5 \\ c_6 \end{bmatrix} + \begin{bmatrix} f_1 \\ f_2 \\ f_4 \\ f_5 \\ f_6 \end{bmatrix} \tag{2.5}$$

for the concentration of the selected components.

Generally, if all steps of S have exactly one product with non-quasicon-

stant concentration, the matrix $\mathbf{K}$ is of the form

$$\mathbf{K} = \begin{bmatrix} -\sum\limits_{j\neq 1} k_{j,1} & k_{1,2} & \cdots & k_{1,m} \\ k_{2,1} & -\sum\limits_{j\neq 2} k_{j,2} & \cdots & k_{2,m} \\ \vdots & \vdots & \ddots & \vdots \\ k_{m,1} & k_{m,2} & \cdots & -\sum\limits_{j\neq m} k_{j,m} \end{bmatrix}, \tag{2.6}$$

where each $k_{k,j}$ is the sum of the apparent rate coefficients of all steps from A_j to A_k, or zero if such steps do not exist. Observe that the matrix $\mathbf{K}$ given by Eq. (2.6) is singular, as its rows add up to zero. The diagonal elements are negative, while the off-diagonal elements are positive.

A system of differential equations

$$\frac{\mathrm{d}\mathbf{c}}{\mathrm{d}t}(t) = \mathbf{K} \cdot \mathbf{c}(t) + \mathbf{f}(t) \tag{2.7}$$

with a matrix $\mathbf{K}$ of the form given in Eq. (2.6) is called an *open compartmental model*. It follows directly from the reaction graph. As before, the compartmental model is represented graphically by the reaction digraph.

Consider a reaction network, the kinetics of which are described by a compartmental model. Often all apparent rate coefficients have well separated magnitudes. S is then called a *multiscale reaction network*. Such a network can be transformed into a simpler, "*dominant*" pseudomonomolecular reaction network for all practical purposes. The kinetics are still described by a compartmental model. Gorban et al. (2010) gave a constructive proof. The apparent rate coefficients of the dominant reaction network are positive monomials of the original apparent rate coefficients. The approach works under the condition that there are no dependences among the latter.

A compartmental model applies if all steps of S have exactly one product having a non-quasiconstant concentration. But compartmental models can be made to apply much more generally. In fact, only an exotic class of pseudomonomolecular reaction networks cannot have its concentrations represented by a compartmental model. The following condition excludes this class.

Condition 2.1. *If a step of S has a reactant A_j and multiple products A_k having non-quasiconstant concentrations, none of the latter can convert back into A_j through a sequence of steps in S.*

A step $A_1 \to A_2 + A_3$, with A_1, A_2, A_3 having non-quasiconstant concentrations, would be allowed, except if there is a reaction sequence from

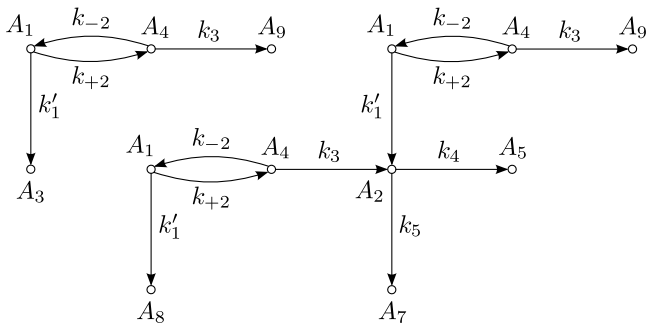

Figure 2.4: Reaction graph representing a compartmental model for the original reaction graph in Fig. 2.2. A_8 and A_9 are virtual components.

A_2 or A_3 back to A_1 involving only steps in S, for example a single step $A_2 \to A_1 + A_5$. Compartmental models can be constructed graphically by splitting vertices representing complexes $\sum_j A_j$ into vertices for the separate components A_j in the complex. Each of these vertices is then embedded in a copied part of the original reaction graph. Appendix B explains the procedure in detail. Concentrations c_j appear in the column vector $\mathbf{c}$ in Eq. (2.7) with the same multiplicity as the corresponding components A_j in the digraph. Call n_c the number of vertices in the transformed reaction graph. Clearly,

$$\mathbf{c}, \mathbf{f} \in \mathbb{R}^{n_c \times 1}. \tag{2.8}$$

Fig. 2.4 shows a reaction digraph obtained from transformation of the reaction digraph in Fig. 2.2. A_8 and A_9 represent newly introduced virtual components.

The theory of Gorban et al. (2010) about the asymptotology of multiscale reaction networks was constructed for reaction graphs such as the one in Fig. 2.3, which has all arc weights mutually independent. Here, generally, several arcs have the same weight. See Fig. 2.4 for example. These weights are therefore not mutually independent. However, inspection of the proof of Gorban et al. (2010) reveals it to hold because there are no directed paths containing equally weighted arcs.

2.7 Conclusions

A description of the kinetics of general reaction networks was provided in the form of the system (2.1) of first-order differential equations. Especially, for the important class of pseudomonomolecular reaction networks,

this system is linear. Kinetic systems, linear or nonlinear, can be represented graphically as reaction graphs. For most pseudomonomolecular reaction networks, a reaction graph can be derived which corresponds to a compartmental kinetic model. Such compartmental kinetics can be described in the Laplace domain. This approach will be presented in the Chapter 3.

Chapter 3

Pseudomonomolecular Reaction Networks: Kinetic Transfer Functions

3.1 Introduction

In Chapter 2, the reader was introduced to the important class of pseudomonomolecular reaction networks with compartmental kinetics. Such kinetics are conveniently described in the Laplace domain, in the form of kinetic transfer functions. The Sections 3.2 and 3.3 will give an analytical treatment. In Section 3.4, it will be shown how these transfer functions can be obtained graph-theoretically from the reaction graph. Especially, the symbolic form of the transfer functions can be found from visual inspection of the reaction graph, based on connectivity features of the reaction networks. The latter will be explained in Section 3.5.

3.2 Linear kinetics from a system-theoretical point of view

As in Chapter 2, consider a uniform and time-isothermal open system in which a pseudomonomolecular reaction network S takes place. The kinetics are described by a compartmental model, represented by a reaction graph such as the one in Fig. 3.1. For this example, the analytical expression of the compartmental model (2.7) is

$$\frac{\mathrm{d}}{\mathrm{d}t}\begin{bmatrix} c_1 \\ c_2 \\ c_3 \end{bmatrix} = \begin{bmatrix} -k_{+1}-k_2 & k_{-1} & 0 \\ k_{+1} & -k_{-1} & k_3 \\ k_2 & 0 & -k_3 \end{bmatrix} \cdot \begin{bmatrix} c_1 \\ c_2 \\ c_3 \end{bmatrix} + \begin{bmatrix} f_1 \\ f_2 \\ f_3 \end{bmatrix}. \tag{3.1}$$

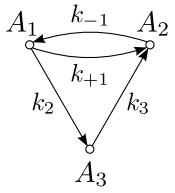

Figure 3.1: A reaction graph representing compartmental kinetics.

Initially,

$$\mathbf{c}(t=0) = \mathbf{c}_0. \tag{3.2}$$

Recall that one component can be represented by several vertices in the digraph representation[1]. Correspondingly, $\mathbf{c}$ can contain identical elements, as well as $\mathbf{f}$. Components A_j can also be virtual, in which case the net source f_j can be taken zero. In any case, if the net sources of the real components are collected in a vector $\mathbf{u}$, $\mathbf{f}$ follows immediately after a linear transformation:

$$\mathbf{f}(t) = \mathbf{F} \cdot \mathbf{u}(t), \tag{3.3}$$

where the elements of $\mathbf{F}$ are 0 or 1. Substitution into Eq. (2.7) yields

$$\frac{\mathrm{d}\mathbf{c}}{\mathrm{d}t}(t) = \mathbf{K} \cdot \mathbf{c}(t) + \mathbf{F} \cdot \mathbf{u}(t). \tag{3.4}$$

Some concentrations are observed, albeit often indirectly. This can be because of two reasons.

- The concentration of A_j is measured outside the system.
- A reaction product A_k of A_j has its concentration measured, either inside or outside the system, where the reaction pathway towards A_k involves steps outside S.

In any case, a column vector of (indirect) *observations* would be given by

$$\mathbf{y} = \mathbf{Y} \cdot \mathbf{c}, \tag{3.5}$$

where the elements of $\mathbf{Y}$ are again 0 or 1.

Eqs. (3.2), (3.4) and (3.5) constitute the respective *initial condition*, *dynamical state equation* and *observation equation* of a *linear time-invariant state-space model* with input $\mathbf{u}$ and output $\mathbf{y}$.

[1]Nevertheless, for the sake of easy representation, each vertex will be given a different label A_j here, without loss of generality.

3.3 Analytical derivation of kinetic transfer functions

The measurements are influenced by $\mathbf{c}$ only through $\mathbf{y}$. Therefore, $\mathbf{c}$ must be eliminated from Eqs. (3.4) and (3.5). Taking into account the initial condition (3.2), the Laplace transform of dynamical state equation (3.4) is

$$s\mathscr{L}\mathbf{c} - \mathbf{c}_0 = \mathbf{K} \cdot \mathscr{L}\mathbf{c} + \mathbf{F} \cdot \mathscr{L}\mathbf{u}, \tag{3.6}$$

where s is the Laplace variable. This can be rewritten as

$$\mathbf{0}_{n_c} = (\mathbf{K} - s\mathbf{I}_{n_c}) \cdot \mathscr{L}\mathbf{c} + \mathbf{F} \cdot \mathscr{L}\mathbf{u} + \mathbf{c}_0, \tag{3.7}$$

where $\mathbf{0}_{n_c}$ is the zero vector with n_c elements and where $\mathbf{I}_{n_c}$ is the unit matrix with dimensions $n_c \times n_c$, in accordance with (2.8). It follows that

$$\mathscr{L}\mathbf{c} = \mathbf{H} \cdot (\mathbf{F} \cdot \mathscr{L}\mathbf{u} + \mathbf{c}_0), \tag{3.8}$$

where $\mathbf{H}$ is defined as

$$\mathbf{H} = (s\mathbf{I}_{n_c} - \mathbf{K})^{-1}. \tag{3.9}$$

$\mathbf{H}$ will be called the *kinetic transfer matrix* and its elements *kinetic transfer functions* of s. Due to the observation equation (3.5), it is found that

$$\mathscr{L}\mathbf{y} = \mathbf{Y} \cdot \mathbf{H} \cdot (\mathbf{F} \cdot \mathscr{L}\mathbf{u} + \mathbf{c}_0), \tag{3.10}$$

The input-output mapping $\mathcal{M}$ from $\mathbf{u}$ to $\mathbf{y}$ follows as

$$\mathcal{M}: \ \mathbf{u} \mapsto \mathscr{L}^{-1}\{\mathbf{Y} \cdot \mathbf{H} \cdot (\mathbf{F} \cdot \mathscr{L}\mathbf{u} + \mathbf{c}_0)\}. \tag{3.11}$$

3.4 Graph-theoretical derivation of kinetic transfer functions

The Laplace graph

The input-output mapping $\mathcal{M}$ was found as Eq. (3.11), where the transfer matrix $\mathbf{H}$ can be found analytically as in Eq. (3.9). The goal of this section is to be able to find $\mathbf{H}$ graph-theoretically. This will provide insight into the nature of the transfer functions.

Eq. (3.7) can be written out for the example. Assume there is no source of A_3, which would be typical if it was a surface species on a heterogeneous catalyst. Additionally, assume A_3 is initially absent.

$$\begin{bmatrix} 0 \\ 0 \\ 0 \end{bmatrix} = \begin{bmatrix} -s - k_{+1} - k_2 & k_{-1} & 0 \\ k_{+1} & -s - k_{-1} & k_3 \\ k_2 & 0 & -s - k_3 \end{bmatrix} \cdot \begin{bmatrix} \mathscr{L}c_1 \\ \mathscr{L}c_2 \\ \mathscr{L}c_3 \end{bmatrix} + \begin{bmatrix} \mathscr{L}f_1 + c_{1,0} \\ \mathscr{L}f_2 + c_{2,0} \\ 0 \end{bmatrix} \tag{3.12}$$

Eq. (3.12) can be made into an open compartmental model by the introduction of a virtual component A_0, with concentration c_0.

$$\begin{bmatrix}0\\0\\0\\0\end{bmatrix} = \begin{bmatrix}0 & s & s & s\\ 0 & -s-k_{+1}-k_2 & k_{-1} & 0\\ 0 & k_{+1} & -s-k_{-1} & k_3\\ 0 & k_2 & 0 & -s-k_3\end{bmatrix} \cdot \begin{bmatrix}\mathscr{L}c_0\\ \mathscr{L}c_1\\ \mathscr{L}c_2\\ \mathscr{L}c_3\end{bmatrix} + \begin{bmatrix}\mathscr{L}f_0 + c_{0,0}\\ \mathscr{L}f_1 + c_{1,0}\\ \mathscr{L}f_2 + c_{2,0}\\ 0\end{bmatrix} \tag{3.13}$$

The concentration c_0 and net source f_0 of A_0 can be chosen arbitrarily. Particularly interesting choices are

$$\mathscr{L}f_0 = -(\mathscr{L}f_1 + c_{1,0}) - (\mathscr{L}f_2 + c_{2,0}) \tag{3.14}$$

and

$$c_0 = \delta\,(t - 0^+) \tag{3.15}$$

so that

$$\mathscr{L}c_0 = 1 \tag{3.16}$$

and $c_{0,0} = 0$. These choices allow the homogeneous reformulation of Eq. (3.7), as a *closed compartmental model*. For the example, Eq. (3.12) becomes

$$\begin{bmatrix}0\\0\\0\\0\end{bmatrix} = \begin{bmatrix}-(\mathscr{L}f_1 + c_{1,0}) & & & \\ -(\mathscr{L}f_2 + c_{2,0}) & s & s & s\\ \mathscr{L}f_1 + c_{1,0} & -s-k_{+1}-k_2 & k_{-1} & 0\\ \mathscr{L}f_2 + c_{2,0} & k_{+1} & -s-k_{-1} & k_3\\ 0 & k_2 & 0 & -s-k_3\end{bmatrix} \cdot \begin{bmatrix}\mathscr{L}c_0\\ \mathscr{L}c_1\\ \mathscr{L}c_2\\ \mathscr{L}c_3\end{bmatrix}. \tag{3.17}$$

Generally,

$$\mathbf{0}_{n_g+1} = \mathbf{K}^* \cdot \mathscr{L}\mathbf{c}^*, \tag{3.18}$$

where $\mathbf{0}_{n_g+1}$ is the zero column vector with $n_g + 1$ elements. Essential is that the elements of each column of $\mathbf{K}^*$ add up to zero. Eq. (3.18) can be solved graph-theoretically as in King and Altman (1956); Yablonskii et al. (1991); Petrov (1992). To this end, it has to be represented by means of a digraph, which can be called the *Laplace graph*. It can be obtained from the reaction graph by addition of

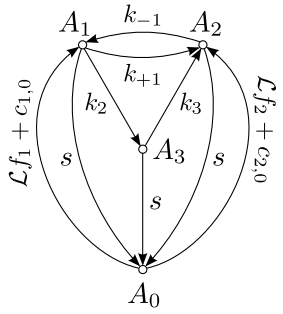

Figure 3.2: A Laplace graph obtained by extension of the reaction graph in Fig. 3.1. A_0 is a virtual component, the concentration of which is defined by Eq. (3.15). $\mathscr{L}f_j$ is the Laplace transform of the net source of A_j, absent for A_3. $c_{j,0}$ is the initial concentration of A_j, zero for A_3.

a) a vertex representing the virtual component A_0

b) an arc from each vertex A_j to A_0 with weight s, which will be called an *s-arc*,

c) if $\mathscr{L}u_j + c_{j,0} \neq 0$, an arc from A_0 to A_j with weight $\mathscr{L}u_j + c_{j,0}$, which will be called a *source-arc*.

Fig. 3.2 shows the Laplace graph obtained by extension of the reaction graph in Fig. 3.1.

The relative values of the unknowns are given by

$$\frac{\mathscr{L}c_j}{\mathscr{L}c_k} = \frac{D_j}{D_k}, \tag{3.19}$$

where D_j and D_k are the *determinants* of the vertices A_j and A_k in the Laplace graph, see Definition A.8 on p. 171. Especially,

$$\frac{\mathscr{L}c_j}{\mathscr{L}c_0} = \frac{D_j}{D_0}, \tag{3.20}$$

which simplifies to

$$\mathscr{L}c_j = \frac{D_j}{D_0} \tag{3.21}$$

taking into account Eq. (3.16).

Back to the reaction graph

The denominator D_0 in Eq. (3.21) is the sum of the weights of the spanning trees of the Laplace graph, rooted in A_0. Such a spanning tree is

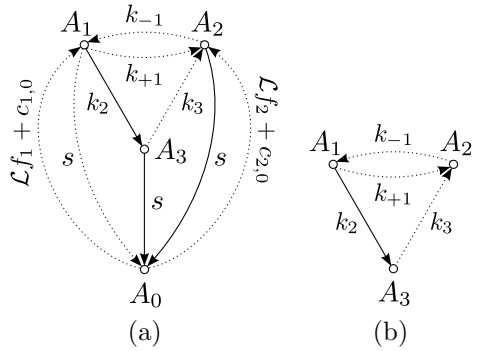

Figure 3.3: A spanning tree in the Laplace graph of Fig. 3.2, rooted in the virtual component A_0 (a). Removal of the s-arcs yields a spanning forest in the reaction graph (b). It contains two trees, the number of s-arcs which have been removed. One of the trees is trivial: A_2.

shown in Fig. 3.3 (a). Clearly, D_0 is a polynomial in s, the weights being proportional to s^q if the corresponding spanning tree contains q s-arcs.

a) Removal of these q s-arcs from such a tree yields a spanning forest of the reaction graph, containing q trees. Fig. 3.3 (b) shows the spanning forest corresponding to the spanning tree in the Laplace graph depicted in Fig. 3.3 (a).

b) Inversely, every spanning forest of the reaction graph containing q trees, yields a spanning tree of the Laplace graph, rooted in A_0, after addition of q s-arcs from all roots to A_0.

This shows how the coefficient of s^q in D_0 is equal to the sum of the weights of the spanning forests containing q trees in the reaction graph. Fig. 3.4 depicts all spanning forests of the reaction graph depicted in Fig. 3.1.

D_j in the numerator in Eq. (3.21) is the sum of the weights of the spanning trees in the Laplace graph, rooted in A_j. Again, this is a polynomial in s, each weight contributing to the qth order term if the tree contains q s-arcs. In order to contain the virtual component A_0, the spanning trees have to contain exactly one source-arc. If D_j is expanded accordingly, the numerator in Eq. (3.21) becomes

$$D_j = \sum_k W_{j,k}(\mathscr{L} f_k + c_{k,0}). \tag{3.22}$$

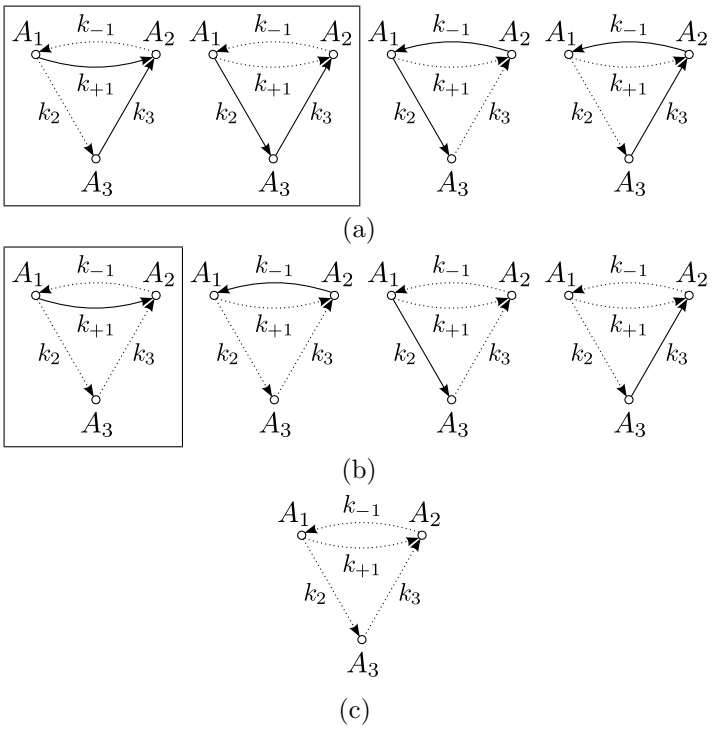

Figure 3.4: Spanning forests of a reaction graph: forests containing one tree (a), forests containing two trees (b), one of which trivial, forest containing three trivial trees (c). The framed graphs contain a tree rooted in A_2 and containing A_1.

Consider the spanning trees of the Laplace graph rooted in A_j and containing the source-arc to A_k. An example is shown in Fig. 3.5 (a), for $j = 2$ and $k = 1$.

a) Removal of the, say q, s-arcs and the source-arc yields a spanning forest of the reaction graph, containing $q + 1$ trees. Especially, one tree is rooted in A_j and contains A_k. This is illustrated by the transformation of Fig. 3.5 (a) into Fig. 3.5 (b).

b) Inversely, any such forest can be transformed into a spanning tree of the Laplace graph by addition of q s-arcs from each root except A_j to A_0 and the source-arc from there to A_k.

Clearly, the coefficient of s^l in $W_{j,k}$ is equal to the sum of the weights of the spanning forests containing $q + 1$ trees in the reaction graph, one of

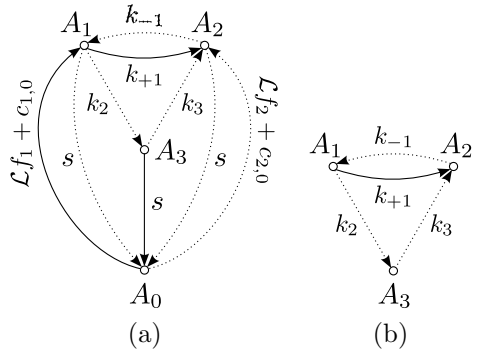

Figure 3.5: Spanning tree in a Laplace graph, rooted in A_2 and containing A_1 (a). Removal of the s- and source-arcs yields a spanning forest in the reaction graph (b). It contains two trees, one more than the number of s-arcs which have been removed. One tree is rooted in A_2 and contains A_1. The other tree is trivial: A_3.

which contains a path from A_k to A_j. In Fig. 3.4, the forests of which the weight contributes to $W_{2,1}$ are framed.

Kinetic transfer functions

The observed concentrations c_j depend on the net sources f_k and initial concentrations $c_{k,0}$ as

$$\mathscr{L}c_j(s) = \sum_k H_{j,k}(s)(\mathscr{L}f_k(s) + c_{k,0}) \tag{3.23}$$

where $H_{j,k}(s)$ is the (j,k) element of the transfer matrix $\mathbf{H}$ in Eq. (3.11). $H_{j,k}(s)$ can be found from the following theorem, which summarizes the graph-theoretical results.

Theorem 3.1. *A kinetic transfer function $H_{j,k}$ is found as a polynomial quotient*

$$H_{j,k}(s) = \frac{N(s)}{D(s)}, \tag{3.24}$$

of which the lth order coefficient

a) in the denominator D is the weight sum of the spanning forests containing q trees in the reaction graph,

b) in the numerator N is the weight sum of the spanning forests containing $q+1$ trees, one of which is rooted in A_j and contains A_k.

Application of Theorem 3.1 to the example, see Fig. 3.4, yields

$$H_{2,1}(s) = \Big[k_{+1}s + \big(k_{+1}k_3 + k_2k_3\big)\Big] \Big/ \Big[s^3 + \big(k_{+1} + k_{-1} + k_2 + k_3\big)s^2 + \big(k_{+1}k_3 + k_2k_3 + k_{-1}k_2 + k_{-1}k_3\big)s\Big]. \quad (3.25)$$

3.5 Symbolic form of kinetic transfer functions

In a reaction graph, consider two (not necessarily different) component vertices A_k and A_j. It is possible to find the symbolic form of the transfer function $H_{j,k}$ from connectivity features of the reaction graph.

Theorem 3.2. *a) A kinetic transfer function $H_{j,k}$ can be written as a polynomial quotient,*

$$H_{j,k}(s) = \frac{N(s)}{D(s)} = \frac{\sum_{q=0}^{n-l-1} \beta_q s^q}{\sum_{q=0}^{n} \alpha_q s^q}, \quad (3.26)$$

where n is the number of vertices which are situated on at least one directed pathway from A_k to A_j, and l is the length of the shortest pathway(s) from A_k to A_j.

b) All coefficients β_q and $\alpha_{q\geqslant 1}$ are strictly positive. α_0 is zero if A_j is in an ergodic strong linkage class and strictly positive otherwise. D is monic: $\alpha_n = 1$. If $j = k$, $N_{j,k}$ is also monic: $\beta_{n-1} = 1$.

c) For each $q \geqslant 1$, $\beta_q < \alpha_{q+1}$. Moreover, if A_j is not in an ergodic strong linkage class,

$$\beta_0 < \alpha_1. \quad (3.27)$$

Proof. Consider all walks (see Appendix A) from A_k to A_j in the reaction graph. Fig. 3.6 (a) shows an example, with the arcs pertaining to these walks highlighted. There are n vertices on the walks, representing A_k, A_j and all intermediates. Reduce the reaction network to the elementary steps represented by the arcs leaving from these vertices. They arrive either in another of these n vertices or in a vertex from which there is no walk to A_j. In the reduced reaction graphs, the latter vertices will become sinks. Call m the number of these sinks. Fig. 3.6 (b) shows the reaction graph resulting from the corresponding reduction of the graph in Fig. 3.6 (a). For this example, $n = 7$ and $m = 4$. The reduction does

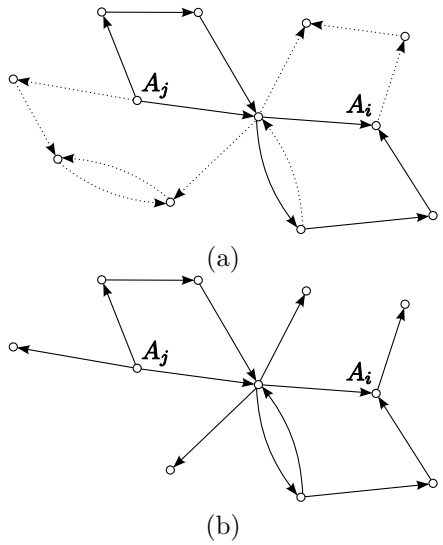

Figure 3.6: A reaction graph showing the walks from A_k to A_j highlighted (a) and a reduced version of this graph, withholding A_k and A_j, the intermediates, and the arcs of which they are the tail (b).

not change the transfer function $H_{j,k}$. Application of Theorem 3.1 to the reduced reaction graph yields

$$H_{j,k}(s) = \frac{\tilde{N}(s)}{\tilde{D}(s)} = \frac{\sum_q \tilde{\beta}_q s^q}{\sum_q \tilde{\alpha}_q s^q}. \tag{3.28}$$

The nonnegativity of the coefficients $\tilde{\alpha}_q$ and $\tilde{\beta}_q$ follows immediately from Theorem 3.1. It also follows immediately that each denominator coefficient $\tilde{\alpha}_q$ is not smaller than the numerator coefficient $\tilde{\beta}_{q-1}$.

The qth order coefficient $\tilde{\beta}_q$ of $\tilde{N}$ is the weight sum of the spanning forests containing $q+1$ trees in the reduced reaction graph, with the restriction that one of them is rooted in A_j and contains A_k. Due to the specific nature of the reduction, it is possible to construct a tree rooted in A_j, containing all vertices representing intermediates. Especially, this tree can be made to contain a shortest directed path from A_k to A_j. Together with m trivial trees for the other vertices, this tree constitutes a spanning forest. The lowest order nonnegative coefficient is therefore $\tilde{\beta}_m$. Disconnecting one of the leaves other than A_k in the nontrivial tree in this forest, yields a new spanning forest, the weight of which contributes to $\tilde{\beta}_{m+1}$, which is therefore also nonzero. This is possible until the nontrivial

tree is reduced to the shortest path. The spanning forest then contains $(m+1)+n-(l+1)$ trees. The highest order nonzero coefficient is therefore $\tilde{\beta}_{m+n-l-1}$. Especially, if $j = k$, $l = 0$ and the "maximal" spanning forest has all trees trivial. This forest is unique and has weight 1, so that $\tilde{\beta}_{m+n-1} = 1$.

The qth order coefficient $\tilde{\alpha}_q$ of $\tilde{D}$ is the weight sum of the spanning forests containing q trees. A spanning forest can consist of no fewer trees than the number of ergodic strong linkage classes. m trivial ergodic strong linkage classes are due to vertices not on any walk from A_k to A_j. An additional ergodic strong linkage class exist only if A_j is in one. The lowest possible number of trees in a spanning forest is therefore m or $m+1$. There is at least one such "minimal" spanning forest. The lowest order nonzero coefficient is therefore $\tilde{\alpha}_m$ or $\tilde{\alpha}_{m+1}$, depending on the case. In any case, especially, there is a "minimal" spanning forest containing a directed path from A_k to A_j. Disconnecting A_k as a leaf in a nontrivial tree makes A_k an additional, trivial, tree in a new spanning forest. On the one hand, this proves that the second lowest order coefficient $\tilde{\alpha}_{m+1}$ or $\tilde{\alpha}_{m+2}$ is nonzero. On the other hand, it proves that this coefficient is strictly greater than the corresponding coefficient $\tilde{\beta}_m$ or $\tilde{\beta}_{m+1}$. Indeed, according to Theorem 3.1, the weight of the described spanning forest contributes to a denominator coefficient, but not to a numerator coefficient. Disconnecting any new leaf in a nontrivial tree again yields an additional, trivial tree in a new spanning forest. The weight of this spanning forest contributes to the third lowest order coefficient of the denominator, but not to the corresponding coefficient of the numerator. The former is therefore nonzero and strictly greater than the latter. The disconnection process is possible until a spanning forest is obtained which contains $n+m$ trees, all trivial. This forest is clearly unique. The highest order coefficient of $\tilde{D}$ is therefore $\tilde{\alpha}_{n+m}$ and equal to its weight, 1.

As the coefficients $\tilde{\alpha}_q$ and β_q are zero for $q < m$, the quotient (3.28) can be simplified as Eq. (3.26), where $D(s) = s^{-m}\tilde{D}(s)$ and $N(s) = s^{-m}\tilde{N}(s)$. This proves part a of the theorem. Parts b and c follow as a translation of the observations above. □

Remark 3.1. If $k \neq j$, the vertices different from A_j and A_k, situated on at least one directed pathway from A_k to A_j, represent the reaction intermediates between A_k and A_j, see Section 1.1. The number n is therefore equal to the number of intermediates plus two. Now consider the case $k = j$. The vertices different from A_j, situated on at least one directed pathway from A_j to itself, can be said to represent intermediates between A_j and itself. In this case, n is the number of intermediates plus one.

Remark 3.2. The overall degree of $H_{j,k}$ follows from Theorem 3.2, part a as $-l-1$. This was to be expected. Indeed, each division by s corresponds to an integration as does each transition from the rate of a reaction step to the concentration of its product along a shortest path in the reaction graph.

Remark 3.3. It is also possible to obtain part a of Theorem 3.2 in a straightforward way from Mason's rule in the signal-flow graph formalism (Mason and Zimmermann, 1960), as was carried out by Happel et al. (1986b). This formalism, however, is not suitable to prove the parts b or c.

Theorem 3.3. *If A_k and $A_{k'}$ are in the same strong linkage class of the reaction graph, for any vertex A_j to which there are directed pathways from A_k and $A_{k'}$, the transfer functions $H_{j,k}$ and $H_{j,k'}$ have the same denominator D:*

$$H_{j,k}(s) = \frac{N_{j,k}(s)}{D(s)},\ H_{j,k'}(s) = \frac{N_{j,k'}(s)}{D(s)}. \tag{3.29}$$

Proof. It is sufficient to observe that the reaction graph reduction introduced in the proof of Theorem 3.2 yields the same result in both cases. □

Theorem 3.4. *Let $I(k)$ represent the set of indices j for which there is at least one directed pathway from A_k to A_j and for which A_j is situated in an ergodic strong linkage class. Then*

$$\sum_{j \in I(k)} \lim_{s \to 0} sH_{j,k}(s) = 1. \tag{3.30}$$

Proof. Suppose all components are initially absent, and only A_k has a net source f_k. Then, due to the conservation of mass as reflected in the stoichiometry, at all times t,

$$\sum_{j \in I} \frac{\mathrm{d}c_j}{\mathrm{d}t}(t) = f_k(t), \tag{3.31}$$

where I represents the set of all vertex indices of the reaction graph. Taking into account the initial absence of all components, Laplace transformation of Eq. (3.31) yields

$$\sum_{j \in I} s\mathscr{L}c_j(s) = \mathscr{L}f_k(s). \tag{3.32}$$

Substitution of Eq. (3.23) and taking limits for $s \to 0$ yields

$$\sum_{j \in I} \lim_{s \to 0} sH_{j,k}(s) = 1. \tag{3.33}$$

$H_{j,k}(s)$ is identically zero if there is no directed path from A_k to A_j. If there is such a path, but A_j is not in an ergodic strong linkage class, $\lim_{s \to 0} sH_{j,k}(s) = 0$ due to Theorem 3.2, part b. The set I can therefore be reduced to $I(k)$, yielding Eq. (3.30). □

Theorem 3.4 imposes an important constraint on the fractions β_0/α_1 in the transfer functions $H_{j,k}$. Especially, if $I(k)$ is a singleton, $\beta_0 = \alpha_1$. This illustrates that Eq. (3.27) does not hold if A_j is in an ergodic strong linkage class.

3.6 Conclusions

Compartmental kinetics for pseudomonomolecular reaction networks have been described in the form of kinetic transfer functions. Theorems have been proposed which allow the deduction of such transfer functions for most types of pseudomonomolecular reaction networks in two ways: analytically and graph-theoretically. Moreover, graph-theoretical theorems have been formulated relating the symbolic form of the kinetic transfer function to connectivity features of the reaction graph. This will provide the basis of Chapter 7 on the identifiability of rate coefficients and Chapter 8 on the model-free extraction of connectivity features of reaction networks from TAP-data.

Compartmental kinetics are typical in TAP, the experimental technique on which the present work focuses. Chapter 4 will provide an introduction to TAP, with a stress on its mathematical model. It will be shown how kinetic transfer functions for compartmental kinetics can be plugged in the physico-chemical model.

Chapter 4

Temporal Analysis of Products

4.1 Introduction

It was explained in Chapter 1 that transient kinetic experiments provide a valuable tool in the determination of reaction networks. The present work focuses on TAP. Section 4.2 will provide a minimum of experimental background information on this technique. The thin-zone-TAP-reactor (TZTR), a special configuration of the TAP reactor, will be introduced. Section 4.3 will present a one-dimensional physico-chemical model for the most common type of TAP-experiments. Finally, Section 4.4 will introduce two ways in which the reactor model can be numerically integrated. The first way starts with the discretization of the axial coordinate. The second way, applying only to pseudomonomolecular reaction networks, uses Fourier techniques. It relies on the kinetic transfer functions of Chapter 3. The TZTR will be treated as a special case.

4.2 Experimental

The TAP-setup (Gleaves et al., 1988; Yablonsky et al., 2003) was designed to assist catalyst development and characterization. Processing data from the TAP-setup is not straightforward. The present work extends the range of available techniques.

Principles

TAP-experiments are performed using a tubular reactor, closed at the inlet and open at the outlet, loaded with a fixed catalyst bed. A schematic representation is shown in Fig. 4.1. All laboratory reactors to study reaction kinetics are designed such, that the physical part of their description

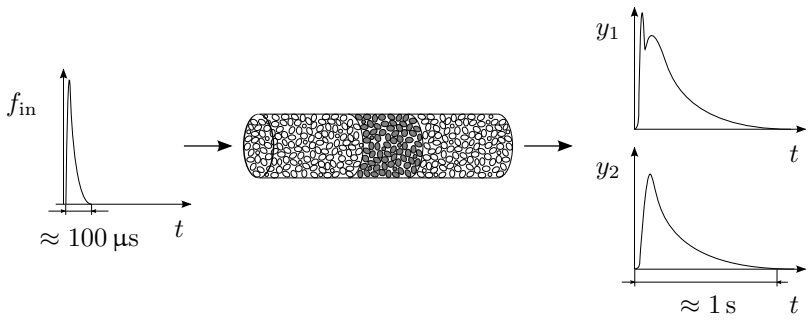

Figure 4.1: A schematic representation of a TAP-experiment. $f_{\text{in}}(t)$ is the molar flow rate of reactants admitted to the reactor by a pulse valve. $y_j(t)$ are responses in V, measured by a mass spectrometer. A response is usually proportional to the molar flow rate of a certain gaseous component out of the reactor.

is simple but accurate. This renders the extraction of the chemical information from the experiment more easy and secure. Most importantly, transport through the reactor is kept as simple as possible. With this principle in mind, the diameter of the TAP-reactor was designed small enough compared to its length, typically 5 mm vs. 3 cm, to ensure radial uniformity (Constales et al., 2001). More importantly, however, the TAP-apparatus allows the pressure inside the reactor to be maintained at a sufficiently low level to ensure all transport through the bed to occur by *Knudsen diffusion*. This means that for each gas phase molecule, the probability of colliding with another gas phase molecule is negligible compared to the probability of colliding with the surface of the reactor bed particles. As a result, gas phase reactions are suppressed in the TAP-reactor, allowing the unequivocal measurement of surface chemistry (Rothaemel and Baerns, 1996). Another, even more important advantage is that in the Knudsen regime, the diffusion coefficient of each component is independent of the local composition of the gas mixture. Moreover, given the bed, any Knudsen diffusion coefficient can be derived from a known Knudsen diffusion coefficient of a reference gas component at a reference temperature. Huizenga and Smith (1986) experimentally verified that the *effective Knudsen diffusion coefficient*, $\mathscr{D}_{e,j}$, of a component A_j through a bed of uniform spheres can be expressed as

$$\mathscr{D}_{e,j} = \frac{4\overline{r}\epsilon_b}{3\tau}\sqrt{\frac{2RT}{\pi M_j}}, \tag{4.1}$$

where ϵ_b is the bed porosity, τ is the tortuosity factor, R is the universal gas constant, T is the absolute temperature and M_j is the molecular mass of A_j. $\overline{r}$ is the mean pore radius, given as

$$\overline{r} = \frac{2}{3} \frac{\epsilon_b}{1 - \epsilon_b} r_s, \tag{4.2}$$

where r_s is the radius of the spherical particles. A more general version of Eq. (4.1), where the bed particles are not necessarily spherical or uniform, is

$$\mathscr{D}_{e,j} = \mathscr{D}_{e,\mathrm{ref}} \sqrt{\frac{T}{T_{\mathrm{ref}}}} \sqrt{\frac{M_{\mathrm{ref}}}{M_i}}, \tag{4.3}$$

which relates the effective diffusion coefficient $\mathscr{D}_{e,j}$ of A_j to the effective diffusion coefficient $\mathscr{D}_{e,\mathrm{ref}}$ of a reference gas component with molecular mass M_{ref} at a reference temperature T_{ref} over the same bed.

When operated in low-pressure mode, the outlet of the TAP-reactor is in contact with a vacuum reservoir. At the inlet, the reactor can be fed by continuous or pulse valves. The latter allow reactants to be admitted in sufficiently narrow pulses to ensure the pressure rise to be small enough for the gas transport to remain in the Knudsen regime. As the reactor is open only at the outlet, all gases eventually leave the reactor there. A portion of the molecules is intercepted by a mass spectrometer, where they are first ionized. The molecules are hereby often fragmented into smaller ions, the fragmentation being component-specific. A quadrupole then acts as an electromagnetic filter, allowing only the ions of a selected mass[1] to pass through to a collector electrode. After amplification by an electron multiplier, the signal produced by the collector electrode is recorded as a *time series*, see below, with up to submillisecond time resolution. The experiment may be repeated several times, the quadrupole being tuned to another mass everytime, yielding n_v signals $y_1(t)$ $y_2(t)$, $y_3(t)$, $\ldots$, $y_{n_v}(t)$, in V.

The reactor tube is heated to a desired temperature by a copper sleeve, while viton o-rings sealing the inlet and outlet of the reactor are water-cooled. Therefore, some temperature nonuniformity along the length of the reactor usually cannot be avoided (Schuurman, 2008). As the reaction kinetics are very temperature dependent, the catalyst temperature has to be maintained uniform, which is ensured as follows. From inlet to outlet, three zones are loaded in the reactor: an inert one (consisting typically of quartz), a catalytic one and another inert one. This is depicted in Fig. 4.1. A particularly popular three-zone configuration is the *thin-zone-TAP-reactor* (TZTR) (Shekhtman, 1999), where the catalytic zone is much

[1] Actually, ions are selected by their mass-to-charge ratio, but this is equivalent, because the charge is always the same.

thinner than the inert ones, so that not only the temperature, but also the composition of the gas phase and the catalyst surface can be assumed uniform along the catalytic zone. This has the advantage that the gas phase concentrations and the rates of production or consumption of the different gas phase components can be calculated from the responses y_j. This is called the *Y-procedure* and is based on Fourier analysis (Yablonsky et al., 2002, 2007).

Some history

The idea of the TAP-reactor was conceived by John T. Gleaves and his team at Monsanto in 1978-1979. A TAP-apparatus has been operational at the Laboratory for Chemical Technology (LCT) since 1989. It pertains to the first generation of TAP-setups, designated as *TAP-1*. Low pressure TAP-1 pulse response data often suffer from low *signal-to-noise ratios* (SNRs). Furthermore, considerable fractions of molecules can be delayed (backscattered) between the moment they leave the reactor and the moment they are collected by the mass spectrometer (Gleaves et al., 1988; Zou et al., 1994). This obviously distorts the data. As a solution to these drawbacks, Gleaves et al. (1997) presented an improved version of the apparatus, called *TAP-2*, in which the mass spectrometer was mounted physically closer to the reactor outlet. Recently, Gleaves et al. (2010) presented the fully automated *TAP-3*-setup, which allows remote operation via the Internet. At the moment this work is being written, such an apparatus is being assembled by order of the LCT.

Types of low-pressure pulse response experiments

The holistic philosophy which has characterized the design of the TAP-apparatus since the early days, allows it to be used to perform many types of kinetic experiments. However, its true innovation lies in the low pressure pulsewise operation. There are two types of such TAP-experiments.

1. During a *state-defining experiment*, the *pulse size*, i.e., the quantity of reactant molecules is much smaller than the quantity of active sites on the catalyst. As a result, one pulse does not significantly perturb the state of the catalyst. As stated in Chapter 1, this has the important advantage that reaction networks become pseudomonomolecular and Fourier analysis can be applied during modeling. Another advantage is that time series collected as a response to a sequence of, typically, some tens of pulses are known to correspond to the same catalyst state. Especially, responses successively

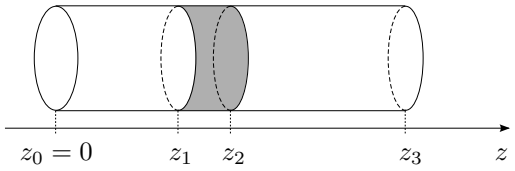

Figure 4.2: The key axial coordinates of a TAP-reactor with three-zone configuration.

collected at different masses can be treated as if they were measured simultaneously as a response to a single pulse. Also, responses subsequently collected at the same mass can be averaged to obtain a single response with higher SNR (Gleaves et al., 1988). A particular type of state-defining experiments is the *pump-probe experiment*, where pulses of different reactants are alternated. By varying the time delay between the pulses, information about the lifetime and reactivity of the adsorbed species can be obtained.

2. As opposed to a state-defining experiment, during a *state-altering experiment*, the quantity of reactant molecules cannot be neglected with respect to the quantity of active sites. This is usually done on purpose, to change the state of the catalyst in a predetermined way. During state-altering experiments, transport through the reactor often occurs partly by *molecular diffusion*, i.e., outside the Knudsen regime. Usually, a long sequence of pulses is admitted to the reactor, the mass spectrometer being tuned to a mass characteristic of the reactant. The uptake of that reactant throughout the series of pulses can then be calculated.

State-defining and state-altering experiments are often alternated in so-called interrogative cycles (Gleaves et al., 1997). In the present work, only state-defining experiments in the Knudsen regime will be considered.

4.3 Reactor model

The TAP-reactor is modeled by a system of partial differential equations with initial and boundary conditions. Very generally, consider a TAP-reactor containing n_z zones. Fig. 4.2 shows such a reactor for $n_z = 3$. In the lth zone, let $\mathbf{c}_g^{(l)}$ be a column vector containing the concentration of all, say n_g, gas components, in mol/m^3: $\mathbf{c}_g^{(l)} \in \mathbb{R}^{n_g \times 1}$. Similarly, if l is a catalytic zone, let $\mathbf{c}_s^{(l)}$ be a column vector of the concentration of the, say n_s, surface components, expressed relative to the catalyst mass, i.e., in

mol/kg: $\mathbf{c}_s^{(l)} \in \mathbb{R}^{n_s \times 1}$. As mentioned in Section 4.2, the concentrations are radially uniform. Because of symmetry, they are also tangentially uniform. Therefore, $\mathbf{c}_g^{(l)}$ and $\mathbf{c}_s^{(l)}$ depend only on the axial coordinate, say z, and the time t. Partial mass balances for each of the components on an infinitesimal slice of the lth zone of the reactor yield the following vectorial partial differential equations. For all $z \in [z_{l-1},\, z_l]$ and $t \geqslant 0$:

$$\epsilon_b^{(l)} \frac{\partial \mathbf{c}_g^{(l)}}{\partial t}(z,t) = \mathscr{D}_e^{(l)} \cdot \frac{\partial^2 \mathbf{c}_g^{(l)}}{\partial z^2}(z,t) + \left(1-\epsilon_b^{(l)}\right) \rho^{(l)} m_f^{(l)} \mathbf{r}_g^{(l)} \left(\mathbf{c}_g^{(l)}(z,t), \mathbf{c}_s^{(l)}(z,t)\right) \tag{4.4a}$$

$$\frac{\partial \mathbf{c}_s^{(l)}}{\partial t}(z,t) = \mathbf{r}_s^{(l)} \left(\mathbf{c}_g^{(l)}(z,t), \mathbf{c}_s^{(l)}(z,t)\right), \tag{4.4b}$$

where $\mathbf{r}_g^{(l)}$ and $\mathbf{r}_s^{(l)}$ are column vectors of specific rates of production of the gaseous and surface components in the lth zone, with unit mol/kg·s. They reflect the reaction kinetics. Furthermore, $\epsilon_b^{(l)}$ is the bed porosity, $\rho^{(l)}$ is the density of the material, in kg/m^3 and m_f is the catalytic mass fraction of that material. $\mathscr{D}_e^{(l)}$ is a diagonal matrix holding the effective Knudsen diffusion coefficients of the gaseous components through the lth zone, in m^2/s. Note that in an inert zone, the second term to the right hand side of Eq. (4.4a) disappears. Eq. (4.4b) disappears as a whole.

The initial gas concentrations are zero, while the initial surface concentrations are assumed known. For all $l \in \{1, 2, \ldots, n\}$ and $z \in [z_{l-1},\, z_l]$:

$$\mathbf{c}_g^{(l)}(z,0) = \mathbf{0} \tag{4.5a}$$

$$\mathbf{c}_s^{(l)}(z,0) = \mathbf{c}_{s,0}^{(l)}(z). \tag{4.5b}$$

The boundary conditions are, for all $t \geqslant 0$,

$$-\mathscr{D}_e^{(1)} \cdot \frac{\partial \mathbf{c}_g^{(1)}}{\partial z}(0,t) = \mathbf{f}_{\text{in}}(t) \tag{4.6a}$$

$$\mathbf{c}_g^{(n)}(z_n,t) = \mathbf{0}. \tag{4.6b}$$

Boundary condition (4.6a) expresses the inward molar flux to be known. Ideally, the time dependence of this flux is as a Dirac pulse:

$$\mathbf{f}_{\text{in}}(t) = \frac{\delta(t-0^+)}{\phi}\, \mathbf{n}, \tag{4.7}$$

where ϕ is the cross-sectional surface area of the reactor and $\mathbf{n}$ is a column vector holding the pulsed quantity of each gas component. Boundary

condition (4.6b) expresses that all gas concentrations at the outlet of the reactor are zero. This is because the outlet side of the reactor is in contact with the vacuum reservoir. In the past, there has been a debate about deviations from the ideal boundary conditions. Constales et al. (2006) showed that such deviations usually do not have to be taken into account. In addition to the initial and boundary conditions, there are transmission conditions between the zones. For all $l \in \{1, 2, \ldots, n-1\}$ and for all $t \geqslant 0$:

$$\mathbf{c}_g^{(l)}(z_l, t) = \mathbf{c}_g^{(l+1)}(z_l, t) \tag{4.8a}$$

$$-\boldsymbol{\mathscr{D}}_e^{(l)} \cdot \frac{\partial \mathbf{c}_g^{(l)}}{\partial z}(z_l, t) = -\boldsymbol{\mathscr{D}}_e^{(l+1)} \cdot \frac{\partial \mathbf{c}_g^{(l+1)}}{\partial z}(z_l, t). \tag{4.8b}$$

The vector of outlet fluxes is given by

$$\mathbf{f}_{\text{out}}(t) = -\boldsymbol{\mathscr{D}}_e^{(n)} \cdot \frac{\partial \mathbf{c}_g^{(n)}}{\partial z}(z_n, t). \tag{4.9}$$

The outlet fluxes are not directly measured. The actual responses are the signals produced by the mass spectrometer. Fragmented in a characteristic way at ionization, each component has a *mass spectrum*, i.e., a discrete distribution of the masses of its fragments. The mass spectra of different components generally overlap. Each signal $y_j(t)$ is therefore a sum of contributions due to different components. Matricially:

$$\mathbf{y}(t) = \phi\, \mathbf{S} \cdot \mathbf{f}_{\text{out}}(t), \tag{4.10}$$

where $\mathbf{y}(t) \in \mathbb{R}^{n_v \times 1}$ and $\mathbf{S} \in \mathbb{R}^{n_v \times n_g}$. The number of responses, n_v, need not be equal to the number of gases, n_g. The matrix $\mathbf{S}$ is called the *calibration matrix*. Its elements are called *calibration coefficients*.

4.4 Numerical calculation of TAP-responses

The idea is to calculate the equivalent of experimental responses from the reactor model described in Section 4.3. This means it is not required to calculate the continuous responses $\mathbf{y}(t)$, but, rather, time series $\mathbf{y}_j$ consisting of n_t samples with *sampling period* or *sampling interval* Δt:

$$\mathbf{y}_j = \begin{bmatrix} y_j(t_1) & y_j(t_2) & \cdots & y_j(t_{n_t}) \end{bmatrix}^T \tag{4.11}$$

where

$$t_k = (k-1)\Delta t \tag{4.12}$$

for all $k \in \{1, 2, \ldots, n_t\}$. The inverse of the sampling interval Δt is called the *sampling frequency*.

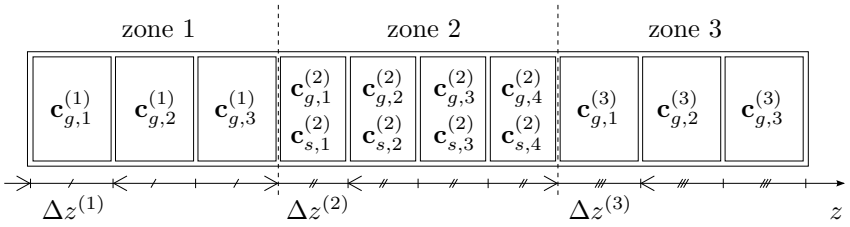

Figure 4.3: Discretization of the axial coordinate z of a three-zone-TAP-reactor.

Method of lines

According to the *method of lines*, the axial coordinate z is discretized (Schiesser, 1991). A one-dimensional grid is applied to the reactor. This is illustrated in Fig. 4.3 for a TAP-reactor with three-zone configuration. In this figure, the reactor is divided into seven axial intervals: three for the zones 1 and 3 and four for zone 2. In reality the number of intervals would typically be on the order of a hundred. As illustrated in the figure, the interval width need not be the same for te different zones. Generally, call this width Δz_l for zone l. Clearly,

$$\Delta z_l = \frac{z_{l+1} - z_l}{n_l} \tag{4.13}$$

if n_l is the number of intervals in zone l.

The intervals are assumed narrow enough to be able to assume the corresponding reactor slices to have uniform concentrations. The gas and surface concentration vectors in slice j of zone l are called $\mathbf{c}_{g,j}^{(l)}$ and $\mathbf{c}_{s,j}^{(l)}$. The initial and boundary value problem is converted into an initial value problem. For slice 1 of zone 1, partial mass balances yield

$$\epsilon_b^{(1)} \frac{\mathrm{d}\mathbf{c}_{g,1}^{(1)}}{\mathrm{d}t}(t) = \frac{1}{\Delta z_1} \mathbf{f}_{\mathrm{in}}(t) + \mathscr{D}_e^{(1)} \cdot \frac{\mathbf{c}_{g,2}^{(1)}(t) - \mathbf{c}_{g,1}^{(1)}(t)}{\left(\Delta z_1\right)^2} + \left(1 - \epsilon_b^{(1)}\right) \rho^{(1)} m_f^{(1)} \mathbf{r}_g^{(1)} \left(\mathbf{c}_{g,1}^{(1)}(t), \mathbf{c}_{s,1}^{(1)}(t)\right) \tag{4.14}$$

for all $t \geqslant 0$. Note that if zone l is inert, the third term to the right hand side of Eq. (4.14) disappears. For any zone l and any slice j in that zone which is not situated at its boundary, i.e., $j \in \{2, 3, \ldots, n_l - 1\}$,

$$\epsilon_b^{(l)} \frac{\mathrm{d}\mathbf{c}_{g,j}^{(l)}}{\mathrm{d}t}(t) = \mathscr{D}_e^{(l)} \cdot \frac{\mathbf{c}_{g,j+1}^{(l)}(t) - 2\,\mathbf{c}_{g,j}^{(l)}(t) + \mathbf{c}_{g,j-1}^{(l)}(t)}{\left(\Delta z_l\right)^2} + \left(1 - \epsilon_b^{(l)}\right) \rho^{(l)} m_f^{(l)} \mathbf{r}_g^{(l)} \left(\mathbf{c}_{g,j}^{(l)}(t), \mathbf{c}_{s,j}^{(l)}(t)\right). \tag{4.15}$$

For the last slice n_l of any zone l except the last one,

$$\epsilon_b^{(l)} \frac{\mathrm{d}\mathbf{c}_{g,n_l}^{(l)}}{\mathrm{d}t}(t) = -\boldsymbol{\mathscr{D}}_e^{(l)} \cdot \frac{\mathbf{c}_{g,n_l}^{(l)}(t) - \mathbf{c}_{g,n_l-1}^{(l)}(t)}{\left(\Delta z_l\right)^2} + \frac{2}{\Delta z_l}\left(\Delta z_l \left(\boldsymbol{\mathscr{D}}_e^{(l)}\right)^{-1} + \Delta z_{l+1}\left(\boldsymbol{\mathscr{D}}_e^{(l+1)}\right)^{-1}\right)^{-1} \cdot \left(\mathbf{c}_{g,1}^{(l+1)}(t) - \mathbf{c}_{g,n_l}^{(l)}(t)\right) + \left(1-\epsilon_b^{(l)}\right)\rho^{(l)} m_f^{(l)} \mathbf{r}_g^{(l)}\left(\mathbf{c}_{g,n_l}^{(l)}(t), \mathbf{c}_{s,n_l}^{(l)}(t)\right). \quad (4.16)$$

For the first slice of any zone l except the first one,

$$\epsilon_b^{(l)} \frac{\mathrm{d}\mathbf{c}_{g,1}^{(l)}}{\mathrm{d}t}(t) = -\frac{2}{\Delta z_l}\left(\Delta z_{l-1}\left(\boldsymbol{\mathscr{D}}_e^{(l-1)}\right)^{-1} + \Delta z_l \left(\boldsymbol{\mathscr{D}}_e^{(l)}\right)^{-1}\right)^{-1} \cdot \left(\mathbf{c}_{g,1}^{(l)}(t) - \mathbf{c}_{g,n_{l-1}}^{(l-1)}(t)\right) + \boldsymbol{\mathscr{D}}_e^{(l)} \cdot \frac{\mathbf{c}_{g,2}^{(l)}(t) - \mathbf{c}_{g,1}^{(l)}(t)}{\left(\Delta z_l\right)^2} + + \left(1-\epsilon_b^{(l)}\right)\rho^{(l)} m_f^{(l)} \mathbf{r}_g^{(l)}\left(\mathbf{c}_{g,1}^{(l)}(t), \mathbf{c}_{s,1}^{(l)}(t)\right). \quad (4.17)$$

For the last slice n_{n_z} of the last zone, because boundary condition (4.6b) is valid for all t,

$$\frac{\mathrm{d}\mathbf{c}_{g,n_{n_z}}^{(n)}}{\mathrm{d}t}(t) = \mathbf{0}. \quad (4.18)$$

Finally, in those zones l which are catalytically active, for each slice j,

$$\frac{\mathrm{d}\mathbf{c}_{s,j}^{(l)}}{\mathrm{d}t}(t) = \mathbf{r}_s^{(l)}\left(\mathbf{c}_{g,j}^{(l)}(t), \mathbf{c}_{s,j}^{(l)}(t)\right). \quad (4.19)$$

The initial conditions are readily translated from Eqs. (4.5a) and (4.5b).

$$\mathbf{c}_{g,j}^{(l)}(0) = \mathbf{0} \quad (4.20a)$$

and, in the zones l which are catalytically active,

$$\mathbf{c}_{s,j}^{(l)}(0) = \mathbf{c}_{s,0}^{(l)}\left(z_{l-1} + (j-1)\Delta z_l\right). \quad (4.20b)$$

Numerical integration of the initial value problem given by the vectorial differential equations (4.14), (4.15), (4.16), (4.17), (4.18), (4.19) and vectorial initial conditions (4.20a) and (4.20b) allows the calculation of the vector of gas outlet fluxes:

$$\mathbf{f}_{\mathrm{out}}(t) \approx -\boldsymbol{\mathscr{D}}_e^{(n)} \cdot \frac{\mathbf{c}_{g,n_{n_z}}^{(n)}(t) - \mathbf{c}_{g,n_{n_z}-1}^{(n)}(t)}{\Delta z_n} = \frac{1}{\Delta z_n}\boldsymbol{\mathscr{D}}_e^{(n)} \cdot \mathbf{c}_{g,n_{n_z}-1}^{(n)}(t) \quad (4.21)$$

Especially, this enables the numerical calculation at the measurement times t_k. The responses follow from Eq. (4.10). Note that numerical integration of the initial value problem requires the Dirac pulse in the expression (4.7) of the inlet flux vector $\mathbf{f}_{\text{in}}$ to be approximated by a finite function:

$$\delta(t-0^+) \approx \frac{t}{\tau^2}\exp\left(-\frac{t}{\tau}\right), \tag{4.22}$$

where τ is a very short duration, for example $\tau = 50\,\mu\text{s}$.

Transfer matrix approach

The *transfer matrix approach* was developed by Constales et al. (2001, 2004). It is based on Fourier analysis and is limited to pseudomonomolecular reaction kinetics and situations where the relevant surface components are initially absent:

$$\mathbf{c}_{s,0}^{(l)} = 0 \tag{4.23}$$

in Eq. (4.5b). Say $\mathbf{f}^{(l)}(z,t)$ is a vector holding the molar fluxes of all gas components in the positive z direction at each axial position z in zone l of the reactor. For all zones l and for all $z \in [z_{l-1},\, z_l]$ and $t \geqslant 0$:

$$\mathbf{f}^{(l)}(z,t) = -\boldsymbol{\mathscr{D}}_e^{(l)} \cdot \frac{\partial \mathbf{c}_g^{(l)}}{\partial z}(z,t). \tag{4.24}$$

Taking Laplace transforms yields

$$\mathscr{L}\mathbf{f}^{(l)}(z,s) = -\boldsymbol{\mathscr{D}}_e^{(l)} \cdot \frac{\partial \mathscr{L}\mathbf{c}_g^{(l)}}{\partial z}(z,s). \tag{4.25}$$

Now consider an infinitesimal slice of the reactor. The net molar flow rates of gas components into this slice per unit mass of catalyst, in mol/kg·s, is

$$\tilde{\mathbf{u}}^{(l)}(z,t) = -\frac{1}{\left(1-\epsilon_b^{(l)}\right)\rho^{(l)} m_f^{(l)}}\,\frac{\partial \mathbf{f}^{(l)}(z,t)}{\partial z}. \tag{4.26}$$

$\tilde{\mathbf{u}}^{(l)}(z,t)$ is a part of the vector $\mathbf{u}$ in Eq. (3.8), which is valid because the kinetics are assumed pseudomonomolecular. The other elements of $\mathbf{u}$ are all zero, as they correspond to surface components. $\mathbf{c}_0$ in Eq. (3.8) is a zero vector, as a consequence of Eq. (4.5a) and the assumption (4.23). Eq. (3.8) may therefore be rewritten as

$$\mathscr{L}\mathbf{c}^{(l)}(z,s) = \mathbf{H}^{(l)}(s) \cdot \tilde{\mathbf{F}}^{(l)} \cdot \mathscr{L}\tilde{\mathbf{u}}^{(l)}(z,s), \tag{4.27}$$

where $\tilde{\mathbf{F}}^{(l)}$ is the result of deleting those columns in $\mathbf{F}^{(l)}$ which correspond to the surface components. Now select the gas components in $\mathscr{L}\mathbf{c}^{(l)}(z,s)$

once[2]. Call $\mathscr{L}\tilde{\mathbf{c}}^{(l)}(z,s)$ and $\tilde{\mathbf{H}}^{(l)}(s)$ the result of selecting the corresponding rows in $\mathscr{L}\mathbf{c}^{(l)}(z,s)$ and $\mathbf{H}^{(l)}(s)$. Then Eq. (4.27) becomes

$$\mathscr{L}\tilde{\mathbf{c}}^{(l)}(z,s) = \tilde{\mathbf{H}}^{(l)}(s) \cdot \tilde{\mathbf{F}}^{(l)} \cdot \mathscr{L}\tilde{\mathbf{u}}^{(l)}(z,s). \tag{4.28}$$

Finally, $\mathscr{L}\mathbf{c}_g^{(l)}$ is found from $\mathscr{L}\tilde{\mathbf{c}}^{(l)}$ by adapting the dimensions

$$\mathscr{L}\mathbf{c}_g^{(l)}(z,s) = \frac{1-\epsilon_b^{(l)}}{\epsilon_b^{(l)}}\, \rho^{(l)} m_f^{(l)}\, \mathscr{L}\mathbf{c}^{(l)}(z,s) \tag{4.29}$$

$$= \frac{1-\epsilon_b^{(l)}}{\epsilon_b^{(l)}}\, \rho^{(l)} m_f^{(l)}\, \tilde{\mathbf{H}}^{(l)}(s) \cdot \tilde{\mathbf{F}}^{(l)} \cdot \mathscr{L}\tilde{\mathbf{u}}^{(l)}(z,s). \tag{4.30}$$

Substitution of the Laplace transform of Eq. (4.26) yields

$$\mathscr{L}\mathbf{c}_g^{(l)}(z,s) = -\frac{1}{\epsilon_b^{(l)}}\, \tilde{\mathbf{H}}^{(l)}(s) \cdot \tilde{\mathbf{F}}^{(l)} \cdot \frac{\partial \mathscr{L}\mathbf{f}^{(l)}(z,s)}{\partial z}. \tag{4.31}$$

Eqs. (4.25) and (4.31) can be summarized as

$$\frac{\partial}{\partial z}\begin{bmatrix}\mathscr{L}\mathbf{c}_g^{(l)}\\ \mathscr{L}\mathbf{f}^{(l)}\end{bmatrix}(z,s) = -\begin{bmatrix}\mathbf{0} & \left(\mathscr{D}_e^{(l)}\right)^{-1}\\ \epsilon_b^{(l)}\left(\tilde{\mathbf{H}}^{(l)}(s)\cdot\tilde{\mathbf{F}}^{(l)}\right)^{-1} & \mathbf{0}\end{bmatrix}\cdot\begin{bmatrix}\mathscr{L}\mathbf{c}_g^{(l)}\\ \mathscr{L}\mathbf{f}^{(l)}\end{bmatrix}(z,s) \tag{4.32}$$

Compare this equation with Eq. (17) in (Constales et al., 2004). Integration of Eq. (4.32) over the length $\Delta z^{(l)}$ of a zone l yields

$$\begin{bmatrix}\mathscr{L}\mathbf{c}_g^{(l)}\\ \mathscr{L}\mathbf{f}^{(l)}\end{bmatrix}(z_{l-1},s) = \mathbf{M}_l(s)\cdot\begin{bmatrix}\mathscr{L}\mathbf{c}_g^{(l)}\\ \mathscr{L}\mathbf{f}^{(l)}\end{bmatrix}(z_l,s), \tag{4.33}$$

where the matrix $\mathbf{M}_l(s)$ is defined as

$$\mathbf{M}_l(s) = \exp\left(\begin{bmatrix}\mathbf{0} & \left(\mathscr{D}_e^{(l)}\right)^{-1}\\ \epsilon_b^{(l)}\left(\tilde{\mathbf{H}}^{(l)}(s)\cdot\tilde{\mathbf{F}}^{(l)}\right)^{-1} & \mathbf{0}\end{bmatrix}\Delta z^{(l)}\right) \tag{4.34}$$

and $\Delta z^{(l)} = z_l - z_{l-1}$ is the zone width.[3] The matrices $\mathbf{M}_l(s)$ can be calculated numerically and sometimes analytically. Especially, an analytical

[2]Recall that one component may be represented multiple times in $\mathscr{L}\mathbf{c}^{(l)}$.

[3]The exponential function of a matrix $\mathbf{A}$ is defined as $\mathbf{I}+\mathbf{A}+\frac{1}{2!}\mathbf{A}^2+\ldots+\frac{1}{n!}\mathbf{A}^n+\ldots$ If $\mathbf{A}$ is diagonalizable, i.e., $\mathbf{A} = \mathbf{P}\cdot\mathbf{D}\cdot\mathbf{P}^{-1}$, $\exp\mathbf{A} = \mathbf{P}\cdot\exp\mathbf{D}\cdot\mathbf{P}^{-1}$. where

$$\mathbf{D} = \begin{bmatrix}d_1 & 0 & \cdots & 0\\ 0 & d_2 & \cdots & 0\\ \vdots & \vdots & \ddots & \vdots\\ 0 & 0 & \cdots & d_n\end{bmatrix} \text{ and } \exp\mathbf{D} = \begin{bmatrix}\exp d_1 & 0 & \cdots & 0\\ 0 & \exp d_2 & \cdots & 0\\ \vdots & \vdots & \ddots & \vdots\\ 0 & 0 & \cdots & \exp d_n\end{bmatrix}.$$

expression is available if l is inert:

$$\mathbf{M}_l(s) = \begin{bmatrix} \mathbf{C}(s) & \mathbf{S}_{1,2}(s) \\ \mathbf{S}_{2,1}(s) & \mathbf{C}(s) \end{bmatrix}, \tag{4.35}$$

where

$$\mathbf{C}(s) = \begin{bmatrix} \cosh\sqrt{s\tau_1^{(l)}} & 0 & \cdots & 0 \\ 0 & \cosh\sqrt{s\tau_2^{(l)}} & \cdots & 0 \\ \vdots & \vdots & \ddots & \vdots \\ 0 & 0 & \cdots & \cosh\sqrt{s\tau_{n_g}^{(l)}} \end{bmatrix}, \tag{4.36}$$

$$\mathbf{S}_{1,2}(s) = \begin{bmatrix} \frac{\sinh\sqrt{s\tau_1^{(l)}}}{\gamma_1^{(l)}\sqrt{s\tau_1^{(l)}}} & 0 & \cdots & 0 \\ 0 & \frac{\sinh\sqrt{s\tau_2^{(l)}}}{\gamma_2^{(l)}\sqrt{s\tau_2^{(l)}}} & \cdots & 0 \\ \vdots & \vdots & \ddots & \vdots \\ 0 & 0 & \cdots & \frac{\sinh\sqrt{s\tau_{n_g}^{(l)}}}{\gamma_{n_g}^{(l)}\sqrt{s\tau_{n_g}^{(l)}}} \end{bmatrix} \tag{4.37}$$

and

$$\mathbf{S}_{2,1}(s) = \begin{bmatrix} \gamma_1^{(l)}\sqrt{s\tau_1^{(l)}}\sinh\sqrt{s\tau_1^{(l)}} & 0 & \cdots & 0 \\ 0 & \gamma_2^{(l)}\sqrt{s\tau_2^{(l)}}\sinh\sqrt{s\tau_2^{(l)}} & \cdots & 0 \\ \vdots & \vdots & \ddots & \vdots \\ 0 & 0 & \cdots & \gamma_{n_g}^{(l)}\sqrt{s\tau_{n_g}^{(l)}}\sinh\sqrt{s\tau_{n_g}^{(l)}} \end{bmatrix}, \tag{4.38}$$

in which

$$\tau_j^{(l)} = \epsilon_b^{(l)}(\Delta z^{(l)})^2/\mathscr{D}_{e,j}^{(l)} \tag{4.39}$$

and

$$\gamma_j^{(l)} = \mathscr{D}_{e,j}^{(l)}/\Delta z^{(l)}. \tag{4.40}$$

An approximate analytical expression of $\mathbf{M}_l(s)$ is also possible if zone l is thin. This is of course useful for a TZTR. In that case, $\left(\boldsymbol{\mathscr{D}}_e^{(l)}\right)^{-1}\Delta z^{(l)}$ is approximately zero and Eq. (4.34) becomes

$$\mathbf{M}_l(s) = \begin{bmatrix} \mathbf{I} & \mathbf{0} \\ \epsilon_b^{(l)}\,\Delta z^{(l)}\,\left(\tilde{\mathbf{H}}^{(l)}(s)\cdot\tilde{\mathbf{F}}^{(l)}\right)^{-1} & \mathbf{I} \end{bmatrix}. \tag{4.41}$$

Substitution of Eq. (4.41) into Eq. (4.33) yields

1.
$$\mathscr{L}\mathbf{c}_g^{(l)}(z_{l-1},s) = \mathscr{L}\mathbf{c}_g^{(l)}(z_l,s) \tag{4.42}$$
or
$$\mathbf{c}_g^{(l)}(z_{l-1},t) = \mathbf{c}_g^{(l)}(z_l,t) \tag{4.43}$$
The concentrations to the left and to the right of the active zone are equal, because this zone is thin. This important property of the TZTR is exploited in the Y-procedure (Yablonsky et al., 2002, 2007), which allows a model-free determination of $\mathbf{c}_g^{(l)}$ and the vector $\mathbf{r}_g^{(l)}$ of rates of consumption of the gas components, see below.

2.
$$\mathscr{L}\mathbf{f}^{(l)}(z_{l-1},s) = \epsilon_b^{(l)}\,\Delta z^{(l)}\,\left(\tilde{\mathbf{H}}^{(l)}(s)\cdot\tilde{\mathbf{F}}^{(l)}\right)^{-1}\cdot\mathscr{L}\mathbf{c}_g^{(l)}(z_l,s) + \mathscr{L}\mathbf{f}^{(l)}(z_l,s). \tag{4.44}$$
As $\Delta z^{(l)}$ is thin, the mass storage capacity of the zone can be neglected. The difference between the outward flux $\mathbf{f}^{(l)}(z_l,t)$ and the inward flux, $\mathbf{f}^{(l)}(z_{l-1},t)$ is then equal to the rate of production per unit cross-sectional surface area, $\mathbf{r}_{g,\phi}^{(l)}$:
$$\mathbf{r}_{g,\phi}^{(l)}(t) = \mathbf{f}^{(l)}(z_l,t) - \mathbf{f}^{(l)}(z_{l-1},t) \tag{4.45}$$
Eq. (4.44) can therefore be rewritten as
$$\mathscr{L}\mathbf{r}_{g,\phi}^{(l)}(s) = -\epsilon_b^{(l)}\,\Delta z^{(l)}\,\left(\tilde{\mathbf{H}}^{(l)}(s)\cdot\tilde{\mathbf{F}}^{(l)}\right)^{-1}\cdot\mathscr{L}\mathbf{c}_g^{(l)}(z_l,s). \tag{4.46}$$
where Eq. (4.42) was also taken into account.

Back to the general case, repeated application of Eq. (4.33), taking into account the transmission conditions (4.8a) and (4.8b), the in- and outlet concentrations and fluxes are found to be bound by
$$\begin{bmatrix}\mathscr{L}\mathbf{c}_{\text{in}}(s)\\ \mathscr{L}\mathbf{f}_{\text{in}}(s)\end{bmatrix} = \mathbf{M}_1(s)\cdot\mathbf{M}_2(s)\cdot\ldots\cdot\mathbf{M}_n(s)\cdot\begin{bmatrix}\mathscr{L}\mathbf{c}_{\text{out}}(s)\\ \mathscr{L}\mathbf{f}_{\text{out}}(s)\end{bmatrix}. \tag{4.47}$$
This expression already incorporates the boundary condition (4.6a). Furthermore, because of boundary condition (4.6b), $\mathscr{L}\mathbf{c}_{\text{out}}(s) = 0$ in Eq. (4.47). Therefore, rewriting the transfer matrix as a block matrix
$$\mathbf{M}_1(s)\cdot\mathbf{M}_2(s)\cdot\ldots\cdot\mathbf{M}_n(s) = \begin{bmatrix}\mathbf{P}_{1,1}(s) & \mathbf{P}_{1,2}(s)\\ \mathbf{P}_{2,1}(s) & \mathbf{P}_{2,2}(s)\end{bmatrix}, \tag{4.48}$$

it follows from Eq. (4.47) that

$$\mathscr{L}\mathbf{f}_{\text{in}}(s) = \mathbf{P}_{2,2}(s) \cdot \mathscr{L}\mathbf{f}_{\text{out}}(s). \tag{4.49}$$

Solving this for $\mathscr{L}\mathbf{f}_{\text{out}}(s)$ yields the main result of (Constales et al., 2004):

$$\mathscr{L}\mathbf{f}_{\text{out}}(s) = \mathbf{P}_{2,2}(s)^{-1} \cdot \mathscr{L}\mathbf{f}_{\text{in}}(s). \tag{4.50}$$

The function $\mathbf{f}_{\text{in}}$ can be formally extended with the negative real axis: for all $t < 0$,

$$\mathbf{f}_{\text{in}}(t) = \mathbf{0} \tag{4.51}$$

Then the Fourier transform of $\mathbf{f}_{\text{in}}$ follows from the Laplace transform:

$$\mathscr{F}\mathbf{f}_{\text{in}}(\omega) = \mathscr{L}\mathbf{f}_{\text{in}}(i\omega). \tag{4.52}$$

If the same is done for $\mathbf{f}_{\text{out}}$, Eq. (4.50) may be rewritten in terms of the Fourier transform:

$$\mathscr{F}\mathbf{f}_{\text{out}}(\omega) = \mathbf{P}_{2,2}(i\omega)^{-1} \cdot \mathscr{F}\mathbf{f}_{\text{in}}(\omega). \tag{4.53}$$

$\mathscr{F}\mathbf{f}_{\text{in}}$ follows from Eq. (4.7) as

$$\mathscr{F}\mathbf{f}_{\text{in}}(\omega) = \frac{1}{\phi}\,\mathbf{n}. \tag{4.54}$$

Especially, Eq. (4.53) allows calculating $\mathscr{F}\mathbf{f}_{\text{out}}$ in the equally spaced pulsations

$$\omega_k = \frac{2\pi(k-1)}{n_t \Delta t}, \tag{4.55}$$

which is enough to calculate the outward fluxes at the necessary discrete times t_j, see Eq. (4.12), using the inverse discrete Fourier transform. For more information, see Appendix C.

Comparison

Two approximations are applied in the method of lines. The first one is the discretization of the axial coordinate. The second one is the numerical solution of the resulting system of ordinary differential equations. The sole approximation applied in the transfer matrix approach is the replacement of the continuous Fourier transform by the discrete Fourier transform. The transfer matrix approach yields more accurate model-calculations than the method of lines. It is also computationally less expensive. The method of lines, on the other hand, is more versatile, being able to simulation experiments with nonlinear kinetics.

Implementation

A simulation and regression program for TAP, TAPFIT, was developed as a part of this work, see Appendix D. The numerical integration of the model equations is implemented in the simulation module of this program. Both numerical methods, the method of lines and the transfer matrix approach, can be applied.

4.5 Conclusions

The reader was introduced to the TAP-technique, including the TZTR. The TAP-reactor was modeled as a one-dimensional initial and boundary value problem. Two strategies have been proposed to solve this problem numerically. The first strategy, the method of lines, consists of converting the initial and boundary value problem into an initial value problem by the discretizing of the axial coordinate. The initial value problem can then be solved using an appropriate numerical routine. The second strategy, the transfer matrix approach, uses Fourier techniques. Especially, this approach allows an elegant calculation of the TZTR. This will be applied in Chapter 8 on the model-free experimental determination of connectivity features of reaction networks. The transfer matrix approach is computationally less expensive and more accurate than the method of lines. However, the former is limited to linear kinetics, while the latter is not. Both approaches have been implemented in the program TAPFIT, developed as a part of this work.

Chapter 5 will focus on a specific aspect of TAP: the noise in the experimental data.

Chapter 5

Noise in TAP Pulse Responses

5.1 Introduction

As a transient kinetic technique, TAP is a suitable technique to determine heterogeneous-catalytic reaction networks, see Chapter 1. The level of detail is limited by the noise in the experimental data. It is therefore important to know the properties of this noise. The investigation of this noise is the subject of this chapter, which is based on (Roelant et al., 2007).

As the TAP-setup provides large amounts of data in a short amount of time, it is possible to perform a thorough analysis of this noise. In fact, such an opportunity is unique in chemical kinetics. Multi-pulse experiments are performed using anywhere from 1 to 30 000 pulses, each pulse being separated by 1 to 30 seconds. The signal recorded by the mass-spectrometer may be looked upon as a superposition of the 'pure' pulse response related to the studied processes and noise. The noise may be a superposition of multiple noise types.

Section 5.2 will provide a stochastic framework for this investigations. The Sections 5.3 and 5.4 will present the experimental data used for this investigation and a correction applied to them. The Sections 5.5, 5.6 and 5.7 will each present one kind of noise present in TAP-data. After a supplementary remark, presented in Section 5.8, a noise analysis procedure will be presented in Section 5.5, which can be applied to any TAP-data. This will be illustrated by some useful examples. In the future, this theoretical framework could be a part of the systematic analysis for distinguishing noises caused by different physical and physico-chemical reasons, particularly for distinguishing process noises and noises of the measuring device. Also based on the results of this noise analysis, the concrete noises related to different subsystems of the device (valve, mass-

spectrometer etc.) have to be identified.

Experimental data obtained on the TAP-1-setup of the LCT and a TAP-2-setup at Washington University Saint Louis are the object of the present study.

5.2 Stochastic processes

Statistical background

Noise is a *stochastic process*: a stochastic variable Y which is a function of a real variable t. Consider a column vector of chronological samples of Y:

$$\mathbf{y} = \begin{bmatrix} Y(t_1) & Y(t_2) & \cdots & Y(t_{n_t}) \end{bmatrix}^T, \tag{5.1}$$

where $t_1 < t_2 < \ldots < t_{n_t}$. $\mathbf{y}$ is called a *random sequence* (Peebles, 1987; Therrien, 1992) or a *discrete-parameter stochastic process* (Seinfeld and Lapidus, 1974; Papoulis, 1991). Consider the most general case where the random variables are complex.

Each *mean* $\mu_Y(t_j)$ is the expected value of the sample at $t = t_j$:

$$\mu_Y(t_j) = E\left[Y(t_j)\right]. \tag{5.2}$$

The vector

$$\boldsymbol{\mu}_Y = \begin{bmatrix} \mu_Y(t_1) & \mu_Y(t_2) & \cdots & \mu_Y(t_{n_t}) \end{bmatrix}^T \tag{5.3}$$

may be called the *mean sequence*. The *autocovariance* $C_Y(t_j, t_k)$ is the covariance of the corresponding samples $Y(t_j)$ and $Y(t_k)$:

$$C_Y(t_j, t_k) = \operatorname{cov}\left[Y(t_j), Y(t_k)\right] \tag{5.4}$$

$$= E\left[\overline{\left(Y(t_j) - \mu_Y(t_j)\right)} \cdot \left(Y(t_k) - \mu_Y(t_k)\right)\right] \tag{5.5}$$

$$= E\left[\overline{Y(t_j)} \cdot Y(t_k)\right] - \overline{\mu_Y(t_j)} \cdot \mu_Y(t_k). \tag{5.6}$$

Note that $C_Y(t_j, t_k)$ and $C_Y(t_k, t_j)$ form a pair of complex conjugates.

A random sequence is called *white noise* if different random variables in the sequence are uncorrelated:

$$j \neq k \Rightarrow C_Y(t_j, t_k) = 0. \tag{5.7}$$

Random sequences which are not white noise are called *colored noise*. The standard deviation $\sigma_Y(t_j)$ of sample j is given by

$$\sigma_Y(t_j) = \sqrt{C_Y(t_j, t_j)}. \tag{5.8}$$

If the standard deviation of all its elements is the same, the random sequence is called *homoskedastic*. If not, it is called *heteroskedastic*.

Finally, the dimensionless *autocorrelation* $\rho_Y(t_j, t_k)$ of the jth and pth sample, is obtained as

$$\rho_Y(t_j, t_k) = \frac{C_Y(t_j, t_k)}{\sigma_Y(t_j)\sigma_Y(t_k)}. \tag{5.9}$$

Estimation of the statistics

As it is liable to stochastic noise, a time series which is measured as a response to a pulse in a TAP-reactor may be modeled as a random sequence $\mathbf{y}$, see (5.1), where t_j is given by Eq. (4.12). The mean or expected pulse response is obtained by estimating

$$\mu_Y(t_j) = \frac{1}{n_r}\sum_{k=1}^{n_r} y^{(k)}(t_j), \tag{5.10}$$

where $y^{(k)}(t_j)$ is the sample taken at time t_j in a kth replicate experiment. n_r is the number of such replicate experiments. The autocovariance is estimated by

$$C_Y(t_j, t_k) = \frac{1}{n_r - 1}\sum_{k=1}^{n_r}\big(y^{(k)}(t_j) - \mu_Y(t_j)\big)\cdot\big(y^{(k)}(t_k) - \mu_Y(t_k)\big) \tag{5.11}$$

This estimation is also used for the standard deviation $\sigma_Y(t_j)$, using Eq. (5.8).

The Fourier transform

The Fourier transform of random sequence $\mathbf{y}$ can be subjected to the discrete Fourier transform $\mathcal{F}$, such that the kth element of $\mathcal{F}\mathbf{y}$ is

$$(\mathcal{F}\mathbf{y})_k = \mathcal{F}\mathbf{y}(\omega_k) = \frac{1}{\sqrt{n_t}}\sum_{j=1}^{n_t} Y(t_j)\exp\left(-2\pi i\,\frac{(k-1)(j-1)}{n_t}\right), \tag{5.12}$$

where the pulsations ω_j are given by Eq. (4.55) and correspond to frequencies ν_j:

$$\nu_j = \frac{\omega_j}{2\pi} = \frac{j-1}{n_t\Delta t}. \tag{5.13}$$

Clearly, the transformed random sequence is a random sequence itself. Estimations similar to (5.10) and (5.11) can be performed for $\mu_{\mathcal{F}Y}(\omega_j)$, $C_{\mathcal{F}Y}(\omega_j, \omega_k)$ and $\sigma_{\mathcal{F}Y}(\omega_j)$ in the frequency domain.

As all $Y(t_j)$ are real stochastic variables, definition (5.12) implies that

$$\mathcal{F}Y\omega_{n_t-j} = \overline{\mathcal{F}Y\omega_j}. \tag{5.14}$$

For this reason, beyond the so called *Nyquist pulsation*,

$$\omega_N = \frac{\pi}{\Delta t}, \tag{5.15}$$

corresponding to the *Nyquist frequency*,

$$\nu_N = \frac{1}{2\Delta t}, \tag{5.16}$$

no extra information can be extracted from the discrete Fourier transform. The Nyquist pulsation is the highest pulsation at which the discrete Fourier transform has physical meaning.

5.3 Experimental

An evident basis for the current statistical study is a dataset resulting from a large number of state-defining experiments, see Section 4.2. The easiest way to achieve this is by feeding an inert gas and/or by loading the TAP-reactor with an inert bed. Another option is to load the TAP-reactor with a catalyst and saturate it with a reactant. Additional pulses of that reactant then no longer adsorb on the catalyst, which makes it possible to collect a large number of state-defining experiments.

A set of data which have been collected at the TAP-1-setup of the LCT contains 600 pulse responses. An estimated average number of $1.2 \cdot 10^{15}$ oxygen molecules was pulsed over a three-zone-TAP-reactor at 773 K. In central position was a bed of Ti_HV5_H catalyst (Sack et al., 2006), V_2O_5 based and obtained by DC magnetron sputtering on a ZrO_2–SiO_2 support. This zone was 21.78 mm long and sandwiched between two beds of quartz beads, the first one of which 1.34 mm long and the second one 5.3 mm long. Both the quartz beads and the catalyst support particles had diameters of 250 to 425 µm. The catalyst was not further oxidized by the oxygen pulses. Therefore, the oxygen responses are uniform and fit for the statistical analysis. Each pulse response is stored as a sequence of 1000 samples taken every 0.4 ms. The *collection time* per pulse thus adds up to 0.4 s. An extra time gap of 0.5 s was left between the end of the collection of each pulse response and the next pulse.

5.4 Baseline-correction

Fig. 5.1 (a) shows the average non-baseline-corrected oxygen pulse response. Figure (b) is a magnification of the second half of this response,

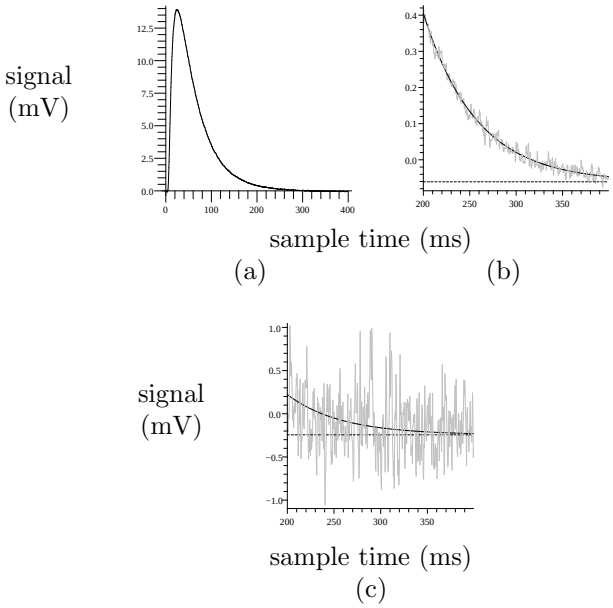

Figure 5.1: (a) Average of non-baseline-corrected oxygen pulse responses obtained at UGent. These were obtained on a TAP-1-system loaded with a V_2O_5 catalyst (Sack et al., 2006) sandwiched between two zones packed with quartz beads of the same diameter as the catalyst particles. The bed was at 773 K. The catalyst is not further oxidized by the pulses. (b) The grey curve represents the second half of (a). Clearly, the signal is not yet completely extinct at the end of the pulse recording. For this reason, the position of the baseline cannot, as is customary, be estimated as the average of the last couple of hundreds of samples. Rather, the grey curve is nonlinearly regressed with an exponential curve $y = a \exp(-bt) + c$. The result is shown as the black full line. The black dashed line represents its horizontal asymptote $y = c$, which is a reliable estimate for the baseline. (c) The last 500 samples of an example pulse response in grey. The full black line represents the fitted exponential curve for this particular pulse response. The black dashed line shows the estimated position of the baseline.

close to extinction. It is apparent that the signal is not yet completely extinct by the time the response is stopped being recorded. Therefore, the position of the baseline cannot, as is customary, be estimated as the average of the last couple of hundreds of samples. A more refined approach consists of regressing the second half of the average pulse response with an exponential curve $y = a \exp(-bt) + c$. The baseline is then estimated as the horizontal asymptote $y = c$ of this curve. All pulse responses are separately *baseline-corrected* this way. As an extra time gap of 0.5 s was left between any two successive pulses, it can be assumed that the former response is extinct by the time the recording of the latter is started.

A second data set from a TAP-2-setup operational at Washington University Saint Louis contains 1000 pulse responses. Here, an estimated number of $2.8 \cdot 10^{14}$ krypton atoms was pulsed over a 31.8 mm long bed of quartz particles with a diameter of 210 to 250 µm. The temperature of the bed was 50 °C. The collection time was 4 s and 1000 samples are taken per pulse response, making the sampling interval 4 ms. An extra time gap of about 0.1 s was applied between the collection of successive pulses.

To perform the baseline-correction of all pulse responses, the method used for the data from the LCT was also applied here. As before, the last 500 samples out of 1000 were used for the estimation of the baseline position. This time only an extra 0.1 s is left between the end of a pulse recording and the next pulse. Therefore, some krypton atoms of the former pulse can be expected still to be present in the bed when the latter is given. However, their number can be assumed to have a negligible effect. In the remainder of the chapter, the data sets from the LCT and Washington University Saint Louis will be referred to as the UGent set and the WUStL set, respectively. They contain the baseline-corrected pulse responses.

Fig. 5.2 depicts semilogarithmic graphs of the average baseline-corrected pulse responses of the UGent and WUStL sets. Figure (b) for the WUStL set clearly shows how the tail of the pulse response is the superposition of two logarithmic decays. The first tail is due to the diffusive release of krypton atoms. The second tail is probably due to the detection of krypton atoms that were scattered after they left the reactor. The corresponding exponential decay $a \exp(-bt)$ is the one found in preparation for the baseline-correction. It is represented by the grey line. Figure (a) also shows some convexity of the tail for the UGent set. This is probably due to a reversible interaction of oxygen with the catalyst.

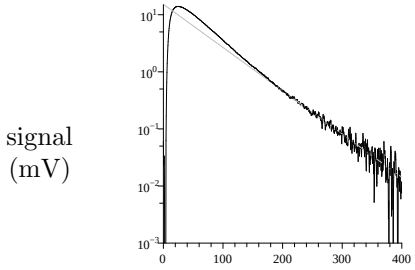

Figure 5.2: (a) Semilogarithmic graph (in black) of the average of 600 baseline-corrected oxygen pulse responses obtained at UGent, over a three-zone-TAP-reactor with central V_2O_5 catalytic zone. (b) Semilogarithmic graph (in black) of the average of 1000 baseline-corrected krypton pulse responses obtained at WUStL, over a single quartz zone. The grey lines in (a) and (b) represent the final exponential decay.

5.5 Gaussian noise

Normal distribution and standard deviation

Fig. 5.3 depicts the mean pulse response $\boldsymbol{\mu}_Y$, estimated from all pulse responses of the UGent set as in Eq. (5.10). It also shows an example of a pulse response and its deviation from the mean.

Traditionally, the deviations from the mean would be assumed normally distributed around zero. For the UGent data set, this assumption is verified in Fig. 5.4. It shows histograms of the deviations from the average of samples taken before, near and after the peak of the pulse response, believed to be representative for the whole pulse response. These

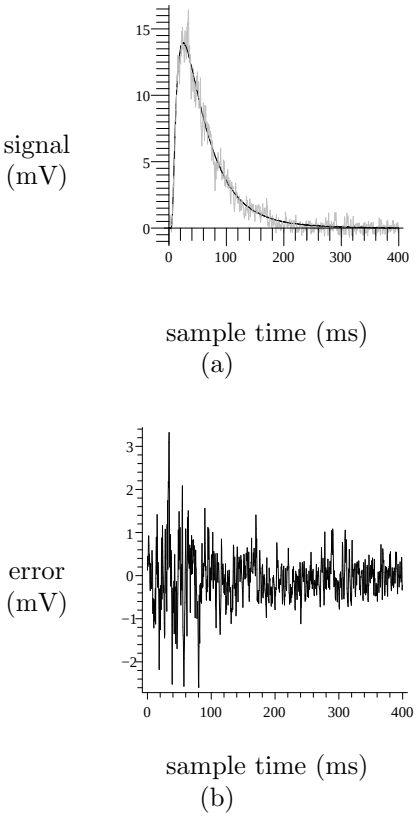

Figure 5.3: (a) An oxygen pulse response (in grey) and the average of 600 such pulses from the UGent data set (in black). (b) The deviation of this response from the average response.

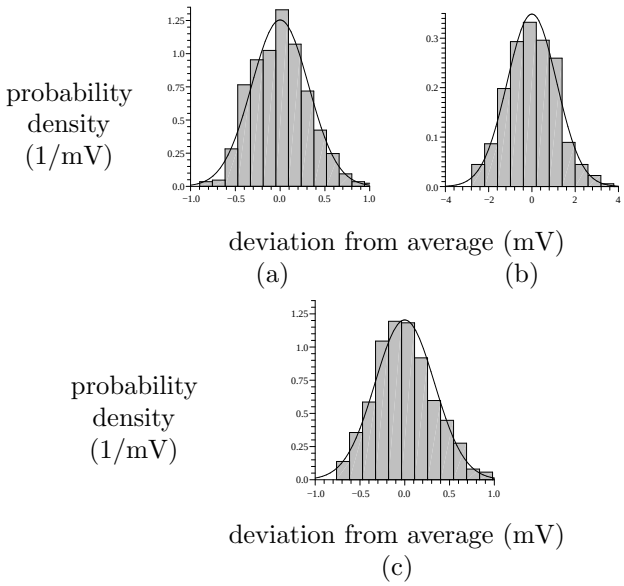

Figure 5.4: Histograms of the deviation from average of samples in the pulse responses from the UGent data set. (a) An early sample taken at 0.4 ms after the pulse. (b) A sample taken at 26 ms, about the peak of the pulse response. (c) A late sample taken at 384 ms. Comparison to normal probability density functions (black lines) around 0 mV and with standard deviations estimated from the data shows that all deviations from average can be considered normally distributed in good approximation.

are compared to normal (Gaussian) probability density curves with mean zero and standard deviation estimated from the experimental data. Because of the apparent resemblance of the histograms and the Gaussian curves, all samples $Y(t_j)$ along the pulse response are considered normally distributed around the mean $\mu_Y(t_j)$. The Gaussian deviation from this mean is symbolized as $\Phi(t_j)$.

The estimated standard deviation profile $\boldsymbol{\sigma}_Y$ is shown in Fig. 5.5. The pulse response is heteroskedastic: a part of the standard deviation is proportional to the strength of the signal, while another part is constant. This becomes clearer if the standard deviation σ_Y is plotted versus the mean μ_Y, eliminating time. The result is shown in Fig. 5.6. Clearly, an appropriate interpolation allows to predict the standard deviation from the strength of the signal.

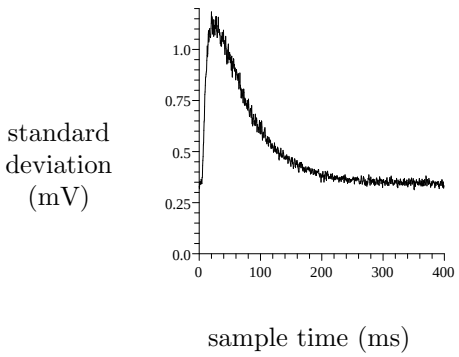

Figure 5.5: Standard deviation of all samples in a pulse response from the UGent set versus their sample time.

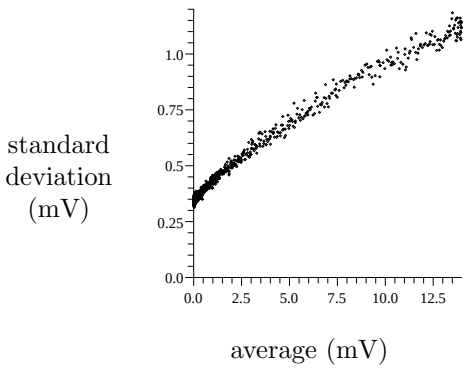

Figure 5.6: Standard deviation of the samples as a function of their mean for the UGent set, resulting from elimination of the sample times. The graph shows that the standard deviation is an increasing function of the signal strength. An analytic form of this function could be derived from appropriate interpolation.

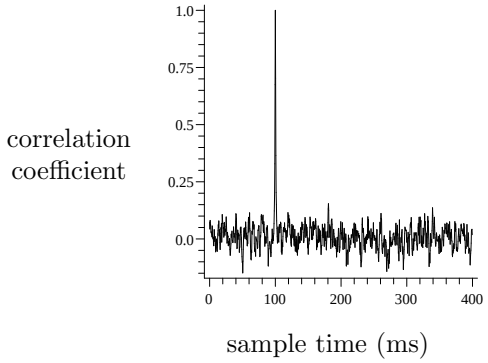

Figure 5.7: Correlation coefficient between the sample taken at 100 ms after the pulse and all samples from the UGent set. The graph shows a steep peak with height 1 around 100 ms. The rest of the profile is noisy with average 0.

Colored noise: the Ornstein-Uhlenbeck model

Fig. 5.7 shows the profile of the correlation coefficient between a base sample taken at 100 ms, in the tail of the curve, and all samples. This figure shows a single steep peak at 100 ms amid noise about the zero of correlation. It is trivial that the correlation coefficient between the sample taken at 100 ms and itself is 1. However, zooming in on the peak shows a correlation peak, see Fig. 5.8. This reveals that the noise is colored, i.e., the correlation coefficient does not drop to zero immediately around the base sample. Specifically, these graphs, showing correlation profiles with base samples chosen at the beginning, the peak and the end of the peak response, suggest an exponential correlation relaxation towards past and future. This, as well as the normality, is a typical feature of an *Ornstein-Uhlenbeck stochastic process* (also called a *Gauss-Markov stochastic process*):

$$\rho_\Phi(t_j,\, t_k) = \exp\left(-\frac{|t_k - t_j|}{\theta}\right), \tag{5.17}$$

where θ is the *correlation time*, see *Doob's theorem* (Doob, 1942). The Ornstein-Uhlenbeck process was originally presented as a model for the velocity of a particle in Brownian motion (Uhlenbeck and Ornstein, 1930; Wang and Uhlenbeck, 1945). Here, it is a suitable model for the noise divided by its standard deviation: $\Phi(t_j)/\sigma_\Phi(t_j)$.

Even though the TAP-reactor operates under high vacuum, enough molecules are collected by the mass spectrometer to consider the non-sampled electronic signal a continuous one. Hence, to ensure this conti-

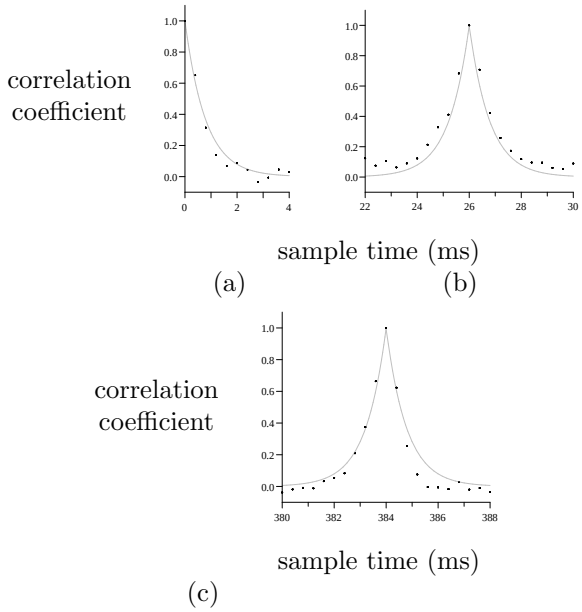

Figure 5.8: Fragments of correlation profiles derived for the UGent data set. (a) Coefficient of correlation between the first sample (taken as the pulse was admitted) and neighboring samples (black dots). (b) Correlation coefficient between the sample taken at 26 ms after the pulse admission time and neighboring samples. (black dots). (c) Correlation coefficient between the sample taken at 384 ms after pulse admission and neighboring samples (black dots). These graphs suggest an exponential decrease of the correlation coefficient towards past and future. The grey lines in (a), (b) and (c) represent such an exponential relation with correlation time θ estimated from regression of the standard deviation profile in the frequency domain, see Fig. 5.10, with Eq. (5.22). The correspondence is satisfactory.

nuity, correlation between very rapidly succeeding samples must approach 1 as the sampling interval goes to zero. Therefore, there must always exist a certain correlation time θ, that can only be neglected if Δt has been chosen well over θ, in which case a white noise Gaussian model is satisfactory. In the other case however, as will be clear from the following, a colored noise model, and more precisely an Ornstein-Uhlenbeck model is in order.

The effect of autocorrelation in the spectrum

Call $\left(\sigma^2\right)_M$ the time average variance of the pulse response. Then

$$n_t \left(\sigma^2\right)_M = \sum_{j=1}^{n_t} \sigma_Y^2(t_j) = \sum_{k=1}^{n_t} \sigma_{\mathcal{F}Y}^2(\omega_k), \tag{5.18}$$

where the second equality is a consequence of *Parseval's theorem*. In words, the variance in the time domain is *redistributed* in the frequency domain. As a consequence, $\left(\sigma^2\right)_M$ is the frequency average as well as the time average variance.

It is proven in Appendix E that the autocovariance of the discrete Fourier transform of the Gaussian noise is approximated very well by

$$C_{\mathcal{F}\Phi}(\omega_p, \omega_q) = \frac{1}{\sqrt{n_t}} \frac{\left(1-\rho^2\right) \mathcal{F}\sigma^2\left(\omega_p - \omega_q\right)}{1 - 2\rho\cos\left(\frac{\omega_p+\omega_q}{2}\Delta t\right) + \rho^2}, \tag{5.19}$$

where it is assumed that $\omega_p \geqslant \omega_q$ [1]. ρ is the coefficient of correlation of two consecutive samples. Δt is the sampling interval. The expression involves the discrete Fourier transform $\left(\mathcal{F}\sigma^2\left(\omega_j\right)\right)$ of the variance profile in the time domain. Respecting Eq. (5.17), ρ is related to θ as

$$\rho = \exp\left(-\frac{\Delta t}{\theta}\right). \tag{5.20}$$

A special case of Eq. (5.19) is given by

$$\sigma_{\mathcal{F}\Phi}^2(\omega_p) = \frac{\left(1-\rho^2\right)\ \left(\sigma^2\right)_M}{1 - 2\rho\cos\left(\omega_p \Delta t\right) + \rho^2}. \tag{5.21}$$

It can be proven that Eq. (5.21) obeys Eq. (5.18) following from Parseval's theorem.

[1] In the opposite case $\omega_p < \omega_q$, $C_{\mathcal{F}\Phi}(\omega_p, \omega_q)$ is found with $\mathcal{F}\sigma^2\left(\omega_p - \omega_q\right)$ replaced by $\overline{\mathcal{F}\sigma^2\left(\omega_q - \omega_p\right)}$ in Eq. (5.19).

Following directly from Eq. (5.21),

$$\sigma_{\mathcal{F}\Phi}(\omega_p) = \sqrt{\frac{1-\rho^2}{1-2\rho\cos\left(\omega_p \Delta t\right)+\rho^2}}\left(\sigma^2\right)_M^{1/2}. \tag{5.22}$$

Observe that Eq. (5.22) implies that the heteroskedasticity of the pulse response, as apparent in Fig. 5.5, is not reflected in the standard deviation pattern in the frequency domain, but only in the covariance pattern via $\mathcal{F}\sigma^2$ in Eq. (5.19).

Limit values of (5.21) are given by

$$\sigma^2_{\mathcal{F}\Phi}(0\,\mathrm{Hz}) = \frac{1+\rho}{1-\rho}\left(\sigma^2\right)_M = \coth\left(\frac{\Delta t}{2\theta}\right)\left(\sigma^2\right)_M \tag{5.23}$$

$$\sigma^2_{\mathcal{F}\Phi}(\omega_N) = \frac{1-\rho}{1+\rho}\left(\sigma^2\right)_M = \tanh\left(\frac{\Delta t}{2\theta}\right)\left(\sigma^2\right)_M, \tag{5.24}$$

where ω_N is the Nyquist pulsation, given by Eq. (5.15). The second equalities in Eqs. (5.23) and (5.24) are achieved by substituting Eq. (5.20).

Correlation ρ between successive samples taken by the mass spectrometer causes an increase of the variance of the discrete Fourier transform at low frequencies and a decrease at high frequencies. This contrast becomes more pronounced if ρ increases. For example, as it may be derived from Eq. (5.23), in case the sampling interval Δt is half the correlation time θ, the standard deviation is doubled by the correlation effect. This effect can become very important when sampling at high frequencies is required by, e.g., fast diffusion of the pulse through the reactor bed.

Consider the profile of the modulus of the average signal in the frequency domain, as depicted in Fig. 5.9. Clearly, the relevant information contained in the discrete Fourier transform is concentrated in the frequency domain from 0 Hz to 150 Hz, while the Nyquist frequency, given by Eq. (5.16), is 1250 Hz. Generally spoken, at reasonably low sampling intervals Δt, the information contained in the spectrum of a recorded TAP-signal is restricted to the low frequency region. This is precisely the region where autocorrelation causes an increase of the standard deviation. It is concluded that this autocorrelation causes an unfavorable increase of the level of uncertainty. As was already stated, this effect becomes important when sampling is carried out at high frequencies.

It can be derived from Eq. (5.23) that if the sampling interval is higher than 2.5 times the correlation time θ, the low frequency standard deviation stays within 10 % of $\left(\sigma^2\right)_M^{1/2}$. In this case, the unfavorable time autocorrelation effect can be neglected. Increasing the number of samples n_t by increasing the sampling frequency $1/\Delta t$ while keeping the total collection time $t_c = n_t \Delta t$ constant essentially does not change the mean

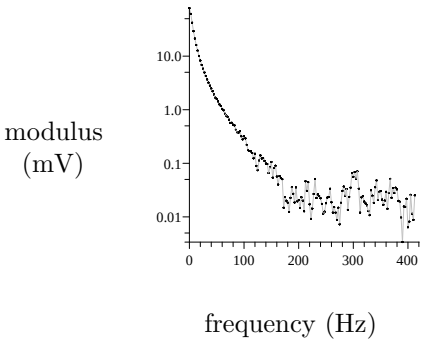

Figure 5.9: Semilogarithmic graph of the modulus of the average pulse response's discrete Fourier transform, for the UGent set. This graph shows that no meaningful information can be extracted from the spectrum beyond 150 Hz, where noise becomes dominant.

variance $\left(\sigma^2\right)_M$ in the time domain. As a consequence of Parseval's theorem (see Eq. (5.18)), $\left(\sigma^2\right)_M$ is also equal to the mean variance in the frequency domain and also, as there is assumed not to be a time autocorrelation effect, the mean variance at 0 Hz:

$$\sigma^2_{\mathcal{F}\Phi}(0\,\mathrm{Hz}) \approx \left(\sigma^2\right)_M . \tag{5.25}$$

On the other hand, consider the limit case in which the sampling interval is much smaller than the correlation time. In that case, Eq. (5.23) can be approximated by

$$\sigma^2_{\mathcal{F}\Phi}(0\,\mathrm{Hz}) \approx \frac{2\theta}{\Delta t}\left(\sigma^2\right)_M = n_t \cdot \frac{2\theta}{t_c}\left(\sigma^2\right)_M . \tag{5.26}$$

As the interesting frequency region is around 0 Hz, the relative error of $\mathcal{F}Y\,(0\,\mathrm{Hz})$ gives a good idea of the quality of the estimation of any physico-chemical parameters carried out by regression of the mean pulse response with suitable expressions. Firstly, it follows from definition (5.12) that

$$\mu_{\mathcal{F}Y}(0\,\mathrm{Hz}) = \frac{1}{\sqrt{n_t}} \sum_{k=1}^{n_t} \mu_Y(t_k) \tag{5.27}$$

$$\approx \frac{M_0}{\sqrt{n_t}\Delta t} = \sqrt{n_t} \cdot \frac{M_0}{t_c}, \tag{5.28}$$

where M_0 is the *zeroth moment*: the surface area under the ideal continuous pulse response. In the low sampling frequency limit, the relative

error of $\mathcal{F}Y\,(0\,\mathrm{Hz})$ is found from Eqs. (5.25) and (5.28):

$$\frac{\sigma_{\mathcal{F}\Phi}(0\,\mathrm{Hz})}{\mu_{\mathcal{F}Y}(0\,\mathrm{Hz})} \approx \frac{1}{\sqrt{n_t}} \cdot \frac{t_c}{M_0} \sqrt{(\sigma^2)_M}. \tag{5.29}$$

The relative error is inversely proportional to the square root of the number n_t of samples. This shows that as long as the sampling interval Δt is kept well above the correlation time θ, increasing the sampling frequency while keeping the total collection time t_c constant will improve the precision of parameter estimations by regression. In the high sampling frequency limit however, combination of Eqs. (5.26) and (5.28) yields

$$\frac{\sigma_{\mathcal{F}\Phi}(0\,\mathrm{Hz})}{\mu_{\mathcal{F}Y}(0\,\mathrm{Hz})} \approx \frac{\sqrt{2\,t_c\theta}}{M_0} \sqrt{(\sigma^2)_M}. \tag{5.30}$$

The relative error is no longer dependent on the number n_t of samples. This means that the precision of parameter estimations by regression will hardly improve by increasing the sampling frequency even further. In summary, increasing the sampling frequency will improve the precision of parameter estimations by regression. However, once the sampling interval Δt has been made smaller than the correlation time θ, this quality will approach its upper limit.

The memory required to store the pulse responses is proportional to the sampling frequency. Assume that the sampling frequency is already high enough for the spectrum to cover even the fastest of the observable physico-chemical phenomena. Then increasing the number of recorded pulse responses rather than the number of samples per pulse (keeping t_c constant) is a better strategy to improve parameter estimations. Indeed, this improvement will be at least as high as if the extra memory needed to do so was used to increase the sampling frequency. Of course, the number of recorded pulse responses is still limited to the point where the change of the catalyst state can no longer be considered insignificant (see Section 4.2). Suppose an experimentalist plans to record a series of TAP pulse responses and attaches great importance to the precision of the resulting average pulse response. In this case, he should collect a considerable number of responses taking care, however, to avoid a significant change of the catalyst state. Secondly, he should establish a sampling interval Δt about the correlation time θ or less. There is little point to applying even higher sampling frequencies.

Noise characterization

The parameters $\left(\sigma^2\right)_M^{1/2}$ and ρ can be estimated from regressing the observed standard deviation pattern in the frequency domain, $\left(\sigma_{\mathcal{F}Y}(\omega_j)\right)$,

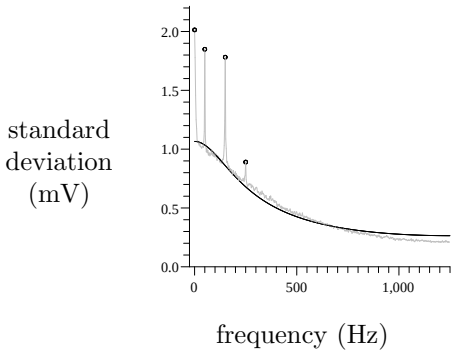

Figure 5.10: Estimated standard deviation versus frequency of the discrete spectrum of the pulse responses from the UGent set (grey curve). Steep peaks about 0 Hz, 50 Hz, 150 Hz and 250 Hz are marked by a small black circle. Abstracting these peaks, regression with Eq. (5.22) gives a reasonably good correspondence to the experimental profile. The curve resulting from the regression is shown in black.

with the right hand side of Eq. (5.22). Fig. 5.10 shows this profile. Steep peaks about 0 Hz, 50 Hz, 150 Hz and 250 Hz attract attention. These are due to other random phenomena which will be discussed in the subsequent sections. For now, it suffices to note that these effects can easily be abstracted by deleting the narrow peaks from the profile. Such an abstraction is impossible in the time domain, which is why it would be imprecise to estimate $\left(\sigma^2\right)_M$ directly as the average of $C_Y(t_j, t_j)$ using Eq. (5.11) for all j from 0 to $n_t - 1$. For the same reason, it would not be advisable to estimate ρ directly from correlation graphs such as these in Fig. 5.8.

Nonlinear regression of the experimental sequence $\left(\sigma_{\mathcal{F}Y}(\omega_j)\right)$ with Eq. (5.22) is carried out. The resulting curve is shown in Fig. 5.10 and the corresponding parameter estimations are $\rho = 0.603 \pm 0.006$ and $\left(\sigma^2\right)_M^{1/2} = 0.531 \pm 0.003\,\mathrm{mV}$ (95% confidence intervals).

The correlation time θ can be derived from ρ using Eq. (5.20). This yields $\theta = 1.97 \cdot \Delta t$ ($= 0.789\,\mathrm{ms}$). This value can be verified by plotting the theoretical prediction (5.17) of the correlation profile $\left(\rho_Y(t_j)\right)$ together with its experimental estimation, which has been done in Fig. 5.8. As is clear from the foregoing, the deviations are largely due to the presence of the non-Gaussian random processes that will be discussed in the subsequent sections.

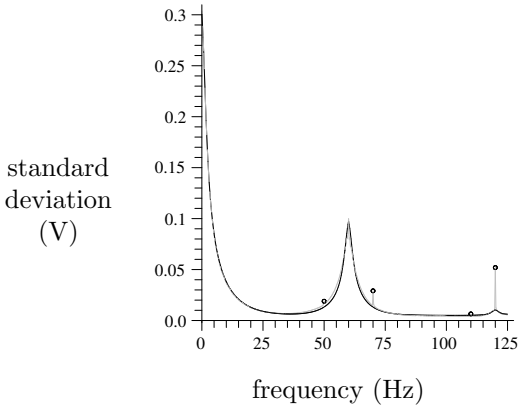

Figure 5.11: Estimated standard deviation versus frequency of the discrete spectrum of the pulse responses from the WUStL set (grey curve). Small black circles mark steep peaks at 50, 70, 110 and 120 Hz. The black curve shows the result of regression with Eq. (5.51), after abstraction of the marked peaks. The result is satisfactory, although the regression of the peak about 60 Hz is not perfect. This suggests that a simple proportional relation is not the perfect model for the interdependence of the amplitude of the 60 Hz noise and the signal strength.

5.6 Spectrally localized noise: mains frequency interference

Consider the estimated standard deviation profile in the frequency domain of the WUStL set, shown in Fig. 5.11. A large peak at 60 Hz and a smaller one at 120 Hz attract the attention. Similar peaks, at 50 Hz, 150 Hz and 250 Hz, were present in the standard deviation profile of the UGent set (see Fig. 5.10). The mains frequency in America, where the WUStL data set was collected, is 60 Hz. The mains frequency in Europe, where the UGent data set was collected, is 50 Hz. Apparently, some noise present is *spectrally localized* about the harmonics of the frequency of the electric energy transmission[2]. This must be due to an interfering effect exerted by electric devices near the mass spectrometer, or an undesired direct influence of the mass spectrometer's AC power supply. Small peaks about 50 Hz, 70 Hz and 110 Hz are also present in the standard deviation profile of the WUStL set in the frequency domain. This shows that noise can

[2]It is notable for the UGent set that only the odd harmonics are present. The cause of the absence of the even multiples is unknown. However, even multiples were observed beside the odd multiples in other pulse response sets collected at UGent.

also be spectrally localized at frequencies that are no harmonics of the mains frequency. However, interfering effects exerted by electric devices present near the mass spectrometer can still be believed to underlie this noise. These devices may be part of the TAP-apparatus itself.

As a model for the transient process, consider that a pulse response $Y(t_j)$ is the superposition of the ideal pulse response $\mu_Y(t_j)$ and a stochastic process $\Gamma(t_j)$ representing an oscillatory noise with fixed pulsation $\omega_p = 2\pi p/n_t\Delta t \in]0,\, \pi/\Delta t[$ but amplitude $A(t_j)$ variable along the pulse response, as $\sigma_\Phi(t_j)$ was variable in the Gaussian noise.

$$\Gamma(t_j) = A(t_j)\cos\left(\omega_p t_j + \Theta_m\right), \tag{5.31}$$

where Θ_m is a random variable representing the random initial phase of the oscillation.

Autocorrelation in the time domain is readily found to be

$$C_\Gamma(t_j,\, t_k) = \frac{A(t_j)A(t_k)}{2}\cos\big(\omega_p(t_j - t_k)\big). \tag{5.32}$$

Clearly, the TAP-noise is colored. The variance profiles in the time and frequency domain are given by

$$\sigma^2_\Gamma(t_j) = \frac{A(t_j)^2}{2} \tag{5.33}$$

$$\sigma^2_{\mathcal{F}\Gamma}(\omega_j) = \frac{1}{4}\Big(\left|\mathcal{F}A\left(\omega_{|p-j|}\right)\right|^2 + \left|\mathcal{F}A\left(\omega_{f(p+j)}\right)\right|^2\Big), \tag{5.34}$$

respectively, where

$$f(k) = \begin{cases} k & \text{when } k < n_t \\ k - n_t & \text{when } k \geqslant n_t \end{cases}. \tag{5.35}$$

In a first approximation, it is useful to assume that the amplitude is linearly related to the signal strength:

$$A(t_j) = \alpha\,\mu_Y(t_j) + \beta \tag{5.36}$$

so that

$$\mathcal{F}A\left(\omega_j\right) = \alpha\,\mathcal{F}\mu_X\left(\omega_j\right) + \beta\,\sqrt{n_t}\,\delta_{j0}, \tag{5.37}$$

where α and β are positive. The Kronecker delta symbol, δ_{jk}, equals 1 if j is equal to k but 0 else.

Substitution of Eq. (5.37) into Eq. (5.34) yields after some manipulations

$$\sigma^2_{\mathcal{F}\Gamma}(\omega_j) = \frac{1}{4}\Bigg[\alpha^2\Big(\underbrace{\left|\mathcal{F}\mu_X\left(\omega_{|p-j|}\right)\right|^2}_{a} + \underbrace{\left|\mathcal{F}\mu_X\left(\omega_{f(p+j)}\right)\right|^2}_{b}\Big) + n_t\delta_{pj}\Big(\beta^2 + 2\alpha\beta\mu_{Y,M}\Big)\Bigg], \quad (5.38)$$

where $\mu_{Y,M}$ is the time average mean signal strength. If the amplitude $A(t_j)$ is constant, $\alpha = 0$, there is a discrete standard deviation peak at the pulsation ω_p of the oscillation. If $A(t_j)$ is purely proportional to the signal strength, $\beta = 0$, there is a continuous peak about ω_p. In other words, variability of the amplitude causes broadening of the standard deviation peak in the frequency domain. Mostly, term b in Eq. (5.38) can be neglected with respect to term a. Therefore, the flanks of the peak have the shape of the modulus profile in the frequency domain. If both α and β in Eq. (5.36) differ from zero, the standard deviation peak consists of a discrete peak at ω_p superposed on a continuous peak around ω_p. The model presented will be validated in Section 5.10.

If possible, spectrally localized noise should be reduced by preventing the electrical interference at its root. However, its complete elimination might prove unattainable. The presence of spectrally localized noise reduces the quality of parameter estimations carried out by regression if it overlaps spectrally with the ideal signal. Specifically, noises localized around low frequencies are most disadvantageous.

5.7 Pulse size and mass spectrometer sensitivity

In many cases, the size of the TAP reactant pulses is poorly reproducible. In reality, different trends may be observed and overlapped:

1. The drop in pulse size over a long pulse series could be due to a decrease in pressure in the blend tank due to depletion, even though the number of molecules per pulse is small (10^{13} - 10^{15} molecules).

2. The temperature of the pulse valve tends to increase with use so the resistance in the wire coils increases, causing a slight decrease in the pulse size.

3. The pulse size drifts if the manifold temperature changes significantly (Gleaves et al., 1988).

Fig. 5.12 gives an impression of the variability of the pulse size for the WUStL data set. Each point corresponds to the surface area under the

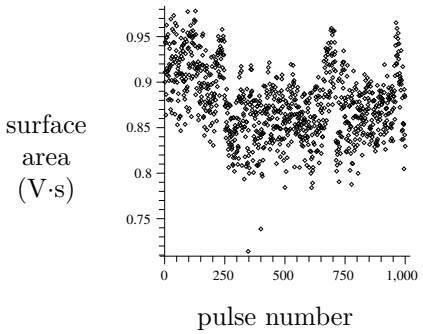

Figure 5.12: Surface area under the pulse response curve vs. the number of the pulse for the WUStL data set. As the area is proportional to the size of the pulse, this gives an impression of the variability of this size. The graph shows short term random behavior and slow trends.

curve of a pulse response. The graph shows short term random behavior superposed on slower fluctuations. No periodic phenomena have been revealed by taking the discrete Fourier transform.

In the case where no reactions or only pseudomonomolecular reactions take place in the reactor, the shape of the pulse response is not affected by the size of the pulse. Therefore, the influence of the variability of the pulse size can be modeled by thinking the mean pulse response $\mu_Y(t_j)$ is multiplied by a random factor $1 + \zeta\Lambda$, so that the pulse response $Y(t_j)$ becomes the superposition of $\mu_Y(t_j)$ and the stochastic process $\Psi(t_j)$:

$$\Psi(t_j) = \zeta\Lambda\mu_Y(t_j), \tag{5.39}$$

ζ is a dimensionless constant smaller than 1 and Λ is a stochastic variable with mean 0 and standard deviation 1 but unknown distribution. Obviously, ζ must be expected different for each pulse valve. In fact, as the pulse size is amenable to trends, ζ must be expected different for each experimental series.

Although the uncertain contribution $\Psi(t_j)$ mostly has to do with an imperfect pulse gas delivery, as reflected in the enumeration 1 to 3 above, it can also be rooted in slow fluctuations of the mass spectrometer's sensitivity. In either case it would not be appropriate to denote $\Psi(t_j)$ as noise as it is no time-varying stochastic phenomenon but a phenomenon varying from pulse to pulse.

It is easily verified that the autocovariances in the time and the frequency domain are given by

$$C_\Psi(t_j,\, t_k) = \zeta^2\, \mu_Y(t_j)\,.\,\mu_Y(t_k) \tag{5.40}$$

and

$$C_{\mathcal{F}\Psi}(\omega_p,\, \omega_q) = \zeta^2\, \mathcal{F}\mu_X\,(\omega_p)\;.\overline{\mathcal{F}\mu_X\,(\omega_q)}, \tag{5.41}$$

respectively. Especially, the variance profiles $\left(\sigma^2_\Psi(t_j)\right)$ and $\left(\sigma^2_{\mathcal{F}\Psi}(\omega_j)\right)$ are defined by

$$\sigma^2_\Psi(t_j) = \zeta^2\, \mu_Y(t_j)^2 \tag{5.42}$$

and

$$\sigma^2_{\mathcal{F}\Psi}(\omega_j) = \zeta^2\; \left|\mathcal{F}\mu_X\,(\omega_j)\right|^2. \tag{5.43}$$

Variability of the pulse size is reflected in a standard deviation peak about 0 Hz. Fig. 5.11 indeed shows such a peak. As is clear from Eq. (5.43), its flank has the shape of the modulus profile in the frequency domain.

In practice, *area-normalization* after baseline-correction rules out the uncertainty caused by the variability of the pulse size or mass spectrometer sensitivity. Area-normalization amounts to dividing a pulse responses by its zeroth moment. However, as to some extent it would deform the noise present, area-normalization was not applied to the data sets presently used with the purpose to characterize the noise.

5.8 Absence of cross-effects

Consider the natural case where multiple noise types are present in the pulse responses. In the most general case, a pulse response must be considered a superposition of the ideal pulse response and stochastic processes due to the uncertainty concerning the size of the pulses (type Ψ, Section 5.7), an Ornstein-Uhlenbeck noise (type Φ, Section 5.5) and multiple spectrally localized noises (type Γ, Section 5.6) with different pulsations ω_p.

Having different origins, stochastic processes of type Ψ, Φ and Γ can be considered stochastically independent. Cross-correlations are therefore absent, and the autocovariances can simply be added up. In the time domain:

$$C_Y(t_j,\, t_k) = C_\Psi(t_j,\, t_k) + C_\Phi(t_j,\, t_k) + C_\Gamma(t_j,\, t_k) \tag{5.44}$$

$$\sigma^2_Y(t_j) = \sigma^2_\Psi(t_j) + \sigma^2_\Phi(t_j) + \sigma^2_\Gamma(t_j), \tag{5.45}$$

and in the frequency domain:

$$C_{\mathcal{F}Y}(\omega_j, \omega_k) = C_{\mathcal{F}\Psi}(\omega_j, \omega_k) + C_{\mathcal{F}\Phi}(\omega_j, \omega_k) + C_{\mathcal{F}\Gamma}(\omega_j, \omega_k) \quad (5.46)$$

$$\sigma^2_{\mathcal{F}Y}(\omega_j) = \sigma^2_{\mathcal{F}\Psi}(\omega_j) + \sigma^2_{\mathcal{F}\Phi}(\omega_j) + \sigma^2_{\mathcal{F}\Gamma}(\omega_j). \quad (5.47)$$

Multiple spectrally localized noises (type Γ) with different pulsations ω_p have a common origin: the electric energy transmission. Therefore, it is not a priori ensured that they are stochastically independent. However, if their mutual phase differences at the start of each new pulse response recording is completely random, i.e., has no expected value, they are uncorrelated. This is a fair assumption, even if there is a constant phase difference between the oscillations in the global time frame[3]. The mutual phase differences between spectrally localized noises with equal pulsation can be expected to be constant. Therefore, cross-effects cannot be excluded in this case.

It can be concluded that the autocovariances of all stochastic processes can simply be added to give the autocovariance of the pulse response, both in the time and the frequency domain, as long as there are no multiple spectrally localized noises with equal pulsation.

5.9 Deviation from normality

Of the three forms of uncertainty discussed, only the first is Gaussian. The distribution of the samples of a spectrally localized noise $\big(\Gamma(t_j)\big)$ defined by Eq. (5.31) is known, but non-Gaussian, U-shaped:

$$P[y < \Gamma(t_j) < y + \mathrm{d}y] = \frac{\mathrm{d}y}{\pi\sqrt{A(t_j)^2 - y^2}}, \text{ for all } -A(t_j) < y < A(t_j). \quad (5.48)$$

The distribution of the samples of a stochastic process $\Psi(t_j)$ defined by Eq. (5.39), due to uncertain pulse size or mass spectrometer sensitivity, is unknown. Only the standard deviation profile $\sigma^2_\Psi(t_j)$ can be estimated and the mean is known to be zero everywhere, by definition. As this form of uncertainty is liable to drifts, the stochastic process $\Psi(t_j)$ can be expected to differ from experimental series to experimental series and to be non-Gaussian.

[3] As an example, consider as noise an oscillation with frequency 60 Hz, the American mains frequency. Say a pulse is given every 5 s. This is exactly 300 times the period of the oscillation. Therefore, the phase of the oscillation is expected to be the same at the moment each pulse recording is started. However, the mains frequency is not 100 % constant and 100 % precision is neither attained by the pulse timer. For these reasons, the initial phase of the oscillation can be considered random. To gain absolute certainty about this, a small random time interval could be left between the end of each pulse recording and the next one.

As a consequence, the distribution of the deviation from the mean

$$Y(t_j) - \mu_Y(t_j) = \Phi(t_j) + \sum_{k=1}^{S} \Gamma_k(t_j) + \Psi(t_j) \tag{5.49}$$

is generally not normal. As known, the traditional mean-square regression method for determining model parameters is based on the assumption of normal distribution, see, e.g., (Mateu, 1997). Therefore, its direct application to TAP data analysis is generally not valid. Thus, in principle, the deviations from average have to be transformed to become normally distributed prior to the regression. During the regression, the heteroskedasticity of the pulse response must be taken into account.

5.10 Full noise analysis

It was justified in Section 5.8 that the variance profiles due to the different uncertainty effects can simply be added to obtain the total variance profile. In the most general case where there is Gaussian noise, an uncertain pulse size and S spectrally localized noises, an expression derived from Eqs. (5.21), (5.43) and (5.38) applies:

$$\begin{aligned}\sigma^2_{\mathcal{F}Y}(\omega_j) = {} & \frac{(1-\rho^2)\,\left(\sigma^2\right)_M}{1 - 2\rho\cos\left(\omega_p \Delta t\right) + \rho^2} + \zeta^2\,\left|\mathcal{F}\mu_Y\left(\omega_j\right)\right|^2 \\ & + \frac{1}{4}\sum_{k=1}^{S}\Bigg[\alpha_k^2\Big(\left|\mathcal{F}\mu_Y\left(\omega_{|p_k - j|}\right)\right|^2 + \left|\mathcal{F}\mu_Y\left(\omega_{f(p_k+j)}\right)\right|^2\Big) \\ & \qquad + n_t\delta_{p_k j}\Big(\beta_k^2 + 2\alpha_k\beta_k\mu_{Y,M}\Big)\Bigg]. \end{aligned} \tag{5.50}$$

As an example, the noise present in the WUStL data set has been analyzed. Here, the sampling interval is 4 ms. If it is assumed that the correlation time θ is about the same as the one found for the UGent set: $\theta \approx 0.789$ ms, the ratio $\Delta t/\theta$ is about 5. As this value is higher than 2.5, the unfavorable autocorrelation effect on the variance profile in the frequency domain can be neglected (see Section 5.5). This amounts to putting $\rho = 0$ in Eq. (5.50).

Fig. 5.11 shows five spectrally localized noises: at 50 Hz, 60 Hz, 70 Hz, 110 Hz and at 120 Hz[4]. The noises with frequencies of 50 Hz and 110 Hz are neglected. Therefore, in Eq. (5.50), $S = 3$ and, from Eq. (5.13), $p_1 = n_t\Delta t\,.\,60$ Hz, $p_2 = n_t\Delta t\,.\,70$ Hz and $p_3 = n_t\Delta t\,.\,120$ Hz.

[4]The peak about 0 Hz is due to a variable pulse size.

Table 5.1: Parameter estimates with their 95 % confidence intervals obtained by nonlinear regression of the observed standard deviation profile in the frequency domain with Eq. (5.51). The regression is shown in Fig. 5.11.

parameter	value	unit
$\left(\sigma^2\right)_M^{1/2}$	0.0050 ± 0.0003	V
ζ	0.0434 ± 0.0002	–
α_1	0.0281 ± 0.0003	–
α_3	0.0027 ± 0.0004	–

Eight parameters remain unknown: $\left(\sigma^2\right)_M$, ζ, α_1, β_1, α_2, β_2, α_3 and β_3. Multiple regression attempts have shown that the most meaningful correspondence between the observed and theoretical standard deviation profile is obtained assuming that the amplitude of the oscillation of 60 Hz is perfectly proportional to the signal strength, $\beta_1 = 0$, and that the amplitude of the noise about 70 Hz is constant, $\alpha_2 = 0$.

If the values $j \in \{p_2, p_3\}$ are excluded from the domain of interest, it is derived from Eq. (5.50) that

$$\sigma_{\mathcal{F}Y}(\omega_j) = \Bigg[\left(\sigma^2\right)_M + \zeta^2 \left|\mathcal{F}\mu_Y\left(\omega_j\right)\right|^2 + \frac{1}{4} \sum_{k \in \{1,\,3\}} \alpha_k^2 \Big(\left|\mathcal{F}\mu_Y\left(\omega_{|p_k - j|}\right)\right|^2 + \left|\mathcal{F}\mu_Y\left(\omega_{f(p_k + j)}\right)\right|^2 \Big) \Bigg]^{\frac{1}{2}}. \quad (5.51)$$

Eq. (5.14) stated that the elements of the discrete Fourier transform beyond the Nyquist pulsation can be derived from those before. For that matter

$$\sigma^2_{\mathcal{F}\mu_Y}(\omega_j) = \sigma^2_{\mathcal{F}\mu_Y}(\omega_{n_t - j}). \quad (5.52)$$

Therefore, the domain of interest is further reduced to the first half of the discrete Fourier transform.

Eq. (5.51) has four unknown parameters: $\left(\sigma^2\right)_M^{1/2}$, ζ, α_1 and α_3. These are estimated by nonlinear regression of the observed standard deviation profile with Eq. (5.51), abstracting the singular points at 50 Hz, 70 Hz, 110 Hz and at 120 Hz to improve the regression. The result is shown in Fig. 5.11 and yields the results listed in Table 5.1.

The standard deviation profile resulting from this regression may be symbolized as $\sigma_{\mathcal{F}Y,\mathrm{fit}}(\omega_j)$. From comparison of Eqs. (5.50) and (5.51), it

is clear that there is still a deficit at the frequencies 70 Hz and 120 Hz:

$$\sigma_{\mathcal{F}Y}(\omega_{p_2})^2 - \sigma_{\mathcal{F}Y,\mathrm{fit}}(\omega_{p_2})^2 = \frac{n_t}{4}\beta_2^2 \tag{5.53}$$

$$\sigma_{\mathcal{F}Y}(\omega_{p_3})^2 - \sigma_{\mathcal{F}Y,\mathrm{fit}}(\omega_{p_3})^2 = \frac{n_t}{4}\big(\beta_3^2 + 2\alpha_3\beta_3\mu_{Y,M}\big). \tag{5.54}$$

Estimations of β_2 and β_3 can be obtained simply by solving the Eqs. (5.53) and (5.54). This yields estimates

$$\beta_2 = 0.00166\,\mathrm{V} \tag{5.55}$$

and

$$\beta_3 = 0.00270\,\mathrm{V}. \tag{5.56}$$

In conclusion, the uncertainty the pulse responses from the WUStL set are subjected to, can be modeled as the stochastic process $\big(Y(t_j) - \mu_Y(t_j)\big)$:

$$\begin{aligned} Y(t_j) - \mu_Y(t_j) = {} & \big(\sigma^2\big)_M^{1/2} G(t_j) + \zeta\Lambda\mu_Y(t_j) + \alpha_1\mu_Y(t_j)\cos\left(\omega_{p_1}t_j + \Theta_1\right) \\ & + \beta_2\cos\left(\omega_{p_2}t_j + \Theta_2\right) + \big(\alpha_3\mu_Y(t_j) + \beta_3\big)\cos\left(\omega_{p_3}t_j + \Theta_3\right) \end{aligned} \tag{5.57}$$

where

- $\big(G(t_j)\big)$ is white Gaussian noise with mean 0 and time average standard deviation 1,
- Λ is a stochastic variable with mean 0 and standard deviation 1,
- $\omega_{p_1} = 2\pi \cdot 60\,\mathrm{Hz}$, $\omega_{p_2} = 2\pi \cdot 70\,\mathrm{Hz}$ and $\omega_{p_3} = 2\pi \cdot 120\,\mathrm{Hz}$,
- Θ_1, Θ_2 and Θ_3 are stochastic variables with uniform distribution over $[0,\, 2\pi]$,
- the parameters $\big(\sigma^2\big)_M^{1/2}$, ζ, α_1 and α_3 are listed in Table 5.1,
- the parameters β_2 and β_3 are given by Eqs. (5.55) and (5.56), respectively.

Consider the experimental interdependence of the standard deviation and the mean, shown in Fig. 5.13. In good approximation, the standard deviation is proportional to the signal strength, although it differs slightly from zero at zero signal strength. This corresponds to the result of the noise analysis. Indeed, the most important uncertainty effects, about

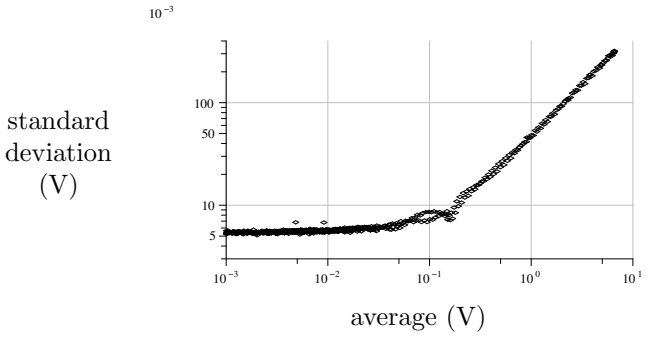

Figure 5.13: Logarithmic graph of the standard deviation of the samples as a function of their mean for the WUStL set, resulting from elimination of the sample times. The graph shows that the standard deviation is more or less proportional to the signal strength, although the standard deviation axis intercept differs from zero. This means that some noise remains present once the pulse response is near extinction.

0 Hz and 60 Hz, are found to be more or less proportional to the signal strength, while less important ones depend less on this signal strength.

The Ornstein Uhlenbeck noise is not believed to be due to avoidable interference. Therefore, it may be called "essential". This analysis shows the standard deviation of the essential noise in the WUStL case to amount to about 0.1 % of the peak response. In the case of the UGent set, this was about 4 % (see Section 5.5). This difference is not surprising, as the UGent data set was collected on a TAP-1-setup, while the WUStL set was collected on a TAP-2-setup. Compared to the TAP-1-system, the TAP-2 has the advantage that the mass spectrometer collects a higher fraction of the molecules leaving the reactor. Therefore, the signal is stronger and less sensitive to essential noise. In the case of the presently analyzed noise (WUStL data set), the Gaussian noise is clearly negligible with respect to the spectrally localized noise and the uncertainty caused by a variable pulse size. From the parameter estimates listed in Table 5.1, or even the mere observation of Fig. 5.11, it is clear that the spectrally localized noise is rather important. For example, the amplitude of the 60 Hz oscillation is about 3 % of the signal strength. Clearly it would be interesting to examine if the interference causing the spectrally localized noise could be reduced in a physical manner. The present noise analysis, applied to data collected at WUStL, revealed a pulse size variability of about 4 %. This is a typical number (Gleaves et al., 1997) and similar variabilities have been derived from data collected at UGent.

5.11 Conclusions

Noise limits the amount of information which can be extracted from experimental data on reaction networks. TAP pulse responses have been found to be liable to two types of noise. The first is Gaussian with standard deviation increasing as a function of the signal strength. When this type of noise is dominant, which is likely in pulse responses recorded on TAP-1-setups, its colored character puts a limit to the improvement of the precision of the parameter estimations achievable by increasing the sampling frequency of the signal. The second type of noise is spectrally localized, mostly around harmonics of the mains frequency. This noise is caused by interference by electric devices near the mass spectrometer, possibly part of the TAP-apparatus itself, or directly by the mass spectrometer's AC power supply.

Analytical expressions have been presented for the autocovariance of the pulse response, both in the time and the frequency domain. Specifically, regression of the observed standard deviation profile in the frequency domain with the analytical expression, allowed to derive quantitative information about the fine structure of the noise. The presently developed error analysis can be applied to single-pulse TAP-data resulting from diffusion/reaction phenomena.

The noise characteristics found served as a source of inspiration for the development of a novel regression strategy, which will be presented in Chapter 6. This strategy will improve the precision of the estimates of kinetic parameters and provide accurate quantitative information on this precision. Knowledge of the characteristics of the noise, more particularly in the frequency domain, will also show useful in Chapter 8, where a model-free procedure will be presented for determining connectivity features of reaction networks from TZTR-data.

Chapter 6

Second-order Statistical Regression

6.1 Introduction

The interpretation of data obtained from transient kinetic experiments usually involves tests of physico-chemical models against the experimental data, adjusting the kinetic parameters appearing in the former. The kinetic parameters are rate coefficients in case of *isothermal data*, i.e., if all data have been collected at the same temperature. If the data are *nonisothermal*, the kinetic parameters are pre-exponential factors and activation energies.

Regression is a statistical tool in the hands of the empiricist to investigate the causal relation between certain well-known *independent variables*, often controlled by the empiricist, on the one hand, and some observed *dependent variables* on the other. Regression analysis is useful in those cases where a causal model is known (or assumed valid) except for some parameters occurring in it, such as pre-exponential factors and activation energies in kinetic models. By regression, these parameters are estimated as those that make the model-calculated dependent variables coincide as near as possible with the empirical ones.

By far, the most widely applied regression technique is least-squares regression. Some recent text books on the matter are (Seber and Lee, 2003; Seber and Wild, 2003) (mathematical) and (Graybill and Iyer, 1994; Draper and Smith, 1998) (applied). If the model-calculated dependent variables are linear functions of the unknown parameters, their estimates can be found in a direct linear-algebraic way. If not, they are to be found iteratively, starting from some initial estimates, which is computationally more expensive. The Levenberg-Marquardt iterative method is commonly

used (Levenberg, 1944; Marquardt, 1963).

Hougen and Watson (1947) introduced the least-squares regression approach as a means to estimate kinetic parameters from stationary kinetic experiments. They rearranged the concentration and rate variables in Langmuir-Hinshelwood-Hougen-Watson type rate equations to render them linear in the parameters to be estimated. This allowed them to apply the computationally inexpensive linear least-squares regression theory. With the advent of the digital computer, direct nonlinear regression of the reaction rates was preferred over this method (Kittrell et al., 1965). Cutlip et al. (1972) first applied *nonlinear least-squares regression* (NLSQ regression) to transient kinetic data.

It was discussed in Section 1.3 that data from transient kinetic experiments are typically used to determine reaction networks. NLSQ regression of kinetic data is the key to the statistically sound discrimination between rival kinetic models and, hence, between the corresponding reaction mechanisms (Froment and Hosten, 1981). NLSQ regression with a certain physico-chemical reaction model yields estimates of the parameters occurring in this model and valuable statistical judgments about their significance in the form of confidence intervals. However, the unbiasedness of the estimates, the validity of the confidence intervals and that of the model discrimination algorithms depend on whether the experimental data obey certain statistical prerequisites which are discussed in Section 6.2 of this chapter.

All too frequently, these conditions are tacitly assumed fulfilled. However, the assumption that the experimental errors are homoskedastic and uncorrelated are not always valid. The autocorrelation of experimental errors when recording time series is well-known and is referred to as 'colored noise'. The necessary conditions unverified, there is a real danger that experimentalists draw unfounded conclusions. They may, for example, conclude that there is significant experimental support for certain mechanistic details of a reaction while in there is not. This chapter presents a second-order statistical regression as a way to prevent such mistakes if replicate-experimental data are available (Roelant et al., 2008).

A theoretical background will be provided in Section 6.2. Section 6.3 provides a linear conditioning transform which can be used to precondition the data for least-squares regression if the variance pattern of the noise is known. As the latter is usually not true, Section 6.4 presents an adaptation where the variance pattern is to be estimated from replicate-experimental data. In Section 6.5, the novel approach will be validated using synthetic and two sets of experimental data. The first set stems from a TAP-experiment of the adsorption of oxygen on a V_2O_5 based catalyst. The second set consists of TAP-data on the interaction of propane with a CuO–CeO_2 catalyst.

6.2 Theoretical background

Experimental time series

Transient kinetic experiments yield data in the form of time series. Examples of transient kinetic experiments are SSITKA, TPD and TAP, see Section 1.3. This chapter applies to all kinds of kinetic time series, but TAP-data will be used for illustration in this chapter. They all have been collected at the TAP-1-setup operational at the Laboratory for Chemical Technology.

During transient experiments, the experimentalist controls the experimental conditions and forces a well-defined variation of at least one of them in time. The experimental conditions and those parameters characterizing their change will be referred to as the experimental conditions in a broad sense. Let them be collected in a column vector $\boldsymbol{\xi}$. In a way dependent on $\boldsymbol{\xi}$, n_v physical variables, η_1, η_2, ..., η_{n_v}, evolve as the experiment progresses. They are recorded by measuring devices, resulting in time series of values measured at equally spaced time points t_j: $t_{j+1} - t_j = \Delta t$, for all $j \in \{1, 2, \ldots, n_t\}$. Δt is the sampling interval. Assume n_e multiresponse experiments are carried out at conditions $\boldsymbol{\xi}_1$, $\boldsymbol{\xi}_2$, ... and $\boldsymbol{\xi}_{n_e}$. At each condition $\boldsymbol{\xi}_e$, $e \in \{1, 2, \ldots, n_e\}$, this results in one time series for each physical variable η_v, $v \in \{1, 2, \ldots, n_v\}$:

$$\mathbf{y}_{e,v} = \begin{bmatrix} y_{e,v}(t_1) \\ y_{e,v}(t_2) \\ \vdots \\ y_{e,v}(t_{n_t}) \end{bmatrix} \in \mathbb{R}^{n_t \times 1}, \tag{6.1}$$

represented here as a column vector. Think of these time series as being stacked in a single composite column vector $\mathbf{y} \in \mathbb{R}^{n \times 1}$, with

$$n = n_e \, n_v \, n_t. \tag{6.2}$$

The mass spectrometer of the TAP-setup records a fixed mass of the spectrum so that unless use is made of a multitrack system (Nijhuis et al., 1997), to observe multiple components, the experiment has to be repeated as least as many times as there are components to be monitored. For TAP, the variables η_1, η_2, ..., η_{n_v} are thus the mass spectrometer measurements, in V, at the selected spectrum masses. The pressure varies in time and space in a way fully determined by the reactant pulse size. Hence, unless it is unknown, the latter is an experimental condition but the former is not. The reaction temperature is another experimental condition. As an example, Fig. 6.1 shows a typical experimental TAP pulse response.

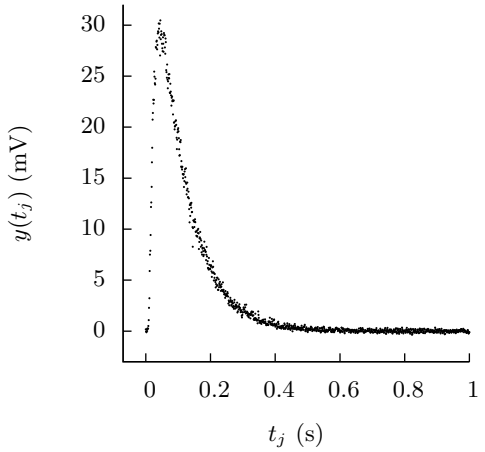

Figure 6.1: A typical TAP pulse response, consisting of a thousand samples: $j \in \{1, 2, \ldots, 1000\}$. For this response, argon was pulsed over quartz.

Model-calculated time series

The TAP-reactor is modeled by a system of partial differential equations with initial and boundary conditions, see Section 4.3. Usually, numerical techniques are applied to integrate the model equations, see Section 4.4, although an analytical integration is possible in some cases. In general, time series equivalent to those experimentally recorded can be calculated from reactor simulations. As a rule, use has to be made of calibration data of the measurement equipment in a final stage. For TAP for example, the calibration matrix has to be known to be able to convert the product flow rate pulse responses in mol/s, calculated from the reactor model, to the mass spectrometer signals measured in V.

The time series calculated from the model depend on some physicochemical parameters $b_1, b_2, \ldots, b_p$ (mostly kinetic and transport parameters) appearing in the reactor model. These are collected in a vector $\mathbf{b} \in \mathbb{R}^{p\times 1}$. The model-calculated time series can therefore be represented as

$$\mathbf{f}_v(\boldsymbol{\xi}_e, \mathbf{b}) = \begin{bmatrix} f_v(t_1, \boldsymbol{\xi}_e, \mathbf{b}) \\ f_v(t_2, \boldsymbol{\xi}_e, \mathbf{b}) \\ \vdots \\ f_v(t_{n_t}, \boldsymbol{\xi}_e, \mathbf{b}) \end{bmatrix}, \tag{6.3}$$

with $e \in \{1, 2, \ldots, n_e\}$ and $v \in \{1, 2, \ldots, n_v\}$. Furthermore, let $\mathbf{f}(\mathbf{b}) \in \mathbb{R}^{n\times 1}$ be the model-calculated analogue of $\mathbf{y}$: a composite of all vectors

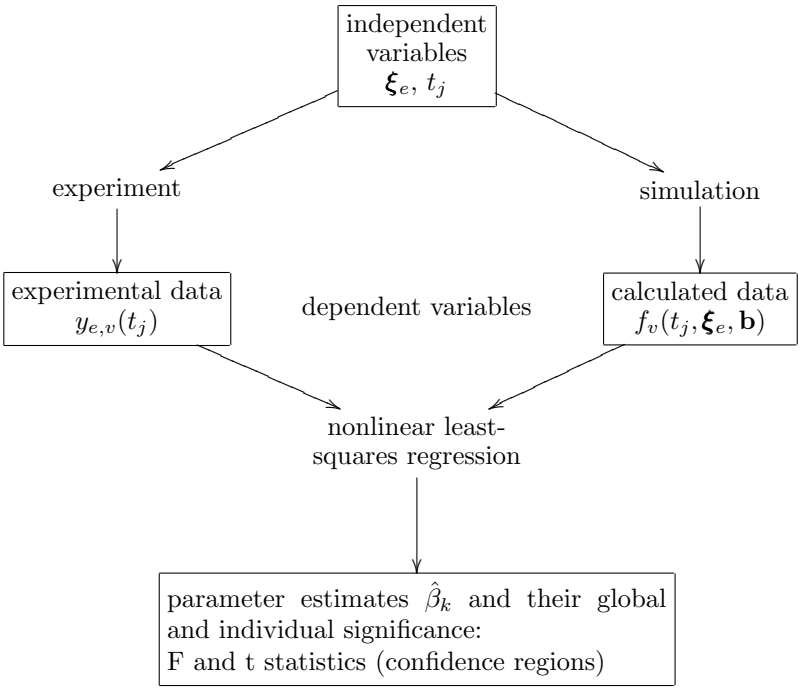

Figure 6.2: Overall scheme of the direct regression approach as a means to estimate physico-chemical parameters from transient kinetic data.

$\mathbf{f}_v(\boldsymbol{\xi}_e, \mathbf{b})$. $\mathbf{f}$ is then the *model function* (Graybill and Iyer, 1994).

Least-squares regression of time series

In transient kinetic experiments, the independent variables are the experimental conditions $\boldsymbol{\xi}_{e,v}$ and the time t. The dependent variables are the experimental recordings $\mathbf{y}_{e,v}$. The physico-chemical parameters $\mathbf{b}$ are to be estimated by nonlinear least-squares regression. Fig. 6.2 gives a schematic overview. The number of parameters that can be estimated is limited to the dimension of the data set $\mathbf{y}$:

$$p \leqslant n. \tag{6.4}$$

Strictly speaking, least-squares regression should only be applied under the following six conditions.

Condition 6.1. *The independent variables contain no experimental errors.*

Condition 6.2. *The model is* adequate.

Condition 6.3. *The mean experimental error is zero.*

Condition 6.4. *All errors are normally distributed.*

Condition 6.5. *The errors are homoskedastic.*

Condition 6.6. *The errors are uncorrelated.*

Condition 6.1 requires the vectors $\boldsymbol{\xi}_e$ and t to be known without (significant) error. In kinetic studies, the experimental conditions are usually temperature and pressure. These are typically known with very good accuracy and precision. The same is true for the time t. The adequacy of the model referred to in Condition 6.2 means that it applies with some real, unknown parameters $\boldsymbol{\beta}$, aside from additive random experimental errors $\boldsymbol{\epsilon}$ (Draper and Smith, 1998):

$$\mathbf{y} = \mathbf{f}(\boldsymbol{\beta}) + \boldsymbol{\epsilon}. \tag{6.5}$$

In fulfillment of the other conditions, $\boldsymbol{\epsilon}$ has to be a random error vector with multidimensional normal distribution with mean zero ($\mathbf{0}_n$) and variance matrix $\mathbf{I}_n \sigma^2$:

$$\boldsymbol{\epsilon} \sim N\left(\mathbf{0}_n, \mathbf{I}_n \sigma^2\right). \tag{6.6}$$

If Conditions 6.1 to 6.6 are fulfilled, the parameters $\hat{\boldsymbol{\beta}}$ minimizing of the residual sum of squares $S(\mathbf{b})$ are the maximum-likelihood estimates of the real parameters $\boldsymbol{\beta}$. (Joint) confidence regions of the parameter estimates $\hat{\boldsymbol{\beta}}$ can be estimated, which allow the experimentalist to judge the significance of the regression and of the individual parameter estimates. Appendix F gives a concise overview of the theory.

Generally, at best a simplifying model can be conceived of the experimental system, failing to grasp all its subtleties. Condition 6.2 is then fulfilled at most in approximation, and practically translates to the requirement that the bias between experimental and model-calculated time series, so-called *lack of fit* (Graybill and Iyer, 1994; Draper and Smith, 1998), is small compared with the experimental error. In the context of time series the latter consists of *noise*: similarly to $\mathbf{y}$ and $\mathbf{f}(\mathbf{b})$, $\boldsymbol{\epsilon}$ in Eq. (6.5) is a composite vector containing the noise $\boldsymbol{\epsilon}_{e,v}$ in all time series $\mathbf{y}_{e,v}$. As is always the case in regression analysis, Condition 6.2 is assumed valid. Condition 6.3 expresses a basic experimental requirement and is also assumed fulfilled here on that account.

Assumption 6.1. *The Conditions 6.1, 6.2 and 6.3 are fulfilled.*

The fulfillment of the Conditions 6.4, 6.5 and 6.6 should not be taken for granted. For TAP pulse responses, at least, they are generally not met, see Chapter 5 and (Schuurman, 2007). Condition 6.5 requires the level of noise to be constant in time, its variance σ^2 unvarying. Moreover, in absolute terms, the noise must be equally important in all experimental time series, σ^2 being independent of the experimental conditions $\boldsymbol{\xi}_e$ and the variable η_v monitored. Fulfillment of Condition 6.6 implies different noise time series to have no cross-correlation. In this paper, the latter is assumed to be valid as a relaxed form of Condition 6.6.

Assumption 6.2. *Different experimental time series have no cross-correlation.*

In particular, Assumption 6.2 involves the n_v time series measured during each experiment to have no cross-correlation. This is the case for most TAP-systems, where a single 'experiment' requires a series of n_v independently repeated experiments at the same experimental conditions, see Section 6.2. Additionally to Assumption 6.2, Condition 6.6 requires all noise to be *white*, i.e., free of time autocorrelation. This is not assumed to be the case in this paper: the population variance matrix

$$\mathbf{V}(\boldsymbol{\epsilon}_{e,v}) = E\left[\boldsymbol{\epsilon}_{e,v}\boldsymbol{\epsilon}_{e,v}^T\right] \tag{6.7}$$

need not be diagonal.

This paper will show how the Conditions 6.4, 6.5 and 6.6 can be fulfilled. Section 6.3 attends to the case where $\mathbf{V}(\boldsymbol{\epsilon}_{e,v})$ is known, a situation rarely met in practice. By contrast, in Section 6.4, $\mathbf{V}(\boldsymbol{\epsilon}_{e,v})$ is not assumed known.

6.3 Population principal component analysis of known noise and rescaling

By its nature, the population variance matrix $\mathbf{V}(\boldsymbol{\epsilon}_{e,v})$ of the noise $\boldsymbol{\epsilon}_{e,v}$ in an experimental time series $\mathbf{y}_{e,v}$ is a symmetric, positive definite matrix. Thus, there exists an eigendecomposition

$$\mathbf{V}(\boldsymbol{\epsilon}_{e,v}) = \mathbf{U}_{e,v} \cdot \boldsymbol{\Lambda}_{e,v} \cdot \mathbf{U}_{e,v}^T, \tag{6.8}$$

where $\boldsymbol{\Lambda}_{e,v} \in \mathbb{R}^{n_t \times n_t}$ is a diagonal matrix holding the positive eigenvalues of $\mathbf{V}(\boldsymbol{\epsilon}_{e,v})$ in its diagonal, ranked from high to low:

$$\boldsymbol{\Lambda}_{e,v} = \begin{bmatrix} \sigma^2_{e,v,1} & 0 & \cdots & 0 \\ 0 & \sigma^2_{e,v,2} & \cdots & 0 \\ \vdots & \vdots & \ddots & \vdots \\ 0 & 0 & \cdots & \sigma^2_{e,v,n_t} \end{bmatrix}, \tag{6.9}$$

with

$$\sigma_{e,v,1} \geqslant \sigma_{e,v,2} \geqslant \ldots \geqslant \sigma_{e,v,n_t} > 0 \tag{6.10}$$

and $\mathbf{U}_{e,v}$ is a $n_t \times n_t$ matrix having the associated, orthonormal eigenvectors as columns:

$$\mathbf{U}_{e,v} = \begin{bmatrix} | & | & & | \\ \mathbf{u}_{e,v,1} & \mathbf{u}_{e,v,2} & \cdots & \mathbf{u}_{e,v,n_t} \\ | & | & & | \end{bmatrix}, \tag{6.11}$$

with

$$\mathbf{u}_{e,v,k}^T \cdot \mathbf{u}_{e,v,l} = \begin{cases} 1 \text{ if } k = l \\ 0 \text{ else.} \end{cases} \tag{6.12}$$

In matrix form, the orthonormality (6.12) of the eigenvectors translates to

$$\mathbf{U}_{e,v}^T \cdot \mathbf{U}_{e,v} = \mathbf{I}_{n_t}. \tag{6.13}$$

Consider the linear transformation of time series $\mathbf{y}_{e,v}$ by $\mathbf{U}_{e,v}^T$:

$$\mathbf{y}'_{e,v} = \mathbf{U}_{e,v}^T \cdot \mathbf{y}_{e,v}. \tag{6.14}$$

The random part $\boldsymbol{\epsilon}_{e,v}$ of $\mathbf{y}_{e,v}$ is hereby transformed to the random part $\boldsymbol{\epsilon}'_{e,v}$ of $\mathbf{y}'_{e,v}$:

$$\boldsymbol{\epsilon}'_{e,v} = \mathbf{U}_{e,v}^T \cdot \boldsymbol{\epsilon}_{e,v}. \tag{6.15}$$

The variance matrix of $\boldsymbol{\epsilon}'_{e,v}$ is found as

$$\begin{aligned} \mathbf{V}(\boldsymbol{\epsilon}'_{e,v}) &= E\left[\boldsymbol{\epsilon}'_{e,v} \cdot {\boldsymbol{\epsilon}'_{e,v}}^T\right] && (6.16) \\ &\overset{(6.15)}{=} E\left[\mathbf{U}_{e,v}^T \cdot \boldsymbol{\epsilon}_{e,v} \cdot \boldsymbol{\epsilon}_{e,v}^T \cdot \mathbf{U}_{e,v}\right] \\ &\overset{(6.7)}{=} \mathbf{U}_{e,v}^T \cdot \mathbf{V}(\boldsymbol{\epsilon}_{e,v}) \cdot \mathbf{U}_{e,v} \\ &\overset{(6.8)}{=} \mathbf{U}_{e,v}^T \cdot \mathbf{U}_{e,v} \cdot \boldsymbol{\Lambda}_{e,v} \cdot \mathbf{U}_{e,v}^T \cdot \mathbf{U}_{e,v} \\ &\overset{(6.13)}{=} \boldsymbol{\Lambda}_{e,v}. && (6.17) \end{aligned}$$

$\boldsymbol{\epsilon}'_{e,v}$ is the result of expressing $\boldsymbol{\epsilon}_{e,v}$ in a coordinate system constituted by the orthonormal eigenvectors of $\mathbf{V}(\boldsymbol{\epsilon}'_{e,v})$. In other words, for each k, the kth component of $\boldsymbol{\epsilon}'_{e,v}$ is the Euclidean length of the orthogonal projection of the random noise vector $\boldsymbol{\epsilon}_{e,v}$ on $\mathbf{u}_{e,v,k}$. According to Eqs. (6.17), (6.9) and (6.10), these components are mutually uncorrelated and have variances decreasing as a function of k. Apparently, the largest variability of the noise is parallel to the first eigenvector $\mathbf{u}_{e,v,1}$, the second largest variability parallel to the second eigenvector $\mathbf{u}_{e,v,2}$, etc. For this reason, the

eigenvectors, and particularly the first few of them, are called the *population principal components* (pPCs) of the noise. The linear transformation (6.15) is called the *population principal component analysis* (pPCA) or the *discrete Karhunen-Loève transformation* of the noise (Therrien, 1992; Massart et al., 1997; Vandeginste et al., 1998; Jolliffe, 2004). In fulfillment of Condition 6.6 for least-squares regression, transformation (6.14) projects the time series on the pPCs of their noise. Simple rescaling of the components of the resulting vector $\mathbf{y}'_{e,v}$ by the reciprocal of their standard deviation suffices to also render their errors homoskedastic, in fulfillment of Condition 6.5. Define

$$\begin{aligned}\mathbf{y}''_{e,v} &= \mathbf{\Lambda}_{e,v}^{-1/2} \cdot \mathbf{y}'_{e,v} \\ &= \mathbf{\Lambda}_{e,v}^{-1/2} \cdot \mathbf{U}_{e,v}^{T} \cdot \mathbf{y}_{e,v}\end{aligned} \tag{6.18}$$

with

$$\mathbf{\Lambda}_{e,v}^{-1/2} = \begin{bmatrix} 1/\sigma_{e,v,1} & 0 & \cdots & 0 \\ 0 & 1/\sigma_{e,v,2} & \cdots & 0 \\ \vdots & \vdots & \ddots & \vdots \\ 0 & 0 & \cdots & 1/\sigma_{e,v,n_t} \end{bmatrix}. \tag{6.19}$$

Then, taking into account that $\mathbf{\Lambda}_{e,v}^{-1/2}$ is symmetric, the variance matrix of the random part

$$\boldsymbol{\epsilon}''_{e,v} = \mathbf{\Lambda}_{e,v}^{-1/2} \cdot \boldsymbol{\epsilon}'_{e,v} \tag{6.20}$$

of $\mathbf{y}''_{e,v}$ becomes

$$\begin{aligned}\mathbf{V}(\boldsymbol{\epsilon}''_{e,v}) &= E\left[\boldsymbol{\epsilon}''_{e,v} \cdot \boldsymbol{\epsilon}''_{e,v}{}^{T}\right] \\ &\overset{(6.20)}{=} E\left[\mathbf{\Lambda}_{e,v}^{-1/2} \cdot \boldsymbol{\epsilon}'_{e,v} \cdot \boldsymbol{\epsilon}'_{e,v}{}^{T} \cdot \mathbf{\Lambda}_{e,v}^{-1/2}\right] \\ &\overset{(6.16)}{=} \mathbf{\Lambda}_{e,v}^{-1/2} \cdot \mathbf{V}(\boldsymbol{\epsilon}'_{e,v}) \cdot \mathbf{\Lambda}_{e,v}^{-1/2} \\ &\overset{(6.17)}{=} \mathbf{\Lambda}_{e,v}^{-1/2} \cdot \mathbf{\Lambda}_{e,v} \cdot \mathbf{\Lambda}_{e,v}^{-1/2} \\ &= \mathbf{I}_{n_t}.\end{aligned} \tag{6.21}$$

Assumption 6.2 implies that there is no cross-correlation between the different transformed noise vectors $\boldsymbol{\epsilon}''_{e,v}$. Hence, it follows from Eq. (6.21) that the variance matrix of their composite vector $\boldsymbol{\epsilon}''$ is

$$\mathbf{V}(\boldsymbol{\epsilon}'') = \mathbf{I}_n. \tag{6.22}$$

This fulfills Conditions 6.5 and 6.6 for regression of $\mathbf{y}''$ with $\mathbf{f}''(\mathbf{b})$, the composite vectors of $\mathbf{y}''_{e,v}$ and

$$\mathbf{f}''_v(\boldsymbol{\xi}_e, \mathbf{b}) = \mathbf{\Lambda}_{e,v}^{-1/2} \cdot \mathbf{U}_{e,v}^{T} \cdot \mathbf{f}_v(\boldsymbol{\xi}_e, \mathbf{b}), \tag{6.23}$$

respectively. The fulfillment of the Conditions 6.1, 6.2 and 6.3, see Assumption 6.1, holds. However, Condition 6.4 generally remains unfulfilled. Moreover, observe that the matrices $\mathbf{\Lambda}_{e,v}$ and $\mathbf{U}_{e,v}$ were calculated from the noise's population variance matrix $\mathbf{V}(\boldsymbol{\epsilon}_{e,v})$, while this matrix is usually not known. These problems can be solved making use of replicate experiments, as will be explained in the Sections 6.4 and 6.4.

6.4 Second-order statistical regression of replicate-experimental data

Sample principal component analysis and rescaling

It is often possible to replicate transient experiments at low additional cost. The replicate time series recorded must be stochastically homogeneous and mutually independent. Therefore, for catalytic experiments, the experimentalist has to make sure that any changes in the catalyst's surface between the replicate experiments remain negligible. The availability of replicate experiments offers three advantages.

1. Replicate time series can be averaged to obtain time series with an increased SNR. Regression of such averages thus yields more significant information.

2. The noise of the average of, say, minimum ten time series can be considered normally distributed in good approximation, whatever the distribution of the original noise, because of the *central limit theorem*. This fulfills Condition 6.4 for least-squares regression of the average time series.

3. From replicates, second-order statistical information (the variance matrix) can be derived about the noise. This information can be used to transform linearly the time series to fulfill the Conditions 6.5 and 6.6. An approach similar to the one presented in Section 6.3 can be followed.

Advantage 2 involves an assumption.

Assumption 6.3. *A sufficient amount of replicate time series is available to consider the noise of the average time series normally distributed in good approximation.*

Assume there are $n_{r,e} \geqslant 2$ replicates of each experimental time series $\mathbf{y}_{e,v}$: $\mathbf{y}_{e,v}^{(1)}$, $\mathbf{y}_{e,v}^{(2)}$, …, $\mathbf{y}_{e,v}^{(n_{r,e})}$. Not all experiments have to be replicated an equal amount of times, which is why a subscript e is provided in $n_{r,e}$.

Define $\overline{\mathbf{y}}_{e,v}$ as the average time series and the error matrix $\mathbf{E}_{e,v} \in \mathbb{R}^{n_t \times n_{r,e}}$ as the block matrix

$$\mathbf{E}_{e,v} = \begin{bmatrix} | & | & & | \\ \mathbf{y}_{e,v}^{(1)} - \overline{\mathbf{y}}_{e,v} & \mathbf{y}_{e,v}^{(2)} - \overline{\mathbf{y}}_{e,v} & \cdots & \mathbf{y}_{e,v}^{(n_{r,e})} - \overline{\mathbf{y}}_{e,v} \\ | & | & & | \end{bmatrix} \tag{6.24}$$

Then the population variance matrix $\mathbf{V}(\boldsymbol{\epsilon}_{e,v})$ of the noise $\boldsymbol{\epsilon}_{e,v}$ in the time series $\mathbf{y}_{e,v}$ can be estimated from the replicates as the sample variance matrix

$$\hat{\mathbf{V}}(\boldsymbol{\epsilon}_{e,v}) = \frac{1}{n_{r,e} - 1} \mathbf{E}_{e,v} \cdot \mathbf{E}_{e,v}^T. \tag{6.25}$$

Normally, the following assumption applies.

Assumption 6.4. *The number of replicate experiments does not exceed the number of samples in one time series:*

$$n_{r,e} \leqslant n_t. \tag{6.26}$$

In the case of TAP for example, $n_{r,e}$ would typically be 20 while n_t would be 1000.

By construction and Assumption 6.4, $\hat{\mathbf{V}}(\boldsymbol{\epsilon}_{e,v}) \in \mathbb{R}^{n_t \times n_t}$ is a symmetric, positive-semidefinite matrix of rank $n_{r,e} - 1$. Thus, there exists an eigendecomposition

$$\hat{\mathbf{V}}(\boldsymbol{\epsilon}_{e,v}) = \hat{\mathbf{U}}_{e,\,v} \cdot \hat{\boldsymbol{\Lambda}}_{e,\,v} \cdot \hat{\mathbf{U}}_{e,\,v}^T, \tag{6.27}$$

where $\hat{\boldsymbol{\Lambda}}_{e,\,v} \in \mathbb{R}^{(n_{r,e}-1)\times(n_{r,e}-1)}$ is a diagonal matrix with the $n_{r,e} - 1$ nonzero eigenvalues of $\hat{\mathbf{V}}(\boldsymbol{\epsilon}_{e,v})$ as diagonal elements, ranked from high to low, i.e.,

$$\hat{\boldsymbol{\Lambda}}_{e,\,v} = \begin{bmatrix} s_{e,v,1}^2 & 0 & \cdots & 0 \\ 0 & s_{e,v,2}^2 & \cdots & 0 \\ \vdots & \vdots & \ddots & \vdots \\ 0 & 0 & \cdots & s_{e,v,n_{r,e}-1}^2 \end{bmatrix}, \tag{6.28}$$

with

$$s_{e,v,1} \geqslant s_{e,v,2} \geqslant \ldots \geqslant s_{e,v,n_{r,e}-1} > 0 \tag{6.29}$$

and $\hat{\mathbf{U}}_{e,\,v}$ is a $n_t \times (n_{r,e} - 1)$ matrix with the associated eigenvectors as columns:

$$\hat{\mathbf{U}}_{e,\,v} = \begin{bmatrix} | & | & & | \\ \hat{\mathbf{u}}_{e,v,1} & \hat{\mathbf{u}}_{e,v,2} & \cdots & \hat{\mathbf{u}}_{e,v,n_{r,e}-1} \\ | & | & & | \end{bmatrix}. \tag{6.30}$$

The eigenvectors are orthonormal:

$$\hat{\mathbf{u}}_{e,v,k}^T \cdot \hat{\mathbf{u}}_{e,v,l} = \begin{cases} 1 \text{ if } k = l \\ 0 \text{ else.} \end{cases} \tag{6.31}$$

In matrix form:

$$\hat{\mathbf{U}}_{e,\,v}^T \cdot \hat{\mathbf{U}}_{e,\,v} = \mathbf{I}_{n_{r,e}-1}. \tag{6.32}$$

Analogously to Eq. (6.14), say

$$\mathbf{y}'_{e,v} = \hat{\mathbf{U}}_{e,\,v}^T \cdot \mathbf{y}_{e,v}. \tag{6.33}$$

$\mathbf{y}'_{e,v}$ is $\mathbf{y}_{e,v}$ orthogonally projected on the space spanned by the eigenvectors of $\hat{\mathbf{V}}(\boldsymbol{\epsilon}_{e,v})$ corresponding to nonzero eigenvectors, expressed in the orthonormal coordinate system they constitute. Observe that the transformed replicates of $\mathbf{y}_{e,v}$ can be considered replicates themselves of $\mathbf{y}'_{e,v}$. For each $k \in \{1, 2, \ldots, n_{r,e}\}$, define

$$\mathbf{y}'^{(k)}_{e,v} = \hat{\mathbf{U}}_{e,\,v}^T \cdot \mathbf{y}^{(k)}_{e,v}. \tag{6.34}$$

Moreover the average of the transforms is equal to the transformed average, $\overline{\mathbf{y}}'_{e,v}$. Corresponding to Eq. (6.24), define the error matrix

$$\mathbf{E}'_{e,v} = \begin{bmatrix} | & | & & | \\ \mathbf{y}'^{(1)}_{e,v} - \overline{\mathbf{y}}'_{e,v} & \mathbf{y}'^{(2)}_{e,v} - \overline{\mathbf{y}}'_{e,v} & \cdots & \mathbf{y}'^{(n_{r,e})}_{e,v} - \overline{\mathbf{y}}'_{e,v} \\ | & | & & | \end{bmatrix} \tag{6.35}$$

$$= \hat{\mathbf{U}}_{e,\,v}^T \cdot \mathbf{E}_{e,v}. \tag{6.36}$$

The variance matrix $\mathbf{V}(\boldsymbol{\epsilon}'_{e,v})$ is estimated as

$$\begin{aligned} \hat{\mathbf{V}}(\boldsymbol{\epsilon}'_{e,v}) &= \frac{1}{n_{r,e}-1}\, \mathbf{E}'_{e,v} \cdot {\mathbf{E}'_{e,v}}^T \\ &\overset{(6.36)}{=} \frac{1}{n_{r,e}-1}\, \hat{\mathbf{U}}_{e,\,v}^T \cdot \mathbf{E}_{e,v} \cdot \mathbf{E}_{e,v}^T \cdot \hat{\mathbf{U}}_{e,\,v} \\ &\overset{(6.25)}{=} \hat{\mathbf{U}}_{e,\,v}^T \cdot \hat{\mathbf{V}}(\boldsymbol{\epsilon}_{e,v}) \cdot \hat{\mathbf{U}}_{e,\,v} \\ &\overset{(6.27)}{=} \hat{\mathbf{U}}_{e,\,v}^T \cdot \hat{\mathbf{U}}_{e,\,v} \cdot \hat{\boldsymbol{\Lambda}}_{e,\,v} \cdot \hat{\mathbf{U}}_{e,\,v}^T \cdot \hat{\mathbf{U}}_{e,\,v} \\ &\overset{(6.32)}{=} \hat{\boldsymbol{\Lambda}}_{e,\,v}. \end{aligned} \tag{6.37}$$

As this matrix is diagonal, the transformation is expected to fulfill Condition 6.6 for least-squares regression. The eigenvectors $\hat{\mathbf{u}}_{e,v,1}$, $\hat{\mathbf{u}}_{e,v,2}$, …, $\hat{\mathbf{u}}_{e,v,n_{r,e}-1}$ are called *sample principal components* (sPCs) of the noise. Transformation (6.36) is analogous to the pPCA (6.15) and is referred

to as *sample principal component analysis* (sPCA). As before, rescaling enables to meet Condition 6.5. Define

$$\begin{aligned}\mathbf{y}''_{e,v} &= \hat{\mathbf{\Lambda}}_{e,\,v}^{-1/2} \cdot \mathbf{y}'_{e,v} \\ &= \hat{\mathbf{\Lambda}}_{e,\,v}^{-1/2} \cdot \hat{\mathbf{U}}_{e,\,v}^{T} \cdot \mathbf{y}_{e,v},\end{aligned} \tag{6.38}$$

where $\hat{\mathbf{\Lambda}}_{e,\,v}^{-1/2}$ is defined analogously to $\mathbf{\Lambda}_{e,v}^{-1/2}$ in (6.19). Then the sample variance matrix of the error $\boldsymbol{\epsilon}''_{e,v}$ of $\mathbf{y}''_{e,v}$ is the unit matrix:

$$\hat{\mathbf{V}}\left(\boldsymbol{\epsilon}''_{e,v}\right) = \mathbf{I}_{n_{r,e}-1}. \tag{6.39}$$

The sample variance matrix $\hat{\mathbf{V}}(\boldsymbol{\epsilon}''_{e,v})$ is an estimate of the unknown population variance matrix $\mathbf{V}(\boldsymbol{\epsilon}''_{e,v})$ based on the replicate data available. While transformation (6.38) was constructed to equate the first with the unit matrix $\mathbf{I}_{n_{r,e}-1}$, the latter is close but probably not equal to $\mathbf{I}_{n_{r,e}-1}$:

$$\mathbf{V}(\boldsymbol{\epsilon}''_{e,v}) \approx \mathbf{I}_{n_{r,e}-1}. \tag{6.40}$$

Correspondingly, the components of $\boldsymbol{\epsilon}''_{e,v}$ are neither fully uncorrelated nor perfectly homoskedastic. However, the approximate validity of Eq. (6.40) improves as more replicates become available.

As a consequence of Eq. (6.39), the sample variance matrix of the error vector $\bar{\boldsymbol{\epsilon}}''_{e,v}$ of the transformed average time series, $\overline{\mathbf{y}}''_{e,v} = \hat{\mathbf{\Lambda}}_{e,\,v}^{-1/2} \cdot \hat{\mathbf{U}}_{e,\,v}^{T} \cdot \overline{\mathbf{y}}_{e,v}$, is calculated as

$$\hat{\mathbf{V}}\left(\bar{\boldsymbol{\epsilon}}''_{e,v}\right) = \frac{1}{n_{r,e}-1}\,\mathbf{I}_{n_{r,e}-1}. \tag{6.41}$$

A subsequent rescaling

$$\begin{aligned}\overline{\mathbf{y}}'''_{e,v} &= \sqrt{n_{r,e}-1}\,\overline{\mathbf{y}}''_{e,v} \\ &= \sqrt{n_{r,e}-1}\,\hat{\mathbf{\Lambda}}_{e,\,v}^{-1/2} \cdot \hat{\mathbf{U}}_{e,\,v}^{T} \cdot \overline{\mathbf{y}}_{e,v}\end{aligned} \tag{6.42}$$

enables to obtain

$$\hat{\mathbf{V}}\left(\bar{\boldsymbol{\epsilon}}'''_{e,v}\right) = \mathbf{I}_{n_{r,e}-1}, \tag{6.43}$$

where $\bar{\boldsymbol{\epsilon}}'''_{e,v}$ is the random part of $\overline{\mathbf{y}}'''_{e,v}$. All transformed average time series $\overline{\mathbf{y}}'''_{e,v} \in \mathbb{R}^{(n_{r,e}-1)\times 1}$ can then be stacked in a single vector $\overline{\mathbf{y}}''' \in \mathbb{R}^{n'''\times 1}$, with n''' the total number of replicate-experimental times series,

$$n''' = n_v \sum_{e=1}^{n_e} (n_{r,e}-1). \tag{6.44}$$

It follows from Assumption 6.2 and Eq. (6.43) that the sample variance matrix of the random part $\bar{\boldsymbol{\epsilon}}'''$ of $\overline{\mathbf{y}}'''$ is calculated as

$$\hat{\mathbf{V}}(\bar{\boldsymbol{\epsilon}}''') = \mathbf{I}_{n'''}. \tag{6.45}$$

$\overline{\mathbf{y}}'''$ can now be regressed with its model-calculated analogue $\mathbf{f}'''(\mathbf{b})$, a composite vector of transformed model-calculated time series $\mathbf{f}_v'''(\boldsymbol{\xi}_e, \mathbf{b})$:

$$\mathbf{f}_v'''(\boldsymbol{\xi}_e, \mathbf{b}) = \sqrt{n_{r,e} - 1}\, \hat{\mathbf{\Lambda}}_{e,\,v}^{-1/2} \cdot \hat{\mathbf{U}}_{e,\,v}^{T} \cdot \mathbf{f}_v(\boldsymbol{\xi}_e, \mathbf{b}). \tag{6.46}$$

Conditions 6.5 and 6.6 are expected to be fulfilled by Eq. (6.45). Moreover, as the transformation presented is linear, the fulfillment of the Conditions 6.2, 6.3 and 6.4, assured by the Assumptions 6.1 and 6.3, holds. In summary, $\overline{\mathbf{y}}'''$ is provisionally found suited for regression with $\mathbf{f}'''(\mathbf{b})$. Obviously, this regression is only possible if the number of parameters is not larger than the dimensionality of these vectors. This is assumed in this paper.

Assumption 6.5. *The number of parameters does not exceed the total number of replicate-experimental time series:*

$$p \leqslant n'''. \tag{6.47}$$

Taking into account Eqs. (6.2), (6.44) and (6.26), comparison of Eq. (6.47) with Eq. (6.4) teaches that by application of the sPCA (6.33), the number of parameters that can be estimated was reduced. In reality, rarely more than, say, ten parameters have to be estimated. Keeping in mind Assumption 6.3, the limitation is unlikely to raise problems in practice. The dimensionality reduction would decrease the computational load of the regression, were it not that the most time-consuming part is the evaluation of the model function $\mathbf{f}$, which generally requires the numerical integration of one or more systems of partial differential equations. On the other hand, because $\mathbf{y}'''$ and $\mathbf{f}'''(\mathbf{b})$ have less components than their originals, the transformation is noninvertible. Hence, a part of the information is lost for regression. This can lead to an unnecessary increase of the width of the parameter confidence intervals. Preferably, $\mathbf{y}$ is well aligned with the vector space $\mathscr{S}$ spanned by all sPCs. In that case, the orthonormal coordinate system they constitute is able to describe $\mathbf{y}$ well, $\mathbf{y}$'s orthogonal projection on $\mathscr{S}$ not differing so much from its original. The angle ψ between $\mathbf{y}$ and the space $\mathscr{S}$ can be calculated from

$$\cos\psi = \frac{\|\overline{\mathbf{y}}'\|}{\|\overline{\mathbf{y}}\|}, \tag{6.48}$$

where $\overline{\mathbf{y}}'$ is the composite of all vectors $\overline{\mathbf{y}}'_{e,v}$. ψ is a measure for the distortion of the experimental set by switching to a smaller coordinate system at sPCA. In other words, ψ is a rough measure of the fraction of information lost. In the most favorable case, evidently, $\psi \approx 0°$.

Fig. 6.3 visualizes the first four sPCs calculated from a set of eight hundred replicate TAP pulse responses, one of which was shown in Fig. 6.1.

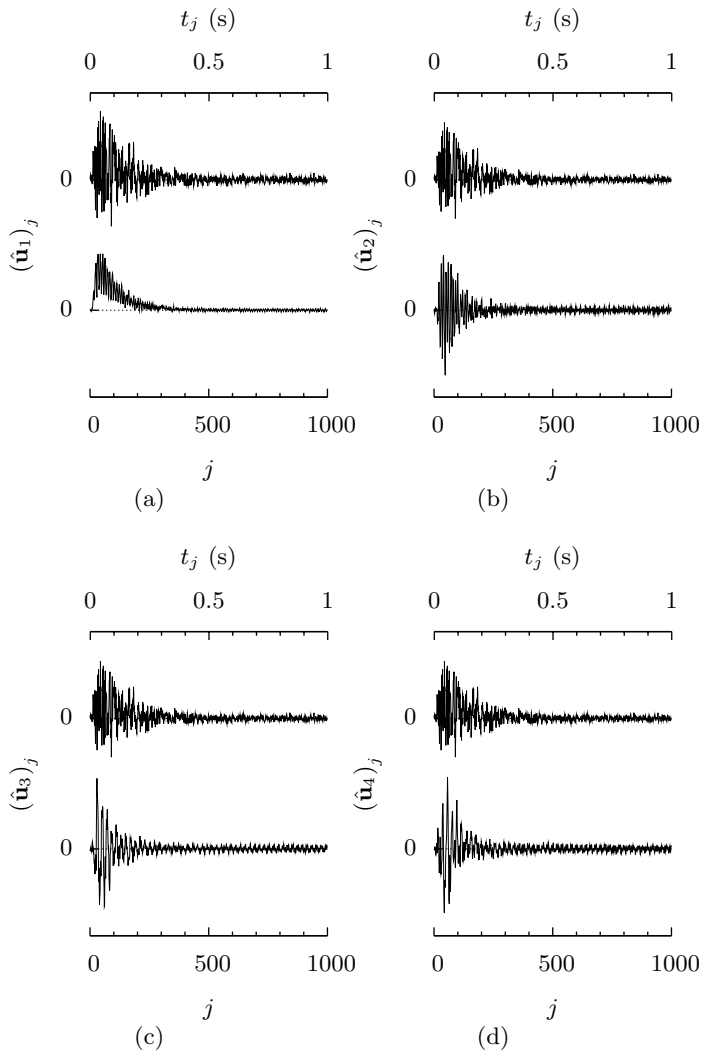

Figure 6.3: The first (a), second (b), third (c) and fourth (d) sample principal noise component calculated from a set of replicate-experimental TAP pulse responses. $(\hat{\mathbf{u}}_k)_j$ refers to the jth element of the kth sample principal component $\hat{\mathbf{u}}_k$. The lower graphs show the sample principal components calculated from eight hundred replicates. The upper graphs show those calculated from twenty replicates.

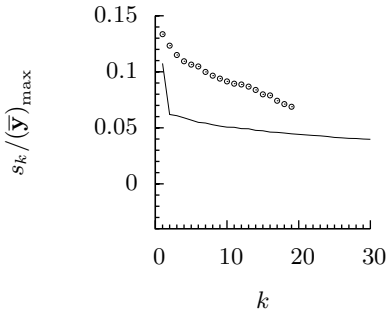

Figure 6.4: The noise's sample standard deviations s_k along the first few of its sample principal components, calculated from a set of replicate-experimental TAP pulse responses and rendered dimensionless by dividing by the peak $(\overline{\mathbf{y}})_{\max}$ of the average pulse response $\overline{\mathbf{y}}$. The full line connects the first thirty sample standard deviations calculated from a set of eight hundred replicates. The circles represent the nineteen sample standard deviations calculated from a reduced set of twenty replicates.

Fig. 6.4 shows the sample standard deviations along the first few sPCs. The data used stem from argon pulsed over quartz at room temperature. Hence, the experiment was non-reactive, so that the reactor bed was not affected by the gas pulses. This made it possible to collect a number of replicates as large as eight hundred, see the remark on catalytic experiments at the beginning of this section. Figs. 6.3 and 6.4 also show sPCs and sample standard deviations calculated from a reduced set of twenty replicates, a realistic number. The angle ψ calculated for the full set of 800 replicates was found to be 1.3°. This would perhaps be acceptable, but for the reduced set of twenty replicates, $\psi = 53°$. This is by all means unacceptable. Section 6.4 will show how preconditioning the data enables reduction of the information loss.

Data preconditioning

On the basis of replicates, Section 6.4 presented the sPCA as a way to decorrelate the experimental data. This was at the expense of a dimensionality reduction. The coordinate system constituted by the sPCs $\hat{\mathbf{u}}_{e,v,1}$, $\hat{\mathbf{u}}_{e,v,2}$, $\ldots$, $\hat{\mathbf{u}}_{e,v,n_{r,e}-1}$ was found unable to describe the time series well, resulting in a serious loss of experimental information at sPCA. Compare the sPCs calculated for a set of replicate TAP pulse responses, shown in Fig. 6.3, with one of these responses depicted in Fig. 6.1. While the pulse response shows a relatively slow variation, the sPCs show very

fast random fluctuations. This is probably a general feature. It is no surprise that the coordinate system constituted by the sPCs is unable to give a good representation of the (average) pulse response. A better result would be obtained if the sPCs were smoother. This can be achieved by transforming the original time series so that their noise, although still random, becomes smoother. To this end, the experimental time series will be submitted to an extra conditioning transformation before least-squares regression.

Observe that *any* linear transformation preserves the fulfillment of the Conditions 6.2, 6.3 and 6.4 (Assumptions 6.1 and 6.3). It is therefore allowed to transform linearly the time series, before performing a sPCA and rescaling in fulfillment of Conditions 6.5 and 6.6. Indeed, say $\mathbf{T}$ is a nonsingular $n_t \times n_t$ matrix. Then $\mathbf{T}\mathbf{y}_{e,v}$ contains all the information of $\mathbf{y}_{e,v}$. Instead of regressing the $\overline{\mathbf{y}}'''_{e,v}$, defined by Eq. (6.42), with $\mathbf{f}'''_v(\boldsymbol{\xi}_e, \mathbf{b})$ from Eq. (6.46), vectors

$$\overline{\mathbf{y}}'''_{e,v,\mathbf{T}} = \sqrt{n_{r,e} - 1}\, \hat{\boldsymbol{\Lambda}}^{-1/2}_{e,v,\mathbf{T}} \cdot \hat{\mathbf{U}}^{T}_{e,v,\mathbf{T}} \cdot \mathbf{T} \cdot \overline{\mathbf{y}}_{e,v} \tag{6.49}$$

can just as well be regressed with

$$\mathbf{f}'''_{v,\mathbf{T}}(\boldsymbol{\xi}_e, \mathbf{b}) = \sqrt{n_{r,e} - 1}\, \hat{\boldsymbol{\Lambda}}^{-1/2}_{e,v,\mathbf{T}} \cdot \hat{\mathbf{U}}^{T}_{e,v,\mathbf{T}} \cdot \mathbf{T} \cdot \mathbf{f}_v(\boldsymbol{\xi}_e, \mathbf{b}). \tag{6.50}$$

In the latter two expressions, a subscript $\mathbf{T}$ has been added to the matrices $\hat{\mathbf{U}}_{e,\,v}$ and $\hat{\boldsymbol{\Lambda}}_{e,\,v}$ to indicate that an eigendecomposition is performed of $\hat{\mathbf{V}}(\mathbf{T}\boldsymbol{\epsilon}_{e,v})$ instead of $\hat{\mathbf{V}}(\boldsymbol{\epsilon}_{e,v})$, so that $\hat{\mathbf{U}}_{e,v,\mathbf{T}}$ and $\hat{\boldsymbol{\Lambda}}_{e,v,\mathbf{T}}$ indeed depend on $\mathbf{T}$. Many matrices $\mathbf{T}$ have the desired smoothing effect on the noise. As an example, the lower triangular matrix,

$$\mathbf{T} = \begin{bmatrix} 1 & 0 & \cdots & 0 \\ 1 & 1 & \cdots & 0 \\ \vdots & \vdots & & \vdots \\ 1 & 1 & \cdots & 1 \end{bmatrix} \Delta t, \tag{6.51}$$

involves the replacement of each sample $y(t_j)$ in the time series by the *Riemann sum* $\sum_{k=1}^{j} y(t_k)\Delta t$ of the preceding samples and itself.

Fig. 6.5 shows the average $\overline{\mathbf{y}}$ of the eight hundred Ar pulse responses used in Section 6.4, and its Riemann cumulative $\mathbf{T} \cdot \overline{\mathbf{y}}$. Still for the same set of experimental data, Fig. 6.6, analogous to Fig. 6.3, visualizes the first four sPCs of the transformed pulse responses. Fig. 6.7, analogous to Fig. 6.4, shows the sample standard deviations along the first few sPCs. As desired, the sPCs are smoother. This was explained intuitively at the beginning of this section, but there is also a mathematical explanation. The linear transformation $\mathbf{T}$ renders the unknown population variance

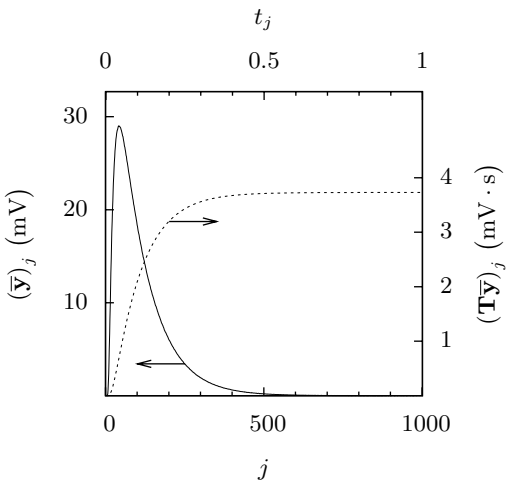

Figure 6.5: Average pulse response $\overline{\mathbf{y}}$ of a set of eight hundred replicated pulse responses and its Riemann cumulative $\mathbf{T}\cdot\overline{\mathbf{y}}$. The subscript j in $(\overline{\mathbf{y}})_j$ and $(\mathbf{T}\cdot\overline{\mathbf{y}})_j$ refers to the jth element of both vectors.

matrix near-singular in such a way that the population standard deviations along the latter $n_t-(n_{r,e}-1)$ pPCs, $\sigma_{n_{r,e}}$, $\sigma_{n_{r,e}+1}$, $\ldots$, σ_{n_t}, become negligible. As a consequence, the sPCs and the corresponding standard deviations can be considered nearly unbiased estimates of the pPCs and the corresponding standard deviations. The pPCs are generally smooth and hence so are their estimates, the sPCs, apart from their random part. That the sPCs and the corresponding standard deviations indeed evolve to the smooth pPCs and the corresponding standard deviations is apparent in Fig. 6.6 and Fig. 6.7. As intended, the relative smoothness of the sPCs causes a better alignment of the space $\mathscr{S}$ they span and the experimental data $\mathbf{y}$. This is illustrated by the angle ψ which is $0.0022°$ for the complete data set of eight hundred replicates and still $0.47°$ for the reduced set of twenty replicates.

The regression of $\overline{\mathbf{y}}'''_{\mathbf{T}}$, composite vector of the $\overline{\mathbf{y}}'''_{e,v,\mathbf{T}}$ with $\mathbf{f}'''_{\mathbf{T}}(\mathbf{b})$, composite of the $\mathbf{f}'''_{v,\mathbf{T}}(\boldsymbol{\xi}_e,\mathbf{b})$ with a suitable $\mathbf{T}$ will be called *second-order statistical regression* (SOSR). Fig. 6.8 gives a summarizing overview.

Fig. 6.7 illustrates that the sample standard deviation along the successive sPCs drops to zero very quickly. This means that the first few of them already account for most of the variability of the noise. In some cases, a physical meaning can be attributed to one or more of the principal components. For example, comparison of Fig. 6.6 (a) with Fig. 6.5 shows that the first sPC, in particular, assumes the shape of the Riemann-

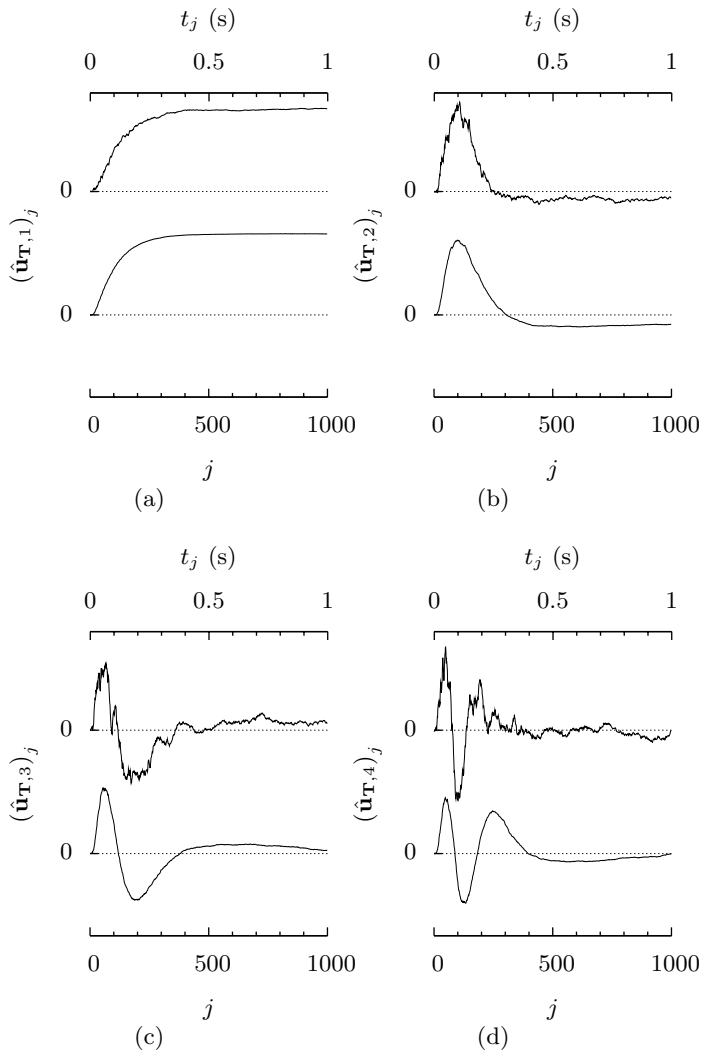

Figure 6.6: The first (a), second (b), third (c) and fourth (d) sample principal noise component of the Riemann cumulative of an experimental TAP pulse response. $(\hat{\mathbf{u}}_{\mathbf{T},k})_j$ refers to the jth element of the kth sample principal component $\hat{\mathbf{u}}_{\mathbf{T},k}$. The lower graphs show the sample principal components estimated from eight hundred replicates. The upper graphs show those estimated from twenty replicates.

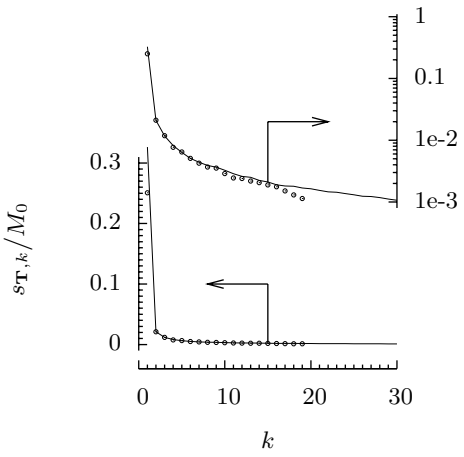

Figure 6.7: The sample standard deviations $s_{\mathbf{T},k}$ along the first few sample principal components of the noise in the Riemann cumulative $\mathbf{T}\cdot\overline{\mathbf{y}}$ of an experimental argon TAP pulse response. They were estimated from a set of replicates and rendered dimensionless by dividing by $M_0 = (\mathbf{T}\cdot\overline{\mathbf{y}})_{n_t} = \Delta t \cdot \sum_{j=1}^{n_t}(\overline{\mathbf{y}})_j$, the zeroth moment of the average. In both the linear and the semilogarithmic plot, the full line connects the first thirty standard deviations calculated from a set of eight hundred replicate-experimental pulse responses. The circles represent the nineteen standard deviations calculated from a reduced set of twenty replicates.

cumulated pulse response itself. Accordingly, the first sPC shown in Fig. 6.3 (a), assumes the shape of the pulse response itself. These observations show that the most important variability in the pulse responses is in their size and not so much in their shape. This is rooted in the experimental hardware, the size of the TAP inlet pulse being poorly reproducible. The pulse size is proportional to the zeroth moment the average pulse response, which is

$$M_0 = \Delta t \cdot \sum_{j=1}^{n_t}(\overline{\mathbf{y}})_j = (\mathbf{T}\cdot\overline{\mathbf{y}})_{n_t}, \tag{6.52}$$

where $(\mathbf{T}\cdot\overline{\mathbf{y}})_{n_t}$ is the n_tth component of vector $\mathbf{T}\cdot\overline{\mathbf{y}}$ with $\mathbf{T}$ chosen as in Eq. (6.51). M_0's standard deviation relates to the standard deviation $s_{\mathbf{T},1}$ corresponding to the first sPC as

$$s_{M_0} = s_{\mathbf{T},1}(\hat{\mathbf{u}}_{\mathbf{T},1})_{n_t}. \tag{6.53}$$

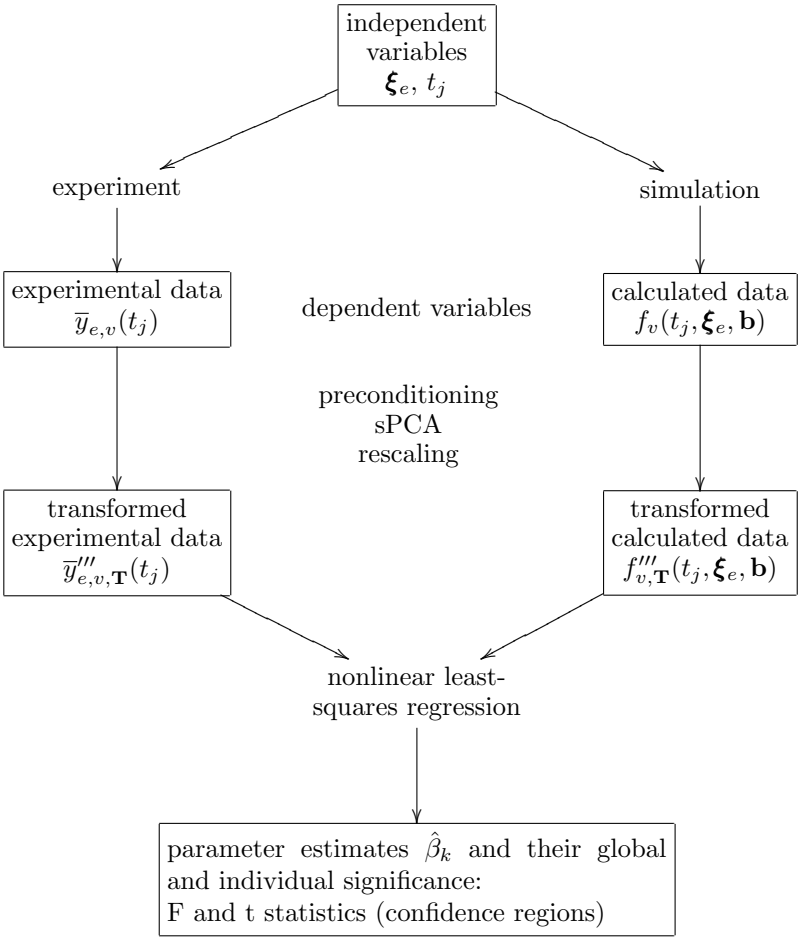

Figure 6.8: Overall scheme of the second-order statistical regression (SOSR) approach as a means to estimate physico-chemical parameters from transient kinetic data. SOSR performs a nonlinear least-squares (NLSQ) regression of linearly transformed data. The idea of the three-part transformation is to fulfill certain conditions for NLSQ regression as best as possible. It is inferred from replicate-experimental time series.

The relative error of M_0 and therefore also of the pulse size is quantified here as

$$\frac{s_{M_0}}{M_0} \approx 1.13\,\% \tag{6.54}$$

using Eqs. (6.52) and (6.53) for the full set of eight hundred replicates. This is a typical number, see Chapter 5 and (Gleaves et al., 1997).

The ordinary NLSQ regression as well as the SOSR were implemented in the program TAPFIT, see Appendix D.

6.5 Validation of the second-order statistical regression

Numerical experiment

The theory presented above was tested with a numerical experiment. A realistic TAP-experiment was simulated using TAPFIT. Numerical integration occurred by the transfer matrix approach, see Section 4.4. The simulation was performed assuming an inert species A was pulsed in a 3 cm long TAP-reactor filled with an inert packing at a constant, unspecified temperature, $n_e = 1$. As only species A is to be monitored: $n_v = 1$. The only model parameter is the effective Knudsen diffusivity $\mathscr{D}_e$ of A through the reactor tube. A simulation was carried out with a realistic value of $2 \cdot 10^{-3}\,\mathrm{m^2/s}$ for $\mathscr{D}_e$. The pulse response calculated from this simulation, was hereupon subjected four hundred times to artificial TAP-noise with some typical characteristics, see Chapter 5:

1. A normally distributed variability of the zeroth moment with relative standard deviation of 5 %.

2. Oscillatory noise with a frequency of 50 Hz and a time-varying amplitude of 2 % of the calculated response signal strength. For each pulse response, the initial phase was chosen between 0 and $2\,\pi$ in a uniformly random way.

3. Ornstein-Uhlenbeck noise, also called Gauss-Markov noise, with a correlation time of 0.789 ms. The standard deviation was taken partly constant (0.5 % of the response maximum), and partly proportional (5 %) to the signal strength.

The set of four hundred pulse responses was divided in twenty groups of twenty. Each of these were used to estimate $\mathscr{D}_e$ by regression. This was done twice each time: once by NLSQ regression of the average pulse response and once by SOSR. Conditions 6.1, 6.2 and 6.3 presented in Section 6.2 are fulfilled by construction. Hence, the artificial TAP pulse

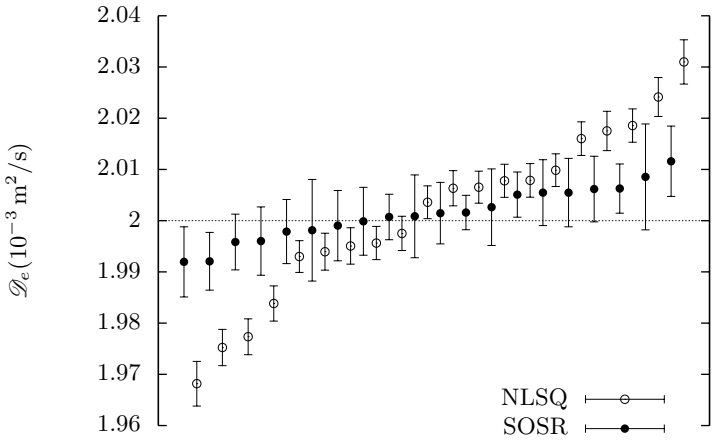

Figure 6.9: 95 % confidence intervals for the Knudsen diffusivity $\mathscr{D}_e$ estimated by NLSQ regression and SOSR, ranked from low to high. The data used were groups of twenty artificial TAP pulse responses, calculated from a model with $\mathscr{D}_e = 2 \cdot 10^{-3}\,\mathrm{m}^2/\mathrm{s}$, with typical noise superposed.

responses are consistent with Assumption 6.1. The responses were also constructed to be consistent with Assumption 6.2.

Fig. 6.9 shows the 95 % confidence intervals obtained for $\mathscr{D}_e$. In the case of the NLSQ regression, the true value lies within the confidence interval only once. In the case of the new regression, this number increases to fifteen. With a confidence limit of 95 %, the true value would be expected to lie in the confidence interval in nineteen out of twenty cases. That a similar number is not attained even with the new regression approach, can be understood because a number of replicates as small as twenty gives rise to imperfect second-order statistical estimates. The sPCs inherit to a certain extent the randomness of the data set and are thus not able to fulfill Conditions 6.5 and 6.6 perfectly, see Sections 6.4 and 6.4. Note that the confidence intervals aside, the parameter estimates themselves are more accurate with the new regression approach than with the classical NLSQ regression.

Fig. 6.10 shows the ranked parameter estimates in a normal probability graph. The fraction of estimates that fall below values indicated on the x-axis are presented on the y-axis. The y-axis has a normal probability scaling. If the estimates are normally distributed around the true value, a straight line through the point $(2 \cdot 10^{-3}\,\mathrm{m}^2/\mathrm{s}, 50\,\%)$ is expected. This is more or less the case for both regression approaches, which is in

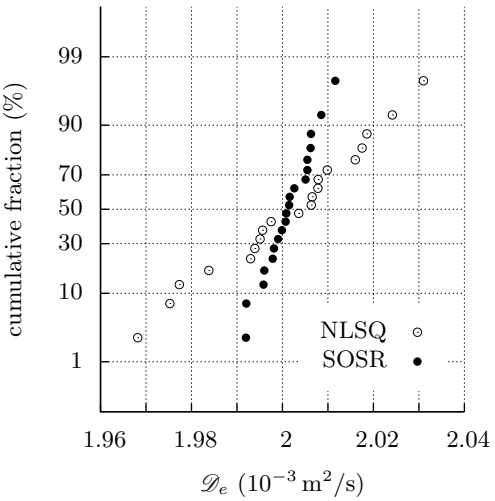

Figure 6.10: Normal probability graph of estimates of the Knudsen diffusivity $\mathscr{D}_e$, obtained by regression of different statistically homogeneous artificial TAP data sets. The fraction of estimates that fall below values indicated on the x-axis are presented on the y-axis, which has a normal probability scaling. If the estimates are normally distributed around the true value, straight lines through the point ($2 \cdot 10^{-3}$ m^2/s, 50 %) are expected.

conformity with Property F.1, see p. 189.

Regression of experimental TAP-data

Irreversible adsorption of oxygen on a V_2O_5 based catalyst

A TAP-experiment was performed to study the model V150 catalyst (Poelman et al., 2007): $V_2O_5|SiO_2$–ZrO_2. Oxygen was pulsed over a three-zone-TAP-reactor at 773 K. The diameter of the reactor tube was 5 mm. A 4.0 mm long catalytic bed was sandwiched between two inert zones filled with quartz beads. The one at the inlet was 4.4 mm long, the one at the outlet 20.0 mm. The interparticle porosity was assumed equal in all zones, because the inert and catalyst particles had the same size (diameters of 250 to 425 µm). It was estimated at 0.53. The total catalyst mass was 189 mg. Twenty replicate oxygen pulse responses were collected after reduction of the catalyst surface. The responses were baseline-corrected. The position of the baseline was estimated as the horizontal asymptote of a descending exponential fitted through the last

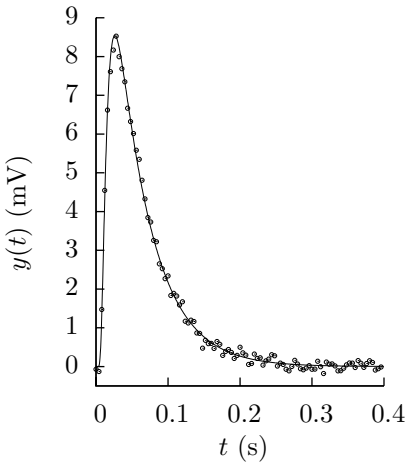

Figure 6.11: The average of twenty replicate-experimental oxygen pulse responses over a three-zone-TAP-reactor with central V_2O_5/SiO_2 catalytic zone and the model-calculated analogue resulting from SOSR. Only one tenth of the experimental points were shown for the sake of clarity. The TAP reactor model used assumes irreversible adsorption of oxygen on the catalyst.

400 samples, see Section 5.4. The calibration coefficient was estimated at $9.9 \cdot 10^5$ V·s/mol.

The interaction between oxygen and the catalyst was modeled as simple irreversible adsorption. The kinetics of this adsorption are pseudomonomolecular in oxygen, with a specific adsorption rate r in mol/kg·s, expressed as

$$r = kc_{O_2}, \tag{6.55}$$

where k is the specific adsorption rate coefficient in m^3/kg·s and c_{O_2} the concentration of oxygen in the interparticle pores, in mol/m^3.

Using the program TAPFIT, the oxygen pulse responses were regressed with responses calculated using the transfer matrix approach, once by NLSQ regression of the average pulse response and once by SOSR. Aside from the kinetic parameter k, two physical parameters were estimated: the average oxygen pulse size n_{O_2} and the Knudsen diffusion coefficient $\mathscr{D}_{e,O_2}$ through the reactor bed. Knudsen diffusion is indeed expected to proceed at an equal speed in all three zones as both the catalytic and inert particles were nonporous and had the same size.

Differences between the pulse responses calculated from direct NLSQ regression and SOSR are hardly observable. Therefore, only the latter is shown in Fig. 6.11. However, there is quite some difference in the corre-

Table 6.1: Parameter estimates and approximate individual 95% probability level confidence limits by regression of a set of twenty replicate-experimental oxygen TAP pulse responses. The regression was carried out by NLSQ regression, and by SOSR.

	NLSQ	SOSR
k ($10^{-3}\,\mathrm{m^3/kg{\cdot}s}$)	4.724 ± 0.212	5.676 ± 0.602
$\mathscr{D}_{e,\,\mathrm{O_2}}$ ($10^{-3}\,\mathrm{m^2/s}$)	2.586 ± 0.019	2.502 ± 0.059
$n_{\mathrm{O_2}}$ (nmol)	0.851 ± 0.011	0.903 ± 0.045

sponding parameter estimates, which are displayed in Table 6.1. SOSR applies a transformation to fulfill the conditions for the subsequent NLSQ regression. Therefore, the parameter estimates from SOSR are more reliable than those obtained from direct NLSQ regression. The same is true a fortiori for the statistics accompanying the parameter estimates: the width of the parameter confidence intervals. Indeed, no meaning should be attached to these statistics if they are supplied by the direct NLSQ regression. In the latter case, the confidence intervals are narrower, which is misleading.

For the sake of completeness, Table 6.2 displays the estimates of the binary correlation coefficients $\rho\big(\hat{\beta}_j, \hat{\beta}_k\big)$ between the parameter estimates resulting from SOSR:

$$\rho\big(\hat{\beta}_j, \hat{\beta}_k\big) = \mathrm{cov}\big(\hat{\beta}_j, \hat{\beta}_k\big) \Big/ \sqrt{\mathrm{var}\big(\hat{\beta}_j\big) \cdot \mathrm{var}\big(\hat{\beta}_k\big)}. \tag{6.56}$$

They follow directly from the estimated variance matrix $\hat{\mathbf{V}}\big(\hat{\boldsymbol{\beta}}\big)$, see Eq. (F.9) in Appendix F. The estimated binary correlation coefficients all are between -0.9 and 0.9. Such mild correlations would certainly be unattainable from stationary experiments. k is actually the only parameter of interest. Its estimate is most correlated with the Knudsen diffusivity $\mathscr{D}_{e,\mathrm{O_2}}$, which indicates that if the latter would be known in advance, a narrower confidence interval would be obtained for k. At the same time however, it is clear that the value assumed for $\mathscr{D}_{e,\mathrm{O_2}}$ should be accurate, since it strongly affects the estimate for k. In general, an accurate independent determination of the physical parameters $\mathscr{D}_{e,\mathrm{O_2}}$ and $n_{\mathrm{O_2}}$ is advisable.

Interaction of propane with a CuO–CeO_2 catalyst

CuO–$CeO_2/\gamma{-}Al_2O_3$ was studied as a total oxidation catalyst for volatile organic compounds (VOCs). Propane, chosen as model VOC, was pulsed over a three-zone-TAP-reactor at 773 K. Part of the propane reacts with

Table 6.2: Estimates of the binary correlation coefficients ρ between the parameter estimates obtained by SOSR of twenty replicate-experimental oxygen TAP pulse responses.

	k	$\mathscr{D}_{e,\mathrm{O_2}}$	$n_{\mathrm{O_2}}$
k	1	−0.86	0.80
$\mathscr{D}_{e,\mathrm{O_2}}$		1	−0.85
$n_{\mathrm{O_2}}$			1

the catalyst surface oxygen to form carbon dioxide and water. The first and third zones contained quartz beads and had a length of 2.5 mm and 25.0 mm. The central zone contained 48.6 mg of catalyst and was 3.6 mm long. The interparticle porosity of all zones was 0.53. Ten replicate propane pulse responses were collected after oxidation of the catalyst surface. One thousand samples were collected for each, applying a sampling interval of 1 ms. The propane pulse responses were submitted to baseline-correction before regression. The position of the baseline was estimated as the average of the last 500 samples, which were collected after extinction of the response. The calibration coefficient for propane was $4.6 \cdot 10^5$ V·s/mol.

The interaction between propane and the catalyst was found to be modeled well by reversible adsorption followed by an irreversible surface reaction. Schematically:

$$\mathrm{C_3H_8} + * \overset{1}{\leftrightarrows} \mathrm{C_3H_8^*} \tag{6.57a}$$

$$\mathrm{C_3H_8^*} \overset{2}{\rightarrow} \ldots, \tag{6.57b}$$

The oxidation steps following the latter do not affect the propane response. Adsorption (6.57a) is pseudomonomolecular in propane, because the pulsed quantity of propane is assumed negligible with respect to the number of active sites $*$. The specific rates r_{+1} and r_{-1} of propane adsorption and desorption (6.57a), and r_2 of reaction (6.57b), all in mol/kg·s, are expressed as

$$r_{+1} = k_{+1}\, c_{\mathrm{C_3H_8}}, \tag{6.58a}$$

$$r_{-1} = k_{-1}\, c_{\mathrm{C_3H_8^*}}, \tag{6.58b}$$

$$r_2 = k_2\, c_{\mathrm{C_3H_8^*}}, \tag{6.58c}$$

where $c_{\mathrm{C_3H_8}}$ is the concentration of propane, in mol/m^3, and $c_{\mathrm{C_3H_8^*}}$ the quantity of propane reversibly adsorbed per unit mass of catalyst, in

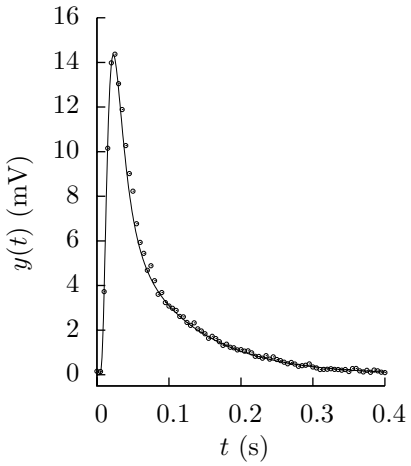

Figure 6.12: The average of ten replicate-experimental propane pulse responses over a three-zone-TAP-reactor with central CuO–CeO_2 catalytic zone and model-calculated analogue resulting from SOSR. For the sake of clarity, only one fifth of the experimental points are shown. The interaction of propane with the catalyst is modeled as reversible adsorption followed by an irreversible surface reaction.

mol/kg. The adsorption rate coefficient k_{+1} is in m^3/kg·s. The rate coefficients k_{-1} and k_2 are in Hz. All three rate coefficients were estimated by regression. The former example revealed that the simultaneous estimation of unknown physical variables has a negative effect on the width of the confidence intervals of the chemical parameters. Therefore, the (average) quantity of propane pulsed and the effective Knudsen diffusion coefficient were determined independently, by pulsing propane diluted with inert (90 mol% propane, 10 mol% krypton) instead of pure propane. The responses to propane were collected in alternation with responses to krypton. The zeroth moment of the average krypton response, together with the known composition of the feed mixture, allowed to determine the total quantity of propane pulsed as 8.40 nmol. The effective diffusivity of krypton was estimated at $2.33 \cdot 10^{-3}\,m^2/s$. After a correction for the difference in molecular mass, see Eq. (4.3), the effective diffusivity of propane was obtained as $3.21 \cdot 10^{-3}\,m^2/s$.

Fig. 6.12 shows the average of the ten propane pulse responses and the corresponding SOSR-fitted model-calculated response. The NLSQ-fitted pulse response is not depicted as it is again hardly distinguishable from the SOSR-fitted response. The parameter estimates resulting from

Table 6.3: Parameter estimates and approximate individual 95% probability level confidence limits by regression of a set of ten replicate-experimental propane TAP pulse responses. The regression was carried out by NLSQ regression, and by SOSR.

	NLSQ	SOSR
k_{+1} (10^{-3} m^3/kg·s)	354 ± 2	356 ± 126
k_{-1} (Hz)	17.8 ± 0.3	15.5 ± 2.2
k_2 (Hz)	11.0 ± 0.2	9.99 ± 0.52

Table 6.4: Estimates of the binary correlation coefficients ρ between the parameter estimates obtained by SOSR of ten replicate-experimental propane TAP pulse responses.

	k_{+1}	k_{-1}	k_2
k_{+1}	1	0.81	0.46
k_{-1}		1	0.76
k_2			1

both regressions are shown in Table 6.3. Again, the confidence intervals obtained from SOSR are wider than those from NLSQ regression. This shows again that the confidence intervals from NLSQ regression can mislead the experimentalist if the Conditions 6.1 to 6.6 are not fulfilled.

Finally, Table 6.4 displays the binary correlation coefficients of the parameters estimated by SOSR. The correlations are again rather mild. As was already pointed out in the former example, this is due to the transient nature of the experiment.

6.6 Conclusions

A sample principal component analysis (sPCA) of replicate data has lead to a maximum-likelihood parameter regression technique with higher accuracy for both the estimates and the corresponding statistics. The SOSR technique allows to relax several of the assumptions that underlie the classic regression techniques, in particular the assumptions of whiteness and homoskedasticity.

The proposed technique can be applied in a straightforward way to time series related to chemical reaction kinetics or other physico-chemical phenomena. Although based on second-order statistics, i.e., covariances,

the procedure does not require the explicit calculation of the latter and is not computationally demanding.

Even in the ideal case where noise is absent, regression does not always allow the estimation of kinetic parameters. This will be explained in Chapter 7.

Chapter 7

Identifiability of Rate Coefficients from Isothermal Transient Linear Kinetics

7.1 Introduction

Suppose a series of isothermal transient experiments is carried out to study a reaction with known reaction network. Based on the experimental results, it is not always possible to identify all rate coefficients uniquely. Typically, reaction intermediates are unobserved, especially surface species in heterogeneous catalysis. The risk of unidentifiability then becomes important, although it exists even if all component concentrations are measured and recorded (Craciun and Pantea, 2008). Furthermore, the risk of unidentifiability is typical for reaction networks consisting only of pseudomonomolecular elementary steps. As an illustration, while there are plenty of reasonable and simple examples of unidentifiability for pseudomonomolecular reaction networks, Vajda and Rabitz (1994) found none for networks with essential multimolecular steps. This chapter is devoted to pseudomonomolecular reaction networks. It contains the main results of Roelant et al. (2010).

Section 7.2 will introduce the necessary terminology. Section 7.3 will present a necessary condition for identifiability of the apparent rate coefficients. This amounts to a test, which can be readily carried out after visual inspection of the reaction network. The theoretical background of this test is supplied by the generic results of Chapter 3. The test will be applied to an experimental case: the interaction of propane with a CuO–CeO_2 catalyst.

7.2 Definitions

Consider an experimental reactor under transient operation. Suppose certain pseudomonomolecular elementary steps proceed, the apparent rate coefficients of which are to be investigated for identifiability. The set S of these steps is a pseudomonomolecular reaction network. Recall from Chapter 2 that the kinetics of such a reaction network can usually be described by a compartmental model (2.7), where the matrix $\mathbf{K}$ is of the form (2.6). Such a model is represented by a reaction graph in which each vertex represents a component. Some vertices represent an input as there is a net source of the component they represent. Some vertices represent an output as the concentration of their component is (indirectly) measured. Let the values of the selected rate coefficients be collected in a vector $\mathbf{b}$. Then the complete influence of $\mathbf{b}$ on the measurement is concentrated in the input-output mapping $\mathcal{M}(\mathbf{b})$, defined by Eq. (3.11) for a uniform and time-isothermal open system. If $\mathbf{b}$ is replaced by another vector $\mathbf{b}^*$, so that $\mathcal{M}(\mathbf{b}^*) = \mathcal{M}(\mathbf{b})$, then the measurements will not be affected. Hence $\mathbf{b}$ and $\mathbf{b}^*$ will be indistinguishable. Let B be the set in which $\mathbf{b}$ takes its values and let $S_{\mathbf{b}}$ be the set of parameter vectors indistinguishable from $\mathbf{b}$:

$$S_{\mathbf{b}} = \{\mathbf{b}^* \in B \,|\, \mathcal{M}(\mathbf{b}^*) = \mathcal{M}(\mathbf{b})\}. \tag{7.1}$$

Definition 7.1 (structural identifiability)**.** If, for almost any value of $\mathbf{b} \in B$, $S_{\mathbf{b}}$ reduces to the singleton $\{\mathbf{b}\}$, the set K of apparent rate coefficients is *structurally globally identifiable*. If $S_{\mathbf{b}}$ is denumerable (usually finite), K is *structurally locally identifiable*. If $S_{\mathbf{b}}$ is not denumerable, K is *unidentifiable*.

In heterogeneous catalysis, the surface intermediates are typically unobserved, so that there are few observed concentrations c_j (outputs). There are also few components for which there is a net source u_k (inputs). Indeed, net mass transfer of surface components, possible only by surface diffusion across the boundary of the system, is typically negligible. This does not mean that surface diffusion as such is negligible. In fact, net diffusion can also be negligible if its time scale is small enough compared to the time scale of reaction for the surface concentrations to become uniform. This makes heterogeneous catalytic reaction networks especially vulnerable to structural unidentifiability.

The assessment of structural identifiability of a (generally nonlinear) model is very closely related to the assessment of distinguishability of different models. Tests for both properties have been proposed over the last decades by authors active in multiple pure and applied scientific domains (Walter and Pronzato, 1996). Which of the different approaches is more

efficient depends on the nature of the problem. Some experience helps to make an appropriate choice. The mathematical manipulations often get intricate, and success is not guaranteed, even for linear models. These problems restrain most experimentalists from carrying out an a priori, i.e., before processing any experimental data, identifiability assessment of assumed reaction networks. This involves the risk that incorrect estimates of rate coefficients, obtained by least-squares regression of experimental data, for example, are taken for granted. As was already mentioned, this risk is higher for pseudomonomolecular reaction networks. However, it will be shown that for this class of networks, many conclusions regarding at least structural local identifiability can be drawn from visual inspection. If a reaction network is structurally locally identifiable, it is possible in principle to estimate all rate coefficients as long as the initial estimates are close enough to their real unknown values. Compared to the already existing tests, some unidentifiability detection power is given up in return for a more straightforward application. The framework is deterministic, which means that the structural identifiability is studied under the assumption of ideal experimental conditions, in absence of experimental errors.

Common approaches to assess the structural identifiability of a linear reaction network are the *similarity transformation* and the *Laplace transform* approaches (Vajda and Rabitz, 1988; Walter et al., 1989). The *differential algebra* approach applied by Asadullin et al. (1996) differs only formally from the Laplace transform approach. The Laplace transform approach is especially suited for catalytic reaction networks, where there are few inputs and outputs and many nonexistent reactions between the components (Happel et al., 1986a).

7.3 Structural local identifiability of reaction networks

General

Consider a pseudomonomolecular reaction network S. Suppose the structural local identifiability of its set K of apparent rate coefficients is to be investigated. Whether or not this is the case depends on the input-output mapping $\mathcal{M}$, see Section 3.3. Inspection of Eq. (3.11) reveals that $\mathcal{M}$ is influenced by the vector $\mathbf{b}$ of rate coefficients only through the transfer matrix $\mathbf{H}$. The influence is exerted more specifically through the coefficients α_k and β_k appearing in its elements, see Eq. (3.26). In this section, a necessary condition will be formulated for the structural local identifiability of K. α_k and β_k depend on $\mathbf{b}$ in a way which can be

found analytically, by application of Eq. (3.9), or graph-theoretically, by application of Theorem 3.1, see p. 22. However, to evaluate the necessary condition for local identifiability, it will suffice to know their number and some readily derived dependences existing among them. Proceed as follows:

1. Apply Theorem 3.2, see p. 23, to find the symbolic form of all kinetic transfer functions, elements of the kinetic transfer matrix $\mathbf{H}$.

2. Taking into account Theorem 3.3 on p. 26, list all different coefficients α_k and β_k which are not identical to 0 or 1.

3. Whenever there is a linear dependence among certain coefficients, as revealed by Theorem 3.4 on p. 26, remove one of them. The remaining coefficients will be referred to as the (*moment*) *invariants*, and can be stacked in a vector $\mathbf{\Phi}(\mathbf{b})$ (Berman and Schoenfeld, 1956; Vajda and Rabitz, 1988).

As the measurements are not affected in any other way than through $\mathbf{\Phi}$, it is possible to state a more operational version of Eq. (7.1):

$$\mathcal{S}_{\mathbf{b}} = \{\mathbf{b}^* \in B \mid \mathbf{\Phi}(\mathbf{b}^*) = \mathbf{\Phi}(\mathbf{b})\}. \tag{7.2}$$

Whenever $\mathbf{\Phi}(\mathbf{b})$ contains fewer elements than $\mathbf{b}$ does, the number of elements of $\mathcal{S}_{\mathbf{b}}$ will be non-denumerable (Gorskii and Spivak, 1989). The set K of apparent rate coefficients is then structurally unidentifiable. This does not exclude that some, though not all the elements of $\mathbf{b}^*$ in $\mathcal{S}_{\mathbf{b}}$ still have a denumerable number of allowed values.

Theorem 7.1. *In order for a the set K of apparent rate coefficients to be structurally locally identifiable, there have to be at least as many invariants as rate coefficients.*

This provides a necessary condition for structural local identifiability.

Remark 7.1. As a special case, assume that in a reaction network S, there are a single input, a net source u_k of A_k, and a single output, a concentration c_j of A_j. In that case, the kinetic transfer matrix $\mathbf{H}$ reduces to a kinetic transfer function $H_{j,k}$. It can then be derived from the Theorems 3.2 and 3.4 that the number of invariants is equal to $2n-l$, $2n-l-1$ or $2n-l-2$, where l is the length of a shortest path from A_k to A_j. The role of l is counterintuitive: if the shortest paths traverses a smaller portion of the reaction network, the chance increases that the reaction network is structurally locally identifiable.

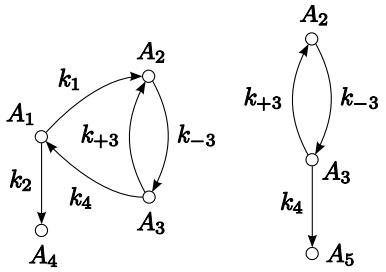

Figure 7.1: A reaction network $S = \{s_1,\, s_2,\, s_{+3},\, s_{-3},\, s_4\}$ (a) and the reduced network $S' = \{s_{+3},\, s_{-3},\, s_4\}$ (b). In the latter, A_5 is virtual.

In order to be certain that K is structurally locally identifiable, it should be verified nonetheless that the rank of the Jacobian

$$\mathbf{J} = \frac{\partial \mathbf{\Phi}}{\partial \mathbf{b}} \tag{7.3}$$

is in all except a denumerable number of vectors $\mathbf{b}$ of B equal to the number of rate coefficients. In order to establish whether a reaction network is structurally globally identifiable, the set of polynomial equations in Eq. (7.2) has to be solved by elimination theory, see Walter and Lecourtier (1982); Raksanyi et al. (1985); Asadullin et al. (1996). This is often marked by difficulties. Most importantly, it is difficult to reach a conclusion as the number of solutions often depends on the value of $\mathbf{b}$. Recently, Walter et al. (2004) and Lagrange et al. (2008) applied interval analysis (Jaulin et al., 2001) as numerical alternatives. However, these methods are limited to bounded sets B. Even if the reaction network can be proven to be structurally globally identifiable, there is still a risk that some rate coefficients are *practically* unidentifiable, due to experimental errors, however small they may be. Practical unidentifiability cannot be revealed a priori and may even remain hidden after parameter estimation.

Example

Consider the reaction network $S = \{s_1,\, s_2,\, s_{+3},\, s_{-3},\, s_4\}$ depicted in Fig. 7.1 (a). Assume there is a source only of A_1 and the concentration c_4 of A_4 is the only (indirect) observation. Then the kinetic transfer matrix $\mathbf{H}$ reduces to the transfer function $H_{4,1}$. From Theorem 3.2, it is found that the symbolic form of this transfer function is given by

$$H_{4,1}(s) = \frac{\beta_2 s^2 + \beta_1 s + \beta_0}{s^4 + \alpha_3 s^3 + \alpha_2 s^2 + \alpha_1 s}. \tag{7.4}$$

Moreover, application of Theorem 3.4 yields

$$\lim_{s\to 0} sH_{4,1}(s) = \frac{\beta_0}{\alpha_1} = 1 \tag{7.5}$$

so that $\beta_0 = \alpha_1$. The vector of invariants is therefore

$$\mathbf{\Phi} = \begin{bmatrix}\alpha_1 & \alpha_2 & \alpha_3 & \beta_1 & \beta_2\end{bmatrix}^T. \tag{7.6}$$

In this case, there as many rate coefficients as invariants. There is therefore no reason to assume that $K = \{k_1, k_2, k_{+3}, k_{-3}, k_4\}$ is structurally locally unidentifiable.

However, consider the reduced reaction network $S' = \{s_{+3}, s_{-3}, s_4\}$, for which the reaction graph is shown in Fig. 7.1 (b). The virtual component A_5 is 'observed'[1]. There is a source u_2 of A_2, as a result of conversion of A_1 through step s_1. Again, the transfer matrix reduces to a transfer function, $H_{5,2}$. According to Theorem 3.2, its symbolic form is given by

$$H_{5,2}(s) = \frac{\beta_0}{s^3 + \alpha_2 s^2 + \alpha_1 s}, \tag{7.7}$$

where again, as a consequence of Theorem 3.4, $\beta_0 = \alpha_1$. This time, there are two invariants, α_1 and α_2, while there are three unknown rate coefficients, k_{+3}, k_{-3} and k_4. It can therefore be concluded that the rate coefficients of S' are structurally locally unidentifiable. Of course this also means that the rate coefficients of S are also unidentifiable, although this was not revealed by the first identifiability test.

General guideline

Suppose a reaction network S (a set of elementary steps) is to be investigated for structural local identifiability of its apparent rate coefficients. As the previous example illustrates, to obtain the maximum unidentifiability detection power out of Theorem 3.2, it should be applied to each subnetwork (subset of elementary steps). Suppose that such a subnetwork consists of a number of linkage classes. Then it is clear that these linkage classes can be separately subjected to Theorem 3.2. This theorem therefore only has to be applied to linked subnetworks. For a larger reaction network, this can be a tedious task. Some experience helps to reduce the load, but, more importantly, the tests can be limited those subnetworks of which the rate coefficients are most likely to be unidentifiable. These typically have a single input and a single output, so that the

[1] The rate of step s_4 is observed indirectly as it leads to A_4 in the greater reaction network. The concentration c_5 of the virtual component A_5 reflects this rate and is therefore observed indirectly.

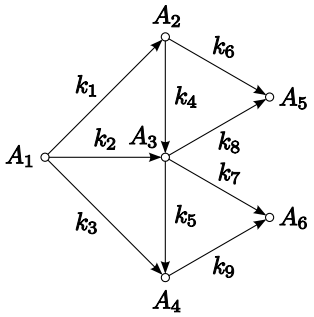

Figure 7.2: A reaction graph.

kinetic transfer matrix reduces to a scalar, and a relatively large amount of steps. Reaction network S' in Fig. 7.1 (b) is an example.

Limitations of the approach

As it was mentioned in Section 7.2, the approach presented here, as opposed to others, can be applied upon simple visual inspection. It does not however have the same unidentifiability detection power. This can be illustrated by means of an example, where the approach presented here fails to reveal structural local unidentifiability, while investigation of the Jacobian (7.3) does. Consider the reaction network $S = \{s_1, s_2, s_3, \ldots, s_9\}$ of which the reaction graph is shown in Fig. 7.2. Suppose there is a source only of A_1, and observations (direct or indirect) of the concentration of A_5 and A_6. The kinetic transfer matrix for S is then given by

$$\mathbf{H}(s) = \begin{bmatrix} H_{5,1}(s) \\ H_{6,1}(s) \end{bmatrix}. \tag{7.8}$$

Application of Theorem 3.2, yields

$$H_{5,1}(s) = \frac{\beta_1 s + \beta_0}{s^4 + \alpha_3 s^3 + \alpha_2 s^2 + \alpha_1 s} \tag{7.9}$$

$$H_{6,1}(s) = \frac{\beta'_2 s^2 + \beta'_1 s + \beta'_0}{s^5 + \alpha'_4 s^4 + \alpha'_3 s^3 + \alpha'_2 s^2 + \alpha'_1 s}. \tag{7.10}$$

As a consequence of Theorem 3.4,

$$\frac{\beta_0}{\alpha_1} + \frac{\beta'_0}{\alpha'_1} = 1. \tag{7.11}$$

Taking into account Eqs. (7.9), (7.10) and (7.11), the vector of invariants can be chosen[2] as

$$\mathbf{\Phi} = [\alpha_1\ \alpha_2\ \alpha_3\ \alpha_1'\ \alpha_2'\ \alpha_3'\ \alpha_4'\ \beta_0\ \beta_1\ \beta_1'\ \beta_2']^T \tag{7.12}$$

the number of invariants is eleven, greater than the number of rate coefficients (nine). The test does therefore not reveal unidentifiability. It is neither possible to find a subnetwork for which the test does. However, the rank of the Jacobian (7.3) turns out to be eight[3], one lower than the number of rate coefficients. S is therefore structurally locally unidentifiable.

7.4 Real-life example: TAP-study of the interaction of propane with a CuO–CeO_2 catalyst

Consider again the set of TAP-responses collected to study the interaction of propane with CuO–$CeO_2/\gamma-Al_2O_3$, the second example of Section 6.5. Extend the reaction network (6.57) with one elementary step representing the irreversible adsorption of propane on an active site $\star$, different from $*$:

$$C_3H_8 + \star \xrightarrow{3} C_3H_8^\star \tag{7.13}$$

The adsorption step (7.13) is assumed pseudomonomolecular, like adsorption (6.57a). The reaction graph corresponding to this reaction network is depicted in Fig. 7.3 (a), where $A_1 = C_3H_8$ and $A_2 = C_3H_8^*$ and where A_3 is a virtual component representing $C_3H_8^\star$ and the unknown product of surface reaction (6.57b). An attempt was made to estimate the rate coefficients k_{+1}, k_{-1}, k_2 and k_3 using TAPFIT. As before, the simulation was performed using the transfer matrix approach, see Section 4.4. The regression occurred by SOSR. The estimates are given in Table 7.1, in line (a). As the regression algorithm did not attain a Gauss-Newton stage, no valid confidence limits were obtained. This indicates that the estimates are unsound.

It is worthwhile to carry out an assessment of the structural local identifiability. There is a net source only of the gaseous component propane. Moreover, the only observed variable is the concentration of propane. The kinetic transfer matrix $\mathbf{H}$ reduces to the scalar $H_{1,1}$. It follows from Theorem 3.2 that its symbolic form is

$$H_{1,1}(s) = \frac{s + \beta_0}{s^2 + \alpha_1 s + \alpha_0}. \tag{7.14}$$

[2] β_0 could be replaced by β_0', for example.

[3] The rank of the symbolic matrix was calculated using Maple 11. The calculation took approximately 400 s on an Intel Pentium 4 3 GHz processor.

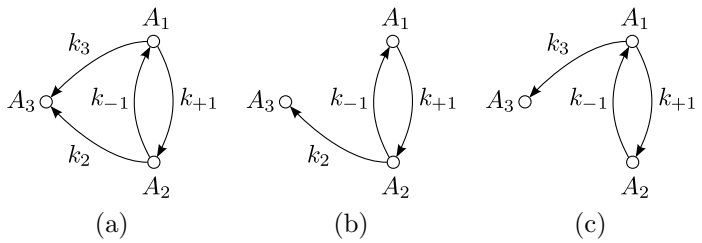

Figure 7.3: Reaction graph (a) representing the interaction of propane with a CuO–$CeO_2/\gamma-Al_2O_3$-catalyst, as described by the elementary steps (7.13)–(6.57b). $A_1 = C_3H_8$, $A_2 = C_3H_8^*$ and A_3 represents both $C_3H_8^*$ and the unknown product of surface reaction (6.57b). The reduced reaction graphs (b) and (c) correspond to $k_3 = 0$ and $k_2 = 0$, respectively.

Table 7.1: Estimated rate coefficients, resulting from three regressions of the same experimental data. At regression (a), no Gauss-Newton stage is attained. Confidence limits are therefore not available. During regressions (b) and (c), k_3 and k_2 are fixed at zero, respectively. The parameter estimates are shown with their 95% probability level confidence limits.

	k_{+1} (10^{-3} m^3/kg·s)	k_{-1} (Hz)	k_2 (Hz)	k_3 (10^{-3} m^3/kg·s)
(a)	240	23.05	2.47	117
(b)	356 ± 126	15.5 ± 2.2	9.99 ± 0.52	–
(c)	216 ± 87	25.5 ± 2.4	–	140 ± 39

There are three invariants, but four rate coefficients. The latter are therefore structurally locally unidentifiable. There is an infinite number of alternatives for the vector of parameter estimates resulting from regression (a), given in Table 7.1. Which one is found depends on the initial estimates. Figs. 7.3 (b) and (c) show simplified reaction networks. Network (b) corresponds to the reaction network (6.57) considered before in Section 6.5. In network (c) the reversibly adsorbed propane does not undergo the irreversible surface step (7.13). The transfer functions $H_{1,1}$ for networks (b) and (c) have the same symbolic form (7.14) as for the greater reaction network. There are still three invariants, but now there are just three unknown rate coefficients. The test does therefore not reveal structural local unidentifiability for the reduced reaction networks.

A SOSR with network (b) was already carried out in Section 6.5. A SOSR was also carried out with network (c). In both cases, the Levenberg-Marquardt algorithm attained a Gauss-Newton stage. The parameter estimates and their 95 % probability confidence limits are shown

in Table 7.1. The model-calculated propane responses resulting from all three regressions collide exactly and are thus all represented by the line in Fig. 6.12. It can be verified that the different columns of parameter estimates in Table 7.1 indeed give rise to the same transfer function $H_{1,1}$. The reaction networks (b) and (c) are indistinguishable in this case. This example illustrates how identifiability and distinguishability of reaction networks are related subjects, as was already mentioned in Section 3.3.

7.5 Conclusions

Unidentifiability of rate coefficients from transient experimental data is a typical issue for linear reaction networks. This is especially so in heterogeneous catalysis, where the surface intermediates typically

1. have a concentration which is not amenable to measurement,
2. have a negligible net mass transfer by surface diffusion.

Structural local unidentifiability of a reaction network most often leads to incorrect estimates for the rate coefficients. A necessary condition for structural local identifiability was formulated, which can be verified by visual inspection. If the rate coefficients are structurally locally identifiable, it is possible in principle to estimate them, as long as the initial estimates are chosen close enough to their real unknown values.

Chapter 8 will present a unique way of extracting connectivity features of reaction networks from isothermal TZTR-data without the need to postulate candidate networks. Possible unidentifiability issues are thereby avoided.

Chapter 8

Model-free Deduction of Connectivity Features of Reaction Networks from Thin-Zone TAP-data

8.1 Introduction

The classical strategy to determine catalytic reaction networks from kinetic data is by

1. postulating a list of candidates networks,
2. deriving corresponding physico-chemical models of the experiment,
3. submitting the data to regression with each of these models,
4. selecting the reaction networks which provide the best fit.

Unfortunately, this strategy is not optimal. Firstly, the list of candidate reaction networks is never exhaustive. If the actual reaction network is not among the postulated ones, it will never be selected. Secondly, parameter unidentifiability issues may arise for isothermal data, see Chapter 7, as well as the indistinguishability between several of the candidates. If not deterministic, parameter unidentifiability or network indistinguishability can still be practical, i.e., due to the level of noise. An alternative route, avoiding these problems, will be explored in this chapter. Connectivity features of reaction networks, rather than the reaction networks themselves, will be determined.

It was proven in Chapter 3, see Theorem 3.2a on p. 23, that kinetic transfer functions $H_{j,k}(s)$ reflect connectivity features of the reaction network:

1. the number of intermediates from A_k to A_j,
2. the length of the shortest reaction pathway from A_k to A_j.

It will be shown in Section 8.2 how in many cases, the kinetic transfer functions $H_{j,k}$ can be calculated in discrete points of the frequency domain on a model-free basis. State-defining TZTR experiments, involving gas phase components A_j and A_k, serve as a basis of this calculation. It can be hoped that the reaction network connectivity features can be observed in a model-free manner. Section 8.3 proposes a strategy, which will be examined for feasibility on the basis of a case-study, presented in Section 8.4. Synthetic TZTR data have been used to verify the feasibility of this strategy. They consist of model-calculated data produced by the program TAPFIT. Artificial noise, typical of a TAP-1-setup, see Chapter 5, has been added.

8.2 Model-free calculation of values of the kinetic transfer functions

Suppose A_1 and A_2 are gas phase components. In order for values of the kinetic transfer function $H_{2,1}$ to be computable, three assumptions have to be made.

Assumption 8.1. *A_1 reacts irreversibly to A_2:*

$$A_1 \rightarrow \nu_2 A_2, \tag{8.1}$$

where ν_2 is a stoichiometric coefficient.

Assumption 8.2. *If gas components other than A_1 or A_2 are present in the reactor, none of them can convert into A_1 or A_2.*

Assumption 8.3. *The reaction network responsible for reaction* (8.1) *is pseudomonomolecular.*

Assumption 8.1 is usually fulfilled for the fast reactions typically studied in the TAP-reactor, such as oxidation reactions. Assumption 8.2 requires all intermediates to be catalyst surface components. Assumption 8.3 is normally fulfilled for state-defining TAP-experiments.

Because of Assumption 8.2, the concentrations of A_1 and A_2 in the TZTR can be modeled separately. On account of Assumption 8.3, the

transfer matrix approach can be used to model the reactor, see Section 4.4. The transfer matrix for the thin reactive zone was approximately given by Eq. (4.41). Because of Assumption 8.1, the matrix $\tilde{\mathbf{H}}^{(l)}(s)\cdot\tilde{\mathbf{F}}^{(l)}$ appearing there is given here by[1]

$$\tilde{\mathbf{H}}^{(2)}(s)\cdot\tilde{\mathbf{F}}^{(2)} = \begin{bmatrix} H_{1,1}(s) & 0 \\ \nu_2\, H_{2,1}(s) & H_{2,2}(s) \end{bmatrix}. \tag{8.2}$$

Eq. (4.46) therefore becomes

$$\begin{bmatrix} \mathscr{L}r^{(2)}_{g,\phi,1} \\ \mathscr{L}r^{(2)}_{g,\phi,2} \end{bmatrix}(s) = -\epsilon_b^{(2)}\Delta z^{(2)} \begin{bmatrix} \frac{1}{H_{1,1}(s)} & 0 \\ -\frac{\nu_2 H_{2,1}(s)}{H_{1,1}(s)H_{2,2}(s)} & \frac{1}{H_{2,2}(s)} \end{bmatrix} \cdot \begin{bmatrix} \mathscr{L}c^{(2)}_{g,1} \\ \mathscr{L}c^{(2)}_{g,2} \end{bmatrix}(s) \tag{8.3}$$

or

$$\mathscr{L}r^{(2)}_{g,\phi,1}(s) = -\frac{\epsilon_b^{(2)}\Delta z^{(2)}}{H_{1,1}(s)}\,\mathscr{L}c^{(2)}_{g,1}(s) \tag{8.4}$$

$$\mathscr{L}r^{(2)}_{g,\phi,2}(s) = -\frac{\epsilon_b^{(2)}\Delta z^{(2)}}{H_{2,2}(s)}\,\mathscr{L}c^{(2)}_{g,2}(s) + \nu_2\,\frac{H_{2,1}(s)}{H_{2,2}(s)}\,\frac{\epsilon_b^{(2)}\Delta z^{(2)}}{H_{1,1}(s)}\,\mathscr{L}c^{(2)}_{g,1}(s). \tag{8.5}$$

Solving Eq. (8.4) for $H_{1,1}(s)$ yields

$$H_{1,1}(s) = -\epsilon_b^{(2)}\Delta z^{(2)}\,\frac{\mathscr{L}c^{(2)}_{g,1}(s)}{\mathscr{L}r^{(2)}_{g,\phi,1}(s)}. \tag{8.6}$$

Recognizing the right hand side of Eq. (8.4) in Eq. (8.5), allows rewriting the latter as

$$\mathscr{L}r^{(2)}_{g,\phi,2}(s) = -\frac{\epsilon_b^{(2)}\Delta z^{(2)}}{H_{2,2}(s)}\,\mathscr{L}c^{(2)}_{g,2}(s) - \nu_2\,\frac{H_{2,1}(s)}{H_{2,2}(s)}\,\mathscr{L}r^{(2)}_{g,\phi,1}(s). \tag{8.7}$$

Solving for $H_{2,1}(s)$ gives

$$H_{2,1}(s) = -\frac{H_{2,2}(s)\mathscr{L}r^{(2)}_{g,\phi,2}(s) + \epsilon_b^{(2)}\Delta z^{(2)}\mathscr{L}c^{(2)}_{g,2}(s)}{\nu_2\mathscr{L}r^{(2)}_{g,\phi,1}(s)}. \tag{8.8}$$

Eqs. (8.6) and (8.8) can be rewritten in terms of the Fourier transform:

$$H_{1,1}(i\omega) = -\epsilon_b^{(2)}\Delta z^{(2)}\,\frac{\mathscr{F}c^{(2)}_{g,1}(\omega)}{\mathscr{F}r^{(2)}_{g,\phi,1}(\omega)} \tag{8.9}$$

[1] The zone number $l = 2$ for the active zone in a TZTR.

$$H_{2,1}(i\omega) = -\frac{H_{2,2}(i\omega)\mathscr{F}r^{(2)}_{g,\phi,2}(\omega) + \epsilon_b^{(2)}\Delta z^{(2)}\mathscr{F}c^{(2)}_{g,2}(\omega)}{\nu_2\mathscr{F}r^{(2)}_{g,\phi,1}(\omega)}. \tag{8.10}$$

Values of the Fourier transforms $\mathscr{F}c^{(2)}_{g,1}$, $\mathscr{F}c^{(2)}_{g,2}$, $\mathscr{F}r^{(2)}_{g,\phi,1}$ and $\mathscr{F}r^{(2)}_{g,\phi,2}$ to the right hand side can be calculated in a model-free way from a state-defining experiment where A_1 is pulsed. The calculation is performed by applying a set of equations which lie at the basis of the Y-procedure (Yablonsky et al., 2002, 2007):

$$\mathscr{F}c^{(2)}_{g,j}(\omega) = \frac{\sinh\sqrt{i\omega\tau_j^{(3)}}}{\gamma_j^{(3)}\sqrt{i\omega\tau_j^{(3)}}}\mathscr{F}f_{\mathrm{out},j}(\omega) \tag{8.11a}$$

$$\begin{aligned}\mathscr{F}r^{(2)}_{g,\phi,j}(\omega) = &-\frac{1}{\cosh\sqrt{i\omega\tau_j^{(1)}}}\mathscr{F}f_{\mathrm{in},j}(\omega)\\ &+\left(\cosh\sqrt{i\omega\tau_j^{(1)}} + \frac{\gamma_j^{(1)}}{\gamma_j^{(3)}}\sqrt{\frac{\tau_j^{(1)}}{\tau_j^{(3)}}}\frac{\sinh\sqrt{i\omega\tau_j^{(1)}}\sinh\sqrt{i\omega\tau_j^{(3)}}}{\cosh\sqrt{i\omega\tau_j^{(1)}}}\right)\mathscr{F}f_{\mathrm{out},j}(\omega).\end{aligned} \tag{8.11b}$$

$f_{\mathrm{in},j}$ and $f_{\mathrm{out},j}$ are the in- and outlet fluxes of A_j, in mol/m^2 s. The inlet flux $f_{\mathrm{in},1}$ of A_1 is usually modeled as a Dirac pulse, see Eq. (4.7). Analogously to Eq. (4.54), it may therefore be written that

$$\mathscr{F}f_{\mathrm{in},1} = \frac{n_1}{\phi}, \tag{8.12}$$

where n_1 is the pulsed quantity, in mol, of A_1. As no A_2 is pulsed, $\mathscr{F}f_{\mathrm{in},2} = 0$. The outlet fluxes $f_{\mathrm{out},1}$ and $f_{\mathrm{out},2}$, in mol/m^2 s, can be calculated from two experimental pulse responses y_1 and y_2, in V, recorded by the mass spectrometer at characteristic masses. If follows from Eq. (4.10) that

$$\begin{bmatrix} f_{\mathrm{out},1} \\ f_{\mathrm{out},2} \end{bmatrix}(t) = \frac{1}{\phi}\,\mathbf{S}^{-1}\cdot\begin{bmatrix} y_1 \\ y_2 \end{bmatrix}(t), \tag{8.13}$$

where $\mathbf{S}$ is the calibration matrix, in Vs/mol. The responses y_j are given in the form of time series: they are known in discrete time points t_k, given by Eq. (4.12). Correspondingly, the Fourier transforms $\mathscr{F}f_{\mathrm{out},j}$, are known in discrete pulsations ω_k, given by Eq. (4.55). The calculation of the Fourier transforms is described in Appendix C. The variables $\tau_j^{(l)}$ and $\gamma_j^{(l)}$, in s and m/s, are given by Eqs. (4.39) and (4.40) and describe diffusional transport of A_j through zone l. For a symmetric TZTR,

Eq. (8.11b) reduces to

$$\frac{\mathscr{F} r^{(2)}_{g,\phi,j}(\omega)}{\phi} = \frac{-\mathscr{F} f_{\mathrm{in},j}(\omega) + \cosh\left(2\sqrt{i\omega\tau_j^{(3)}}\right)\mathscr{F} f_{\mathrm{out},j}(\omega)}{\cosh\sqrt{i\omega\tau_j^{(3)}}}. \tag{8.14}$$

The only remaining unknown to the right hand side of Eqs. (8.9) and (8.10) is $H_{2,2}(i\omega_j)$. This $H_{2,2}(i\omega_j)$ can be calculated from a separate experiment where A_2 is being pulsed instead of A_1, using an equation analogous to Eq. (8.9):

$$H_{2,2}(i\omega) = -\epsilon_b^{(2)}\Delta z^{(2)}\,\frac{\mathscr{F} c^{(2)}_{g,2}(\omega)}{\mathscr{F} r^{(2)}_{g,\phi,2}(\omega)}. \tag{8.15}$$

Especially, if A_2 is known to desorb irreversibly, in Eq. (8.10):

$$H_{2,2}(i\omega) = \frac{1}{i\omega}. \tag{8.16}$$

This yields

$$H_{2,1}(i\omega) = -\frac{\epsilon_b^{(2)}\Delta z^{(2)} i\omega \mathscr{F} c^{(2)}_{g,2}(\omega) + \mathscr{F} r^{(2)}_{g,\phi,2}(\omega)}{\nu_2 i\omega \mathscr{F} r^{(2)}_{g,\phi,1}(\omega)}. \tag{8.17}$$

In this case it is not necessary to determine $H_{2,2}$ experimentally.

8.3 Interpretation: connectivity of the reaction network

Graph-theoretically inspired expressions for the kinetic transfer functions can be obtained from Theorem 3.2:

$$H_{j,k}(s) = \frac{\prod_{q=1}^{n_{j,k}-l_{j,k}-1}\left(s - z^{(q)}_{j,k}\right)}{\prod_{q=1}^{n_{j,k}}\left(s - p^{(q)}_{j,k}\right)}. \tag{8.18}$$

$n_{j,k}$ is the number of intermediates between A_k to A_j plus two if $k \neq j$ or plus one if $k = j$. $l_{j,k}$ is the length of the shortest pathway from A_k to A_j, see Remark 3.1 on p. 25. $l_{1,1}$ and $l_{2,2}$ are zero. $z^{(q)}_{j,k}$ is the qth *zero* of $H_{j,k}(s)$ while $p^{(q)}_{j,k}$ is the qth *pole* of $H_{j,k}(s)$. It follows from part b of Theorem 3.2 that the zeroes and poles have a strictly negative real part,

possibly with the exception of one pole which is zero if and only if A_2 is in an ergodic strong linkage class, see Theorem 3.2b. Pairs of complex conjugate zeroes or poles would occur only in rare reaction networks containing pseudomonomolecular reaction cycles. In the present work, the zeroes $z_{j,k}^{(q)}$ and poles $p_{j,k}^{(q)}$ are assumed real. The transfer functions are calculated in $s = i\omega_k$, where the pulsations ω_k are given by Eq. (4.55) and correspond to frequencies ν_k:

$$\nu_k = \frac{k}{n_t \Delta t}. \tag{8.19}$$

The transfer functions $H_{j,k}$ are most clearly represented by Bode plots. The Bode magnitude plot shows the modulus, $|H_{j,k}|$, as a function of the frequency ν, while the Bode phase plot shows the argument, $\arg(H_{j,k})$, as a function of ν. The magnitude plot has a double logarithmic scaling. The phase plot has a logarithmically scaled ν axis and a linearly scaled phase axis. If the *corner frequencies* are defined as

$$\tilde{z}_{j,k}^{(q)} = -\frac{z_{j,k}^{(q)}}{2\pi} \tag{8.20a}$$

and

$$\tilde{p}_{j,k}^{(q)} = -\frac{p_{j,k}^{(q)}}{2\pi}, \tag{8.20b}$$

the logarithm of the modulus of the transfer function is given by

$$\log|H_{j,k}(2\pi i\nu)| = \sum_{q=1}^{n_{j,k}-l_{j,k}-1} \log\sqrt{\tilde{z}_{j,k}^{(q)\,2} + \nu^2} - \sum_{q=1}^{n_{j,k}} \log\sqrt{\tilde{p}_{j,k}^{(q)\,2} + \nu^2} - (l_{j,k}+1)\log(2\pi) \tag{8.21a}$$

and the argument is given by

$$\arg(H_{j,k}(2\pi i\nu)) = \sum_{q=1}^{n_{j,k}-l_{j,k}-1} \arctan\left(\frac{\nu}{\tilde{z}_{j,k}^{(q)}}\right) - \sum_{q=1}^{n_{j,k}} \arctan\left(\frac{\nu}{\tilde{p}_{j,k}^{(q)}}\right). \tag{8.21b}$$

Travelling on the frequency axis in the positive direction, passing a corner frequency $\tilde{z}_{j,k}^{(q)}$ results in an increase of the slope of the magnitude curve by one and a shift of the phase curve by $\pi/2$. Analogously, passing a corner frequency $\tilde{p}_{j,k}^{(q)}$ on the frequency axis results in a slope decrease by one and a phase shift by $-\pi/2$. If there is a zero pole, the initial slope of the magnitude curve is minus one and the initial phase is $-\pi/2$. Otherwise, the initial slope of the magnitude curve and the initial phase are zero.

The latter occurs if and only if A_j is in an ergodic strong linkage class. The limit slope for high frequencies of the magnitude curve is equal to the overall degree of the transfer function: $-l_{j,k} - 1$. Correspondingly, the high-frequency limit phase for high frequencies is equal to $-(l_{j,k}+1)\,\pi/2$. Especially, for a transfer function $H_{j,j}$, the final slope of the magnitude curve is minus one and the final phase is $-\pi/2$.

The values of the kinetic transfer functions $H_{j,k}$ found from Eqs. (8.9), (8.10) and (8.15) can be represented in Bode plots. In the ideal case, by identifying all shifts in the slope of the magnitude curve and the phase curve, the number of zeroes and poles can be determined. The length $l_{j,k}$ of the shortest reaction pathway from A_k to A_j is derived from the limit phase. $n_{j,k}$ is the number of intermediates between A_k and A_j plus two if $k \neq j$ or plus one if $k = j$. According to Theorem 3.2a, $n_{j,k}$ is equal to the number of poles. Of course it is often difficult to identify all shifts in the Bode plots. Firstly, these shifts may be outside the window of observable frequencies. Secondly, corner frequencies $\tilde{z}_{j,k}^{(q)}$ and $\tilde{p}_{j,k}^{(q)}$ can be situated close to each other on the frequency axis, in which case they practically cancel each other out. Indeed, the shifts in the slope of the magnitude curve and the phase curve are gradual. Phase shifts, for example, start about 1 decade before the corner frequency and finish about 1 decade after. The limitations may cause errors in estimated numbers of intermediates or an estimated shortest reaction path length. However, as it will be illustrated in Section 8.4, such errors often have a physical background. For example, an elementary step may turn out to be unobservable because it proceeds too fast. For this reason, an estimated number of intermediates will be termed the *observable number of intermediates*. Similarly, an estimated shortest reaction path length will be termed the *observable shortest reaction path length*.

8.4 Synthetic data based feasibility study

Three experimental cases have been simulated, where a reaction (8.1) took place in a symmetric TZTR reactor, a different reaction network being assumed responsible each time. In each case, the outlet flux time series $f_{\mathrm{out},1}$ of A_1 and $f_{\mathrm{out},2}$ of A_2 were model-calculated as responses to pulses of first A_2 and then A_1. The pulsed quantities were taken as $n_1 = n_2 = 2 \cdot 10^{-9}\,\mathrm{mol}$. Each time, two masses were monitored by the imaginary mass spectrometer, resulting in responses y_1 and y_2. The calibration matrix $\mathbf{S}$ in Eq. (8.13) was taken diagonal:

$$\mathbf{S} = \begin{bmatrix} 10^6\,\frac{\mathrm{V\,s}}{\mathrm{mol}} & 0 \\ 0 & 10^6\,\frac{\mathrm{V\,s}}{\mathrm{mol}} \end{bmatrix}. \tag{8.22}$$

The proportionality factors, the diagonal elements of $\mathbf{S}$, have a typical magnitude for a TAP-1-apparatus.

The reactor configuration was taken equal in all cases. The central, active zone was given a width of $\Delta z^{(2)} = 1\,\mathrm{mm}$. Both inert zones were given a width of $\Delta z^{(1)} = \Delta z^{(3)} = 14.5\,\mathrm{mm}$. This is a realistic TZTR configuration. The porosity was taken equal in all zones: $\epsilon_b^{(1)} = \epsilon_b^{(2)} = \epsilon_b^{(3)} = 0.5$. Similarly, the effective Knudsen diffusion coefficient was taken equal in all zones and for both gas components A_1 and A_2: $\mathscr{D}_{e,1}^{(1)} = \mathscr{D}_{e,1}^{(2)} = \mathscr{D}_{e,1}^{(3)} = \mathscr{D}_{e,2}^{(1)} = \mathscr{D}_{e,2}^{(2)} = \mathscr{D}_{e,2}^{(3)} = 2 \cdot 10^{-3}\,\mathrm{m^2/s}$. The cross-sectional surface area was $1.86 \cdot 10^{-5}\,\mathrm{m^2}$.

The pulse responses were calculated using the transfer matrix approach, see Section 4.4. The initial and boundary conditions were the ideal ones described in Section 4.3. The relevant surface components were assumed initially absent in the active zone: $\mathbf{c}_{s,0}^{(2)}(z) = \mathbf{0}$. Eqs. (8.11a), (8.11b) and (8.14) have been derived for a TZTR with infinitely thin active zone. For the model-calculation of the pulse responses, the active zone was not modeled as infinitely thin, but as having its actual realistic width $\Delta z^{(2)} = 1\,\mathrm{mm}$, see above. Should there be any errors caused by applying Eqs. (8.11a), (8.11b) and (8.14) to a realistic TZTR, they will therefore be revealed by the case studies to follow. In order to avoid inaccurate model-calculations due to too low a Nyquist frequency ν_N, see Appendix C, three interjacent samples were calculated between each pair of actual samples. Similarly, to ensure completely extinct pulse responses, they were calculated with double collection times. The extra samples were immediately discarded.

Pulse response y_1 and y_2 were calculated using TAPFIT, see Appendix D. Twenty replicates were synthesized, artificial noise being superposed on each of them. The noise had characteristics typical for a TAP-1-setup.

1. A 2 % standard deviation of the zeroth moment, due to a variable pulse size and/or a variability of the mass spectrometer sensitivity.

2. Ornstein-Uhlenbeck noise with a correlation time of $\theta = 0.789\,\mathrm{ms}$. This noise was set to contain a constant contribution of 0.3 mV and a relative contribution of 4 % of the signal strength.

3. Noise spectrally localized about the European mains frequency, 50 Hz, to mimic electromagnetic interference. The noise was made to consist of an oscillation with an amplitude containing a constant contribution of 1 mV and a relative contribution of 3 % of the signal strength.

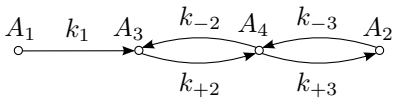

Figure 8.1: A reaction graph for Case 1, responsible for the irreversible reaction of the gas component A_1 into the gas component A_2. A_3 and A_4 represent surface components.

This is a worst case scenario. The level of noise would be smaller on the newer TAP-2- or TAP-3-setups. All twenty replicates of each pulse response were averaged before they were processed.

The synthetic pulse responses were processed as if they had been obtained experimentally. It is assumed that the experimentalist has accurate estimates of all relevant physical parameters ($\mathscr{D}_{e,j}^{(l)}$, $\epsilon_b^{(l)}$, n_j, $\mathbf{S}$, ...) at his disposal. Needless to state that this would require a considerable experimental effort.

As a first step in the processing of the synthetic data, using Eq. (8.13), the average responses were converted into the outlet flux time series $f_{\text{out},1}$ and $f_{\text{out},2}$. The latter were then subjected to the discrete approximation $\mathscr{F}_d$ of the continuous Fourier transform, see Appendix C. Subsequently, the base equations (8.11a) and (8.14) of the Y-procedure were applied to find the concentrations $c_{g,j}^{(2)}$ and consumption rates $r_{g,j}^{(2)}$ in the active zone, in the frequency domain. Slightly corrected widths $\Delta' z^{(1)} = \Delta' z^{(3)}$ were applied in Eqs. (8.11a) and (8.14) for the calculation of the transport parameters $\tau_j^{(1)} = \tau_j^{(3)}$ and $\gamma_j^{(1)} = \gamma_j^{(3)}$:

$$\Delta' z^{(1)} = \Delta z^{(1)} + \frac{\Delta z^{(2)}}{4} = \Delta' z^{(3)} = \Delta z^{(3)} + \frac{\Delta z^{(2)}}{4}. \tag{8.23}$$

This was found to give the best results. Finally, the transfer functions $H_{2,2}$ (if necessary), $H_{1,1}$ and $H_{2,1}$ were calculated using Eqs. (8.15), (8.9) and (8.10) or (8.17).

Case 1

The reaction graph depicted in Fig. 8.1 was taken to describe the activity of the catalyst in the active zone. A_3 and A_4 represent surface components. The rate coefficients were taken as

$$k_1 = 800\,\text{Hz},\ k_{+2} = 10\,\text{Hz},\ k_{-2} = 40\,\text{Hz},\ k_{+3} = 500\,\text{Hz},\ k_{-3} = 1000\,\text{Hz}. \tag{8.24}$$

The rate coefficients k_1 and k_{-3} are taken high to ensure significant adsorptions despite the small width of the active zone. The desorption rate

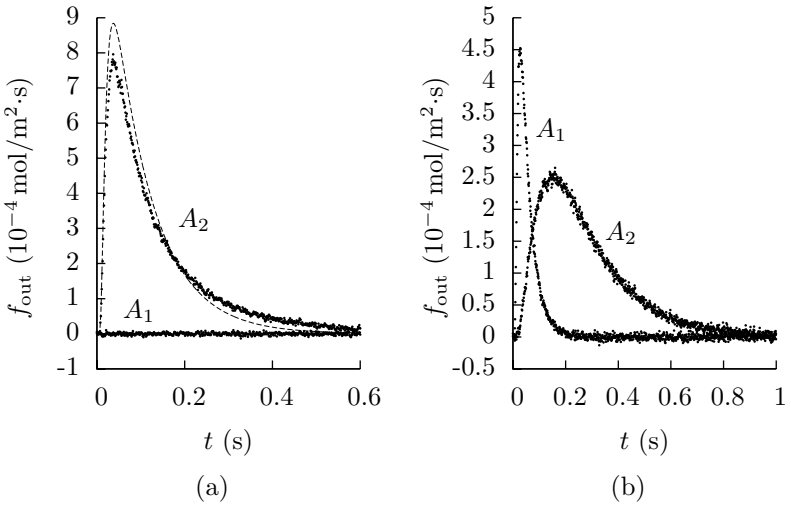

Figure 8.2: The synthetic outlet flux time series $f_{\text{out},1}$ of A_1 and $f_{\text{out},2}$ of A_2 as a response to pulses of A_2 (a) and A_1 (b) for Case 1. The dashed line in Fig. (a) represents the purely diffusional response which would be expected if A_2 did not interact with the catalyst.

coefficient k_{+3} had to be taken comparably high to ensure a significant desorption.

Fig. 8.2 (a) represents the synthetic outlet flux time series $f_{\text{out},1}$ of A_1 and $f_{\text{out},2}$ of A_2 as a response to a pulse of A_2. Fig. 8.2 (b) represents the same time series as a response to a pulse of A_1. In both cases, the number of samples was a thousand and the collection time was 1 s. For the sake of clarity, only the first 0.6 s are shown in Fig. 8.2 (a).

If the responses of Fig. 8.2 were to be obtained experimentally, the first observation would be that no A_1 leaves the reactor as a response to a pulse of A_2. Assumption 8.1 is therefore known to be fulfilled. If, as a response to the pulse of A_1, gas components other than A_2 would be observed, in fulfillment of Assumption 8.2, none should convert into A_1 or A_2. This can be verified by pulsing them over the reactor. The next question would be whether A_2 desorbs reversibly or irreversibly. In the first case, to calculate $H_{2,1}$, Eq. (8.10) has to be applied, and $H_{2,2}$ has to be calculated beforehand. In the second case, Eq. (8.17) can be applied, without the need to calculate $H_{2,2}$. The dashed line in Fig. 8.2 (a) shows the model-calculated purely diffusional response which would be expected if A_2 did not interact with the catalyst. The difference with the synthetic responses y_2 proves an interaction of A_2 with the catalyst. However, as

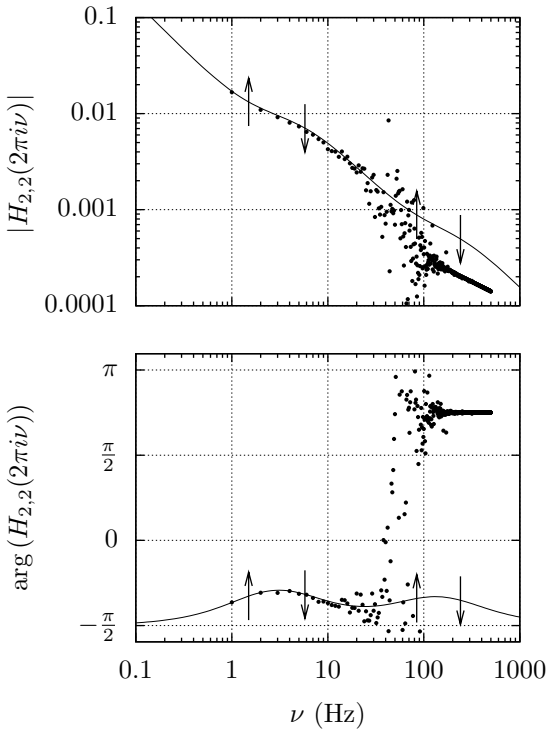

Figure 8.3: Bode magnitude (top) and phase plot (bottom) of the kinetic transfer function $H_{2,2}$ for Case 1. The dots are calculated from the synthetic data. The lines are obtained from the known analytical expression. The arrows mark the position of corner frequencies, calculated analytically. The upward arrows correspond to zeroes, while the downward arrows correspond to poles.

no net conversion of A_2 is observed, A_2 must be in an ergodic strong linkage class of the reaction graph.

Fig. 8.3 shows the Bode plots of the kinetic transfer function $H_{2,2}$. The dots were calculated using Eq. (8.15). They are available until the Nyquist frequency ν_N, see Eq. (5.16), which is in this case 500 Hz. The full lines represent the real continuous transfer function, $H_{2,2}$, calculated

analytically:

$$H_{2,2}(s) = \frac{s^2 + (k_{+2} + k_{-2} + k_{+3})s + k_{+2}k_{+3}}{s^3 + (k_{+2} + k_{-2} + k_{+3} + k_{-3})s^2 + (k_{+2}k_{-3} + k_{-2}k_{-3} + k_{+2}k_{+3})s} \tag{8.25}$$

The dots do not coincide perfectly with the lines. The small deviations at frequencies smaller than 10 Hz are systematic and due to the application of the Y-procedure base equations to data from a TZTR with finite width of the active zone. These small deviations exist also at the higher frequencies, but there they are obscured by important other deviations. The random deviations at frequencies between 10 Hz and 100 Hz are due to the noise in the synthetic pulse responses. These random deviations increase as a function of the frequency ν. This is because the base equations (8.11a), (8.11b) and (8.14) of the Y-procedure amplify high frequency noise. Especially, the important noise contribution spectrally localized about 50 Hz is considerably amplified. As an essential part of the Y-procedure, the higher frequencies are dampened. Here, no such dampening is necessary. The user should just discard the higher frequencies where noise gets the upper hand of $\mathscr{F}c^{(2)}_{g,j}$ and $\mathscr{F}r^{(2)}_{g,j}$. Here, this would be the frequencies beyond about 30 Hz. Recall that the data were synthesized with noise typical for a TAP-1-apparatus. Due to a lower level of noise, the observable frequency window would be wider for the newer TAP-2- and TAP-3-setups. Beyond 100 Hz, the level of random noise decreases, but instead important systematic deviations can be observed between the dots and the lines. These deviations, though systematic, are due to the random noise in the synthetic data. Indeed, in Eq. (8.14), due to the presence of noise in $\mathscr{F}f_{\mathrm{out},j}(\omega)$, the second term in the numerator of the fraction to the right hand side becomes dominant for high frequencies. It can be readily verified that substitution of the resulting limit equation and Eq. (8.11a) in Eq. (8.15) yields

$$H_{1,1}(2\pi i\nu) \approx \frac{\epsilon^{(2)}_b \Delta z^{(2)}}{\gamma^{(3)}_2 \phi \sqrt{8\pi\nu\tau^{(3)}_2}} \exp\left(i\,\frac{3}{4}\pi\right). \tag{8.26}$$

Observe that for the transfer function $H_{2,2}$, values of which were obtained from Eq. (8.15), the final slope in the magnitude plot and the final argument in the phase plot are indeed $-1/2$ and $3\pi/4$.

The upward arrows mark the position of the corner frequencies $\tilde{z}^{(1)}_{2,2}$ and $\tilde{z}^{(2)}_{2,2}$, calculated analytically. The arrows are directed upward, because these frequencies, as they correspond to zeroes, involve an increase

of the slope of the magnitude curve as well as an increase of the phase curve. Similarly, the downward arrows mark corner frequencies $\tilde{p}_{2,2}^{(2)}$ and $\tilde{p}_{2,2}^{(3)}$, corresponding to the nonzero poles which involve a decrease of the magnitude curve slope and the phase. As A_2 is known to be in an ergodic strong linkage class, one pole is situated at the zero frequency. The corresponding corner frequency $\tilde{p}_{2,2}^{(1)} = 0$ is of course not represented on the Bode plots.

As there is a pole at the zero frequency, the initial slope of the magnitude curve is known to be minus one. For the same reason, it is known that the initial phase is $-\pi/2$. The overall degree of the transfer function $H_{2,2}$ is a priori known to be minus one. The final slope of the magnitude is therefore minus one, and the final phase is $-\pi/2$. Assume the full line is not known, which would be the case in an experimental situation. The information on the initial and final slopes and phases, together with the trends in the dots in the Bode plots, allows the perception of the corner frequencies $\tilde{z}_{2,2}^{(1)}$ and $\tilde{p}_{2,2}^{(2)}$, and their approximate location on the frequency axis. Knowledge of the two poles corresponding to the frequencies $\tilde{p}_{2,2}^{(1)}$ and $\tilde{p}_{2,2}^{(2)}$, where the former is zero, and the zero corresponding to $\tilde{z}_{2,2}^{(1)}$ is in correspondence with the known behavior at the low and high frequency ends. There is therefore no reason to assume that poles or zeroes lie in the invisible high-frequency end of the spectrum. It would be concluded that the observable number of intermediates from A_2 to itself is one.

Because the corner frequencies $\tilde{z}_{2,2}^{(2)}$ and $\tilde{p}_{2,2}^{(3)}$ are not perceived, one intermediate is not observed. Indeed, the actual number of intermediates is two: A_3 and A_4, see Fig. 8.1. Consider the analytical expression (8.25) of $H_{2,2}$. The rate coefficients k_{+3} and k_{-3} are much larger than the coefficients k_{+2} and k_{-2}. Moreover, for the low frequency end of the spectrum, k_{+3} and k_{-3} are also much larger than $|s|$. Eq. (8.25) can therefore be simplified as

$$H_{2,2}(s) \approx \frac{k_{+3}s + k_{+2}k_{+3}}{(k_{+3} + k_{-3})s^2 + (k_{+2}k_{-3} + k_{-2}k_{-3} + k_{+2}k_{+3})s} \tag{8.27}$$

This expression shows one zero and two poles, including the zero frequency. This is in correspondence with what was observed from the Bode plots. It can be concluded that the intermediate A_4 is not observed because the adsorption and desorption of A_2 are too fast to observe, in other words because A_2 is in *quasi-equilibrium* with its adsorbate A_4.

Fig. 8.4 shows the Bode plots for the kinetic transfer function $H_{1,1}$. The analytical expression of the transfer function is given by

$$H_{1,1}(s) = \frac{1}{s + k_1}. \tag{8.28}$$

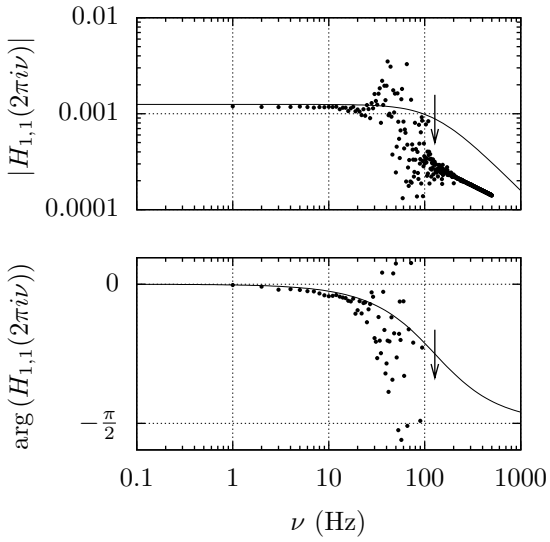

Figure 8.4: Bode magnitude (top) and phase plot (bottom) of the kinetic transfer function $H_{1,1}$ for Case 1. The dots are calculated from the synthetic data. The lines are obtained from the known analytical expression. The downward arrows mark the position of a corner frequency corresponding to a pole.

There is one corner frequency $\tilde{p}^{(1)}_{1,1}$, corresponding to the pole $p^{(1)}_{1,1} = -k_1$.

The corner frequency $\tilde{p}^{(1)}_{1,1}$ can be perceived from the values of the transfer function calculated using Eq. (8.9), more specifically from the downward trend of the dots in the phase plot about 10 Hz. A_1 is obviously not in an ergodic strong linkage class of the reaction diagram. Otherwise there would not be any conversion. There is therefore no zero frequency pole, so that the initial slope of the magnitude plot and the initial phase are zero. The overall degree is known to be minus one, so that the final slope of the magnitude plot is minus one, and the final phase is $-\pi/2$. The perception of one corner frequency $\tilde{p}^{(1)}_{1,1}$ is in correspondence with this limit behavior. There is therefore no reason to assume the existence of other corner frequencies in the invisible high frequency end of the Bode plots. The observable number of intermediates is therefore zero. In this case, this is equal to the actual number of intermediates. If the corner frequency was more to the high frequency end of the spectrum, the final downward trend of the phase plot would perhaps not be visible. In that case, however, its presence could still be inferred from the final phase,

which is a priori known to be $-\pi/2$.

Fig. 8.5 represents the Bode plots of the transfer function $H_{2,1}$. The analytical expression of the transfer function is given by

$$H_{2,1}(s) = \frac{k_1}{s+k_1} \cdot \frac{k_{+2}k_{+3}}{s^3 + (k_{+2}+k_{-2}+k_{+3}+k_{-3})s^2 + (k_{+2}k_{-3}+k_{-2}k_{-3}+k_{+2}k_{+3})s}. \tag{8.29}$$

There are no corner frequencies corresponding to zeroes. One pole is present at the zero frequency. There are three corner frequencies, $\tilde{p}_{1,1}^{(2)}$, $\tilde{p}_{1,1}^{(3)}$ and $\tilde{p}_{1,1}^{(4)}$, corresponding to the other poles.

The dots in Fig. 8.5 were calculated using Eq. (8.10), where the transfer function $H_{2,2}$ calculated before from Eq. (8.10) was substituted. The spectrum is obscured beyond 30 Hz. Observe the peak in the magnitude plot at about 50 Hz, due to the spectrally localized noise in the synthetic data. The pole at the zero frequency is a priori known, because A_2 is known to be in an ergodic strong linkage class of the reaction graph. The low frequency limit of the slope of the magnitude plot is therefore known to be minus one, while the low frequency limit of the phase is $-\pi/2$. The high frequency limits are not a priori known, because they depend on the length of the shortest reaction pathway from A_1 to A_2. The transfer function calculated using Eq. (8.10) allows only the perception of the corner frequency $\tilde{p}_{1,1}^{(2)}$. There is no reason to assume other corner frequencies, because the high frequency limit behavior is not known. The observable number of intermediates from A_1 to A_2 is therefore zero. The observable shortest reaction path length is one. The observations correspond to a simplified version of Eq. (8.29) for $k_1, k_{+3}, k_{-3} \ggg |s|, k_{+2}, k_{-2}$:

$$H_{2,1}(s) = \frac{k_{+2}k_{+3}}{(k_{+3}+k_{-3})s^2 + (k_{+2}k_{-3}+k_{-2}k_{-3}+k_{+2}k_{+3})s}. \tag{8.30}$$

The intermediates A_3 and A_4 are not observed, because the former is formed almost instantly from A_1 and the latter is in quasi-equilibrium with A_2.

Case 2

The reaction graph shown in Fig. 8.6 and the following corresponding rate coefficients were assumed:

$$k_1 = 550\,\text{Hz},\ k_2 = 5\,\text{Hz},\ k_3 = 50\,\text{Hz},\ k_4 = 1.5\,\text{Hz},\ k_5 = 1\,\text{Hz}. \tag{8.31}$$

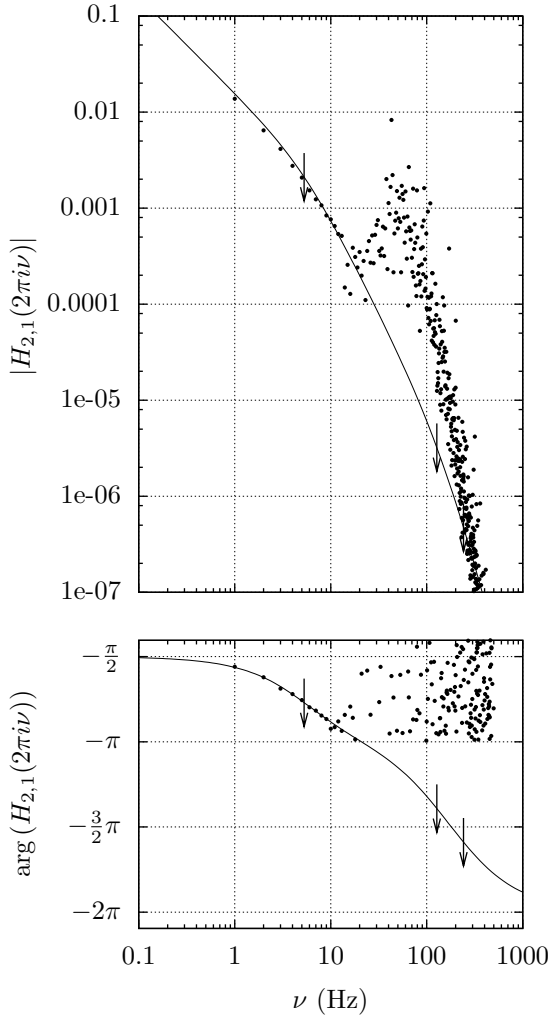

Figure 8.5: Bode magnitude (top) and phase plot (bottom) of the kinetic transfer function $H_{2,1}$ for Case 1. The dots are calculated from the synthetic data. The lines are obtained from the known analytical expression. The downward arrows mark the position of corner frequencies corresponding to poles. These positions were calculated analytically.

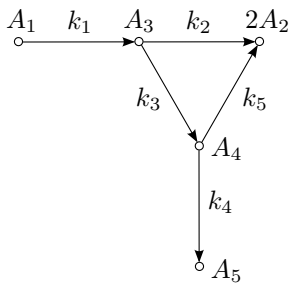

Figure 8.6: A reaction graph for Case 2, responsible for the irreversible reaction of the gas component A_1 into two molecules of the gas component A_2. A_3 and A_4 represent surface components. A_5 represents another surface component or an unobserved gas phase component.

Observe that one molecule of A_1 converts into two molecules of A_2. The stoichiometric coefficient ν_2 in (8.1) is therefore equal to two. The adsorption rate coefficient is again large compared to the other rate coefficients to ensure a significant conversion of A_1.

Fig. 8.7 (a) represents the synthetic outlet flux time series $f_{\text{out},1}$ of A_1 and $f_{\text{out},2}$ of A_2 as a response to a pulse of A_2. Fig. 8.7 (b) represents the same time series as a response to a pulse of A_1. The synthetic time series consisted a thousand samples. The collection time was taken as 2 s in both cases, although only the first 0.6 s are shown in Fig. 8.7 (a) for the sake of clarity. The collection time was taken larger than in Case 1, but the number of samples was maintained at one thousand. The sampling interval was therefore larger than in Case 1: $\Delta t = 2\,\text{ms}$. As a result, the Nyquist frequency is smaller: $\nu_N = 250\,\text{Hz}$.

The first observation is again that Assumption 8.1 is fulfilled, as no A_1 leaves the reactor as a response to a pulse of A_2. The dashed line in Fig. 8.7 (a) represents the outlet flux of A_2 which would be expected if A_2 did not interact with the catalyst. As it coincides with the synthetic response, it is concluded that the desorption of A_2 is indeed irreversible. There is therefore no need to calculate the transfer function $H_{2,2}$ and the transfer function $H_{2,1}$ can be calculated from Eq. (8.17). Furthermore, A_2 is known to constitute a trivial ergodic strong linkage class of its own.

Fig. 8.8 shows the Bode plots for the kinetic transfer function $H_{1,1}$. The analytical expression of the transfer function is again given by Eq. (8.28). A single corner frequency $\tilde{p}_{1,1}^{(1)}$, corresponding to the pole $p_{1,1}^{(1)} = -k_1$.

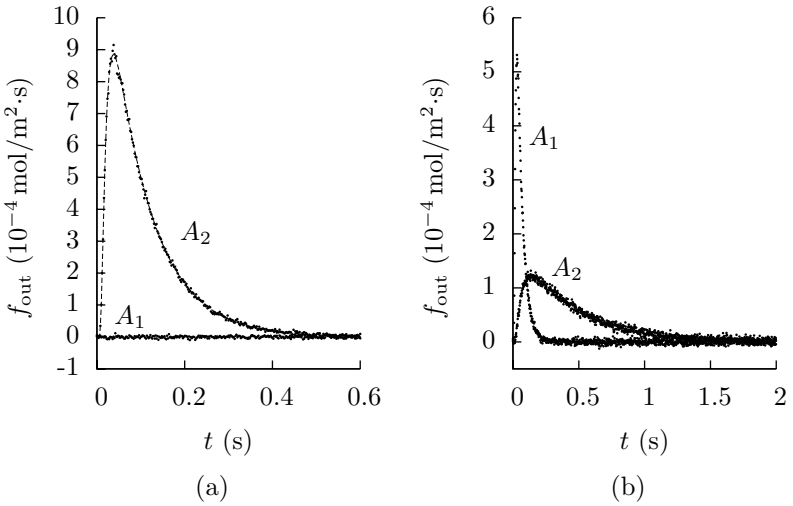

Figure 8.7: The synthetic outlet flux time series $f_{\mathrm{out},1}$ of A_1 and $f_{\mathrm{out},2}$ of A_2 as a response to pulses of A_2 (a) and A_1 (b) for Case 2. The dashed line in Fig. (a) represents the purely diffusional response which would be expected if A_2 did not interact with the catalyst.

As before, the presence of $\tilde{p}_{1,1}^{(1)}$ is apparent from the values of the transfer function calculated using Eq. (8.9), more specifically from the final downward trend of the dots in the phase plot. Even if the final downward trend of the phase plot would not be visible, the presence of $\tilde{p}_{1,1}^{(1)}$ could be inferred from the final phase, which is a priori known to be $-\pi/2$.

Fig. 8.9 represents the Bode plots of the transfer function $H_{2,1}$. There are one zero $z_{2,1}^{(1)}$ and four poles $p_{2,1}^{(1)}$, $p_{2,1}^{(2)}$, $p_{2,1}^{(3)}$ and $p_{2,1}^{(4)}$. The first pole $p_{2,1}^{(1)}$ is zero.

The dots in Fig. 8.9 were calculated using Eq. (8.17). The pole $p_{2,1}^{(1)} = 0$ is a priori known, because A_2 is known to be in an ergodic strong linkage class of the reaction graph. The low frequency limit of the slope of the magnitude plot is therefore known to be minus one, while the low frequency limit of the phase is $-\pi/2$. The dots in Fig. 8.9 allow the perception of the corner frequencies $\tilde{p}_{1,1}^{(2)}$, $\tilde{z}_{1,1}^{(1)}$ and, with some effort, $\tilde{p}_{2,1}^{(3)}$. $\tilde{p}_{2,1}^{(4)}$ remains hidden. One observed zero and three observed poles correspond to an observable number of intermediates equal to one and an observable length of the shortest reaction pathway equal to one. The intermediate A_3 is not observed, because it is formed almost instantly

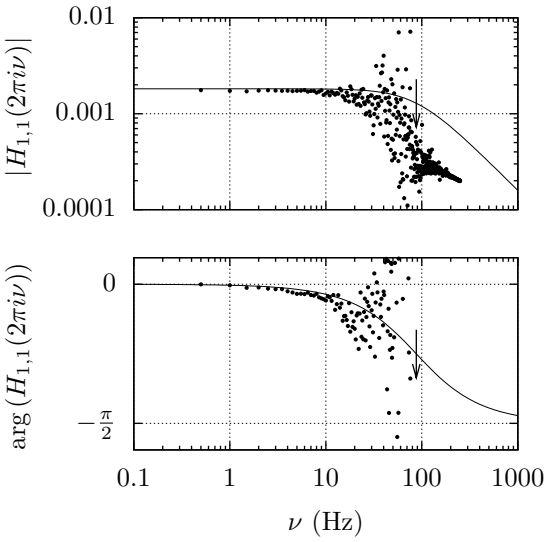

Figure 8.8: Bode magnitude (top) and phase plot (bottom) of the kinetic transfer function $H_{1,1}$ for Case 2. The dots are calculated from the synthetic data. The lines are obtained from the known analytical expression. The downward arrows mark the position of a corner frequency corresponding to a pole.

out of A_1. The intermediate A_4 is observed, and known not to be on the shortest reaction pathway from A_1 to A_2.

Case 3

Again, the reaction graph depicted in Fig. 8.6 was assumed responsible for the activity of the catalyst. This time, the rate coefficients were assumed to be

$$k_1 = 550\,\text{Hz},\ k_2 = 20\,\text{Hz},\ k_3 = 30\,\text{Hz},\ k_4 = 22\,\text{Hz},\ k_5 = 10\,\text{Hz} \quad (8.32)$$

Fig. 8.10 (a) represents the synthetic outlet flux time series $f_{\text{out},1}$ of A_1 and $f_{\text{out},2}$ of A_2 as a response to a pulse of A_2. Fig. 8.10 (b) represents the time series as a response to a pulse of A_1. The synthetic time series consisted a thousand samples. The collection time was taken as 1 s in both cases, although only the first 0.6 s are shown in Fig. 8.7 (a).

Assumption 8.1 is obviously fulfilled because no A_1 is formed in response to a pulse of A_2. A_2 does not interact with the catalyst, which shows from comparison of the synthetic outlet flux $f_{\text{out},2}$ of A_2 with the

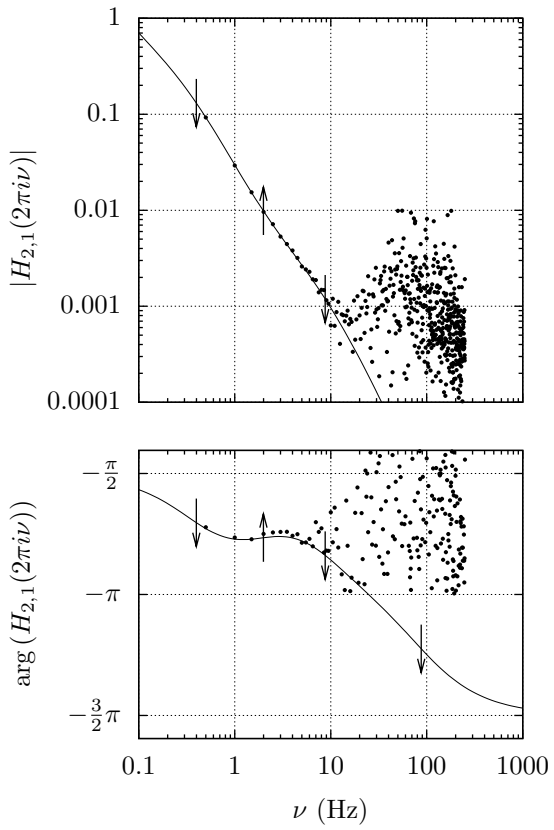

Figure 8.9: Bode magnitude (top) and phase plot (bottom) of the kinetic transfer function $H_{2,1}$ for Case 2. The dots are calculated from the synthetic data. The lines are obtained from the known analytical expression. The arrows mark the position of corner frequencies, calculated analytically. The upward arrows correspond to zeroes, while the downward arrows correspond to poles.

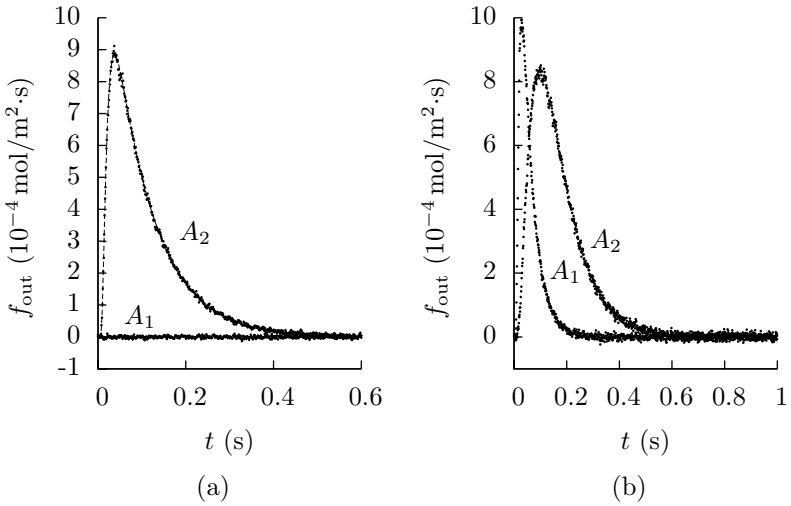

Figure 8.10: The synthetic outlet flux time series $f_{\text{out},1}$ of A_1 and $f_{\text{out},2}$ of A_2 as a response to pulses of A_2 (a) and A_1 (b) for Case 3. The dashed line in Fig. (a) represents the purely diffusional response which would be expected if A_2 did not interact with the catalyst.

model-calculated purely diffusional flux represented by the dashed line in Fig. 8.10 (a). There is again no need to calculate the transfer function $H_{2,2}$ and the transfer function $H_{2,1}$ can be calculated from Eq. (8.17). As before, A_2 is known to constitute a trivial ergodic strong linkage class.

The Bode plots for the kinetic transfer function $H_{1,1}$ are not shown, because they are very similar to the ones previously shown in Fig. 8.8. For that matter, the treatment is completely analogous. Moving on immediately to the transfer function $H_{2,1}$, consider Fig. 8.11. It is immediately clear that the particular rate coefficients (8.32) cause the corner frequencies $\tilde{z}_{2,1}^{(1)}$ and $\tilde{p}_{2,1}^{(3)}$ to be situated very close to each other on the frequency axis. This prevents them from being apparent from the values of the transfer function $H_{2,1}$ calculated from Eq. (8.17), even though they are within the observable frequency window. In analytical terms, the factors $s - z_{2,1}^{(1)}$ in the numerator and $s - p_{2,1}^{(3)}$ in the denominator of $H_{2,1}(s)$ in Eq. (8.18) practically cancel each other out. Besides the a priori known pole $p_{2,1}^{(1)} = 0$, the only perceivable pole is $p_{2,1}^{(2)}$. The observable number of intermediates is therefore zero, and the observable shortest reaction path length from A_1 to A_2 is one. As before, the intermediate A_3 is unobservable, because it is formed almost instantly out of A_1. This time, the intermediate A_4 is also unobservable, because of the particular value of

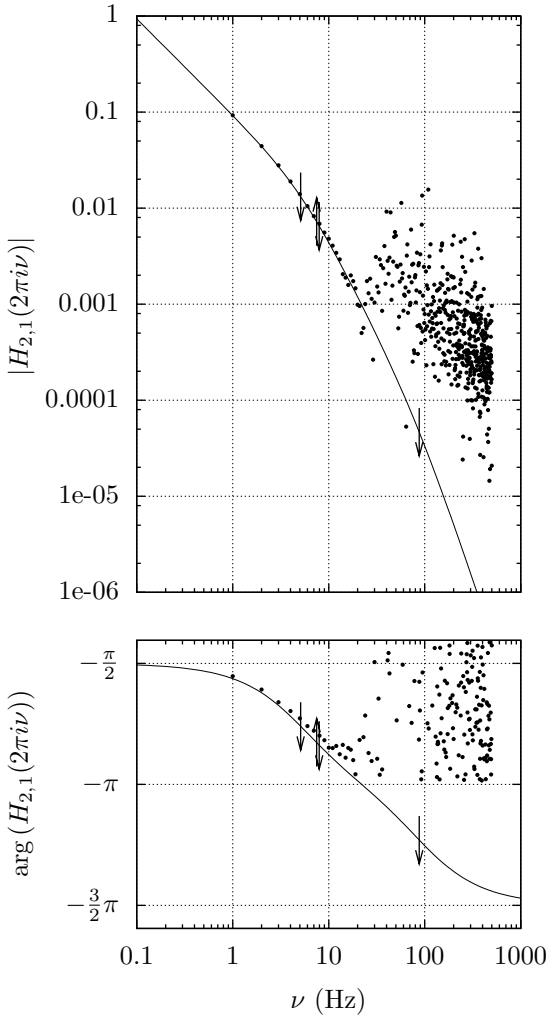

Figure 8.11: Bode magnitude (top) and phase plot (bottom) of the kinetic transfer function $H_{2,1}$ for Case 3. The dots are calculated from the synthetic data. The lines are obtained from the known analytical expression. The arrows mark the position of corner frequencies, calculated analytically. The upward arrows correspond to zeroes, while the downward arrows correspond to poles.

the parameters. It can be verified readily from an analytical derivation that this situation is due to

$$k_2 + k_3 \approx k_4 \left(1 + \frac{k_3}{k_2}\right), \tag{8.33}$$

see (8.32).

8.5 Conclusions

If the Assumptions 8.1, 8.2 and 8.3 are fulfilled, responses of the gas phase components A_1 and A_2 to pulses of A_1 and A_2 over TZTRs allow the extraction of connectivity features of the reaction network. Such information is obtained through a novel procedure which proceeds in a model-free manner, i.e., without the need to postulate candidate reaction networks. To this end, values of the kinetic transfer functions $H_{2,1}$, $H_{1,1}$ and $H_{2,2}$ are calculated in equally-spaced points of the frequency domain, relying on the base equations of the Y-procedure. After representation of these transfer functions in Bode plots, the observable shortest reaction path length from A_1 to A_2 is determined from the high-frequency limit of the argument of $H_{2,1}$. Observable numbers of intermediates follow from observed trends in the Bode plots. Numerical experiments have confirmed the feasibility of this procedure. In the Bode plots, the window of observable frequencies is only limited by spectrally localized noise, due to electromagnetic interference of the mass spectrometer, and irreducible high-frequency noise.

Chapter 9

Regression of TAP-Data: Best Practices

9.1 Introduction

The TAP-reactor itself is relatively simple, see Section 4.3. But this reactor is just a small part of a complex apparatus. This complexity ensues from three ambitiously imposed qualities:

1. the possibility of operating at pressures low enough (peak local pressures below about 10^{-1} Pa) to ensure Knudsen diffusion, see Section 4.2,
2. the admission of very small quantities (on the order of 10^{-9} mol or lower) of gas in a time span allowing them to be approximated by Dirac pulses,
3. the accurate measurement of the outlet fluxes with up to submillisecond time resolution.

Despite continuous technical improvements (Gleaves et al., 1988, 1997, 2010), the user has to prepare and perform the experiments meticulously, taking into account certain technical limitations:

1. a rather poor reproducibility of the pulse size and fluctuations of the mass spectrometer sensitivity, see Section 5.7,
2. the presence of noise, in particular noise spectrally localized about the mains frequency and its harmonics, due to electromagnetic interference, see Section 5.6,
3. the impossibility of one mass spectrometer to monitor more than one mass.

Guidelines regarding the operation of the TAP-reactor with the purpose of extracting quantitative information, will be given in Section 9.3. The statistically most rigorous method to process experimental TAP-data is to subject them to least-squares regression with model-calculated data. This should also occur with the greatest care. Section 9.4 will present good practices. The purpose of this work was to propose procedures to determine catalytic reaction networks. Section 9.5 will present the Bayesian information criterion as a way to select a reaction network from a set of postulated candidates, after repeated regression of TAP-data. Finally, a fully elaborated example will be treated in Section 9.6. The data used for this example will already be used as illustrative material in the Sections 9.3 and 9.4. Therefore, the experimental background of these experiments will be given first, in Section 9.2.

9.2 Experimental data

The data which will be processed as an illustration were collected to study the EL10V1 catalyst, which consists of vanadia (V_2O_5) supported by titania (TiO_2) (Sack, 2006; Balcaen et al., 2009). This catalyst is used to perform the oxidative dehydrogenation of short chain alkanes to alkenes. Propane responses were collected over a three-zone TAP-reactor at six temperatures: 698 K, 723 K, 748 K, 773 K, 798 K and 823 K. The inert zone at the reactor inlet was 3.31 mm long. The inert zone at the reactor outlet was 15.27 mm long. Both beds consisted of quartz beads with diameters between 250 and 425 µm. The middle zone was 9.41 mm long and consisted of 99.8 mg of catalyst particles diluted with 99.7 mg of the same quartz beads as were used for the inert zone. At another time, propene response experiments were performed at 723 K over a similar three-zone reactor. This time, the inlet and outlet inert zones measured 3.6 mm and 14.7 mm, while the middle zone had a width of 9.86 mm. The latter contained 100 mg of catalyst diluted with 102 mg of quartz. In all cases, the interparticle porosity was assumed equal in all zones and estimated at 0.53.

All experimental time series consisted of one thousand samples,

$$n_t = 1000, \tag{9.1}$$

collected with a sampling interval of

$$\Delta t = 4\,\text{ms}. \tag{9.2}$$

The collection time was therefore 4 s. The time spacing between the pulses was 6 s. During the propane pulse experiments, the mass spectrometer alternately collected time series at 29 amu (due to propane) and

41 amu (due to propene and propane). This sequence of experiments was repeated twenty times. During the propene pulse experiments, the mass spectrometer collected fifteen replicate time series at 41 amu (propene). All time series were baseline-corrected, where the position of the baseline was estimated as the average of the last 500 samples of each time series. This was possible because these samples were collected after the responses were extinct, see Section 9.3.

The responses depend on the outlet fluxes as in Eq. (4.10):

$$\begin{bmatrix} y_{29\,\mathrm{amu}} \\ y_{41\,\mathrm{amu}} \end{bmatrix}(t) = \underbrace{\begin{bmatrix} 17.66 & 0 \\ 3.003 & 13.46 \end{bmatrix} 10^5 \, \frac{\mathrm{Vs}}{\mathrm{mol}}}_{\mathbf{S}} \cdot \phi \begin{bmatrix} f_{\mathrm{C_3H_8}} \\ f_{\mathrm{C_3H_6}} \end{bmatrix}(t), \tag{9.3}$$

where the elements of $\mathbf{S}$, the calibration coefficients, have been estimated separately from large sequences of propane and propene pulse responses over an inert bed. The total quantity of molecules pulsed was then calculated from the pressure drop in the closed feed line, using the ideal gas law.

9.3 Experimental guidelines

Knudsen diffusion

As a distinct feature of TAP, the pressure inside the reactor can be kept at all times low enough to ensure mass transfer by Knudsen diffusion only. This offers an important advantage at modeling, see Chapter 4. Eq. (4.3) is particularly useful, as it allows the derivation of the Knudsen diffusion coefficient of reactive components from the one of inert components. Another advantage of working in the Knudsen domain is the suppression of gas-phase reactions (Rothaemel and Baerns, 1996), which allows the unequivocal measurement of catalytic reaction kinetics.

Pulses of inert gases can be admitted to catalytic reactors to verify whether, given the pulse size, the diffusion is of the Knudsen type. This can be achieved by subjecting the resulting responses to regression with a Knudsen model. If this model provides an accurate description of those responses, the diffusion is of the Knudsen type. Alternatively, a simple test can be applied (Gleaves et al., 1997; Yablonsky et al., 2003). To that end, a response to an inert pulse is first area-normalized. If, subsequently, the product of the response maximum and the time at which this maximum is reached is approximately 0.31, the diffusion is derived to be of the Knudsen type.

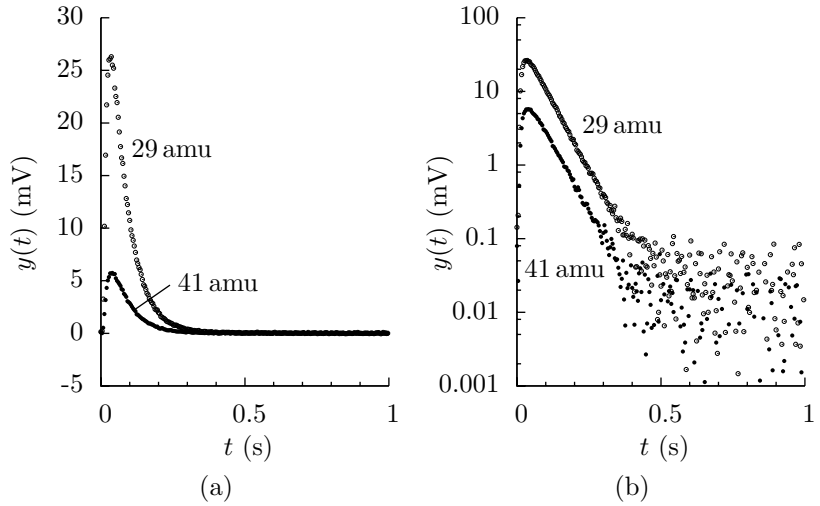

Figure 9.1: Normal (a) and semilogarithmic (b) representation of the first 250 samples of the time series collected as a response to pulses of C_3H_8 at 773 K.

Collection time and baseline-correction

The collection time of the responses should be chosen long enough, at least for state-defining experiments. If a pulse is admitted at a time when the initial state of the reactor is not yet restored after the previous one, the shape of its response will be distorted. If enough samples are collected beyond the time of extinction of the response, these samples can be averaged to yield an accurate estimate of the position of the baseline. Section 5.4 demonstrated a way of applying a baseline-correction if the responses are not extinct at the end of the collection time, but this approach only works if the response ends in a clearly defined exponential decay.

Whether the collection time was taken long enough and whether the baseline-correction was successful, can be most readily judged from a semilogarithmic representation of the responses. Fig. 9.1 (a) shows the two responses to C_3H_8 for the reactor temperature 773 K, after baseline-correction. Fig. 9.1 (b) shows the same responses with logarithmic scaling of the response axis. The image is what is expected after a successful baseline-correction. Each tail shows up as a linear decrease, until this decrease is completely obscured by noise. That happens at the time of extinction, here at about 0.6 s. Note that from there, half of the points correspond to a negative voltage and are hence not shown on the semilog-

arithmic graph.

Spectrally localized noise

Spectrally localized noise is a frequently recurring issue in TAP pulse responses. This noise is especially disadvantageous if its spectrum overlaps with the region of interest to the kineticist, see Chapter 8. Spectrally localized noise is either due to electromagnetic interference by electric devices present near the setup or direct interference through the power supply of the mass spectrometer. It should be avoided if possible.

Choice of the sampling interval

The TAP-technique is known for its submillisecond time resolution. This means that the mass spectrometer can sample with time intervals smaller than 1 ms. However, it was argued in Section 5.5 that there is little point in applying sampling intervals smaller than the correlation time θ of the Gaussian noise. θ was estimated at 0.789 ms for data collected on the TAP-setup of the LCT. A sampling frequency of 1 kHz should therefore suffice as a guideline. It would be better, if possible, to collect a higher number of replicates than to apply a higher sampling frequency.

Replicate experiments

Replicate state-defining experiments have been traditionally performed in the TAP-community. This is done to increase the SNR by averaging the replicate times series (Gleaves et al., 1988). Additionally, the SOSR presented in Chapter 6 extracts second-order statistical information from the replicates in order to condition the average for NLSQ regression.

To investigate whether the responses of a series of pulses can be considered replicates, it has to be verified whether there is any systematic variation between them. If the variation is purely random, the responses are replicates. As an extra, this indicates the experiment to be state-defining. Usually, it suffices to plot the variation of the *zeroth moment* M_0, i.e., the surface area under the response curves. Indeed, if this shows no systematic trends, the responses can normally be considered replicates. Fig. 9.2 shows such graphs for the twenty successively collected pulse responses at 29 amu to propane for the reactor temperatures 698 K (a), 723 K (b), 748 K (c), 773 K (d), 798 K (e) and 823 K (f). Fig. 9.2 (g) represents the M_0 for the fifteen replicate responses at 41 amu to propene at 723 K. In each graph, a straight line $M_0 = aj + b$ was fitted through the points. The estimates of a and b and their 95 % confidence limits are given in Table 9.1. None of the estimates of a are significantly different

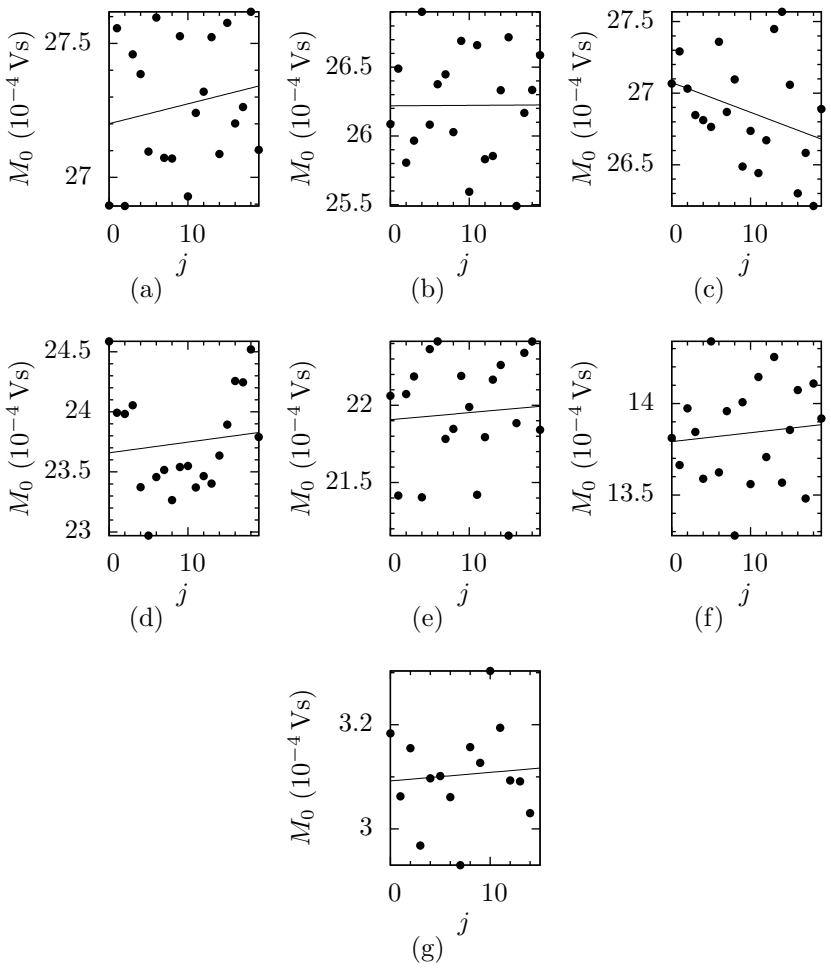

Figure 9.2: Variation of the zeroth moment M_0 of twenty responses measured at 29 amu to propane at 698 K (a), 723 K (b), 748 K (c), 773 K (d), 798 K (e), 823 K (f) and fifteen replicate responses measured at 41 amu to pulses of propene at 723 K (g) over the EL10V1 catalyst. j represents the response number. Each graph shows a fitted line $M_0 = aj + b$. The estimates a and b and their 95 % confidence intervals are shown in Table 9.1.

Table 9.1: Relative error σ/μ of the zeroth moment M_0 of responses to pulses of propane and propene at different reactor temperatures T. a and b are the coefficients appearing in a linear relation $M_0 = aj + b$ with which the data were regressed. The table shows the estimates with their 95 % confidence limits.

	T	σ/μ (%)	a (10^{-7} Vs)	b (10^{-5} Vs)
propane	698 K	0.9	7.4 ± 20.4	272.0 ± 2.3
	723 K	1.5	0.3 ± 33.0	262.1 ± 3.7
	748 K	1.4	-20.8 ± 29.4	270.7 ± 3.3
	773 K	1.8	8.9 ± 36.1	236.6 ± 4.0
	798 K	1.7	4.6 ± 30.9	219.1 ± 3.4
	823 K	2.0	4.9 ± 23.1	137.9 ± 2.6
propene	723 K	3.0	1.6 ± 12.3	30.9 ± 1.0

from zero, leading to the conclusion that there are no trends in the values of M_0. The successively collected responses can therefore be considered replicates. This is also enough to conclude on the state-defining character of the experiments.

Suppose the experimentalist wishes to perform a state-defining experiment feeding a component A. Suppose n_A is the maximum pulse size to ensure the change of the catalyst state to remain insignificant. It is possible to pulse the whole quantity in once, or to divide it into, say n_r, pulses with size n_A/n_r. The latter would yield n_r replicates. This may seem less appealing to the experimentalist as the separate replicate responses would show up on the monitor screen with a factor $\sqrt{n_r}$ lower SNR. However, the average of those replicates has the same SNR as the response to the big pulse of size n_A. Feeding a large quantity in one or in several pulses therefore seems equivalent. However, the latter has several advantages over the former:

1. The average of the replicates can be subjected to SOSR, while the response to the big pulse cannot. This allows to obtain more accurate estimates and corresponding statistical information.

2. With smaller pulses, there is a smaller risk of leaving the Knudsen domain for diffusion. Larger pulse sizes may cause local and temporary viscous flow, which is not typically accounted for in TAP-models.

3. Smaller pulsed quantities are more likely to cause pseudomonomolecular kinetics. This is favorable, as it significantly narrows down the

number of candidate kinetic models which could explain the observations, see Section 9.4.

4. Smaller pulse sizes are less likely to cause nonisothermicity of the reactor in case of highly exothermal reactions (Schuurman, 2007).

5. Diluting the small pulses of the reactant A_1 with a known quantity of an inert gas A_2 and alternately monitoring A_1, its products and A_2 allows an accurate determination of the average pulsed quantity n_A/n_r, see below.

Taking into account a poorly reproducible pulse size

In view of the small duration (typically 100 µs) of the pulses, the high-speed pulse valves are probably technically the most advanced part of the TAP-setup. A short-term random variation on the order of 5 % of the pulse size, see Section 5.10, is probably unavoidable. As an illustration, the relative standard deviation of the random variation of the M_0's represented in Fig. 9.2 is given in Table 9.1.

Knowledge of the pulse size is generally an important advantage during the estimation of kinetic coefficients, but determining it is not an easy task. A well-known technique consists of mixing known quantities of a reactant A_1 and an inert gas A_2. The mixture with known composition is then fed pulsewise to the reactor in order to collect a series of replicates of a state-defining experiment. The mass spectrometer alternately records time series at masses due to A_1 and its products, and the inert A_2. As far as the latter is concerned, the mass spectrometer should monitor a mass uniquely due to A_2, i.e., without contributions of A_1 or one of its reaction products. With known calibration coefficient and assuming a stable sensitivity of the mass spectrometer, calculation of the M_0 of the corresponding time series allows to determine the average quantity of A_2 pulsed. As the composition of the feed mixture is known, the average quantity of A_1 pulsed can be readily derived. Even though the masses due to A_1, its products and A_2 are monitored as a response to different pulses with random size, it can be assumed that averaging attenuates the random differences sufficiently. The quality of this approximation obviously improves if more replicates are collected.

If the aforementioned technique cannot be applied, it may be necessary to treat them as unknown parameters during regression. The drawback is that this will broaden the confidence intervals of the relevant kinetic parameters to an extent depending mainly on the binary correlation coefficients between the latter and the unknown pulse sizes. Of course it has to be verified whether the estimated pulse sizes are within the range of credibility. For the collection of data presented in Section 9.2, pure

propane and propene were pulsed. It was therefore not possible to obtain a precise estimate of the average pulse size. The pulse sizes have therefore been treated as unknown parameters during regression, see Section 9.6.

Pseudomonomolecular kinetics

The smaller the size of the pulse, the more likely the kinetics degenerate to pseudomonomolecular. This is favorable:

1. Information about a reaction network is often extracted by identifying the kinetic model. The space of candidate linear kinetic models is considerably smaller than the space of candidate general kinetic models. This renders the identification of the model less arduous.

2. Initial surface concentrations and the total concentrations of active sites need not be known at regression, although estimated apparent rate coefficients or pre-exponential factors do generally depend on them. Knowledge of the type of adsorption (Langmuir/Temkin/Freundlich) is not needed either, at least not in the isothermal case.

3. Pulse responses can be model-calculated using the transfer matrix approach, see Section 4.4. This occurs faster and more accurately than the alternative, the method of lines.

4. If a TZTR is used, certain connectivity features of the reaction network can be determined in a model-free manner after applying the Y-procedure, see Chapter 8.

9.4 Regression of data from state-defining experiments

Parsimonious kinetic models

The TAP-reactor, like any laboratory reactor to study reaction kinetics, was designed to keep the transport mechanism mathematically as simple and experimentally as well-defined as possible, see Section 4.2. If possible, simplicity should also be pursued in the kinetic model, albeit for a different reason. Complexity of the model can be expressed as its *dimension*: its number of unknown parameters. Regression with high-dimensional kinetic models involves certain risks:

1. With many parameters, there is a high chance that after some iterative adjustments of their values, small individual variations of

some of these parameters no longer significantly affect the model-calculations. Another possibility is that certain parameters show a high level of correlation. This means that variations of any of them are near-perfectly compensated for by variations of any of the others. In the best case, both phenomena cause intolerably wide confidence intervals of certain parameters. In a worse case, parameters are 'dropped' by the iterative regression procedure, because the model-calculations are completely insensitive to them, taking into account the numerical round-off errors. In the worst case, the iterative estimation algorithm overadjusts the value of certain parameters. These parameters then take on unrealistic values which cause the model-calculation routine and therefore the whole regression attempt to fail. Advanced regression routines allow setting boundaries of acceptability for each parameter, which prevents this issue.

2. High-dimensional models show a larger chance of multiple local minima for the sum of square residuals. If the initial estimates are not chosen appropriately, the iteration will lead to nonoptimal estimates.

3. A regression with many parameters is more likely to yield a better degree of correspondence between the experimental and model-calculated responses, because there are more degrees of freedom for the model to adjust to the data. The more complex the model, however, the higher the chance that certain subtleties of the observations are artificially accounted for, i.e., without the kinetic model being physically representative. Indeed, other but equally complex kinetic models would probably provide a similar quality of correspondence. The subtleties of the observations can actually be due to inaccuracies of the physical instead of the kinetic model, for example.

Whether one of the problems mentioned under 1 has occurred, is immediately apparent from the results of the regression. This will be illustrated by the example in Section 9.6. It is more difficult to recognize problem 2. Schuurman (2007) advised the experimentalist to try several sets of initial values. Finally, it is essentially impossible to identify problem 3. Indeed, there is unfortunately no way to assess whether or not certain subtleties of a complex kinetic model are representative for the reality or not. This is the most important reason to avoid high-dimensional models, although this is a relative concept. Data sets rich in information certainly justify higher-dimensional models.

The construction of candidate reaction networks should not be driven by an urge for chemical completeness. Indeed, it is highly unlikely that all actually occurring elementary steps are manifested in the experimental data. It is far more realistic to believe that the rate coefficients have well-separated magnitudes, leading to asymptotic kinetics which can be described by simplified reaction networks, see Section 2.6. The experimentalist should therefore first try parsimonious kinetic models to describe the data. If those do not provide a good correspondence between model and experiment, he should gradually increase the level of complexity.

Regression of raw experimental data

Consider a set of raw experimental pulse responses $\mathbf{y}_v$, $v \in \{1, 2, \ldots, n_v\}$,

$$\mathbf{y}_v = \begin{bmatrix} y_v(t_1) \\ y_v(t_2) \\ \vdots \\ y_v(t_{n_t}) \end{bmatrix}, \tag{9.4}$$

where the times t_k are given by Eq. (4.12). The raw time series $\mathbf{y}_v$ in V are usually transformed into molar flow rate time series $\tilde{\mathbf{y}}_g$ in mol/s, where g represents one of the n_g gas component present: $g \in \{1, 2, \ldots, n_g\}$. This, however, is not always possible. Each element of the raw time series generally depends on all molar flow rates:

$$\begin{bmatrix} y_1(t_k) \\ y_2(t_k) \\ \vdots \\ y_{n_v}(t_k) \end{bmatrix} = \mathbf{S} \cdot \begin{bmatrix} \tilde{y}_1(t_k) \\ \tilde{y}_2(t_k) \\ \vdots \\ \tilde{y}_{n_g}(t_k) \end{bmatrix}, \tag{9.5}$$

where $k \in \{1, 2, \ldots, n_t\}$. If the number n_v of masses monitored by the mass spectrometer is equal to the number of gases n_g, $\mathbf{S}$ is a square matrix and the vector of molar flow rates can be readily estimated as

$$\begin{bmatrix} \tilde{y}_1(t_k) \\ \tilde{y}_2(t_k) \\ \vdots \\ \tilde{y}_{n_g}(t_k) \end{bmatrix} = \mathbf{S}^{-1} \cdot \begin{bmatrix} y_1(t_k) \\ y_2(t_k) \\ \vdots \\ y_{n_v}(t_k) \end{bmatrix}. \tag{9.6}$$

If n_v is larger than n_g, the inverse $\mathbf{S}^{-1}$ in Eq. (9.6) can be replaced by the more general *Moore-Penrose inverse* or *pseudoinverse* $\mathbf{S}^{\dagger}$,

$$\mathbf{S}^{\dagger} = (\mathbf{S}^T \cdot \mathbf{S})^{-1} \cdot \mathbf{S}^T. \tag{9.7}$$

This amounts to calculating a least-squares estimate of the molar flow rates from redundant spectrometric data. If fewer masses are monitored by the mass spectrometer than the number of gases, $n_v < n_g$, it is essentially impossible to derive the molar flow rates from the spectrometric data in a model-free manner. This, however, does not mean that such data are not eligible for regression.

Even if $n_v \geqslant n_g$, it may be impossible to transform the raw time series into molar flow rate time series. Recall that each raw time series is the result of a different pulse experiment, since the different masses of the spectrum cannot be monitored simultaneously by the mass spectrometer. It is therefore possible that each time series is recorded with a different collection time and/or sampling interval. In this case an inversion like Eq. (9.6) is generally not possible, because a full vector of measurements corresponding to the same time is needed to the right hand side. An inversion such as Eq. (9.6) is also not possible if the different raw time series have been collected as a response to pulses of different sizes.

Suppose it ís possible to calculate molar flow rate time series $\tilde{\mathbf{y}}_g$. Then usually, a vector $\mathbf{b}$ of unknown parameters would be estimated by subjecting these time series $\tilde{\mathbf{y}}_g$ to NLSQ regression with their model calculated analogues. However, it was demonstrated in Chapter 6 that if replicate-experimental data are available, it is better to apply the SOSR. Compared to direct NLSQ regression, SOSR yields a more accurate estimate of $\mathbf{b}$ and more accurate statistics about this estimate. Observe, however, that Assumption 6.2 on p. 79 is generally fulfilled for the raw time series $\mathbf{y}_v$, because each is obtained independently, but not for the molar flow rate time series $\tilde{\mathbf{y}}_g$. Indeed, the elements in the vector to the right hand side of Eq. (9.6) are statistically independent, but those of the vector to the left hand side are generally not. Indeed, cross-correlations generally exist between the time series $\tilde{\mathbf{y}}_g$. The error in $y_{e,1}(t_k)$, for example, generally has an influence on all of the elements $\tilde{y}_{e,g}(t_k)$, $g \in \{1, 2, \ldots, n_g\}$. The latter are therefore generally statistically dependent and correlated. It is therefore better practice to regress the raw data $\mathbf{y}_v$ than the processed data $\tilde{\mathbf{y}}_g$. Model-calculated analogues of $y_v(t_k)$ are obtained by applying Eq. (9.5) with a vector of model-calculated molar flow rates to the right hand side.

In order to illustrate that SOSR of the raw data is to the best practice, consider a numerical experiment. A three-zone TAP reactor was assumed, in which each zone had the same width: $\Delta z^{(1)} = \Delta z^{(2)} = \Delta z^{(3)} = 1\,\mathrm{cm}$. The cross-sectional surface area was $\phi = 1.86 \cdot 10^{-5}\,\mathrm{m}^2$, which corresponds to an inner reactor diameter of about 5 mm. Each zone was assumed to have the same bed porosity: $\epsilon_b^{(1)} = \epsilon_b^{(2)} = \epsilon_b^{(3)} = 0.5$. An experiment was simulated where a quantity $n_1 = 2 \cdot 10^{-9}\,\mathrm{mol}$ of a

component A_1 was pulsed. A_1 converted into another component A_2 in the central zone, in a single apparent elementary step with rate coefficient $k = 40\,\mathrm{Hz}$. A_1 and A_2 were given an equal Knudsen diffusion coefficient of in all three zones: $\mathscr{D}_{e,1}^{(1)} = \mathscr{D}_{e,1}^{(2)} = \mathscr{D}_{e,1}^{(3)} = \mathscr{D}_{e,2}^{(1)} = \mathscr{D}_{e,2}^{(2)} = \mathscr{D}_{e,2}^{(3)} = 2 \cdot 10^{-3}\,\mathrm{m^2/s}$. Two responses y_1 and y_2 were model-calculated using TAPFIT, see Appendix D. The reactor model was integrated using the transfer matrix approach, see Section 4.4. Each consisted of $n_t = 1000$ samples. The sampling interval was $\Delta t = 1\,\mathrm{ms}$. The Nyquist frequency, see Appendix C, was increased by calculating three interjacent samples between each pair of actual samples. Similarly, to ensure completely extinct pulse responses, they were calculated with double collection times. The extra samples were discarded. The calibration matrix was taken as

$$\mathbf{S} = \begin{bmatrix} 10^6 & 5 \cdot 10^5 \\ 5 \cdot 10^5 & 10^6 \end{bmatrix} \frac{\mathrm{V\,s}}{\mathrm{mol}} \tag{9.8}$$

Artificial noise was superposed on the model-calculated responses to produce one hundred sets of each $n_r = 20$ synthetic replicates. The noise had characteristics typical for a TAP-1-setup. These characteristics are the same as the ones applied in Section 8.4.

Again using TAPFIT, each of the hundred sets of synthetic data were subjected to regression to estimate the rate coefficient k as if it was unknown. First, the traditional approach was applied. The raw time series $\mathbf{y}_1$ and $\mathbf{y}_2$ in V were converted into time series $\tilde{\mathbf{y}}_1$ and $\tilde{\mathbf{y}}_2$ representing the molar flow rate of A_1 and A_2 in mol/s. For each of the synthetic data sets, the average of twenty replicates $\tilde{\mathbf{y}}_1$ and $\tilde{\mathbf{y}}_2$ were subjected to NLSQ regression. The dots in Fig. 9.3 (a) represent the synthetic data, while the line represents the model-calculated time series resulting from NLSQ regression. Fig. 9.4 shows the estimated values of k for each of the hundred data sets. The estimates are shown ranked from low to high, with their 95 % confidence intervals. It would be theoretically expected that ninety five of the hundred confidence intervals contain the real value 40 Hz. However, because the statistical requirements for NLSQ regression are not fulfilled, see Chapter 6, the success rate is much lower, only thirty intervals containing the real value. A better approach consists of applying the SOSR to $\tilde{\mathbf{y}}_1$ and $\tilde{\mathbf{y}}_2$. The visual output is not shown, because it is almost indistinguishable from Fig. 9.3 (a). The confidence intervals of k, however, are quite different from the previous approach. They are shown in Fig. 9.5. Fifty nine of the hundred confidence intervals contain the real value. This is already a better result than the previous one. As mentioned above, an even better practice is the SOSR of raw time series $\mathbf{y}_1$ and $\mathbf{y}_2$. The latter are represented by the dots in Fig. 9.3 (b). The line represents the model-calculated time series resulting from SOSR. The

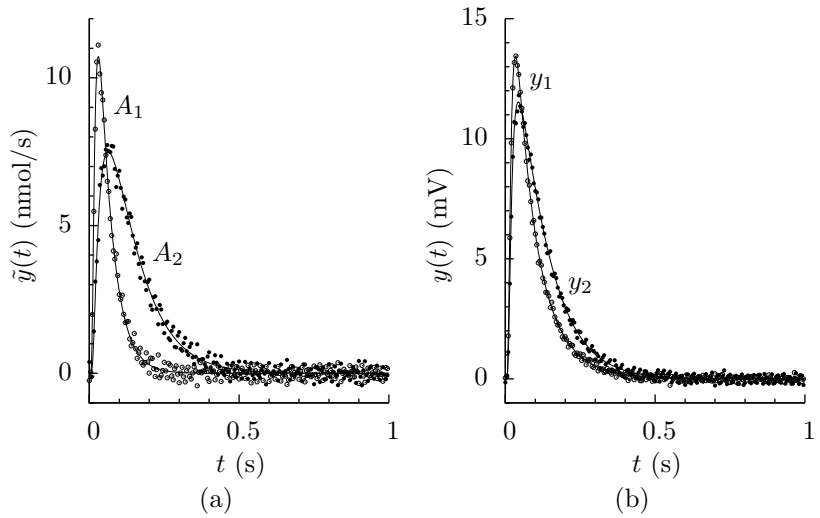

Figure 9.3: Regression of two synthetic TAP time series $\mathbf{y}_1$ and $\mathbf{y}_2$ according to two different approaches. In the first, classical, approach, the raw time series $\mathbf{y}_1$ and $\mathbf{y}_2$, in V, were transformed into two time series $\tilde{\mathbf{y}}_1$ and $\tilde{\mathbf{y}}_2$ representing the molar flow rates of the gas components A_1 and A_2. The latter were then subjected to NLSQ regression. The dots in graph (a) represent $\tilde{\mathbf{y}}_1$ and $\tilde{\mathbf{y}}_2$. The line represents the fitted molar flow rates. In the second approach, the raw time series $\mathbf{y}_1$ and $\mathbf{y}_2$ were directly regressed by SOSR. This is represented in graph (b). In both graphs, only one fifth of data points is shown for the sake of clarity.

estimates of k and their confidence intervals are shown in Fig. 9.6. The real value $k = 40\,\mathrm{Hz}$ is contained in the interval in seventy nine out of a hundred cases. That this result is better than the previous ones illustrates that the best practice for estimating kinetic parameters is the SOSR of raw TAP-data. For that matter, as it was explained above, the regression of preprocessed TAP-data is not always possible as the molar flow rates cannot always be recovered from the raw data. That the success rate is still considerably lower than the theoretically expected one, can be understood because the estimation of second-order statistics, inherent to the SOSR, lacks precision since it is based on just twenty replicates.

The discussion above was limited to the regression of raw time series or molar flow rate time series. An alternative approach is the regression of area-normalized raw pulse responses, in Hz (Weerts et al., 1996; Phanawadee, 1997; Tantake et al., 2007). This is often done if only one mass has been monitored by the mass spectrometer, so that the cali-

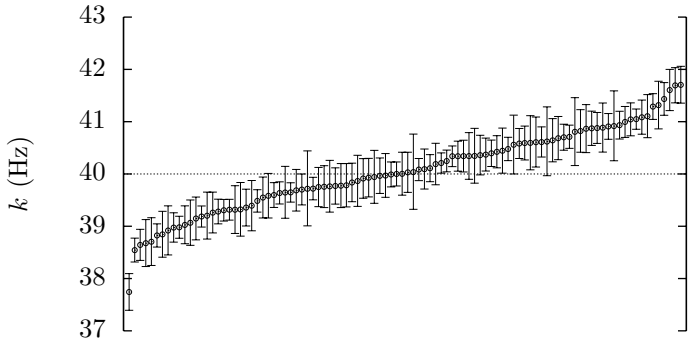

Figure 9.4: Ranked parameter estimates of a rate coefficient k resulting from regression of one hundred sets of each twenty replicate synthetic data. The estimates are shown with their 95 % confidence intervals. In order to obtain the estimates and their confidence intervals, the raw time series in V were first transformed into molar flow rate time series in mol/s, which were then subjected to NLSQ regression.

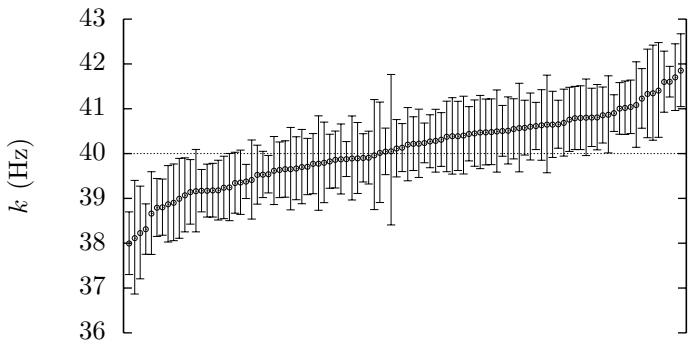

Figure 9.5: Ranked parameter estimates of a rate coefficient k resulting from regression of one hundred sets of each twenty replicate synthetic data. The estimates are shown with their 95 % confidence intervals. In order to obtain the estimates and their confidence intervals, the raw time series in V were first transformed into molar flow rate time series in mol/s, which were then subjected to SOSR.

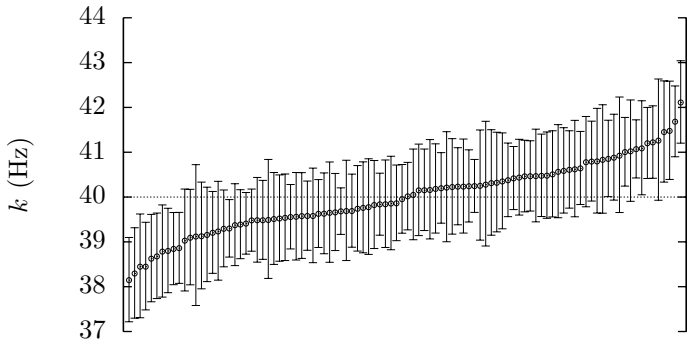

Figure 9.6: Ranked parameter estimates of a rate coefficient k resulting from regression of one hundred sets of each twenty replicate synthetic data. The estimates are shown with their 95 % confidence intervals. In order to obtain the estimates and their confidence intervals, the raw time series in V were directly subjected to SOSR.

bration matrix **S** reduces to a scalar. In the case of linear kinetics, the area-normalized raw pulse responses can be regressed with equally area-normalized model-calculated responses. Thus, only the shape of the pulse responses is being used to extract information. This has the advantage that the calibration coefficient need not be known. The regression of area-normalized raw pulse responses is actually equivalent to the regression of the raw pulse responses, estimating the pulse size as an extra parameter. In this case, a value for the calibration factor does need to be provided by the user. However, possible errors in this calibration factor affect only the estimate of the pulse size, not the estimate of the other parameters. On the other hand, the estimated pulse size should be realistic if the calibration factor is roughly correct. This offers a way to verify whether the result of the regression is realistic. This verification cannot be carried out from regression of area-normalized responses.

Estimation of logarithms of kinetic parameters

It was mentioned in Section 9.3 that iterative least-squares regression routines such as the Levenberg-Marquardt routine sometimes adjust parameters so, that they take on unrealistic values. This can occur if the regression routine does not allow the user to set limits of acceptability for the parameter values, or if the user has neglected to provide them. Specifically, kinetic parameters, such as rate coefficients, pre-exponential

factors and activation energies may become negative, which can cause the model-calculation routine to fail. This can be avoided in a simple way, by estimating logarithms of the kinetic parameters instead of the parameters themselves. Should the optimal value of a kinetic parameter be zero or, unrealistically, negative, its logarithm will be dropped at a very negative value.

Separate estimation of physical variables

The parameters in the physico-chemical model of TAP-experiments, are either physical (pulse sizes, diffusion coefficients, ...) or kinetic (rate coefficients, pre-exponential factors or activation energies) in nature. Of course the kineticist is most interested in the kinetic parameters. Generally, estimating the physical parameters along with the kinetic ones, causes the confidence intervals of the latter to widen. This is especially true for kinetic parameters the estimates of which show a high correlation with the estimate of at least one physical parameter. As an example, consider the adsorption coefficient k_a of oxygen on the V150 catalyst, estimated from a TAP-experiment, together with the effective Knudsen diffusion coefficient $\mathscr{D}_{e,\mathrm{O}_2}$ of oxygen, the pulse size n_{O_2} and baseline position u_0 in Section 6.5. The estimate of k_a was shown to be rather highly correlated with the estimates of $\mathscr{D}_{e,\mathrm{O}_2}$ and n_{O_2}. If possible, physical parameters such as $\mathscr{D}_{e,\mathrm{O}_2}$ and n_{O_2} should be independently estimated from separate, non-reactive experiments. At the same time, it should be clear that their estimation has to be accurate. Indeed, significant errors in these values of the physical variables will cause equally significant errors in the values of the kinetic parameters.

9.5 Reaction network selection

Nonlinear least-squares regression of kinetic data is the key to the statistically sound discrimination between rival kinetic models, and hence between the corresponding reaction networks (Froment and Hosten, 1981). Many statistical criteria are available allowing a selection between models after least-squares regression. Here, the *Bayesian information criterion* (BIC), introduced by Schwarz (1978), will be presented.

The BIC attributes a score with the same name, BIC, to each of the models. The model with the lowest BIC-value is selected. This value is defined for a model j as

$$BIC_j = -2 \ln L_j + p_j \ln n, \tag{9.9}$$

where p_j is the dimension of model j, i.e., its number of parameters, and n is the number of dependent variables. L_j is the likelihood of the model,

after maximization by least-squares estimation of its parameters. Suppose $\mathbf{y}$ is the vector of dependent variables and $\mathbf{f}_j(\hat{\boldsymbol{\beta}}_j)$ is its analogue calculated using model j, where $\hat{\boldsymbol{\beta}}_j$ represents the vector of corresponding parameter estimates. Assume the Conditions 6.4, 6.5 and 6.6 on p. 78 are fulfilled: all dependent variables, the elements of $\mathbf{y}$, are independently normally distributed and their variance σ^2 is constant. Then the likelihood L of model j is given as

$$L_j = \frac{1}{(2\pi\sigma^2)^{n/2}} \exp\left(-\frac{1}{2} \frac{\left\| \mathbf{y} - \mathbf{f}_j(\hat{\boldsymbol{\beta}}_j) \right\|^2}{\sigma^2} \right), \tag{9.10}$$

The variance σ^2 is estimated based on model j as the residual mean square,

$$\sigma^2 \approx s_j^2 = \frac{\left\| \mathbf{y} - \mathbf{f}_j(\hat{\boldsymbol{\beta}}_j) \right\|^2}{n - p_j}, \tag{9.11}$$

Substituting Eq. (9.11) in Eq. (9.10) yields

$$L_j = \frac{\exp\left(-\frac{n-p_j}{2} \right)}{(2\pi s_j^2)^{n/2}}. \tag{9.12}$$

After some manipulations, substitution of Eq. (9.12) in the definition (9.9) gives

$$BIC_j = n\left[1 + \ln\left(2\pi s_j^2\right)\right] + p_j \left(\ln n - 1\right), \tag{9.13}$$

The better the description of the data, the lower s_j and the higher the probability that the model will be selected. The second term in Eq. (9.13) attributes a penalty to each model, depending on its dimension p_j. The more parameters a model needs to describe the data, the lower the probability that it will be selected. This why the BIC is often applied in areas where a low dimension of the models is critical.

Observe that through s_j^2, the BIC-value depends additively on the unit of the dependent variable. But this does not pose a problem, because only the differences between the BIC-values of the candidate models is relevant. If a reference model is chosen, the value

$$\Delta_j BIC = BIC_j - BIC_{\text{ref}} \tag{9.14}$$

does no longer depend on the unit of the dependent variable and can be used for selection.

9.6 Example

Consider again the state-defining TAP-data obtained on the EL10V1 catalyst, see Section 9.2. Using TAPFIT, these data will now be subjected to SOSR with three physico-chemical models, identical apart from the reaction network assumed. For its regression part, TAPFIT relies completely on ODRPACK (Boggs et al., 1987). One of the candidate networks will be selected using the BIC. Each of the candidate reaction networks is pseudomonomolecular. The integration of the TAP reactor models therefore has been carried out using the transfer matrix approach. The initial and boundary conditions were the ideal ones described in Section 4.3. Two interjacent samples were calculated between each pair of actual samples to make sure the Nyquist frequency was high enough for an accurate simulation. The extra samples were immediately discarded. Using the known calibration matrix $\mathbf{S}$ in Eq. (9.3), the model-calculated molar flow rate time series were transformed into analogues of the raw experimental time series.

As it was mentioned in Section 9.3, an accurate estimate of the pulse sizes is not available. The pulse sizes of propane at the six different reactor temperatures, $n_{C_3H_8}(698\,\mathrm{K})$, $n_{C_3H_8}(723\,\mathrm{K})$, $n_{C_3H_8}(748\,\mathrm{K})$, $n_{C_3H_8}(773\,\mathrm{K})$, $n_{C_3H_8}(798\,\mathrm{K})$ and $n_{C_3H_8}(823\,\mathrm{K})$, and the pulse size of propene at 723 K, $n_{C_3H_6}(723\,\mathrm{K})$, therefore have to be estimated along with the kinetic parameters. For each component, the Knudsen diffusion coefficient was assumed equal in all zones. Argon was pulsed over the reactor in a separate experiment at 672 K. Regression of the resulting time series yielded a Knudsen diffusion coefficient of

$$\mathscr{D}_{e,\mathrm{ref}} = 1.866 \cdot 10^{-3}\,\mathrm{m}^2/\mathrm{s} \tag{9.15}$$

All diffusion coefficients were derived from this reference diffusion coefficient using Eq. (4.3).

Reaction network 1

A parsimonious reaction network was postulated to represent the interaction of propane and propene with the catalyst. This reaction network is represented by the reaction graph in Fig. 9.7. The oxidative dehydrogenation of propane to propene apparently occurs in one elementary step, while both propane and propene undergo an irreversible apparent elementary step leading to a surface precursor of carbon monoxide or carbon dioxide in a way which is not further specified. The Arrhenius relation (1.4) has been reparametrized in order to avoid important corre-

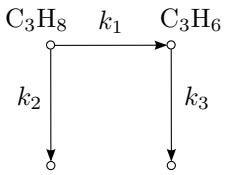

Figure 9.7: A reaction graph representing the interaction of propane and propene with the catalyst according to reaction network 1.

lations between the pre-exponential factors and the activation energies:

$$k_1 = k_{1,\mathrm{ref}} \exp\left(-\frac{E_1}{R}\left(\frac{1}{T} - \frac{1}{T_{\mathrm{ref}}}\right)\right), \tag{9.16}$$

and analogous for k_2 and k_3. $k_{1,\mathrm{ref}}$ represents the rate coefficient k_1 at the reference temperature T_{ref}, which was chosen here as the geometric mean of the extreme temperatures:

$$T_{\mathrm{ref}} = 758\,\mathrm{K} \approx \sqrt{698\,\mathrm{K} \cdot 823\,\mathrm{K}}. \tag{9.17}$$

The natural logarithms

$$k'_{1,\mathrm{ref}} = \ln\left(\frac{k_{1,\mathrm{ref}}}{1\,\mathrm{Hz}}\right),\ E'_1 = \ln\left(\frac{E_1}{1\,\mathrm{J/mol}}\right) \tag{9.18a}$$

$$k'_{2,\mathrm{ref}} = \ln\left(\frac{k_{2,\mathrm{ref}}}{1\,\mathrm{Hz}}\right),\ E'_2 = \ln\left(\frac{E_2}{1\,\mathrm{J/mol}}\right) \tag{9.18b}$$

$$k'_{3,\mathrm{ref}} = \ln\left(\frac{k_{3,\mathrm{ref}}}{1\,\mathrm{Hz}}\right),\ E'_3 = \ln\left(\frac{E_3}{1\,\mathrm{J/mol}}\right) \tag{9.18c}$$

were estimated along with the pulse sizes, by subjecting the raw data to SOSR. The regression was repeated with different sets of initial values. It was found to give the same result in all cases. Fig. 9.8 shows the first 0.6 s of the experimental time series and their model-calculated analogues resulting from SOSR. Fig. 9.8 (a) represents the responses to propane. Only the extreme temperatures 698 K and 823 K are represented for the sake of clarity. Fig. 9.8 (b) represents the responses to propene. The regression has a visibly good quality. The multiple correlation coefficient is 0.998. The parameter estimates and their 95% confidence intervals are given in Table 9.2. Since the logarithms of the kinetic parameters were estimated, their confidence intervals are not symmetric around the estimate. The pulsed quantities of propane are all estimated at realistic values of about 2 nmol. The confidence intervals prove the small variations

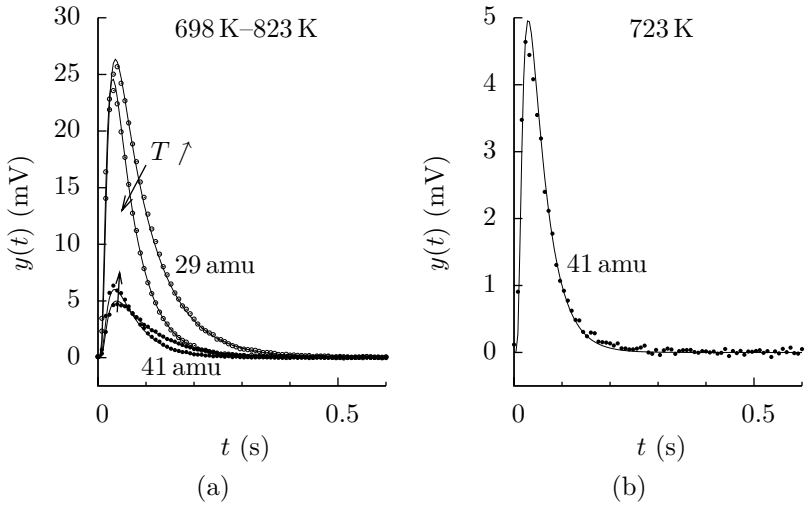

Figure 9.8: Average of twenty replicate-experimental time series measured at 29 amu (propane) and 41 amu (propene, propane) obtained on a three-zone TAP reactor with central zone loaded with EL10V1 catalyst. The time series have been obtained as responses to pulses of propane at reactor temperatures ranging from 698 K to 823 K (a) and propene at 723 K (b). The lines represent the model-calculated time series resulting from SOSR assuming reaction network 1, represented by the reaction graph in Fig. 9.7.

of the estimates significant. This variation could not have been predicted. The pulsed quantity of propene is estimated significantly lower than the pulsed quantities of propane. But this was expected because the pulse valve opening time was set lower than for the propane pulses. Luckily, the confidence intervals of the kinetic parameters are not widened too much by estimating them together with the pulse sizes. Indeed, the estimates of the pulse sizes are rather weakly correlated with the kinetic parameters. Of all binary correlation coefficients, the one having the largest magnitude is

$$\rho\left(n_{\mathrm{C_3H_6}}(723\,\mathrm{K}), k'_{3,\mathrm{ref}}\right) = 0.64. \tag{9.19}$$

The correlation coefficients between the kinetic estimates are shown in Table 9.3. They are all moderate. Thanks to the reparametrization (9.16), the correlation coefficients between the logarithm of the reference rate coefficients, $k'_{j,\mathrm{ref}}$, and the logarithm of the corresponding activation energies, E'_j, is rather weak. The most important correlation is a negative

Table 9.2: Parameter estimates obtained from SOSR of three-zone-TAP-data with the reaction network 1, represented by the reaction graph in Fig. 9.7.

	estimate	95% confidence interval	
$n_{C_3H_8}(698\,K)$ (nmol)	2.000	1.952,	2.047
$n_{C_3H_8}(723\,K)$ (nmol)	2.042	1.988,	2.095
$n_{C_3H_8}(748\,K)$ (nmol)	2.199	2.146,	2.253
$n_{C_3H_8}(773\,K)$ (nmol)	2.098	2.037,	2.160
$n_{C_3H_8}(798\,K)$ (nmol)	2.114	2.057,	2.170
$n_{C_3H_8}(823\,K)$ (nmol)	1.969	1.915,	2.024
$n_{C_3H_6}(723\,K)$ (nmol)	0.654	0.590,	0.719
$k_{1,ref}$ (Hz)	5.031	4.499,	5.626
E_1 (kJ/mol)	66.30	57.89,	75.92
$k_{2,ref}$ (Hz)	4.554	3.941,	5.263
E_2 (kJ/mol)	19.80	9.581,	40.91
$k_{3,ref}$ (Hz)	43.75	39.37,	48.62
E_3 (kJ/mol)	44.83	35.35,	56.87

one between $k'_{1,ref}$ and $k'_{2,ref}$:

$$\rho\left(k'_{1,ref}, k'_{2,ref}\right) = -0.91. \tag{9.20}$$

This can be understood because they have exactly the same effect on the conversion of propane. The most precise kinetic estimates are the ones of $k_{1,ref}$ and E_1. The estimates of $k_{2,ref}$, E_2, $k_{3,ref}$ and E_4 have wider confidence intervals, but are all still significant. Propene and the oxygenated products carbon monoxide and carbon dioxide are formed parallel-consecutively, in correspondence with the results of Sack et al. (Sack, 2006; Balcaen et al., 2009). The oxidative dehydrogenation of propane to propene requires the highest activation: $E_1 = 66.30\,kJ/mol$, while step 3 probably requires more activation than step 2. Even though reaction network 1 already provides a satisfactory description of the data, two slightly more complex reaction networks were tested, each having one more apparent elementary step.

Reaction network 2

Reaction network 2 is represented by the reaction graph depicted in Fig. 9.9. Compared to reaction network 1, it contains an extra reaction step between propane and the other components, possibly representing the adsorption of propane. The visual result of the regression will not be

Table 9.3: Binary correlation coefficients between the kinetic parameter estimates obtained from SOSR of three-zone-TAP-data with the reaction network 1, represented by the reaction graph in Fig. 9.7.

	$k'_{1,\mathrm{ref}}$	E'_1	$k'_{2,\mathrm{ref}}$	E'_2	$k'_{3,\mathrm{ref}}$	E'_3
$k'_{1,\mathrm{ref}}$	1	−0.10	−0.91	−0.41	0.78	0.11
E'_1		1	−0.14	−0.75	−0.03	0.62
$k'_{2,\mathrm{ref}}$			1	0.55	−0.80	−0.24
E'_2				1	−0.34	−0.70
$k'_{3,\mathrm{ref}}$					1	0.06
E'_3						1

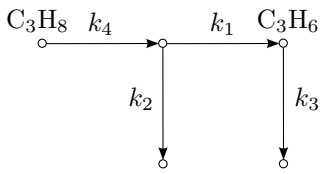

Figure 9.9: A reaction graph representing the interaction of propane and propene with the catalyst according to reaction network 2.

shown, because it is very similar to the one represented in Fig. 9.8. The multiple correlation coefficient is still 0.998. The parameter estimates are given in Table 9.4, while the binary correlation coefficients are shown in Table 9.5. The correlations between the pulse sizes and the kinetic parameters have not been shown. As before, they are rather weak. To mention just the most important one:

$$\rho\left(n_{\mathrm{C_3H_8}}(698\,\mathrm{K}), E'_4\right) = -0.59. \tag{9.21}$$

Clearly, the estimates pertaining to the steps 1 and 2 are problematic. A quick verification shows that the regression routine has made these steps much faster than the other steps, at all temperatures. The final estimates of $k'_{1,\mathrm{ref}}$, E'_1, $k'_{2,\mathrm{ref}}$ and E'_2 are so high, that each pair of them shows a near-perfect correlation, see Table 9.5. As a result, the confidence intervals are infinitely wide. For that matter, when the regression was repeated several times with different sets of initial estimates, different estimates of $k'_{1,\mathrm{ref}}$, E'_1, $k'_{2,\mathrm{ref}}$ and E'_2 were obtained, while the estimates of the other kinetic parameters and the residual sum of squares remained the same. In any case, the estimates were always so, that the rate coefficients k_1 and k_2

Table 9.4: Parameter estimates obtained from SOSR of three-zone-TAP-data with the reaction network 2, represented by the reaction graph in Fig. 9.9.

	estimate	95% confidence interval
$n_{C_3H_8}(698\,K)$ (nmol)	1.990	[1.947, 2.034]
$n_{C_3H_8}(723\,K)$ (nmol)	2.047	[1.991, 2.102]
$n_{C_3H_8}(748\,K)$ (nmol)	2.208	[2.153, 2.263]
$n_{C_3H_8}(773\,K)$ (nmol)	2.099	[2.036, 2.163]
$n_{C_3H_8}(798\,K)$ (nmol)	2.110	[2.052, 2.169]
$n_{C_3H_8}(823\,K)$ (nmol)	1.958	[1.902, 2.014]
$n_{C_3H_6}(723\,K)$ (nmol)	0.666	[0.598, 0.734]
$k_{1,ref}$ (Hz)	$2.228 \cdot 10^{13}$	$[0, +\infty]$
E_1 (kJ/mol)	1969	$[0, +\infty]$
$k_{2,ref}$ (Hz)	$1.953 \cdot 10^{13}$	$[0, +\infty]$
E_2 (kJ/mol)	1914	$[0, +\infty]$
$k_{3,ref}$ (Hz)	3.808	[3.693, 3.922]
E_3 (kJ/mol)	44.81	[33.68, 59.62]
$k_{4,ref}$ (Hz)	9.760	[9.519, 10.01]
E_4 (kJ/mol)	44.16	[41.04, 47.51]

Table 9.5: Binary correlation coefficients between the kinetic parameter estimates obtained from SOSR of three-zone-TAP-data with the reaction network 2, represented by the reaction graph in Fig. 9.9.

	$k'_{1,ref}$	E'_1	$k'_{2,ref}$	E'_2	$k'_{3,ref}$	E'_3	$k'_{4,ref}$	E'_4
$k'_{1,ref}$	1	1.00	1.00	1.00	−0.03	0.05	−0.07	0.07
E'_1		1	1.00	1.00	−0.03	0.05	−0.07	0.07
$k'_{2,ref}$			1	1.00	−0.03	0.05	−0.07	0.07
E'_2				1	−0.03	0.05	−0.07	0.07
$k'_{3,ref}$					1	0.22	−0.19	−0.16
E'_3						1	−0.05	−0.30
$k'_{4,ref}$							1	−0.43
E'_4								1

Table 9.6: Parameter estimates obtained from SOSR of three-zone-TAP-data with the reaction network 3, represented by the reaction graph in Fig. 9.10.

	estimate	95% confidence interval
$n_{C_3H_8}(698\,K)$ (nmol)	2.020	[1.965, 2.075]
$n_{C_3H_8}(723\,K)$ (nmol)	2.055	[1.999, 2.111]
$n_{C_3H_8}(748\,K)$ (nmol)	2.206	[2.152, 2.260]
$n_{C_3H_8}(773\,K)$ (nmol)	2.098	[2.036, 2.159]
$n_{C_3H_8}(798\,K)$ (nmol)	2.107	[2.050, 2.163]
$n_{C_3H_8}(823\,K)$ (nmol)	1.966	[1.911, 2.020]
$n_{C_3H_6}(723\,K)$ (nmol)	0.666	[0.596, 0.733]
$k_{1,ref}$ (Hz)	5.015	[4.482, 5.611]
E_1 (kJ/mol)	69.15	[60.73, 78.74]
$k_{2,ref}$ (Hz)	4.566	[3.953, 5.273]
E_2 (kJ/mol)	14.28	[4.962, 41.11]
$k_{3,ref}$ (Hz)	44.59	[40.11, 49.56]
E_3 (kJ/mol)	43.63	[34.60, 55.02]
$k_{4,ref}$ (Hz)	$4.850 \cdot 10^8$	[0, $+\infty$]
E_4 (kJ/mol)	1133	[0, $+\infty$]

could be considered infinitely large, although their ratio remained the same. All this indicates that there is apparently just one elementary step between propane and propene. Except the near-perfect correlations mentioned above, the binary correlations between the kinetic coefficients is weak.

Taking reaction network 1 as a reference, the BIC-score for reaction network 2 is

$$\Delta_2 BIC = -1.97 + 8.98 = 7.01, \tag{9.22}$$

where the first term is due to the improved description of the data and the second term represents the penalty due to the dimension of the model. The second term prevails, which confirms the supposition that reaction network 2 is not a valuable extension of reaction network 1.

Reaction network 3

Reaction network 3, represented by the reaction graph depicted in Fig. 9.10, is an alternative extension of reaction network 1. It includes an extra step in the oxidative hydrogenation. The visual result of the regression will not be shown, because it is again very similar to the one represented in Fig. 9.8. For that matter, the multiple correlation coefficient remains

Table 9.7: Binary correlation coefficients between the kinetic parameter estimates obtained from SOSR of three-zone-TAP-data with the reaction network 3, represented by the reaction graph in Fig. 9.10.

	E'_1	$k'_{2,\mathrm{ref}}$	E'_2	$k'_{3,\mathrm{ref}}$	E'_3	$k'_{4,\mathrm{ref}}$	E'_4
$k'_{1,\mathrm{ref}}$	−0.21	−0.91	−0.37	0.74	0.09	0.16	0.16
E'_1	1	−0.03	−0.72	−0.02	0.45	−0.18	−0.18
$k'_{2,\mathrm{ref}}$		1	0.51	−0.76	−0.21	−0.14	−0.14
E'_2			1	−0.41	−0.51	0.10	0.10
$k'_{3,\mathrm{ref}}$				1	−0.02	−0.03	−0.03
E'_3					1	0.11	0.11
$k'_{4,\mathrm{ref}}$						1	1.00
E'_4							1

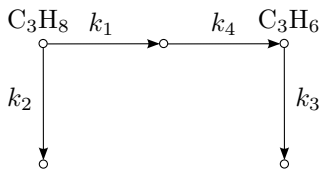

Figure 9.10: A reaction graph representing the interaction of propane and propene with the catalyst according to reaction network 3.

0.998. The parameter estimates are given in Table 9.6, while the binary correlation coefficients for the kinetic parameters are shown in Table 9.7. The correlations between the pulse sizes and the kinetic parameters, not represented in Table 9.7, are again rather weak, the most important correlation being

$$\rho\left(n_{\mathrm{C_3H_6}}(723\,\mathrm{K}), k'_{3,\mathrm{ref}}\right) = 0.68. \tag{9.23}$$

This time, the parameters $k'_{4,\mathrm{ref}}$ and E'_4 pertaining to the step 4 are estimated very high. $k_{4,\mathrm{ref}}$ is estimated at $4.850 \cdot 10^8\,\mathrm{Hz}$, see Table 9.6, which corresponds to $k'_{4,\mathrm{ref}}$ being estimated at 20. This value was provided as an upper limit of acceptability. Without this upper limit, the parameter is given even higher values, which eventually cause the model-calculation routine to fail. This happens more specifically because the matrix $\tilde{\mathbf{H}}^{(l)}(s) \cdot \tilde{\mathbf{F}}^{(l)}$ in Eq. (4.34) becomes quasisingular. In any case, $k'_{4,\mathrm{ref}}$ and E'_4 are estimated so high that they show a near-perfect mutual binary correlation and infinitely wide confidence intervals. It can be readily verified that the regression routine has made step 4 much faster than

the other steps, at all temperatures. Comparison of Table 9.6 with Table 9.2 and of Table 9.7 with Table 9.3 shows that the estimates for $k'_{1,\mathrm{ref}}$, E'_1, $k'_{2,\mathrm{ref}}$, E'_2, $k'_{3,\mathrm{ref}}$ and E'_3 and their mutual binary correlation coefficients are close to their counterparts for reaction network 1. In summary, the regression routine practically reduces reaction network 3 to network 1. This indicates again that there is apparently just one elementary step between propane and propene.

The BIC-score for reaction network 3 is

$$\Delta_3 BIC = -5.50 + 8.98 = 3.48, \tag{9.24}$$

where the first term is due to the improved description of the data and the second term represents the penalty due to the dimension of the model. Albeit less convincingly, the second term prevails. The reaction network selection is therefore concluded in favor of network 1.

9.7 Conclusions

In view of the complexity of the TAP-apparatus, its user has to take into account certain technical limitations. As a result, in order to be able to extract quantitative information, he should observe a set of guidelines. First of all, small pulses should be applied, allowing

1. operation in the Knudsen diffusion regime, ensuring easy modeling and excluding gas-phase reactions;
2. pseudomonomolecular kinetics, reducing the space of candidate reaction networks;
3. the collection of replicate state-defining data, enabling the extraction of second-order statistical information;
4. an isothermal catalytic zone, even if the reaction is highly exothermal;
5. accurate estimation of the pulse size, by alternating pulses of reactant and inert.

Regarding the mass spectrometer, the collection time should be taken long enough to ensure a complete extinction of the pulse response. Spectrally localized noise should be avoided if possible. The sampling interval should not be taken too small. 1 ms suffices as a guideline.

The statistically most rigorous way to extract quantitative data is by least-squares regression. Preconditioning transforms before regression should be limited to baseline-correction. Indeed, transformation of the

raw time series into time series representing molar flow rates introduces cross-correlations between the latter. This has a disadvantageous effect on the accuracy of the parameter estimates and their confidence intervals. In order to avoid widening of these confidence intervals, as far as possible, physical variables such as pulse sizes and diffusion coefficients should be determined independently. Parsimonious kinetic models, representing simple reaction networks, should be given preference in attempts to describe the experimental data. In order to avoid the regression routine to evolve to negative estimates for kinetic parameters, i.e., rate coefficients, pre-exponential factors and activation energies, logarithms of these parameters can be estimated.

The BIC was presented as a criterion to select a reaction network from a set of candidates, after repeated regression of the data. This criterion is particularly suitable since it favors simple reaction networks, represented by parsimonious kinetic models. The criterion was applied to study the nature of the interaction of propane and propene with the EL10V1 catalyst from experimental TAP-data. The results support the idea that propane can be oxidized directly or via propene.

Chapter 10

General Conclusions

In order to study reaction networks, the most valuable data stem from transient experiments. Pseudomonomolecular kinetics can usually be described by a compartmental model. Compartmental kinetics can be represented either analytically or graphically, by a reaction graph. The vertices in this reaction graphs represent components, while arcs connecting them represent elementary steps. The link between the analytical and graphical representations of compartmental kinetics proves especially close in the Laplace-domain, where kinetic transfer functions can be found graph-theoretically from the reaction graph. Kinetic transfer functions $H_{i,j}$ represent the effect of a source of a component A_j on the evolution of the concentration of a component A_i. Especially, the symbolic form of the kinetic transfer functions can be derived from visual inspection of the reaction graph, depending on the number of reaction intermediates between A_j on A_i and the length of the shortest reaction pathway from A_j and A_i. This allowed the formulation of necessary conditions for structural local idenfifiability of the apparent rate coefficients from transient isothermal data in terms of these connectivity features of the reaction network. These conditions were applied to investigate the identifiability of rate coefficients describing the interaction of propane with a $CuO–CeO_2$ catalyst, based on TAP-data. Kinetic transfer functions can be directly implemented in a Laplace-domain expression of the TAP reactor model, allowing the simulation of experiments and the calculation of pulse responses. This method is referred to as the "transfer matrix approach". Albeit somewhat less accurately and with a higher computational cost, simulation is also possible in the wider domain of general kinetics, using the method of lines.

Transient kinetic data can be interpreted in two ways. Either a reaction network is tested or selected, or, if this reaction network is al-

ready assumed known, its kinetic parameters are identified. In both cases, the statistically most rigorous way to proceed is through least-squares regression. Because the reactant pulses in TAP are so small, the mass spectrometer signals are intrinsically weak and therefore sensitive to noise. This noise limits the amount of information which can be extracted by regression. Moreover, TAP-noise was found to have non-ideal properties: non-Gaussian, heteroskedastic and colored. An ideal character of the noise, however, is tacitly assumed when the data are directly subjected to least-squares regression. The matter was resolved by the introduction of the SOSR. The SOSR uses replicate-experimental data to estimate the second-order statistical properties of the noise, relying mainly on PCA. Based on the estimated second-order statistics, the SOSR applies a linear conditioning transform to the data, before subjecting them to least-squares regression. The SOSR results in more accurate parameter estimates and more realistic confidence intervals then direct least-squares regression. This was shown by means of synthetic TAP-experiments. The SOSR was also applied to two experimental examples: the irreversible adsorption of oxygen on the V_2O_5 based V150 catalyst and the interaction of propane with a CuO–CeO_2 catalyst, where the latter was also investigated for identifiability, see above. All this was performed using TAPFIT, a specially developed simulation and regression program. It was shown that the only recommended transform of raw experimental TAP-data before their regression, except for the SOSR conditioning transform, is baseline-correction. Indeed, transformation of the raw time series in V to time series representing molar flow rates in mol/s introduces cross-correlations, which cause inaccurate confidence intervals. This was shown by means of synthetic TAP-data. In any case, due to the technical limitations of the TAP-apparatus, experimentalists should observe certain guidelines. First of all, small pulse sizes have to be applied, not only to ensure Knudsen diffusion and pseudomonomolecular kinetics, see above, but also to be able to collect (more) replicates in view of the SOSR, an isothermal catalytic reactor zone and an accurate estimation of the average pulse size. The pulse spacing and the mass spectrometer collection time have to be taken long enough to ensure a complete extinction of the pulse responses and an accurate baseline-correction. As a rule, the sampling interval need not be chosen smaller than 1 ms. Finally, spectrally localized noise, due to electromagnetic interference, has to be avoided if possible. In preparation of the regression of TAP-data, the physical parameters should be independently identified, if possible. Repeated regression with models assuming different reaction networks, allows the selection of one of them. To this end, the BIC is a particularly attractive criterion, as it favors simple models in the selection. This criterion has been applied to the interaction of propane and propene with

the V_2O_5 based EL10V1 catalyst, as studied by TAP. A simple parallel-consecutive reaction network has been selected, in which propane oxidizes either directly or via the oxidative dehydrogenation to propene.

The selection of a kinetic model among a list of postulated candidates represents the traditional approach of reaction network determination. In this work, a novel approach was explored, allowing the determination of connectivity features of the reaction network in a model-free manner, i.e., without the need to postulate candidate networks. The approach relies on the Y-procedure, as applied to TZTR-data. If certain rather mild conditions are fulfilled, values of the kinetic transfer function can be calculated for equally spaced frequencies. As mentioned above, the symbolic form of the transfer functions reflects connectivity features of the reaction network. Visual inspection of the Bode plots of these functions, allows the determination of these features. The observable shortest reaction path length is determined from the high-frequency limit of the argument. Trends in the Bode plots allow the determination of the observable number of intermediates. Numerical experiments have confirmed the feasibility of this procedure. In the Bode plots, the window of observable frequencies is only limited by spectrally localized and irreducible high-frequency noise.

Appendix A

Graph-Theoretical Notions

Most of the definitions are inspired by (Bang-Jensen and Gutin, 2008).

Definition A.1 (walk)**.** A *walk* of *length* l is an alternating sequence $x_1a_1x_2a_2x_3 \dots x_la_lx_{l+1}$ of vertices x_j and arcs a_j such that for each j, the tail and head of a_j are x_j and x_{j+1}, respectively.

In the digraph shown in Fig. A.1 (a), $x_7a_9x_8a_{10}x_9a_{11}x_8$ is a walk.

Definition A.2 (directed path)**.** A *directed path* of *length* l is a walk of length l in which all vertices are distinct.

Mind that the a_j represent arcs and not weights. Different arcs a_j and a_k can have the same weight, so arc weights generally cannot be used to identify the arc. $x_1a_3x_4a_6x_5a_7x_6$ is a directed path in Fig. A.1 (a). The walk $x_7a_9x_8a_{10}x_9a_{11}x_8$ is not a directed path, as vertex x_8 is visited more than once.

Definition A.3 (cycle)**.** A *cycle* of *length* l is a walk with the same begin- and endvertex, but with all other vertices distinct.

In Fig. A.1 (a), the walk $x_2a_4x_5a_7x_6a_8x_3a_5x_2$ is a cycle.

Definition A.4 (undirected path)**.** An *undirected path* of *length* l is an alternating sequence $x_1a_1x_2a_2x_3 \dots x_la_lx_{l+1}$ of distinct vertices x_j and arcs a_j such that for each j, the tail and head of a_j are x_j and x_{j+1}, irrespective of their order.

Each directed path is also an undirected path. $x_1a_1x_2a_5x_3$ is an undirected path, but not a directed path.

Definition A.5 (linkage, linkage class)**.** If V is the set of vertices of a digraph, a subset is called *linked* if there is at least one undirected path

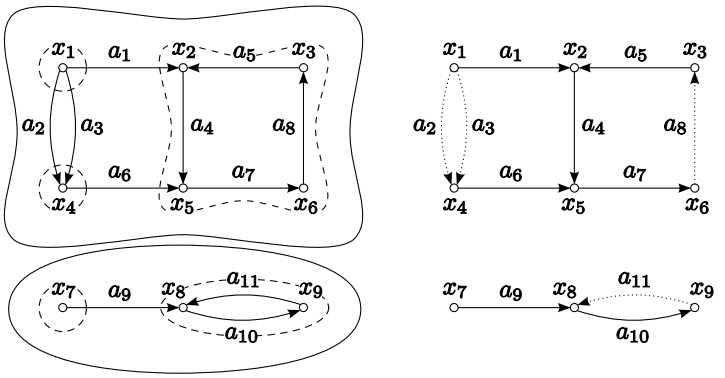

Figure A.1: A digraph partitioned into two linkage classes, delimited by a full line, and five strong linkage classes, delimited by a dashed line.

linking each pair of different vertices contained in V. A vertex singleton is also considered linked. A *linkage class* of a digraph is a maximal linked vertex subset of V.[1] A *trivial linkage class* contains a single vertex.

Definition A.6 (strong linkage, strong linkage class)**.** If V is the set of vertices of a digraph, a subset is called *strongly linked* if there is at least one directed path linking each pair different vertices of V. A vertex singleton is also considered strongly linked. A *strong linkage class* of a digraph is a maximal strongly linked vertex subset of V.[2] A *trivial strong linkage class* contains a single vertex. An *ergodic*[3] *strong linkage class* is a linkage class which has no outgoing arcs.

Each strong linkage class is a subset of a linkage class. The linkage classes in Fig. A.1 (a) have been delimited by a full line. The strong linkage classes have been delimited by a dashed line.

Definition A.7 (source, sink)**.** Call a *source* (*sink*) a vertex which is the head (tail) of no arc.

The sources in the digraph shown in Fig. A.1 (a) are x_1 and x_7. There are no sinks.

[1]The usual term in graph theory is "connected component". However, to avoid confusion with a chemical component represented by a vertex, the term "linkage class", used by Feinberg (1987), is given preference here.

[2]The usual term in graph theory is "strongly connected component". Here, the term "strong linkage class" is used, as in Feinberg (1987).

[3]The term "ergodic" was taken from (Gorban et al., 2010).

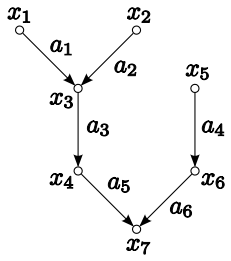

Figure A.2: A rooted tree.

Definition A.8 (rooted tree, leaf, spanning rooted tree, determinant)**.** A *rooted tree* is defined as a digraph in which exactly one arc leaves from all except one vertex, the *root*, from which no arcs leave. Moreover, there is a directed path to the root from each other vertex. A vertex is a *trivial* tree rooted in itself. A *leaf* of a rooted tree is a source of that tree. A *spanning rooted tree* of a weighted digraph is a subgraph which is a rooted tree containing all vertices of the supergraph. In a weighted digraph, the weight of a rooted tree is the product of the weights of its arcs. The weight of a trivial rooted tree is 1, by definition. The *determinant* of a vertex x in a graph is defined as the sum of the weights of all spanning trees rooted in x. If there are no such spanning trees, the determinant is zero.

Fig. A.2 shows a tree rooted in vertex x_7. x_1, x_2 and x_5 are this tree's leaves. The weight of the rooted tree would be $k_1k_2k_3k_4k_5k_6$ if k_j is the weight of arc a_j. In the text, the term "rooted tree" will be shortened to "tree".

Definition A.9 (forest, spanning forest)**.** A *forest* is a disjoint union of trees. Its weight is equal to the product of the weights of the trees. A *spanning forest* of a digraph is a subgraph which is a forest containing all vertices of the supergraph.

Fig. A.1 (b) highlights a spanning forest of the digraph of Fig. A.1 (a).

Appendix B

Graphical Construction of Compartmental Models for Pseudomonomolecular Reaction Networks

This appendix demonstrates how a compartmental model can be constructed graphically for a pseudomonomolecular reaction network if Condition 2.1 on p. 12 is fulfilled. This occurs by transformation of the reaction digraph. This will be illustrated for the pseudomonomolecular reaction network represented by the reaction digraph in Fig. 2.2.

1. Consider a vertex x representing a complex $\sum_j A_j$ of multiple, not necessarily mutually different, components A_j having a non-quasiconstant concentration. x has to be a sink because all steps are assumed pseudomonomolecular. An example is $A_2 + A_3$ in Fig. 2.2. Introduce a virtual component and let its name replace the label of x. Let the complex $\sum_j A_j$ be represented instead by a vertex in a new linkage class. This linkage class contains a copy of all walks to x. Some vertices on such a walk would be the tail of an arc leading away from x: to a vertex from which there is no walk to x. Such arcs are also copied, but directed to a vertex representing a virtual component. The digraph of Fig. 2.2 is transformed into the digraph shown in Fig. B.1. A_8 and A_9 are virtual components.

2. The new linkage class is now multiplied. One copy is provided for each of the components A_j represented in the complex. Each time, the label $\sum_j A_j$ is replaced by a different component A_j of the complex. Condition 2.1 on p. 12 ensures that A_j is not yet represented

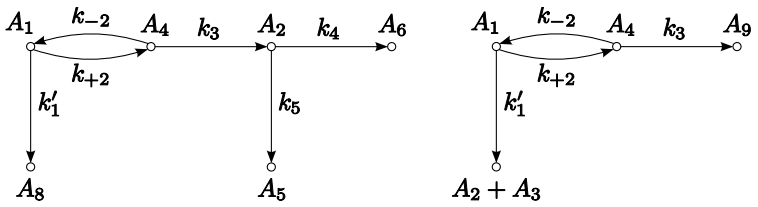

Figure B.1: An intermediate stage in the transformation of the digraph in Fig. 2.2 to the digraph in Fig. 2.4. A_8 and A_9 are virtual components.

by another vertex in the same linkage class. It may however be already represented elsewhere. If this is the case, the vertices have to be contracted. The digraph in Fig. B.1 is transformed into Fig. 2.4. Observe that A_2 is the result of the contraction of two vertices. If there are remaining vertices representing a complex of multiple components, repeat the procedure from step 1. This is not the case for the example.

Appendix C

The Continuous and Discrete Fourier Transforms

Suppose f is a continuous function of the time, t. Its Fourier transform $\mathscr{F}f$ is defined by:

$$(\mathscr{F}f)(\omega) = f(\omega) = \int_{-\infty}^{\infty} f(t) \exp(-i\omega t) \mathrm{d}t. \tag{C.1}$$

g is a complex function of a real variable ω, called the "pulsation". To recover the original f from g, the inverse Fourier transform is to be applied:

$$(\mathscr{F}^{-1}g)(t) = f(t) = \frac{1}{2\pi} \int_{-\infty}^{\infty} g(\omega) \exp(i\omega t) \mathrm{d}\omega. \tag{C.2}$$

Usually, the continuous function f is not known. Instead, a time series would be available consisting of n_t measurements:

$$\mathbf{y} = \left[y(t_1),\, y(t_2),\, \cdots,\, y(t_{n_t})\right]^T, \tag{C.3}$$

where

$$t_j = (j-1)\Delta t. \tag{C.4}$$

Assume $y(t)$ is approximately zero before the time t_1 of the first sample and after the time t_{n_t} of the last sample:

$$y(t) \approx 0 \text{ for } t < t_1 \text{ and } t > t_{n_t}. \tag{C.5}$$

Because of this, the continuous Fourier transform can be approximated by

$$(\mathscr{F}y)(\omega) \approx \int_{t=t_1}^{t_{n_t}} y(t) \exp(-i\omega t) \mathrm{d}t. \tag{C.6}$$

For ω not greater than the Nyquist pulsation, ω_N, see Eq. (5.15), the integral can be approximated by a Riemann sum:

$$(\mathscr{F}y)(\omega) \approx \sum_{j=1}^{n_t} y(t_j) \exp(-i\omega t_j) \Delta t. \tag{C.7}$$

Especially, Eq. (C.7) holds for the equidistant pulsations

$$\omega_k = \frac{2\pi(k-1)}{n_t \Delta t}, \tag{C.8}$$

where $k \in \{1, 2, \ldots, n_t\}$:

$$(\mathscr{F}y)(\omega_k) \approx \sum_{j=1}^{n_t} y(t_j) \exp\left(-i2\pi \frac{k-1}{n_t} \frac{t_j}{\Delta t}\right) \Delta t \tag{C.9}$$

$$\overset{(C.4)}{=} \sum_{j=1}^{n_t} y(t_j) \exp\left(-i2\pi \frac{(k-1)(j-1)}{n_t}\right) \Delta t. \tag{C.10}$$

Comparing this expression with the definition of the *discrete Fourier transform*,

$$(\mathcal{F}\mathbf{y})_k = \frac{1}{\sqrt{n_t}} \sum_{j=1}^{n_t} y(t_j) \exp\left(-i2\pi \frac{(k-1)(j-1)}{n_t}\right), \tag{C.11}$$

it is found that

$$(\mathscr{F}y)(\omega_k) \approx \sqrt{n_t} \Delta t \, (\mathcal{F}\mathbf{y})_k. \tag{C.12}$$

Define the discrete approximation $\mathscr{F}_d$ of the continuous Fourier transform as the vector transformation from $\mathbf{y}$ to

$$\mathscr{F}_d \mathbf{y} = \sqrt{n_t} \Delta t \, \mathcal{F}\mathbf{y}. \tag{C.13}$$

In Eq. (C.12), the pulsation ω_k varies between zero and the Nyquist pulsation ω_N, see Eq. (5.15). This means that k varies from 1 to $\frac{n_t+1}{2}$ if n_t is odd and from 1 to $\frac{n_t}{2}+1$ if n is even. However, the discrete Fourier transform $\mathcal{F}\mathbf{y}$ to the right hand side of Eq. (C.12) actually contains n_t elements. It can be readily proven that conjugate symmetry exists around

the Nyquist pulsation ω_N in $\mathcal{F}\mathbf{y}$ because $\mathbf{y}$ is real. Indeed, any element $(\mathcal{F}\mathbf{y})_{k+1}$ from the latter half can be derived from the first knowing that

$$(\mathcal{F}\mathbf{y})_{n_t-k} = \overline{(\mathcal{F}\mathbf{y})_{k+1}}. \tag{C.14}$$

This is a useful property to find an inverse of $\mathscr{F}_d$.

If n_t is even:

$$\mathscr{F}_d^{-1} : \mathbb{C}^{\frac{n_t}{2}} \times \mathbb{R} \to \mathbb{R}^n \tag{C.15}$$

$$\mathbf{z} \mapsto \frac{1}{\sqrt{n_t}\Delta t}\, \mathcal{F}^{-1}\mathbf{z}^*, \tag{C.16}$$

where $\mathbf{z}^*$ is the conjugate symmetric extension of $\mathbf{z}$. Note that the last element of $\mathbf{z}$ has to be real for a conjugate symmetric extension $\mathbf{z}^*$ to exist. $\mathcal{F}^{-1}$ is the *inverse discrete Fourier transform*.

If n_t is odd:

$$\mathscr{F}_d^{-1} : \mathbb{C}^{\frac{n+1}{2}} \to \mathbb{R}^n \tag{C.17}$$

$$\mathbf{z} \mapsto \frac{1}{\sqrt{n_t}\Delta t}\, \mathcal{F}^{-1}\mathbf{z}^*. \tag{C.18}$$

$\mathscr{F}_d^{-1}$ is a discrete approximation of the inverse Fourier transform. The discrete Fourier transform and its inverse are calculated using the *Fast Fourier Transform* (FFT) algorithm, with an execution time proportional to $n_t \log n_t$.

Suppose a continuous function f of the time is available. Then application of the vector transformation $\mathscr{F}_d$ after sampling of f at the discrete time points t_j offers an approximation for the continuous Fourier transform in the pulsations ω_k. Similarly, applying $\mathscr{F}_d^{-1}$ after sampling of a frequency domain function g in the pulsations ω_k gives an approximation for the continuous inverse Fourier transform of g at the discrete time points t_j. If n_t is even, before being able to apply $\mathscr{F}_d^{-1}$, $g(\omega_N)$ should be made real by removing its imaginary part.

Appendix D

TAPFIT: a Simulation and Regression program for TAP

The program TAPFIT was developed with two purposes:

1. to calculate TAP pulse responses from the reactor model described in Section 4.3,

2. to estimate physico-chemical, especially kinetic, parameters by regression of experimental TAP pulse responses with this model.

TAPFIT was programmed in Fortran 95. During its development, an equilibrium was pursued between versatility, user friendliness and ease of development. Input parameters are passed on to the program in Fortran namelists.

D.1 Model-calculation of TAP pulse responses

The model-calculation of TAP pulse responses can be performed using the two numerical methods presented in Section 4.4. If desired, kinetic rate equations can be automatically generated from a user supplied reaction network. The transfer matrix approach is limited to pseudomonomolecular reaction networks, see Section 4.4. The method of lines can also take user-supplied rate equations.

If the simulation takes place using the method of lines, the program aims at a homogeneous discretization of the axial reactor axis. The user supplies a number of axial intervals per unit length. The program then calculates which number of intervals meets this number best for each zone. The interval lengths $\Delta z^{(l)}$ are therefore different but almost equal for all zones l. The initial value problem given by the vectorial differential

equations (4.14), (4.15), (4.16), (4.17), (4.18), (4.19) and vectorial initial conditions (4.20a) and (4.20b) is solved using the Livermore solver for ordinary differential equations (LSODE) from ODEPACK (Hindmarsh, 1983). The higher the number of intervals per unit length, the more precise the calculated responses, but the more time is needed to perform the required integration. Simulation using the method of lines can be applied to state-defining and state-altering experiments.

Simulation using the transfer matrix approach is limited to state-defining experiment with pseudomonomolecular kinetics. The number of discrete pulsations ω_k at which the outlet fluxes are calculated in the frequency domain can be specified by the user. The complex matrix manipulations are performed using various routines from the Linear Algebra PACKage (LAPACK). The inverse discrete Fourier transform $\mathcal{F}^{-1}$, see Appendix C, is performed using DFFTPACK.

The simulation module of TAPFIT allows the addition of artificial noise of all kinds discussed in Chapter 5. This module relies on the random number generating module RANDOM. ODEPACK, LAPACK, DFFTPACK and RANDOM were taken from the Netlib[1].

D.2 Regression of experimental TAP pulse responses

TAPFIT reads in the experimental data directly from the rough datafiles. The user can choose to perform the regression by ordinary NLSQ regression or SOSR, see Chapter 6. In both cases, the regression is performed using the Levenberg-Marquardt algorithm (Levenberg, 1944; Marquardt, 1963) as implemented in the Orthogonal Distance Regression PACKage (ODRPACK) (Boggs et al., 1987). ODRPACK was used in its ordinary least-squares mode.

Comparison of the Figs. 6.8 and 6.2 shows that the difference between SOSR and NLSQ regression is the application of a three-part conditioning transformation before the regression stage: preconditioning, sample principal component analysis (sPCA) and rescaling. In Chapter 6, the preconditioning transformation used was Riemann cumulation. However, other smoothing operations can also be applied in TAPFIT. The subsequent sPCA and rescaling are based on a calculation of the nonzero eigenvalues and corresponding -vectors of the sample variance matrices $\hat{\mathbf{V}}(\boldsymbol{\epsilon}_{e,v})$, calculated from replicate data as in Eq. (6.25). Explicit calculation of $\hat{\mathbf{V}}(\boldsymbol{\epsilon}_{e,v})$ is not necessary, as the eigenvalues and -vectors can be found directly from the computationally efficient *singular value decomposition* of the error matrices $\mathbf{E}_{e,v}$. The reader is referred to Appendix G

[1] URL: www.netlib.org, consulted on July 15, 2010.

and (Therrien, 1992), (Vandeginste et al., 1998) or (Jolliffe, 2004) for details. Here, the DGESVD routine from LAPACK was used.

Appendix E

Spectrum of Ornstein Uhlenbeck Noise

Because the average of the noise is zero and because the discrete Fourier transform is linear:

$$\mu_{\mathcal{F}\Phi}(\omega_j) = 0, \tag{E.1}$$

for all $j \in \{1, 2, \ldots, \}$.

An simple approximate analytical expression can be found for the autocovariance in the frequency domain. By definition

$$C_{\mathcal{F}\Phi}(\omega_j, \omega_k) = \mathrm{E}\Big[\left(\mathcal{F}\Phi\left(\omega_j\right) - \mu_{\mathcal{F}\Phi(\omega_j)}\right)\overline{\left(\mathcal{F}\Phi\left(\omega_k\right) - \mu_{\mathcal{F}\Phi(\omega_k)}\right)}\Big] \tag{E.2a}$$

$$= E\left[\mathcal{F}\Phi\left(\omega_j\right)\overline{\mathcal{F}\Phi\left(\omega_k\right)}\right]. \tag{E.2b}$$

Application of definition (5.12) yields

$$C_{\mathcal{F}\Phi}(\omega_j, \omega_k) = \mathrm{E}\left[\frac{1}{n_t}\left(\sum_{l=1}^{n_t}\Phi(t_l)\mathrm{e}^{-i\omega_j t_l}\right)\left(\sum_{m=1}^{n_t}\Phi(t_m)\mathrm{e}^{i\omega_k t_m}\right)\right] \tag{E.3a}$$

$$= \frac{1}{n_t}\sum_{l=1}^{n_t}\sum_{m=1}^{n_t} E\left[\Phi(t_l)\Phi(t_m)\right]\mathrm{e}^{-i(\omega_j t_l - \omega_k t_m)}. \tag{E.3b}$$

Because $\big(\Phi(t_j)\big)$ is a real time series with average zero,

$$E\left[\Phi(t_l)\Phi(t_m)\right] = C_\Phi(t_l, t_m) \tag{E.4a}$$

$$= \mathrm{e}^{-\frac{|t_m - t_l|}{\theta}}\sigma_\Phi(t_l)\sigma_\Phi(t_m), \tag{E.4b}$$

where correlation coefficient (5.17) was introduced in the latter step. Substitution of Eq. (E.4b) into (E.3b) gives

$$C_{\mathcal{F}\Phi}(\omega_j, \omega_k) = \frac{1}{n_t} \sum_{l=1}^{n_t} \sum_{m=1}^{n_t} \left(\sigma_\Phi(t_l)\sigma_\Phi(t_m) \mathrm{e}^{-\frac{|t_m - t_l|}{\theta}} \mathrm{e}^{-i(\omega_j t_l - \omega_k t_m)} \right). \tag{E.5}$$

It can be assumed that the correlation time is much smaller than the total recording time:

$$\theta \lll n_t \Delta t. \tag{E.6}$$

For this reason, $\exp(-|t_m - t_l|/\theta)$ will only differ significantly from 0 where

$$|t_m - t_l| \lll n_t \Delta t. \tag{E.7}$$

It is assumed that this relatively small time difference ensures that

$$\sigma_\Phi(t_l)\sigma_\Phi(t_m) \approx \sigma_\Phi^2 \left(\frac{t_l + t_m}{2} \right), \tag{E.8}$$

where $\exp(-|t_m - t_l|/\theta)$ differs significantly from 0. Observe also that

$$\omega_j t_l - \omega_k t_m = \frac{\omega_j + \omega_k}{2}(t_l - t_m) + (\omega_j - \omega_k)\frac{t_l + t_m}{2}. \tag{E.9}$$

In Eq. (E.5), formally consider $\sigma_\Phi : \mathbb{R} \to \mathbb{R}^+$ the continuous-time extension of the time series $\big(\sigma_\Phi(t_j)\big)$, mapping all values outside $[t_1, t_{n_t}]$ to 0. Substitution of Eqs. (4.12), (E.8) and (E.9) into (E.5) then gives:

$$C_{\mathcal{F}\Phi}(\omega_j, \omega_k) \approx \frac{1}{n_t} \sum_{l=-\infty}^{+\infty} \sum_{m=-\infty}^{+\infty} \Bigg(\overbrace{\mathrm{e}^{-\frac{\Delta t|l-m|}{\theta} - i\frac{\omega_j + \omega_k}{2}\Delta t(l-m)}}^{p(l-m)} \cdot \underbrace{\sigma_\Phi^2 \left(\Delta t \,.\, \frac{l+m}{2} \right) \,.\, \mathrm{e}^{-i(\omega_j - \omega_k)\Delta t \frac{l+m}{2}}}_{q(l+m)} \Bigg). \tag{E.10}$$

Replace the dummy variable m by $d = l - m$.

$$C_{\mathcal{F}\Phi}(\omega_j, \omega_k) \approx \frac{1}{n_t} \sum_{l=-\infty}^{+\infty} \sum_{d=-\infty}^{+\infty} p(d)q(2l-d) \tag{E.11a}$$

$$= \frac{1}{n_t} \sum_{d=-\infty}^{+\infty} p(d) \sum_{l=-\infty}^{+\infty} q(2l-d). \tag{E.11b}$$

If $d \in \mathbb{Z}$ is even, the second sum adds up the images under q of all even integers. If d is odd, the second sum adds up the images of all odd integers. (E.11b) can therefore be rewritten as

$$C_{\mathcal{F}\Phi}(\omega_j, \omega_k) \approx \frac{1}{n_t}\left(\sum_{d=-\infty}^{+\infty} p(2d) \cdot \overbrace{\sum_{l=-\infty}^{+\infty} q(2l)}^{S_e} + \sum_{d=-\infty}^{+\infty} p(2d+1) \cdot \underbrace{\sum_{l=-\infty}^{+\infty} q(2l+1)}_{S_o} \right). \quad \text{(E.12)}$$

$2\Delta t S_e$ and $2\Delta t S_o$ are both Riemann sums of the same function q from $-\infty$ to $+\infty$. They are both very good approximations of

$$\int_{-\infty}^{\infty} q(l)\,\mathrm{d}l. \quad \text{(E.13)}$$

Replacing S_o by S_e in Eq. (E.12) gives

$$C_{\mathcal{F}\Phi}(\omega_j, \omega_k) \approx \frac{1}{n_t} \sum_{l=-\infty}^{+\infty} q(2l) \left(\sum_{d=-\infty}^{\infty} p(2d) + \sum_{d=-\infty}^{\infty} p(2d+1) \right) \quad \text{(E.14a)}$$

$$= \frac{1}{n_t} \underbrace{\left(\sum_{l=-\infty}^{+\infty} q(2l) \right)}_{S_q} \cdot \underbrace{\left(\sum_{d=-\infty}^{+\infty} p(d) \right)}_{S_p}. \quad \text{(E.14b)}$$

The factors S_q and S_p can now be studied separately.

From Eq. (4.12) and the definition of q in (E.10):

$$S_q = \sum_{l=-\infty}^{+\infty} \sigma_\Phi^2(t_l).\mathrm{e}^{-i(\omega_k - \omega_j)t_l} \quad \text{(E.15)}$$

or, because $\sigma_\Phi(t)$ disappears for t outside $[t_1, t_{n_t}]$,

$$S_q = \sum_{l=1}^{n_t} \sigma_\Phi^2(t_l).\mathrm{e}^{-i(\omega_k - \omega_j)t_l}. \quad \text{(E.16)}$$

Finally, taking into account Eq. (5.12) defining the discrete Fourier transform,

$$S_q = \begin{cases} \sqrt{n_t}\,\mathcal{F}(\sigma_\Phi^2)(\omega_{k-j}) & \text{if } k \geqslant j \\ \sqrt{n_t}\,\overline{\mathcal{F}(\sigma_\Phi^2)(\omega_{j-k})} & \text{if } k < j \end{cases}. \quad \text{(E.17)}$$

S_p can be written as

$$S_p = \sum_{d=-\infty}^{0} p(d) + \sum_{d=0}^{+\infty} p(d) - p(0). \tag{E.18}$$

From the definition of p in (E.10) it is clear that $p(0) = 1$ and that $p(-d) = \overline{p(d)},\ \forall d \in \mathbb{Z}$. Therefore

$$\begin{aligned} S_p &= 2\,\Re\left(\sum_{d=0}^{+\infty} p(d)\right) - 1 && \text{(E.19a)}\\ &= 2\,\Re\left(\sum_{d=0}^{+\infty} \mathrm{e}^{-\Delta t\left(\frac{1}{\theta}+i\frac{\omega_j+\omega_k}{2}\right)d}\right) - 1 && \text{(E.19b)}\\ &= 2\,\Re\left(\frac{1}{1-\mathrm{e}^{-\Delta t\left(\frac{1}{\theta}+i\frac{\omega_j+\omega_k}{2}\right)}}\right) - 1 && \text{(E.19c)}\\ &= 2\Re\left(\frac{1}{E}\right) - 1 && \text{(E.19d)} \end{aligned}$$

where

$$E = 1 - \mathrm{e}^{-\Delta t\left(\frac{1}{\theta}+i\frac{\omega_j+\omega_k}{2}\right)}. \tag{E.20}$$

Observe that

$$\Re\left(\frac{1}{E}\right) = \frac{\Re E}{\overline{E}\,E} \tag{E.21}$$

where

$$\Re E = 1 - \mathrm{e}^{-\frac{\Delta t}{\theta}} \cos\left(\frac{\omega_j+\omega_k}{2}\Delta t\right) \tag{E.22}$$

and

$$\begin{aligned} \overline{E}E &= \left(1-\mathrm{e}^{-\Delta t\left(\frac{1}{\theta}-i\frac{\omega_j+\omega_k}{2}\right)}\right)\left(1-\mathrm{e}^{-\Delta t\left(\frac{1}{\theta}+i\frac{\omega_j+\omega_k}{2}\right)}\right) && \text{(E.23a)}\\ &= 1 - \mathrm{e}^{-\frac{\Delta t}{\theta}}\left(\mathrm{e}^{i\frac{\omega_j+\omega_k}{2}\Delta t} + \mathrm{e}^{-i\frac{\omega_j+\omega_k}{2}\Delta t}\right) + \mathrm{e}^{-2\frac{\Delta t}{\theta}} && \text{(E.23b)}\\ &= 1 - 2\,\mathrm{e}^{-\frac{\Delta t}{\theta}} \cos\left(\frac{\omega_j+\omega_k}{2}\Delta t\right) + \mathrm{e}^{-2\frac{\Delta t}{\theta}}. && \text{(E.23c)} \end{aligned}$$

Substituting Eqs. (E.22) and (E.23c) in Eq. (E.21) and the resulting expression in Eq. (E.19d) yields

$$S_p = 2\,\frac{1 - \mathrm{e}^{-\frac{\Delta t}{\theta}} \cos\left(\frac{\omega_j+\omega_k}{2}\Delta t\right)}{1 - 2\exp\left(-\frac{\Delta t}{\theta}\right)\cos\left(\frac{\omega_j+\omega_k}{2}\Delta t\right) + \mathrm{e}^{-2\frac{\Delta t}{\theta}}} - 1 \tag{E.24a}$$

$$= \frac{1 - \mathrm{e}^{-2\frac{\Delta t}{\theta}}}{1 - 2\exp\left(-\frac{\Delta t}{\theta}\right)\cos\left(\frac{\omega_j+\omega_k}{2}\Delta t\right) + \mathrm{e}^{-2\frac{\Delta t}{\theta}}}. \tag{E.24b}$$

Observe that $\mathrm{e}^{-\frac{\Delta t}{\theta}}$ is the coefficient of correlation between any two successive samples of $\big(\Phi(t_j)\big)$. If the traditional notation ρ is adopted, substitution of Eqs. (E.17) and (E.24b) into Eq. (E.14b) gives

$$C_{\mathcal{F}\Phi}(\omega_j,\,\omega_k) \approx \begin{cases} \frac{1}{\sqrt{n_t}} \frac{\left(1-\rho^2\right)\,.\,\mathcal{F}(\sigma^2)(\omega_{k-j})}{1-2\rho\cos\left(\frac{\omega_j+\omega_k}{2}\Delta t\right)+\rho^2} & \text{if } k \geqslant j \\ \frac{1}{\sqrt{n_t}} \frac{\left(1-\rho^2\right)\,.\,\overline{\mathcal{F}\sigma^2(\omega_{j-k})}}{1-2\rho\cos\left(\frac{\omega_j+\omega_k}{2}\Delta t\right)+\rho^2} & \text{if } k < j. \end{cases} \tag{E.25}$$

Note that despite their being approximate, the expressions for $C_{\mathcal{F}\Phi}(\omega_j,\,\omega_k)$ and $C_{\mathcal{F}\Phi}(\omega_k,\,\omega_j)$ are complex conjugates, as is theoretically required, see Section 5.2.

The variance of $\mathcal{F}\Phi\,(\omega_j)$ is found as a special case:

$$C_{\mathcal{F}\Phi}(\omega_j) \approx \frac{1}{\sqrt{n_t}} \frac{\left(1-\rho^2\right)\,.\,\mathcal{F}\sigma^2\,(0)}{1 - 2\rho\cos\left(\omega_j\Delta t\right) + \rho^2}. \tag{E.26}$$

Definition (5.12) shows that

$$\mathcal{F}\sigma^2\,(0) = \frac{1}{\sqrt{n_t}} \sum_{k=1}^{n_t} \sigma^2(t_k) \tag{E.27a}$$

$$= \sqrt{n_t}\,(\sigma^2)_m \tag{E.27b}$$

where $(\sigma^2)_m$ is the time-averaged variance of the signal. Substitution into (E.26) gives

$$C_{\mathcal{F}\Phi}(\omega_j) \approx \frac{\left(1-\rho^2\right)(\sigma^2)_m}{1 - 2\rho\cos\left(\omega_j\Delta t\right) + \rho^2}. \tag{E.28}$$

Observe that variability of the variance in time does not affect the variance profile of the spectrum, only the time average does.

Appendix F

Least-Squares Regression

Very generally, say $\mathbf{y} \in \mathbb{R}^{n\times 1}$ is a vector of empirical values and $\mathbf{f}(\mathbf{b})$ its analogue calculated from a model with parameters collected in a vector $\mathbf{b} \in \mathbb{R}^{p\times 1}$. Assume that the model applies with some real, unknown parameters $\boldsymbol{\beta}$:

$$\mathbf{y} = \mathbf{f}(\boldsymbol{\beta}) + \boldsymbol{\epsilon} \tag{F.1}$$

where $\boldsymbol{\epsilon}$ is a random error vector with multidimensional normal distribution with average zero ($\mathbf{0}_n$) and variance matrix $\mathbf{I}_n\,\sigma^2$:

$$\boldsymbol{\epsilon} \sim N\left(\mathbf{0}_n, \mathbf{I}_n\,\sigma^2\right). \tag{F.2}$$

$\boldsymbol{\beta}$ is estimated as $\hat{\boldsymbol{\beta}}$, minimizing the residual sum of squares

$$S(\mathbf{b}) = \|\mathbf{y} - \mathbf{f}(\mathbf{b})\|^2. \tag{F.3}$$

The following important properties apply in good approximation if a first order Taylor expansion of $\mathbf{f}$ is valid in good approximation in a sufficiently large domain about $\boldsymbol{\beta}$:

$$\mathbf{f}(\boldsymbol{\beta} + \Delta\mathbf{b}) \approx \mathbf{f}(\boldsymbol{\beta}) + \mathbf{J}\cdot\Delta\mathbf{b}, \tag{F.4}$$

with $\mathbf{J}$ the Jacobian matrix

$$\mathbf{J} = \frac{\partial \mathbf{f}}{\partial \mathbf{b}}(\boldsymbol{\beta}) \in \mathbb{R}^{n\times p}. \tag{F.5}$$

Property F.1. *$\hat{\boldsymbol{\beta}}$ is multidimensional normally distributed with mean $\boldsymbol{\beta}$ and variance matrix*

$$\mathbf{V}(\hat{\boldsymbol{\beta}}) = \left(\mathbf{J}^T\cdot\mathbf{J}\right)^{-1}\sigma^2. \tag{F.6}$$

It follows that $\hat{\boldsymbol{\beta}}$ is an unbiased and maximum-likelihood estimator of $\boldsymbol{\beta}$. The Jacobian $\mathbf{J}$ is calculated from

$$\mathbf{J} \approx \frac{\partial \mathbf{f}}{\partial \mathbf{b}}(\hat{\boldsymbol{\beta}}) \tag{F.7}$$

and the error variance σ^2 is estimated as the mean square residual:

$$s^2 = \frac{\left(\mathbf{y} - \mathbf{f}(\hat{\boldsymbol{\beta}})\right)^T \cdot \left(\mathbf{y} - \mathbf{f}(\hat{\boldsymbol{\beta}})\right)}{n - p}. \tag{F.8}$$

The variance matrix $\mathbf{V}(\hat{\boldsymbol{\beta}})$ is estimated as

$$\hat{\mathbf{V}}(\hat{\boldsymbol{\beta}}) = (\mathbf{J}^T \cdot \mathbf{J})^{-1} s^2. \tag{F.9}$$

Property F.2. *The variable*

$$t_j = \frac{\hat{\beta}_j - \beta_j}{\sqrt{\hat{V}_{jj}(\hat{\boldsymbol{\beta}})}}, \tag{F.10}$$

where $\hat{V}_{jj}(\hat{\boldsymbol{\beta}})$ is the jth diagonal element of $\hat{\mathbf{V}}(\hat{\boldsymbol{\beta}})$, is distributed as Student's t distribution with $n - p$ degrees of freedom.

This allows to test whether the real, unknown parameter β_j differs significantly from a certain value β_j^*. It is concluded with likelihood $1-\alpha$ that it does not if

$$\left| \frac{\hat{\beta}_j - \beta_j^*}{\sqrt{\hat{V}_{jj}(\hat{\boldsymbol{\beta}})}} \right| < t_{1-\alpha/2\,:\,n-p}, \tag{F.11}$$

where the $t_{1-\alpha/2\,:\,n-p}$ quantile can be calculated with a suitable statistical package. If $\beta_j = \beta_j^*$, there is a probability $1 - \alpha$ that inequality (F.11) leads to the correct conclusion, namely that β_j does not differ significantly from β_j^*. Typically, α is taken to be 0.05. This test can be used to verify whether a parameter differs significantly from a neutral (trivial) value (usually 0), or, shortly, whether the parameter estimate is significant. Eq. (F.11) is readily transformed into

$$\hat{\beta}_j - \frac{\Delta\beta_j}{2} < \beta_j^* < \hat{\beta}_j + \frac{\Delta\beta_j}{2}, \tag{F.12}$$

representing the $1 - \alpha$ *confidence interval* for parameter β_j^*, with

$$\Delta\beta_j = 2\, t_{1-\alpha/2\,:\,n-p} \sqrt{\hat{V}_{jj}(\hat{\boldsymbol{\beta}})}. \tag{F.13}$$

In the frequently occurring case that

$$n - p \ggg 1, \tag{F.14}$$

t_j in Eq. (F.10) can be considered unit normally distributed. Consequently, the approximation

$$t_{1-\alpha/2\,:\,n-p} \approx z_{1-\alpha/2} \tag{F.15}$$

can then be applied in Eqs. (F.11) and (F.13).

Property F.3. *The variable*

$$F = \frac{(\hat{\boldsymbol{\beta}} - \boldsymbol{\beta})^T \cdot \mathbf{J}^T \cdot \mathbf{J} \cdot (\hat{\boldsymbol{\beta}} - \boldsymbol{\beta})}{p\, s^2} \tag{F.16}$$

is distributed as Snedecor's F distribution with p and $n - p$ degrees of freedom.

This allows to test whether $\boldsymbol{\beta}$ differs significantly from a certain vector of parameter values $\boldsymbol{\beta}^*$. It is concluded with likelihood $1 - \alpha$ that it does not if

$$\frac{(\hat{\boldsymbol{\beta}} - \boldsymbol{\beta}^*)^T \cdot \mathbf{J}^T \cdot \mathbf{J} \cdot (\hat{\boldsymbol{\beta}} - \boldsymbol{\beta}^*)}{p\, s^2} < F_{1-\alpha\,:\,p,n-p}. \tag{F.17}$$

Mostly $\boldsymbol{\beta}^*$ is taken to be a vector of neutral parameters (mostly the null vector). Eq. (F.17) then means that the regression is globally insignificant. Inequality (F.17) implicitly defines the joint *confidence region* of all parameters, delimited by a hyperellipsoid. $p\,F$ with F given by Eq. (F.16) can be considered χ^2 distributed with p degrees of freedom if (F.14) is valid. The approximation

$$F_{1-\alpha\,:\,p,n-p} \approx \frac{1}{p}\,\chi^2_{1-\alpha\,:\,p} \tag{F.18}$$

can then be applied in (F.17).

Appendix G

Singular Value Decomposition: Practical

Efficient numerical methods are available to perform the *singular value decomposition* (SVD) of $\mathbf{E}_{e,v} \in \mathbb{R}^{n_t \times r_{e,v}}$ with rank $r_{e,v} - 1$:

$$\mathbf{E}_{e,v} = \mathbf{L} \cdot \mathbf{\Sigma} \cdot \mathbf{R}^T \tag{G.1}$$

with $\mathbf{\Sigma} \in \mathbb{R}^{(r_{e,v}-1)\times(r_{e,v}-1)}$ diagonal, holding the singular values,

$$\mathbf{\Sigma} = \begin{bmatrix} s'_1 & 0 & \cdots & 0 \\ 0 & s'_2 & \cdots & 0 \\ \vdots & \vdots & \ddots & \vdots \\ 0 & 0 & \cdots & s'_{r_{e,v}-1} \end{bmatrix}, \tag{G.2}$$

positive and ranked from high to low ($s'_1 \geqslant s'_2 \geqslant \ldots \geqslant s'_{r_{e,v}-1} > 0$), $\mathbf{L} \in \mathbb{R}^{n_t \times (r_{e,v}-1)}$ having the orthonormal so-called *left-singular vectors* and $\mathbf{R} \in \mathbb{R}^{n_t \times (r_{e,v}-1)}$ having the orthonormal *right-singular vectors* as columns:

$$\mathbf{L}^T \cdot \mathbf{L} = \mathbf{I} \text{ and } \mathbf{R}^T \cdot \mathbf{R} = \mathbf{I}. \tag{G.3}$$

Now observe that

$$\hat{\mathbf{V}}(\boldsymbol{\epsilon}_{e,v}) = \frac{1}{r_{e,v}-1} \mathbf{E}_{e,v} \cdot \mathbf{E}_{e,v}^T \tag{G.4}$$

$$= \frac{1}{r_{e,v}-1} \mathbf{L} \cdot \mathbf{\Sigma} \cdot \mathbf{R}^T \cdot \mathbf{R} \cdot \mathbf{\Sigma} \cdot \mathbf{L}^T \tag{G.5}$$

$$= \frac{1}{r_{e,v}-1} \mathbf{L} \cdot \mathbf{\Sigma}^2 \cdot \mathbf{L}^T. \tag{G.6}$$

Comparison with Eq. (6.8) teaches that the eigenvectors of $\hat{\mathbf{V}}(\boldsymbol{\epsilon}_{e,v})$ are the left singular values of $\mathbf{E}_{e,v}$ and that its eigenvalues are

$$s_j^2 = \frac{{s'_j}^2}{r_{e,v} - 1} \tag{G.7}$$

for all $j \in \{1, 2, \ldots, r_{e,v} - 1\}$.

Glossary

Bode plots	The Bode magnitude plot is a logarithmic plot representing the modulus of a transfer function as a function of the frequency. The Bode phase plot is a semilogarithmic plot representing the phase of a transfer function as a function of the frequency, where the latter is represented on a logarithmically scaled axis.
Colored noise	Noise modeled as a random sequence, any two different elements of which are generally correlated.
Compartmental kinetics	Kinetics described by a compartmental model, represented by a reaction graph.
Directed graph, digraph	A collection of vertices (nodes) and arcs (arrows) going from one vertex to another.
Elementary step	A reaction representing an irreducible event at the molecular level.
Global identifiability	A set of parameters is globally identifiable if almost each combination of values of these parameters can be uniquely identified from experimental data without experimental error.
Homoskedastic random sequence	A random sequence, any two elements of which have the same variance.
Intermediate	A component represented in a reaction network, but not in the net reaction.

Isothermal data	A set of data stemming from kinetic experiments with equal reaction temperature.
Kinetic transfer function	In the Laplace domain, a function of the Laplace variable, which, upon multiplication with the net source of a component, yields the concentration of another, not necessarily different, component. Kinetic transfer functions can be found graph-theoretically for pseudomonomolecular reaction networks.
Knudsen diffusion	Low pressure diffusion through a porous bed, characterized by a diffusion coefficient independent of composition and pressure.
Local identifiability	A set of parameters is locally identifiable if almost each combination of values of these parameters can be deduced to pertain to a denumerable set of candidates, from experimental data without experimental error.
Moment invariant	The observable kinetic behavior of a pseudomonomolecular reaction network is described by kinetic transfer functions. The invariants are parametric functions of the apparent rate coefficients, appearing in these transfer functions.
Ornstein Uhlenbeck noise	Noise modeled as a Gaussian stochastic process Y depending on a real value t, any two samples $Y(t_i)$ and $Y(t_j)$ of which have a correlation which depends on the absolute time difference $\|t_j - t_i\|$ as a descending exponential.
Pseudomonomolecular reaction network	A reaction network consisting of monomolecular and pseudomonomolecular elementary steps. A monomolecular elementary step has a single molecule as reactant. A pseudomonomolecular elementary step has multiple reactant molecules, all but one of which are present in a quasiconstant concentration.

Random sequence	A stochastic vector containing chronological values of a stochastic process.
Reaction graph	A digraph representing a pseudomonomolecular reaction network governed by compartmental kinetics. Each vertex in a reaction graph represents a component (or rather, its concentration) and each arc represents an elementary step.
Reaction network	A set of elementary steps.
Second-order statistical regression (SOSR)	An extension of nonlinear ordinary least-squares regression for time series, where this regression is precluded by a series of conditioning transforms of experimental and model-calculated time series.
Shortest reaction pathway	In a pseudomonomolecular reaction network, the shortest reaction pathway from A_k to A_j is the set of elementary steps represented by the shortest pathway from A_k to A_j in the kinetic graph.
Spectrally localized noise	Noise modeled as a stochastic process, the Fourier transform of which has a standard deviation peak about a certain frequency.
State-altering TAP-experiment	A series of TAP pulse response experiments in which the reactant pulses cause a significant change of the catalyst.
State-defining TAP-experiment	A series of TAP pulse response experiments in which the size of the reactant pulses is low enough to assume them to cause no significant change of the catalyst.
Stochastic process	A stochastic variable which is a function of a real variable, usually time.
TAPFIT	A simulation and regression program for temporal analysis of products.

Temporal analysis of products (TAP)	A transient kinetic experimental technique performed on a continuously evacuated microreactor loaded with a fixed catalyst bed, in which the response to a pulse of reactants is recorded by means of mass spectrometry.
Thin-zone-TAP-reactor	A TAP-reactor packed with three zones, the middle one of which is much thinner than the outer ones. The middle zone is reactive (catalytic) while the outer zones are inert.
Time series	A vector of which the ith element is a value $f(t_i)$, where f is a function of time and $t_i = (i-1)\,\Delta t$. Δt is the positive sampling interval.
Unidentifiability	A set of parameters is unidentifiable if it is not locally identifiable.
White noise	Noise modeled as a random sequence, any two different elements of which are uncorrelated.
Y-procedure	A procedure developed to calculate gas concentrations and gas production (or consumption) in the reactive zone of a thin-zone-TAP-reactor, as a function of time. This procedure does not rely on any a priori assumptions about the reaction kinetics.

Bibliography

Asadullin, R.M., Spivak, S.I., Shavaleev, N.M., 1996. Methods of elimination and the problem of nonuniqueness of inverse problem solutions in models of non-stationary chemical kinetics (linear systems). ACH-Models in Chemistry 133, 107–114.

Balcaen, V., Sack, I., Olea, M., Marin, G.B., 2009. Transient kinetic modeling of the oxidative dehydrogenation of propane over a vanadia-based catalyst in the absence of O_2. Applied Catalysis A: General 371, 31–42.

Bang-Jensen, J., Gutin, G., 2008. Digraphs: Theory, Algorithms and Applications, second ed. Springer, London.

Bennet, C.O., 1982. Understanding heterogeneous catalysis through the transient method. ACS Symposium Series 178, 1–32.

Bennett, C.O., 2000. Experiments and processes in the transient regime for heterogeneous catalysis. Advances in Catalysis 44, 329–416.

Berger, R.J., Kapteijn, F., Moulijn, J.A., Marin, G.B., De Wilde, J., Olea, M., Chen, D., Holmen, A., Lietti, L., Tronconi, E., Schuurman, Y., 2008. Dynamic methods for catalytic kinetics. Applied Catalysis A: General 342, 3–28.

Berman, M., Schoenfeld, R., 1956. Invariants in experimental data on linear kinetics and the formulation of models. Journal of Applied Physics 27, 1361–1370.

Biloen, P., 1983. Transient kinetic methods. Journal of Molecular Catalysis 21, 17–24.

Boggs, P.T., Byrd, R.H., Schnabel, R.B., 1987. A stable and efficient algorithm for nonlinear orthogonal distance regression. SIAM Journal on Scientific and Statistical Computation 8, 1052–1078.

Boudart, M., 1968. Kinetics of Chemical Processes. Prentice-Hall, Englewood Cliffs.

Craciun, G., Pantea, C., 2008. Identifiability of chemical reaction networks. Journal of Mathematical Chemistry 44, 244–259.

Constales, D., Yablonsky, G.S., Marin, G.B., Gleaves, J.T., 2001. Multi-zone TAP-reactors theory and application: II. The three-dimensional theory. Chemical Engineering Science 56, 1913–1923.

Constales, D., Yablonsky, G.S., Marin, G.B., Gleaves, J.T., 2004. Multi-zone TAP-reactors theory and application. III. Multi-response theory and criteria of instantaneousness. Chemical Engineering Science 59, 3725–3736.

Constales, D., Shekhtman, S.O., Yablonsky, G.S., Marin, G.B., Gleaves, J.T., 2006. Multi-zone TAP-reactors theory and application IV. Ideal and non-ideal boundary conditions. Chemical Engineering Science 61, 1878–1891.

Cutlip, M.B., Yang, C.C., Bennett, C.O., 1972. Parameter Estimation from Transient Rate Data. AIChE Journal 18, 1073–1076.

Doob, J.L., 1942. The Brownian movement and stochastic equations. Annals of Mathematics 43, 351–369.

Draper, N.R., Smith, H., 1998. Applied Regression Analysis (3rd ed.). Wiley, New York.

Efstathiou, A.M., Verykios, X.E., 1997. Transient methods in heterogeneous catalysis: Experimental features and application to study mechanistic aspects of the CH_4/O_2 (OCM), NH_3/O_2 and NO/He reactions. Applied Catalysis A: General 151, 109–166.

Evstigneev, V.A., Yablonskii, G.S., 1979. Justification of one relationship for the stationary kinetics of catalytic reactions. Kinetics and Catalysis 20, 1278–1283.

Feinberg, M., 1987. Chemical reaction network structure and the stability of complex isothermal reactors–I. The deficiency zero and deficiency one theorems. Chemical Engineering Science 42, 2229–2268.

Froment, G.F., Hosten, L.H., 1981. Catalytic Kinetics: Modelling. In Anderson, J.R., Boudart, M. (Eds.), Catalysis – Science and Technology, vol. 2. Berlin: Springer-Verlag, chapter 3, pp. 97–170.

Furusawa, T., Suzuki, M., Smith, J.M., 1976. Rate parameters in heterogeneous catalysis by pulse techniques. Catalysis Reviews: Science and Engineering 13, 43–76.

Gleaves, J.T., Ebner, J.R., Kuechler, T.C., 1988. Temporal analysis of products (TAP) – a unique catalyst evaluation system with submillisecond time resolution. Catalysis Reviews: Science and Engineering 30, 49–116.

Gleaves, J.T., Yablonskii, G.S., Phanawadee, P., Schuurman, Y., 1997. TAP-2: an interrogative kinetics approach. Applied Catalysis A: General 160, 55–88.

Gleaves, J.T., Yablonsky, G.S., Zheng, X., Fushimi, R., Mills, P.L., 2010. Temporal analysis of products (TAP)–Recent advances in technology for kinetic analysis of multi-component catalysts. Journal of Molecular Catalysis A: Chemical 315, 108–134.

Goldstein, B.N., 1983. Analysis of cyclic enzyme reaction schemes by the graph-theoretical method. Journal of Theoretical Biology 103, 247–264.

Goldstein, B.N., 2009. Transient enzyme kinetics: Graph-theoretic approach. Biophysical Chemistry 141, 193–197.

Gorban, A.N., Radulescu, O., Zinovyev, A.Y., 2010. Asymptotology of chemical reaction networks. Chemical Engineering Science 65, 2310–2324.

Gorskii, V.S., Spivak, S.I., 1989. Identifiability of parameters – One of the most important steps in constructing mathematical models in chemistry. Journal of Structural Chemistry, 29, 924–930.

Graybill, F.A., Iyer, H.K., 1994. Regression Analysis: Concepts and Applications. Wadsworth, Belmont.

Happel, J., 1978. Transient tracing. Chemical Engineering Science 33, 1569–1978.

Happel, J., Walter, E., Lecourtier, Y., 1986a. Isotopic Assessment of Fundamental Catalytic Mechanisms by Kinetic Modeling. Industrial & Engineering Chemistry Fundamentals 25, 704–712.

Happel, J., Walter, E., Lecourtier, Y., 1986b. Identifiability and distinguishability of catenary and quasi-catenary models. Supplementary material to (Happel et al., 1986a), available upon request from Industrial & Engineering Chemistry Fundamentals.

Hindmarsh, A.C., 1983. ODEPACK, A Systematized Collection of ODE Solvers. In R.S. Stepleman et al. (Eds.), Scientific Computing. Amsterdam: North-Holland.

Hougen, O.A., Watson, K.M., 1947. Chemical Process Principles. Part Three. Kinetics and Catalysis. Wiley, New York.

Huizenga, D.G., Smith, D.M., 1986. Knudsen diffusion in random assemblages of uniform spheres. AIChE Journal 32, 1–6.

Hulburt, H.M., Kim, Y.G., 1966. Reaction mechanisms for engineering design. Industrial & Engineering Chemistry 58, No. 9, 20–31.

Jaulin, L., Kieffer, M., Didrit, O., Walter, E., 2001. Applied Interval Analysis. Springer, Berlin.

Jolliffe, I.T., 2004. Principal Component Analysis (2nd ed.). In P. Bickel et al. (Eds.), Springer Series in Statistics. New York: Springer.

King, E.L., Altman, C., 1956. A schematic method of deriving the rate laws for enzyme-catalyzed reactions. Journal of Physical Chemistry 60, 1375–1378.

Kittrell, J.R., Hunter, W.G., Watson, C.C., 1965. Nonlinear least squares analysis of catalytic rate models. AIChE Journal 11, 1051–1057.

Lagrange, S., Delanoue, N., Jaulin, L., 2008. Injectivity analysis using interval analysis: Application to structural identifiability. Automatica 44, 2959–2962.

Levenberg, K., 1944. A method for the solution of certain non-linear problems in least-squares. Quarterly of Applied Mathematics 2, 164–168.

Marquardt, D.W., 1963. An algorithm for least-squares estimation of nonlinear parameters. Journal of the Society for Industrial & Applied Mathematics 11, 431–441.

Mason, S.J., Zimmermann, H.J., 1960. Electronic circuits, signals, and systems, pp. 92–126. Wiley, New York.

Massart, D.L., Vandeginste, B.G.M., Buydens, L.M.C., De Jong, S., Lewi, P.J., Smeyers-Verbeke, J., 1997. Handbook of Chemometrics and Qualimetrics: Part A. In B.G.M. Vandeginste, S.C. Rutan (Eds.), Data Handling in Science and Technology. Amsterdam: Elsevier.

Mateu, J., 1997. Methods of assessing and achieving normality applied to environmental data. Environmental Management 21, 767–777.

Mills, P.L., Lerou, J.J., 1993. Transient response methods for assisted design of gas phase heterogeneous catalysts: experimental techniques and mathematical modeling. Reviews in Chemical Engineering 9, 1–96.

Nijhuis, T.A., van den Broeke, L.J.P., van de Graaf, J.M., Kapteijn, F., Makkee, M., Moulijn, J.A., 1997. Bridging the gap between macroscopic and NMR diffusivities. Chemical Engineering Science 52, 3401–3404.

Papoulis, A., 1991. Probability, Random Variables, and Stochastic Processes. 3rd Ed., McGraw-Hill, Singapore, p. 285.

Peebles, P. Jr., 1987. Probability, random variables, and random signal principles. In: Director, S.W. (Ed.), McGraw-Hill Series in Electrical Engineering, 2nd Ed., McGraw-Hill, Singapore, p. 142.

Pekař, M., 2005. Thermodynamics and foundations of mass-action kinetics. Progress in Reaction Kinetics and Mechanism 30, 3–113.

Petrov, L.A., 1992. Application of graph theory to study of the kinetics of heterogeneous catalytic reactions, in: Bonchev, D., Rouvray, D.H. (Eds.), Chemical Graph Theory: Reactivity and Kinetics, pp. 1–52. Abacus Press/Gordon & Breach, Philadelphia.

Phanawadee, P., 1999. Theory and methodology of TAP Knudsen pulse response experiment. PhD Dissertation, Washington University, St. Louis, MO.

Poelman, H., Sels, B.F., Olea, M., Eufinger, K., Paul, J.S., Moens, B., Sack, I., Balcaen, V., Bertinchamps, F., Gaigneaux, E.M., Jacobs, P.A., Marin, G.B., Poelman, D., De Gryse, R., 2007. New supported vanadia catalysts for oxidation reactions prepared by sputter deposition. Journal of Catalysis 245, 156–172.

Raksanyi, A., Lecourtier, Y., Walter, E., Venot, E., 1985. Identifiability and distinguishability testing in computer algebra. Mathematical Biosciences 77, 245–266.

Renken, A., 1993. Transient operation for the purpose of modeling heterogeneous catalytic reactions. International Chemical Engineering 33, 61–71.

Roelant, R., Constales, D., Yablonsky, G.S., Van Keer, R., Rude, M.A., Marin, G.B., 2007. Noise in temporal analysis of products (TAP) pulse responses. Catalysis Today 121, 269–281.

Roelant, R., Constales, D., Van Keer, R., Marin, G.B., 2008. Second-order statistical regression and conditioning of replicate transient kinetic data. Chemical Engineering Science 63, 1850–1865.

Roelant, R., Constales, D., Van Keer, R., Marin, G.B., 2010. Identifiability of rate coefficients in linear reaction networks from isothermal transient experimental data. Chemical Engineering Science 65, 2333–2343.

Rothaemel, M., Baerns, M., 1996. Modeling and simulation of transient adsorption and reaction in vacuum using the temporal analysis of products reactor. Industrial & Engineering Chemistry Research 35, 1556–1565.

Sack, I., Balcaen, V., Olea, M., Poelman, H., Marin, G.B., 2006. Kinetic modeling of the reoxidation of vanadia-based catalysts. Catalysis Today 112, 68–72.

Sack, I., 2006. A Kinetic Study of the Reduction and the Reoxidation of Vanadia-Based Catalysts by Temporal Analysis of Products. PhD Dissertation, Ghent University, Gent.

Schiesser, W.E., 1991. The Numerical Method of Lines. Academic Press, San Diego.

Schuurman, Y., 2007. Assessment of kinetic modeling procedures of TAP experiments. Catalysis Today 121, 187–196.

Schuurman, Y., 2008. Aspects of kinetic modeling of fixed bed reactors. Catalysis Today 138, 15–20.

Schwarz, G.E., 1978. Estimating the dimension of a model. Annals of Statistics 6, 461–464.

Seber, G.A.F., Lee, A.J., 2003. Linear Regression Analysis, second ed. Wiley, New York.

Seber, G.A.F., Wild, C.J., 2003. Nonlinear Regression. Wiley, New York.

Seinfeld, J.H., Lapidus, L., 1974. Process Modeling, Estimation, and Identification. In: Amundsen, N.R. (Editor), Mathematical Methods in Chemical Engineering, Vol. 3, Prentice-Hall, Englewood Cliffs, p. 197.

Shekhtman, S.O., Yablonskii, G.S., Gleaves, J.T., Chen, S., 1999. Thin-zone TAP-reactor: theory and application. Chemical Engineering Science 54, 4371–4378.

Tamaru, K., 1964. Adsorption measurements during surface catalysis. Advances in Catalysis and Related Subjects 15, 65–90.

Tantake, P., Phanawadee, P., Boonnumpha, Y., Limtrakul, J., 2007. Comparison between regression analysis and moment analysis for transport and kinetic parameter estimation in TAP experiments under a non-ideal inlet condition. Catalysis Today 121, 261–268.

Therrien, C.W., 1992. Discrete random signals and statistical signal processing. Prentice-Hall, Englewood Cliffs, p. 86.

Uhlenbeck, G.E., Ornstein, L.S., 1930. On the theory of Brownian motion. Physical Review 36, 823–841.

Vajda, S., Rabitz, H., 1988. Identifiability and distinguishability of first-order reaction systems. Journal of Physical Chemistry 92, 701–707.

Vajda, S., Rabitz, H., 1994. Identifiability and distinguishability of general reaction systems. Journal of Physical Chemistry 98, 5265–5271.

Vandeginste, B.G.M., Massart, D.L., Buydens, L.M.C., De Jong, S., Lewi, P.J., Smeyers-Verbeke, J., 1998. Handbook of Chemometrics and Qualimetrics: Part B. In B.G.M. Vandeginste, S.C. Rutan (Eds.), Data Handling in Science and Technology. Amsterdam: Elsevier.

Walter, E., Lecourtier, Y., 1982. Global approaches to identifiability testing for linear and nonlinear state space models. Mathematics and Computers in Simulation 24, 472–482.

Walter, E., Lecourtier, Y., Kao J.-Y., Happel, J., 1989. Identifiability and distinguishability testing for linear models in heterogeneous catalysis. Chemical Engineering Communications 89, 157–172.

Walter, E., Pronzato, L., 1996. On the identifiability and distinguishability of nonlinear parametric models. Mathematics and Computers in Simulation 42, 125–134.

Walter, E., Braems, I., Jaulin, L., Kieffer, M., 2004. Guaranteed Numerical Computation as an Alternative to Computer Algebra for Testing Models for Identifiability, in: Alt, R., Frommer, A., Baker Kearfott, R., Luther, W. (Eds.), Numerical Software with Result Verification. Springer, Berlin, pp. 124–131.

Wang, M.C., Uhlenbeck, G.E., 1945. On the theory of Brownian motion II. Reviews of Modern Physics 17, 323–342.

Weerts, W.L.M., de Croon, M.H.J.M., Marin, G.B., 1996. The adsorption of silane, disilane and trisilane on polycristalline silicon: a transient kinetic study. Journal of Surface Science 367, 321–339.

Yablonskii, G.S., Bykov, V.I., Gorban, A.N., Elokhin, V.I., 1991. Kinetic Models of Catalytic Reactions. Elsevier, Amsterdam, pp. 185–258.

Yablonsky, G.S., Constales, D., Gleaves, J.T., 2002. Multi-scale problems in the quantitative characterization of complex catalytic materials. Systems Analysis Modelling Simulation 42, 1143–1166.

Yablonsky, G.S., Olea, M., Marin, G.B., 2003. Temporal analysis of products: basic principles, applications and theory. Journal of Catalysis 216, 120–134.

Yablonsky, G.S., Constales, D., Gleaves, J.T., 2007. The Y-procedure: How to extract the chemical transformation rate from reaction-diffusion data with no assumption on the kinetic model. Chemical Engineering Science 62, 6754–6767.

Zamostny, P., Belohlav, Z., 2002. Identification of kinetic models of heterogeneously catalyzed reactions. Applied Catalysis A: General 225, 291–299.

Zou, B.S., Duduković, M.P., Mills, P.L., 1994. Modeling of pulsed transport effects in the TAP reactor system. Journal of Catalysis 145, 683–696.

Index